**DE-FC26-00BC15305**

# INTEGRATED APPROACH FOR THE PETROPHYSICAL INTERPRETATION OF POST- AND PRE-STACK 3-D SEISMIC DATA, WELL-LOG DATA, CORE DATA, GEOLOGICAL INFORMATION AND RESERVOIR PRODUCTION DATA VIA BAYESIAN STOCHASTIC INVERSION

**Final Report**
**September 28, 2000 to September 29, 2003**
**By**
**Carlos Torres-Verdín**
**Mrinal K. Sen**

**September 2004**
**Work Performed under Contract No. DE-FC26-00BC15305**
**Prepared for U.S. Department of Energy**

**Purna C. Halder, Project Manager**

U.S. Department of Energy
National Energy Technology Laboratory
One West Third Street
Tulsa, Oklahoma 74103

**Prepared by**

**The University of Texas**
**Center for Petroleum and Geosystems Engineering**
**and the Institute for Geophysics**
**Austin, Texas 78712**

# DISCLAIMER

This report was prepared as an account of work sponsored by an agency of the United States Government. Neither the United States Government nor any agency thereof, nor any of their employees, makes any warranty, express or implied, or assumes any legal liability or responsibility for the accuracy, completeness, or usefulness of any information, apparatus, product, or process disclosed, or represents that its use would not infringe privately owned rights. Reference herein to any specific commercial product, process, or service by trade name, trademark, manufacturer, or otherwise does not necessarily constitute or imply its endorsement, recommendation, or favoring by the United States Government or any agency thereof. The views and opinions of the authors expressed herein do not necessarily state or reflect those of the United States Government or any agency thereof.

# ABSTRACT

The present report summarizes the work carried out between September 30, 2000 and September 30, 2004 under DOE research contract No. DE-FC26-00BC15305.

During the three-year project period, we carried out extensive studies on the inversion post-stack and pre-stack data together with well logs, petrophysical information and fluid flow data. We have achieved all the project goals including development of algorithm for joint inversion of pre-stack seismic data, well logs, and time records of fluid production measurements using stochastic inversion algorithms which were demonstrated on realistic synthetic and field data. Our accomplishments are:

- Joint inversion of post-stack seismic, well log, fluid flow, and petrophysical data: we demonstrated the technique with application to data from the Gulf of Mexico.
- Development of a robust pre-stack full waveform inversion algorithm: A new approach based on iteration-adaptive regularization that makes use of plane wave transformed seismic data, was developed and applied to OBC dataset from the Gulf of Thailand. The algorithm was also implemented on a cluster of personal computers.
- Joint inversion of pre-stack seismic and well-log data: A new stochastic optimization algorithm that makes use of the essential features of seismic and well log data was developed and tested on realistic synthetic dataset.
- Joint inversion of pre-stack seismic and fluid flow data: A novel technique was developed to optimally combine seismic and flow data. The technique makes very realistic estimate of porosity; sensitivity of the flow parameters to two disparate datasets was studied extensively.

- Direct estimation of petrophysical parameters from seismic data: The pre-stack waveform inversion was modified to invert directly for porosity and saturation using the Biot-Gassmann equation at each iteration step.

The final report contains abridged versions of some of our inventions. The works resulted in several peer-reviewed publications. Five papers have been communicated for peer-reviewed publication, and seven papers were presented at conferences. All of these publications and presentations stemmed from work directly related to the goals of our DOE project.

# TABLE OF CONTENTS

# TABLE OF FIGURES

# TABLES OF TABLES

# 1. INTRODUCTION

This report describes work performed by the Center for Petroleum and Geosystems Engineering and the Institute for Geophysics, both with The University of Texas at Austin, between September 30, 2000 and September 30, 2003 under DOE research contract No. DE-FC26-00BC15305.

Work performed by the Center of Petroleum and Geosystems Engineering includes joint inversion of post-stack and pre-stack seismic data, well logs, and time records of fluid production measurements. Work performed by the Institute for Geophysics includes development of a new parallel algorithm for pre-stack waveform inversion for petrophysical parameter estimation. The CPGE and UTIG collaborated on several aspects of the work.

The section Results and Conclusions of this report provides a detailed technical summary of developments and accomplishments stemming from this project.

## 2. EXPERIMENTAL

There are no experimental components of the project to be included in this final report. The tasks and components of the project comprise the development of numerical algorithms and computer software. Likewise, the project includes analysis and interpretation of both field and numerically-simulated data. All of these developments are summarized in the section Results and Conclusions of the report.

# 3. RESULTS AND DISCUSSION

## 3.A. CENTER FOR PETROLEUM AND GEOSYSTEMS ENGINEERING

### 3.A.1: INTRODUCTION

### 3.A.1.1 Problem Statement

Hydrocarbon reservoir characterization aims at providing accurate descriptions of in-place hydrocarbon assets, multi-phase fluid-flow parameters, and reliable appraisals of methods to produce reserves. It is not only important to describe the status of the reservoir prior to commercial production or enhanced recovery operations, but also to forecast fluid behavior accurately under specific production conditions. The ability to forecast production provides a quantitative tool to test whether the assumed reservoir model and fluid-flow properties are reliable. Whenever a discrepancy is found between the forecast and measured fluid production, a feedback loop can be enforced to modify the assumed hydrocarbon reservoir model. Such characterization and evaluation procedure often involves a substantial amount of work and computer time.

The main motivation of this project is to improve the construction of reservoir models amenable to numerical simulation of hydrocarbon production. It is envisioned that improvements to reservoir characterization described in this project will translate into more accurate estimations of reserves, more reliable production forecast, enhanced well placement, and optimal design of asset recovery processes.

The estimation of inter-well petrophysical properties is a central topic of this project. Geophysical inverse theory provides an adequate mathematical framework to infer model parameters from physical measurements of the model's behavior (Tarantola, 1987; Menke, 1989; Sen and Stoffa, 1995). In petroleum applications, in-situ measurements of reservoir properties are difficult to perform due to limited spatial accessibility. Most of the reservoir properties are then inferred from indirect measurements (*e.g.*, well logs, seismic data). Wireline logs and core data are routinely used to estimate petrophysical properties in the vicinity of existing wells (Bassiouni, 1994). Well-log data possess high vertical resolution but quite often well locations are sparsely distributed within the reservoir. This causes the corresponding petrophysical properties to be statistically biased and hence to be rarely representative of the spatial variability within the reservoir. However, this is often overlooked in practical reservoir characterization projects since the well-log data are a primary source of rock and fluid properties.

By contrast, seismic surveys are carried out on a surface grid to infer a three-dimensional (3D) distribution of elastic properties (Brown, 1999). The seismic acquisition process embodies a dense lateral coverage of measurements. Relatively low vertical resolution (anywhere between 5 and 25 m) is the most prominent disadvantage of seismic data (Liner, 1999). Processing errors and low signal-to-noise ratios can further limit the use of these measurements. Different types of seismic measurements are delivered for interpretation depending on the acquisition and processing techniques. Seismic measurements considered in this project comprise pre-stack, pseudo-angle stack, and post-stack traces. Pre-stack seismic data are sensitive to spatial variations of compressional- and shear-wave velocity. On the other hand, post-stack and pseudo-angle stack seismic data are subsets of pre-stack seismic amplitude data and therefore are inherently less sensitive to subsurface variations of elastic parameters (Yilmaz, 2002).

The use of 3D seismic data is widely accepted among reservoir practitioners, especially at the stage of deriving geometrical models of reservoir compartments and for estimating vertical and lateral continuity (Hilterman, 1999). Seismic attributes are also commonly used to guide the interpretation and delineation of reservoir units (Dorn, 1998; Brown 1999). Inversion of post-stack seismic amplitudes into acoustic impedance has also proved of great practical value in reservoir delineation, fluid detection, and well placement (Yilmaz, 2000).

Well logs and core data are traditionally used to estimate reservoir properties that are subsequently extrapolated away from existing wells via geostatistical techniques (Chilès and Delfiner, 1999). There are a number of references that describe the theory and applications of geostatistical estimation techniques (*e.g.*, Journel and Huijbregts, 1978; Isaaks and Srivastava, 1989; Chilès and Delfiner, 1999; Jensen *et al.*, 2000). Fluid samples and laboratory experiments are also used to estimate rock-fluid properties (Tiab and Donalson, 1996). Subsequently, upscaling procedures (Christie, 1996; Kumar *et al.*, 1997; Christie and Blunt, 2001) are employed to construct spatially discretized reservoir models amenable to numerical simulation of multiphase fluid flow.

Those popular reservoir characterization procedures all too often miss a crucial step in which the 3D seismic data could be used to honor the extrapolation of petrophysical variables away from existing wells. Approaches to this problem have been proposed in the technical literature. To the author's knowledge, the first suggestion of the quantitative integration of 3D seismic data and well logs to constrain hydrocarbon reservoir models can be traced back to Journel and Huijbregts (1978). Estimation of porosity based on regression formulas between well-log acoustic impedance (or interval transit time) and porosity were reported by Maureau and Van Wijhe (1979). They applied such regression formulas to infer spatial distributions of porosity from seismic-derived acoustic impedances. Doyen (1988) cokriged average values of porosity at well locations with seismic attributes (*i.e.*, time averages of seismic-derived acoustic impedance, as well as time averages of seismic-derived interval transit times). This approach explicitly enforced the same spatial variability of seismic attributes to the estimated inter-well porosity.

Bortoli *et al.* (1993) and Haas (1993) proposed a stochastic seismic inversion technique that decomposed the 3D volume into vertical cross-sections. Multiple stochastic realizations were performed to populate acoustic impedance along a given cross-section. The cross-section of acoustic impedance that best matched the seismic data was retained for subsequent analysis. Each simulated cross-section of acoustic impedance was conditioned to honor the well-log data and previously accepted cross-sections. Acoustic impedance was then transformed to porosity using calibration functions inferred from well-log data. Haas and Dubrule (1994) improved the latter approach by performing the stochastic inversion on a trace-by-trace basis. Seismic and well-log data were simultaneously honored to produce geostatistical estimates of acoustic impedance. They suggested relating these multiples realizations of acoustic impedance to petrophysical properties such as porosity and permeability. The ensuing estimation technique was referred to as geostatistical seismic inversion. Further developments of Haas and Dubrule's (1994) work can be found in the open technical literature (Debeye *et al.*, 1996; Pendrel and van Riel, 1997; Torres-Verdín *et al.*, 1999; Grijalba *et al.*, 2000). Torres-Verdín *et al.* (2000) compared standard geostatistical estimation techniques with geostatistical inversion of post-stack seismic data for reservoir delineation. They found that geostatistical inversion produced more reliable and robust inter-well distributions of acoustic impedance than standard geostatistical estimation techniques.

The methods for integrated reservoir characterization described above make use of post-stack seismic data. However, pre-stack seismic data are sensitive not only to compressional-wave velocity but also to shear-wave velocity and therefore can be used to improve the construction and reliability of petrophysical reservoir models. Inversion of pre-stack seismic data gives rise to distributions of bulk density, and compressional- and shear-wave acoustic impedances. Common uses of pre-stack seismic data and amplitude-versus-offset (AVO) variations involve the discrimination of fluids and lithology (Castagna *et al.*, 1998; Roy *et al.*, 2002). Recent advances in seismic lithology analysis using AVO can be found in Castagna (2001). Consequently, a robust algorithm is long overdue that can efficiently integrate the information borne by the full gather of 3D pre-stack seismic data with well logs and that can assess the uncertainty of the estimated petrophysical and elastic properties.

The novel algorithm developed in this project constructs reservoir models by quantitatively integrating measurements with distinct lengths of spatial support. The main objective is the extensive and effective use of the full gather of 3D pre-stack seismic amplitude data, well logs, and geological information. Specifically, this project develops a stochastic simulation procedure to extrapolate petrophysical variables laterally away from wells subject to honoring the existing 3D pre-stack seismic data in a direct and accurate manner. Joint probability density functions (PDF) are constructed to establish a non-deterministic (statistical) link between petrophysical properties (*e.g.*, porosity, water saturation) and elastic parameters (*e.g.*, bulk density, elastic velocities or impedances). The joint PDFs are adjusted to reflect a vertical resolution consistent with both well-log and seismic data. A global inversion technique is used to update the initial reservoir model of petrophysical variables, generated with geostatistical simulation techniques, in response to a discrepancy between measured and synthetic 3D pre-stack seismic data. Such a strategy naturally lends itself to an efficient computer algorithm to assess uncertainty of the constructed reservoir models. The estimated property distributions can subsequently be used to guide the reliable and accurate estimation of other important reservoir properties, such as permeability and permeability anisotropy, for instance, to which seismic data have negligible sensitivity. Validation and testing of the algorithm developed in this project is performed on realistic synthetic subsurface models. The main assumptions made by the inversion algorithm include (a) a trace-by-trace local one-dimensional (1D) model of elastic parameters, (b) the existence of support-dependent petrophysical-elastic relationships, (c) seismic signal-to-noise ratios large enough to warrant sensitivity to vertical variations of elastic parameters, and (d) well-log data truly representative of rock formation properties.

### 3.A.1.2 Research Objectives

The main objective of this work was to develop a novel, efficient, accurate, and robust algorithm to quantitatively integrate 3D pre-stack seismic data, well logs, and geological information in the construction of hydrocarbon reservoir models. This new algorithm is based on global inversion techniques and stochastic simulation. Emphasis is placed on the use of 3D seismic data, especially the full gather of 3D pre-stack seismic amplitude data, to take advantage of their relatively dense lateral coverage and of their enhanced sensitivity to subsurface elastic parameters.

### 3.A.1.3 Outline of this Report

This report is divided into three major sections. The first section includes Sections 3.A.1 and 3.A.2. Section 3.A.2 is a brief review of the physical principles, and of the mathematical and statistical formulation of technical topics used throughout the project. It summarizes the fundamentals of rock physics and elastic wave propagation, describes the approach used to numerically simulate seismic data, summarizes the properties of random variables and of their spatial relations, and overviews the principles of fluid flow in porous and permeable media.

The second section consists of Sections 3.A.3 and 3.A.4. This section emphasizes the advantages and disadvantages of the quantitative use of post-stack and pseudo-angle stack seismic data in integrated reservoir characterization studies that make use of global inversion techniques. Section 3.A.3 describes a procedure for the estimation of spatial variations of petrophysical and elastic parameters caused by dynamic reservoir behavior. The estimation is performed from time-lapse seismic measurements. In Section 3.A.4, a detailed study is undertaken to quantify the value of seismic data in the construction of reservoir models and to assess their impact in the forecast of hydrocarbon production.

The last section comprises Sections 3.A.5 and 3.A.6. This section describes novel stochastic inversion algorithms developed in the project to estimate elastic and petrophysical parameters from the full gather of pre-stack seismic data. Section 3.A.5 evaluates different factors that condition the estimation of elastic parameters such as types of global optimization technique, objective function, sampling strategy, and measures of smoothness. Based on this evaluation, a stochastic inversion algorithm is developed that makes use of simulated annealing and geostatistical concepts to concomitantly estimate 1D distributions of elastic parameters and their uncertainty. This global inversion algorithm is also validated against standard inversion techniques. Section 3.A.6 unveils a method for the direct estimation of petrophysical properties (and elastic parameters as by-products) that jointly honors the full gather of pre-stack seismic data, well logs, property histograms, and quantitative geological information. The algorithm is used to estimate reservoir properties, such as porosity, and their associated uncertainty using two-dimensional (2D) and 3D realistic synthetic subsurface models as examples. In addition, static and dynamic comparisons are performed against models generated with standard geostatistical techniques.

Finally, Section 3.A.7 summarizes the overall conclusions of this project and provides recommendations for future research work.

## 3.A.2: MATHEMATICAL PRELIMINARIES

This Section summarizes basic mathematical concepts that are used through the project. A description of inverse problems is presented as well as the methods used to simulate elastic properties, and subsequently seismic data. Some concepts are also discussed concerning wave propagation theory, post-stack and pre-stack seismic inversion, geostatistical estimation, and fluid flow in porous media.

### 3.A.2.1 Introduction

A strong commercial need exists to develop an efficient and robust algorithm that can quantitatively and accurately integrate different types of measurements, such as seismic data, well logs, cores, and production data, to characterize hydrocarbon reservoirs and to assess uncertainty in reservoir production. Figure 3.A.2.1 is a generalized flow diagram that shows a strategy to integrate seismic data into reservoir characterization studies. Most of the hydrocarbon exploration projects start with acquisition, processing, and subsequently interpretation of seismic data. A large amount of the approaches used today involve the use of post-stack seismic data. However these measurements allow one to make only inferences of lithology and fluid properties (see Figure 3.A.2.1). In the following sections a description is presented of the mathematical background of these approaches and of the proposed algorithm that involves the stochastic inversion of 3D pre-stack seismic data and well logs.

### 3.A.2.2 Formulation of the Inverse Problem

The inference of reservoir properties (*e.g.*, porosity, permeability, water saturation) from observed measurements (*e.g.*, seismic data, production data) belongs to the category of inverse or estimation problems. Such inverse problems relate model parameters with observed data through an often nonlinear mathematical representation. The choice of model parameters used to describe the system is not unique. A continuous forward problem, for instance, predicts the measurements for an arbitrary set of model parameters. For the case of continuous and scalar linear inverse problems, the relationship between the model and the data can be written as

$$d(y) = \int C(x,y)m(x)dx \, , \tag{3.A.2.1}$$

where $d$ are the data, $m$ is the model, $C$ is the kernel, and $x$ and $y$ are the model and data space variables, respectively. The measurements normally consist of discrete values. Therefore, equation (3.A.2.1) can be discretized to estimate model parameters using a prescribed objective function and an optimization algorithm. In the more general case, nonlinear inference of model parameters from measurements requires: (a) an initial guess of the unknown model parameters, (b) numerical simulation of the system response using the mathematical representation of the model (*i.e.*, forward operator or mathematical model), (c) perturbation of model parameters using the optimization algorithm, and (d) a convergence criterion (*e.g.*, value of the objective function, number of iterations).

This project deals with the inverse problem of estimating petrophysical parameters (and elastic parameters as by-products) from pre-stack seismic and well-log data and, subsequently, with the dynamic evaluation of the inferred static reservoir models. Thus, the fundamental physical laws that are relevant to this problem are: elastic wave propagation theory for seismic modeling and mass conservation, Darcy's law, and the equation of state for the dynamics of the reservoir. Various statistical and geostatistical techniques are also used in the implementation of the inversion algorithm developed in this project. These fundamental laws and relationships are combined and implemented as a computer algorithm.

### 3.A.2.3 Generation of Elastic Rock Properties

The interest in studying different rock physics models is a result of a subsequent need to simulate consistent elastic properties and then seismic data. Pre-stack seismic data constitute the main input to the proposed inversion algorithms.

#### *3.A.2.3.1 Rock Physics Models*

There are several quantitative relationships published in the open technical literature to link elastic properties of rocks (*i.e.*, $v_p$ and $v_s$) with their pore space, pore fluid, fluid saturation, pore pressure, and rock composition. Many of these relationships are based on empirical correlations and are often applied to specific basins in the world where their validity has been confirmed with experimental data (Wyllie *et al.*, 1958; Hamilton, 1979; Castagna *et al.*, 1985). Other relationships stem from effective medium theory and hence are subject to different types of operating assumptions (Gassmann, 1951; Biot, 1956; Duffy and Mindlin, 1957; Geertsma, 1961). There is no single rock physics model that provides a complete and general formulation. 3.A.7.5.A. Appendix A describes the assumptions and operating conditions adopted by several empirical and theoretical rock physics models.

#### *3.A.2.3.2 Elastic Relationships*

Usage of experimental mechanical models (see 3.A.7.5.A. Appendix A) requires specific petrophysical and mechanical properties of rocks that are not normally available from standard laboratory measurements. Specifically, the relationships introduced by Hamilton (1979) require knowledge of both depth and lithology to calculate velocities. Castagna *et al.*'s (1985) rock physics relationships provide seismic velocity values based on porosity and volume of clay; lithology information is needed for a pure rock system. On the other hand, expressions associated with the theoretical models described in 3.A.7.5.A. Appendix A require knowledge of the bulk moduli of the rock, of the fluid, and of the rock's matrix, of the rock's bulk rigidity modulus, and of the effective pressure, bulk density, and porosity.

A simple, yet practical way to define these material properties is to make use of a combination of values associated with pure components and of additional relationships to link the elastic parameters (*i.e.*, bulk modulus) with petrophysical properties such as porosity, for instance. 3.A.7.5.B. Appendix B describes the set of relationships used in this project to calculate the elastic parameters necessary to uniquely define the rock physics model. Table 3.A.2.1 describes common values obtained from the literature for the elastic parameters of various pure rock components (Mavko *et al.*, 1998). The need to provide specific values for these components follows from the subsequent objective to numerically simulate multiphase flow measurements and seismic data.

### *3.A.2.3.3 Comparison of Rock Physics Models*

The experimental formulation of Hamilton (1979) requires knowledge of depth and lithology to calculate elastic parameters. This approach provides consistent burial trend behavior for the compressional- and shear-wave velocities, but it is independent of fluid content, porosity of the rock, and effective pressure. Another drawback of this formulation is related to the assumption of no lateral variations: two points with the same lithology and depth will exhibit the same velocity. Number 1 in the legend of Figure 3.A.2.2 identifies such a model. On the other hand, Castagna *et al.*'s (1985) rock physics relationships require specific values of porosity, volume of clay, and lithology for the case of a pure component system. The latter approach calculates the elastic velocities taking into account the porosity but ignoring fluid content and in-situ pressure. Elastic velocities could change laterally, however, if two points at different depths exhibit the same porosity, in which case the resulting velocity becomes identical. This means that the normal spatial trends of elastic velocity are not always satisfied.

Geertsma (1961) and Duffy and Mindlin (1957) models were evaluated for the two empirical relationships of bulk modulus. Figure 3.A.2.2 shows a vertical profile of elastic parameters obtained with the application of equations (3.A.7.5.B.3) and (3.A.7.5.B.4) in 3.A.7.5.B. Appendix B. Such profiles are identified with the letters A and B, respectively. Biot-Gassmann-Geertsma's theoretical model was tested for limiting values of mass coupling factor, $\kappa$, equal to infinity (perfect coupling) and one (no fluid-solid coupling)(numbers 2 and 3 in the legend of Figure 3.A.2.2, respectively). Even though this model takes into account porosity changes and fluid content, the burial trend for elastic velocity is not always consistent with nominal burial trends. However, Duffy and Mindlin's (1957) formulation does take into account the presence and variation of effective pressure. Mechanical compaction of rocks affects rock properties (Bourgoyne *et al.*, 1991). Vertical profiles of elastic parameters obtained from this model are identified with the number 4 in Figure 3.A.2.2 and remain consistent with elastic velocity trends and burial-related behavior. There are no significant differences between simulated elastic properties when making use of any of the two approaches to calculate bulk modulus (*i.e.*, equations 3.A.7.5.B.3 and 3.A.7.5.B.4 in 3.A.7.5.B. Appendix B).

Duffy and Mindlin's (1957) model allows one to calculate elastic velocities that include the most important effects (*e.g.*, porosity, fluid content, and mechanical compaction). Such a model provided the most realistic correlation in the presence of shale compaction and is used here in combination with equation (3.A.7.5.B.3) in 3.A.7.5.B. Appendix B to compute a bulk modulus and, subsequently, to generate the input data necessary to perform the forward modeling of post- and pre-stack seismic data. Experimental evidence has shown that this model accurately reproduces a wide variety of velocities measured on rock samples (White, 1983).

### 3.A.2.4 Seismic Modeling

The study of mechanical vibrations, naturally or artificially induced in the subsurface is a subject of central interest to applied seismology. The recordings of these vibrations are referred to as seismograms. Quantitative calculation of such seismograms is based on wave propagation theory. Below, a description is presented of the seismic acquisition and processing, wave propagation theory, and of the methods used to simulate numerically post-stack and pre-stack seismic data.

#### *3.A.2.4.1 Seismic Acquisition, Processing, and Resolution*

Figure 3.A.2.3 is a simplified graphical description of one of the common strategies used for acquisition and processing of seismic data. Panel (a) in this figure shows the array of sources and receivers, whereas panel (b) shows the original record of seismic traces or seismic offsets (where offset is the distance between source and receiver) measured with such an array. Source-receiver offset data are often corrected for travel time differences caused by variations in the ray trajectory. Panel (c) shows the seismic traces (*i.e.*, pre-stack seismic data) after applying a normal moveout (NMO) correction whereas panel (d) shows the seismic data that result from the addition, or stacking, of the pre-stack seismic traces. This stacked seismic trace is normally referred as post-stack seismic trace.

In practical applications, one of the advantages of seismic data is that they provide exhaustive lateral coverage of the subsurface. Reflected seismic signals contain frequencies in the range from a few Hertz to a few hundred Hertz and are normally sampled at rates of 2 and 4ms. The vertical resolution of these measurements is their main practical limitation. Lateral (horizontal) resolution is largely determined by the distance between adjacent traces and commonly ranges between 20-50 m. Vertical resolution remains controlled by the frequency content of the underlying seismic wavelet and commonly ranges between 5-15 m.

### *3.A.2.4.2 Wave Propagation Theory*

For a medium with homogenous and isotropic elastic properties, the general equation of motion may be written as

$$\rho \frac{\partial^2 \mathbf{u}}{\partial t^2} = (\lambda + 2\mu)\left[\nabla(\nabla \cdot \mathbf{u})\right] - \mu(\nabla \times \nabla \times \mathbf{u}), \tag{3.A.2.2}$$

where $\mathbf{u}$ is the displacement vector, $\rho$ is density, $\lambda$ is the Lame's constant, and $\mu$ is shear (rigidity) modulus. Lame's and other elastic constants such as bulk modulus are related to each other (Sheriff, 1984). Equation (3.A.2.2) implies that Newton's second law is defined in term of stress and displacement, and that stress and strain are proportional, that is, they are governed by Hooke's law. It also assumes small displacements. For additional details and applications on the elastic wave equation, the reader is referred to Elmore and Heald (1969) and to Ben-Menahem and Singh (1999).

Compressional-wave propagation is described as a particular case of equation (3.A.2.2) and obtained by taking the divergence of the equation of motion, that is

$$\rho \frac{\partial^2 (\nabla \cdot \mathbf{u})}{\partial t^2} = (\lambda + 2\mu)\left[\nabla \cdot \nabla(\nabla \cdot \mathbf{u})\right]. \tag{3.A.2.3a}$$

By defining the divergence of the displacement vector as $\Phi = \nabla \cdot \mathbf{u}$, one obtains

$$\nabla^2 \Phi = \left(\frac{\rho}{\lambda + 2\mu}\right)\left(\frac{\partial^2 \Phi}{\partial t^2}\right), \tag{3.A.2.3b}$$

or

$$\nabla^2\Phi = \left(\frac{1}{v_p^2}\right)\left(\frac{\partial^2\Phi}{\partial t^2}\right). \tag{3.A.2.3c}$$

This yields

$$v_p^2 = \frac{\lambda + 2\mu}{\rho}, \tag{3.A.2.3d}$$

where $v_p$ is compressional-wave velocity.

The equation for shear-wave propagation is obtained by taking the curl of the equation of motion, that is

$$\rho\frac{\partial^2\left(\nabla\times\mathbf{u}\right)}{\partial t^2} = \mu\left[\nabla^2\left(\nabla\times\mathbf{u}\right)\right]. \tag{3.A.2.4a}$$

By defining the curl of the displacement vector as $\Psi = \nabla\times\mathbf{u}$, one obtains

$$\nabla^2\Psi = \left(\frac{\rho}{\mu}\right)\left(\frac{\partial^2\Psi}{\partial t^2}\right), \tag{3.A.2.4b}$$

or

$$\nabla^2\Psi = \left(\frac{1}{v_s^2}\right)\left(\frac{\partial^2\Psi}{\partial t^2}\right). \tag{3.A.2.4c}$$

This yields

$$v_s^2 = \frac{\mu}{\rho}, \tag{3.A.2.4d}$$

where $v_s$ is shear-wave velocity.

### *3.A.2.4.3 Numerical Simulation of Post-Stack Seismic Data*

Figure 3.A.2.4 is a graphical representation of the phenomenon of reflection and transmission of plane waves at a planar interface separating two media. In the most general case, a single incident plane wave on an interface gives rise to four waves: reflected and transmitted shear waves and reflected and transmitted compressional waves. In seismic signal processing, the primary echoes or reflections are the most commonly used to infer features and properties of the subsurface (Yilmaz, 2000). The ratio of the amplitude of a reflected wave compared to the amplitude of an incident wave is called the reflection coefficient. If the angle of incidence is zero (*i.e.*, the incident plane wave is directed normal to the planar interface), the reflected and transmitted waves do not change direction but do change sign. For the latter situation, the primary reflection coefficient, $r$, for the compressional wave, $r_{pp}$, is an interface property and is given by

$$r_{pp} = \frac{AI_2 - AI_1}{AI_1 + AI_2}, \qquad (3.A.2.5)$$

where $AI$ is acoustic impedance and the subscripts 1 and 2 indicate the particular medium above (1) or below (2) the interface. Acoustic impedance is the product of density, times compressional-wave velocity. For a 1D layered medium, the convolution of the time series of reflection coefficients, $r(t)$, with the seismic wavelet, $w(t)$, generates a zero-offset synthetic seismogram, $s(t)$, or post-stack seismic data. Each post-stack seismic trace measures amplitude variations as a function of seismic travel time. The mathematical representation of this convolution is given by

$$s(t) = \int_{-\infty}^{\infty} w(t-\tau)\, r(t)\, d\tau . \qquad (3.A.2.6)$$

This equation tacitly neglects transmission losses, internal multiples, and frequency dispersion. In the frequency domain, the above convolution becomes the product of the Fourier transforms of the two functions, namely,

$$S(\omega) = W(\omega) R(\omega), \tag{3.A.2.7}$$

where $\omega$ is angular frequency and $S$, $W$, and $R$ are the Fourier transforms of the functions $s$, $w$, and $r$, respectively. This simple convolution model is the forward operator used in the simulation of post-stack seismic data. The main disadvantage of such a model is that acoustic impedance does not provide independent sensitivity to bulk density and compressional-wave velocity.

#### *3.A.2.4.4 Numerical Simulation of Pre-Stack Seismic Data*

Computation of synthetic seismograms for a particular source-receiver arrangement is performed under the assumption of a locally 1D distribution of elastic properties (*i.e.*, medium properties are only a function of depth or time). The theory of seismic wave propagation in such a medium has been extensively studied (Ben-Menahem and Singh, 1999; Aki and Richards, 2002) and there are different methods to approach the numerical simulation (Kennett, 1983; Aki and Richards, 2002).

The reflectivity method (Fuchs and Muller, 1971; Kennett, 1983) computes the full-wave response of a stack of horizontal layers including all wave modes and mode conversions. Source and receivers are located on the surface. Numerical integration of the reflectivities (or the Thomson-Haskell Reflectivity matrix, or propagator matrix) associated with the layered medium is performed in the horizontal wavenumber domain or else over the angle-of-incidence domain. Multiplication of the reflectivity function with the source spectrum (Fourier transform of the seismic wavelet) and then inverse Fourier transformation are necessary to obtain seismograms for a given source-receiver offset. In this project, a simplified version of the reflectivity method is used to efficiently compute synthetic seismograms for compressional wave (primaries only) in offset-time (x, t) domain. The reader is referred to 3.A.7.5.C Appendix C for a general description of the reflectivity method and to Kennett (1983) for more details about wave propagation in stratified media.

### 3.A.2.5 Statistical and Geostatistical Modeling

In petroleum applications, Geostatistics is a tool that allows one to assess inter-well reservoir properties and to perform data integration. It is based on the general theory of random variables and stochastic processes (Chilès and Delfiner, 1999). Reservoir properties at a given location can be treated as random variables governed by PDFs. Most of the stochastic methods used for modeling hydrocarbon reservoir properties are based on two operating assumptions: second-order stationarity and ergodicity. The inversion algorithms developed in this project are stochastic in nature and make use of random variables and of geostatistical concepts to perform the estimation of elastic and petrophysical properties. 3.A.7.5.D Appendix D presents some basic descriptors of random variables and geostatistical concepts used throughout the project. There are also a number of references that explain in more detail the theory and applications of such techniques (*e.g.*, Journel and Huijbregts, 1978; Isaaks and Srivastava, 1989; Chilès and Delfiner, 1999; Jensen *et al.*, 2000).

### 3.A.2.6 Numerical Simulation of Fluid Flow in Porous Media

A general description of the mathematical formulation used for the numerical simulation of a waterflood process is presented in 3.A.7.5.D. Appendix D Seismic data remain insensitive to the small density contrast between oil- and water-saturated rocks; hence, a waterflood becomes a stringent test for the sensitivity analysis pursued in this project. A second reason for selecting a waterflood recovery process for analysis is so that results can provide some insights into potential waterfloods in deepwater reservoirs where seismic is a main data source.

### *3.A.2.6.1 Fluid, Rock, and Rock-Fluid Properties*

Dynamic evaluations of petrophysical models (*i.e.*, porosity) used as reference and those constructed with the join stochastic inversion algorithm developed in this project are performed assuming a waterflood process and using a commercial fluid flow simulator (Eclipse™). These evaluations require not only of the description of the production/injection constraints but also of the description of fluid, rock, and rock-fluid properties. For the purposes of this project the constraints and properties used in the waterflood are clearly defined in each section when appropriate. Additionally, uncertainty associated with fluid and rock-fluid properties is neglected in the analysis. This means that fluid properties and rock-fluid properties (*e.g.*, capillary pressure and relative permeability curves) are assumed to be known precisely. Therefore, dynamic results remain affected only by the description of the porosity model and the assumed porosity-dependent properties.

Permeability is one of the most important rock properties in the assessment of fluid flow through porous media (Bear, 1972; Tiab and Donaldson, 1996). A common practice in reservoir engineering is to relate permeability to porosity using a general transformation, *i.e.*, $\log k = a\phi + b$. The nonlinear form of this equation is consistent with empirical observations that generally show a linear relationship between permeability plotted on a logarithmic scale and porosity plotted on a linear scale. Permeability-porosity relations are notoriously noisy, a factor that is neglected in the dynamic evaluations performed in this project. The explicit nonlinearity of the permeability-porosity relationship contributes significantly to the accuracy of dynamic predictions. Moreover, the interplay between the nonlinearity of such a transformation and the noise is known to lead to additional biases in dynamic predictions of reservoir behavior (Jensen *et al.*, 2000). However, the above described assumptions allow not only to study the impact of the petrophysical models constructed with the proposed joint stochastic inversion algorithm on dynamic evaluations but also to compare dynamic results on an equal footing with reference models. For instance, the benefit of using a known porosity-permeability transformation is that if the true porosity could be estimated then one could accurately estimate permeability.

### 3.A.2.7 Summary

This Section summarizes the physical models and mathematical and statistical concepts used to develop a novel stochastic inversion algorithm. The next section comprises two Sections that explore the sensitivity of seismic and reservoir measurements to petrophysical and elastic properties via nonlinear inversion. The overall analysis highlights the use of seismic data in reservoir monitoring and modeling.

**Table 3.A.2.1: Assumed elastic parameters associated with pure rock components.**

| Pure Component | Dry Bulk Modulus (GPa) | Shear Modulus (GPa) | Density (g/cm$^3$) |
|---|---|---|---|
| Sand | 36 | 32 | 2.65 |
| Shale | 22 | 6.8 | 2.85 |
| Water | 2.3 | - | 1.00 |
| Oil | 1.6 | - | 0.85 |

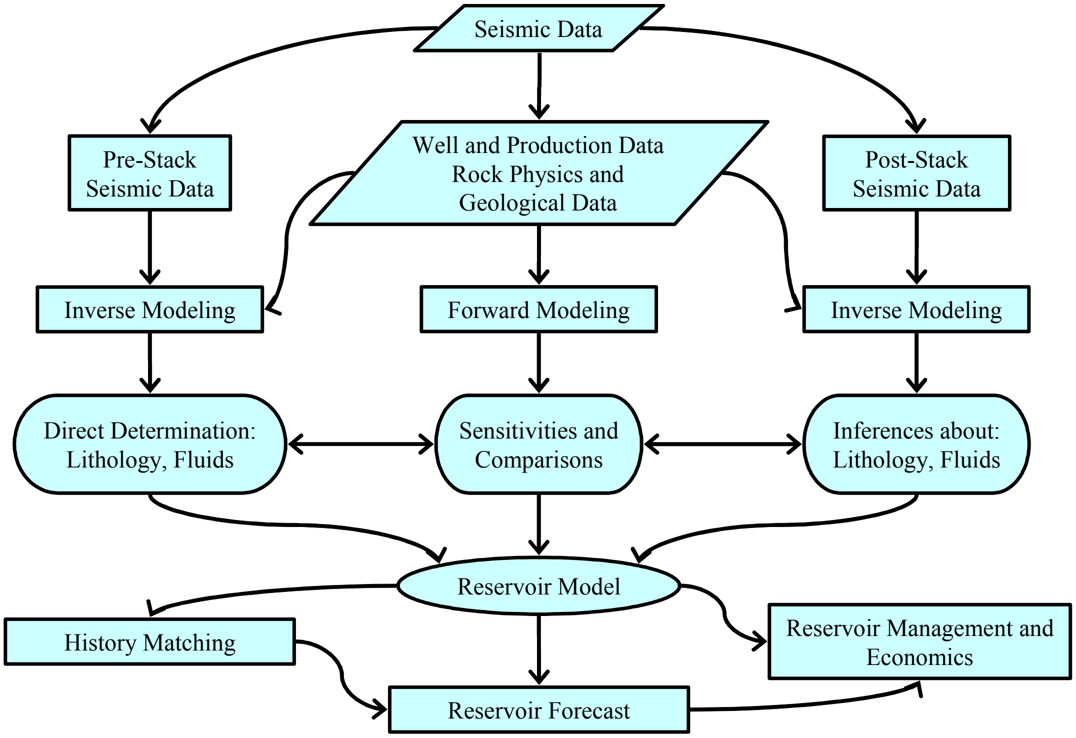

**Figure 3.A.2.1**: Flow diagram for integrated reservoir characterization studies that make use of seismic data.

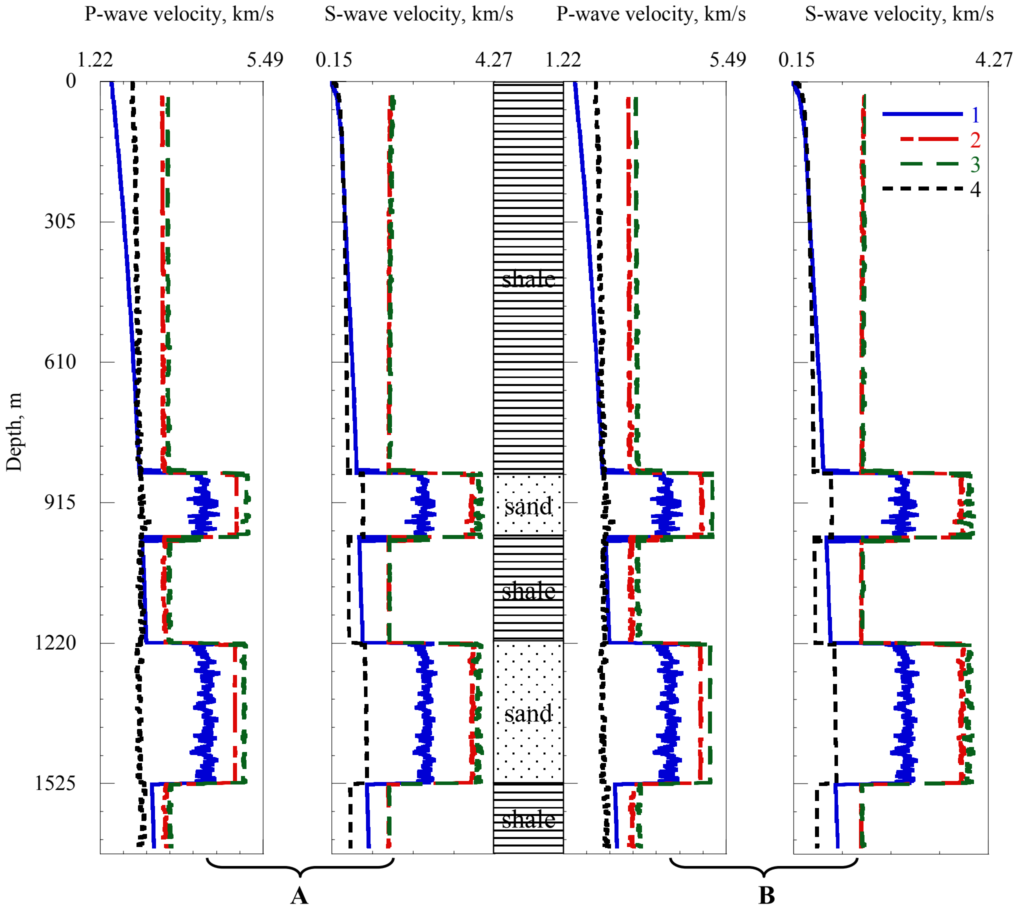

**Figure 3.A.2.2**: Comparison of the simulated one-dimensional distributions of elastic properties using four different rock physics models, namely, 1 = Hamilton, 2 = Biot-Gassmann-Geertsma ( $\kappa = \infty$ ), 3 = Biot-Gassmann-Geertsma ( $\kappa = 1$ ), and 4 = Duffy and Mindlin. Panels A and B show the calculated elastic properties using equation (3.A.7.5.B.3) and (3.A.7.5.B.4) in 3.A.7.5.B. Appendix B, respectively.

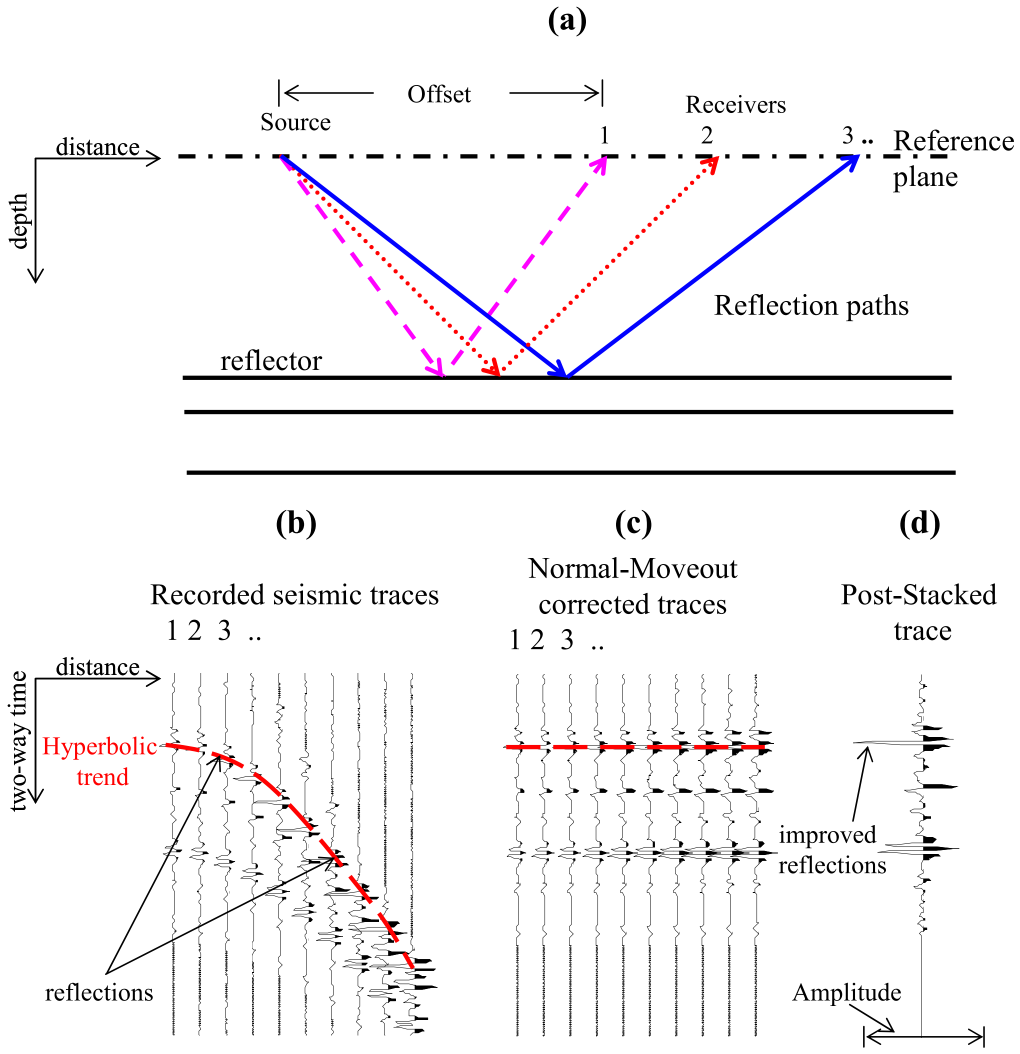

**Figure 3.A.2.3**: Simplified graphical representation of one of the common strategies for the acquisition and processing of seismic traces (Panel a). Panel (b) shows the actual record of acquired seismic traces. Panel (c) shows the same traces after the application of a normal moveout correction (*i.e.*, pre-stack seismic data) and panel (d) shows the stacked seismic trace (*i.e.*, post-stack seismic data).

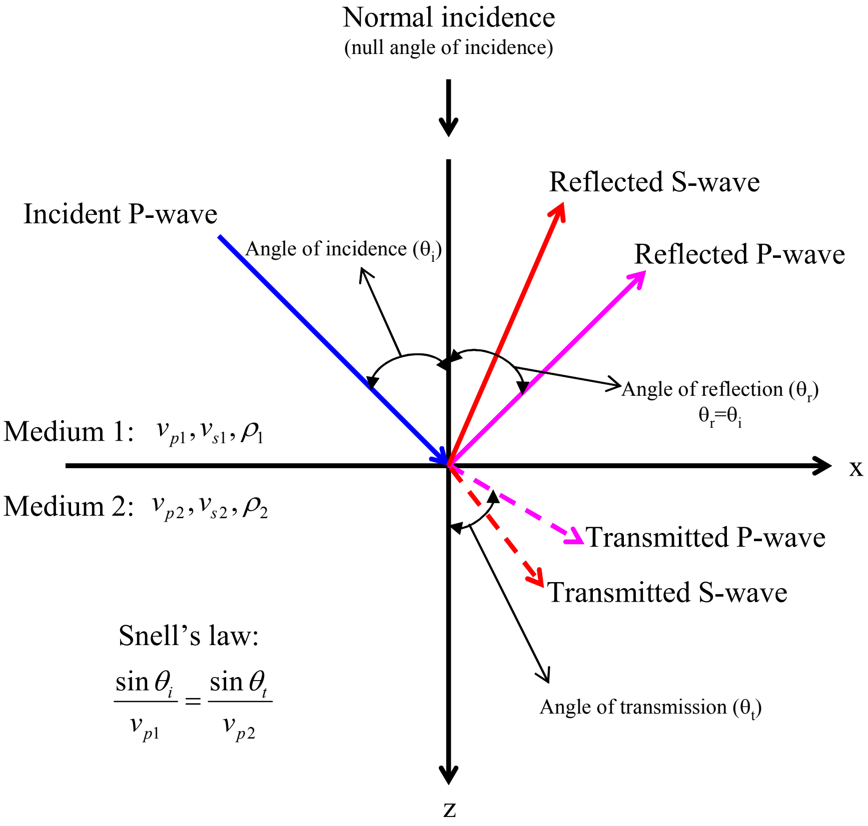

**Figure 3.A.2.4**: Graphical description of the phenomenon of reflection and transmission of plane waves at a planar interface (at $z = 0$) separating two media with different elastic properties.

## 3.A.3: RESERVOIR EVALUATION WITH SEISMIC DATA: QUANTITATIVE USE OF SEISMIC DATA IN RESERVOIR MONITORING

This Section introduces a sensitivity analysis to quantify the value of seismic data in the monitoring of dynamic reservoir behavior. The numerical sensitivity analysis is based on nonlinear inversion. Initially, the problem is formulated, then the subsurface model is described as well as the forward modeling of the petrophysical, elastic, and seismic parameters. Several numerical experiments are performed and examined to assess the value of time-lapse 3D seismic data in detecting dynamic reservoir changes.

### 3.A.3.1 Introduction

An attempt is made in this Section to appraise the ability of time-lapse 3D seismic data to infer spatial distributions of petrophysical properties. To this end, a synthetic, spatially heterogeneous hydrocarbon reservoir model is constructed and subject to numerical simulation of multiphase fluid flow. Hydrocarbon production is assumed in the form of one water injection well and four oil producing wells. The synthetic reservoir model exhibits average porosities of 20% but otherwise poses significant geometrical constraints to the usage of seismic data to ascertain petrophysical changes in the reservoir as a result of production. In addition, the lack of a significant density contrast between oil and water makes this example a non-trivial case for the assessment of the sensitivity of seismic data to time variations in reservoir properties.

Simulation of seismic data is performed in time-lapse mode making use of a rock physics model that includes the effect of differential mechanical compaction between sands and shales as a function of depth of burial. The numerical sensitivity study presented in this Section is strictly based on inversion and hence sheds quantitative light to the spatial resolution properties of noisy 3D seismic data. Inversion of noisy post- and pre-stack 3D seismic data is performed to infer space-time distributions of elastic parameters within the reservoir.

Multiphase fluid-flow parameters have a measurable impact on fluid saturation and pore pressure and hence on the spatial distribution and time evolution of elastic parameters. However, the inverted spatial distributions of elastic parameters at best correlate with smooth spatial averages of the actual distributions of pore pressure and fluid saturation. Because time-lapse seismic amplitude variations are of the order of 5%, such a correlation would be difficult, if not impossible, to ascertain without inversion. It is also shown that the elastic parameters inverted from pre-stack seismic data do provide more degrees of freedom to discriminate between time variations of pore pressure and fluid saturation in the reservoir compared to distributions of acoustic impedance inverted from post-stack seismic data.

### 3.A.3.2 Background and Formulation

The purpose of hydrocarbon reservoir characterization is to construct geological models and their associated spatial distributions of petrophysical properties. Three-dimensional seismic data are widely used to construct geometrical models of reservoir compartments (Dorn, 1998; Brown, 1999; Liner, 1999). Amplitude analysis of seismic data has also proved useful to infer lateral and vertical changes in some petrophysical parameters, notably lithology, porosity, fluid saturation, and pore pressure (Hilterman, 1999). On the other hand, wireline logs and core data are routinely used to provide an initial estimate of petrophysical parameters in the vicinity of existing wells (Descalzi *et al.*, 1988; Johnson, 1994). These estimates are subsequently extrapolated away from wells via geostatistical techniques and upscaling procedures that yield a cellular reservoir model amenable to numerical simulation of multiphase fluid flow (Chilès and Delfiner, 1999). Extrapolation of petrophysical parameters away from wells in some instances can be performed with the use of seismic data, as done with geostatistical inversion (Torres-Verdín *et al.*, 1999; Victoria *et al.*, 2001). More recently, time-lapse seismic data have been acquired and interpreted to gain insight to the dynamic behavior of producing hydrocarbon reservoirs (Al-Najjar *et al.*, 1999; Merke1 *et al.*, 2001; Cominelli *et al.*, 2002).

The objective of this Section is to quantify the spatial resolution of 3D seismic data in the inference of static and dynamic properties of hydrocarbon reservoirs. Measurements consist of pre- and post-stack seismic data acquired in time-lapse (4D) mode as well as wireline logs acquired before and after the onset of production (if wireline logs were not acquired after the onset of production then it is assumed that the original wireline logs were corrected using fluid substitution laws to reflect actual values after the onset of production). Seismic data are simulated numerically from a synthetic reservoir model that exhibits a considerable spatial variability in its associated petrophysical parameters. A waterflood enhanced recovery process is responsible for the dynamic behavior of the reservoir. Fluid production and pore pressure depletion are forecast using a multiphase reservoir simulator. Elastic properties are calculated from petrophysical parameters via rock physics/fluid substitution equations. Subsequently, seismic data are simulated assuming a nominal Ricker wavelet and a local 1D distribution of elastic properties for a given source-receiver gather. The central technical contribution of this Section is the estimation and appraisal of time-lapse reservoir changes by way of inversion.

### 3.A.3.3 Using Inversion to Improve Seismic Amplitude Resolution

Interpretation of 3D seismic data often relies on amplitudes analysis to identify anomalies that could be associated with petrophysical properties of hydrocarbon reservoirs. However, petrophysical interpretation directly from seismic amplitudes can be unreliable and inaccurate because of wavelet and tuning effects as well as deleterious measurement noise.

A way to improve the vertical resolution of seismic amplitudes is to perform inversion (Sams *et al.*, 1999; Torres-Verdín *et al.*, 1999). The latter procedure can substantially reduce wavelet effects and hence deliver elastic parameters with a closer connection to petrophysical parameters than seismic amplitudes. In the case of post-stack seismic data, inversion yields estimates of compressional-wave acoustic impedance (*i.e.*, the product of bulk density times compressional-wave velocity), whereas in the case of pre-stack seismic data, inversion yields estimates of bulk density, compressional-wave velocity, and shear-wave velocity, or compressional-wave acoustic impedance (PAI), and shear-wave acoustic impedance (SAI). Below, a description is presented of the method used in this Section to generate and evaluate time-lapse seismic data using as example a waterflood enhanced recovery process. The same method includes a quantitative analysis of the relative merits of inversion to produce estimates of elastic parameters and indirectly of petrophysical properties.

### 3.A.3.4 Construction of a Synthetic Reservoir Model

#### *3.A.3.4.1 Geological Model*

Figure 3.A.3.1 shows the synthetic geological model considered in this Section. It consists of two sand bodies embedded in a background shale. The upper sand body is water-filled whereas the lower one is saturated with oil. Fine non-conformal sedimentary layering of a fluvial nature was enforced within the sands to subsequently populate petrophysical properties. Geometry and dimensions of the sand bodies were specifically designed to assess the spatial resolution of seismic data in the presence of wavelet tuning. This subsurface model consists of approximately 30 million cells that were used to simulate seismic data and time records of fluid-flow measurements. Dimensions of the subsurface model were also designed to allow for the generation of seismic source-receiver angles of up to 45 degrees. A normal trend of increased mechanical compaction with depth was included in the background shale layer. Table 3.A.3.1

summarizes the geometrical dimensions, average elastic properties, and seismic parameters associated with the hypothetical subsurface model.

### *3.A.3.4.2 Reservoir Parameters and Fluid-Flow Model*

Petrophysical properties within the subsurface model were populated using geostatistical algorithms that enforced lithology dependent probability density functions and spatial semivariograms. The porosity field was assumed to be second-order stationary, normally distributed (mean value = 20%), and to exhibit a spatial correlation described by spherical semivariograms with zero nugget (see Table 3.A.3.1 for details). A fluid-flow numerical simulation grid was constructed to replicate a five-spot waterflood enhanced recovery process (one injector and four producing wells) in the oil-saturated sand. Figure 3.A.3.2 is a 3D view of the oil-saturated sand together with a description of the geometry, dimensions, well spacing, and well locations. Under the assumed conditions, seismic data are not strongly sensitive to the density contrast between water and oil. Therefore, a waterflood enhanced recovery process provides a difficult challenge for the quantification of the value of seismic data.

The same gridblock dimensions used to simulate the seismic data were used to simulate fluid flow behavior; hence mathematical upscaling was not necessary. Relationships between porosity, permeability, and water saturation were enforced using documented paradigms (Tiab and Donalson, 1996) and then used to determine the initial conditions of the reservoir (see Table 3.A.3.1). Both Corey-type relative permeability curves associated with a water-wet medium (Lake, 1989) and corresponding capillary pressure curves were used in the multiphase fluid-flow simulation. Production wells were set to a constant bottomhole pressure whereas the injector well was driven assuming a constant injection pressure. Fluid and rock properties and fluid-flow simulation conditions associated with the waterflood enhanced recovery process are described in Table 3.A.3.2.

The assumed waterflood production schedule was simulated for a time interval of eight years. Snapshots of fluid and pore pressure distributions at times $t_0 = 0$, $t_1 = 4$, and $t_2 = 8$ years after the onset of production were considered for the evaluation of seismic measurements. Subsequently, distributions of petrophysical properties were entered to the rock physics/fluid substitution models described below to calculate the corresponding spatial distributions of elastic parameters.

### *3.A.3.4.3 Simulation of Elastic Properties*

Elastic parameters at the production times $t_0$, $t_1$, and $t_2$ were calculated using a Duffy and Mindlin's rock physics/fluid substitution model (3.A.7.5.A. Appendix A) that included the effect of compaction. Additional elastic relationships and pure component properties necessary for these calculations are described in 3.A.7.5.B. Appendix B and Table 3.A.2.1 in Section 3.A.2, respectively. Rock physics/fluid substitution models relate the elastic properties with fluid and rock properties (*e.g.*, density, porosity, and fluid saturation).

### *3.A.3.4.4 Time to Depth Conversion*

Reservoir simulation models traditionally operate in the depth domain whereas seismic data are naturally displayed in travel-time-domain. A time-to-depth relationship was used to transform the data from one domain to another. Sonic logs, check-shots, and stacking velocities are often used to perform such a transformation. In this Section, snapshots of properties were transformed from depth to seismic time by making use of the corresponding distribution of compressional-wave velocity at a specific time of reservoir production.

### *3.A.3.4.5 Seismic Forward Modeling*

Figure 3.A.3.3 shows the flow diagram adopted in this Section for the forward modeling of post- and pre-stack seismic data. As indicated in Figure 3.A.3.4a, a convolutional model (see Section 3.A.2) was used with a 35 Hz zero-phase Ricker wavelet to generate post-stack seismic data at the production times $t_0$, $t_1$, and $t_2$. The simulation of post-stack and pre-stack seismic data was performed assuming a time sampling interval of 2ms and a local 1D subsurface model. On the other hand, pre-stack seismic data were simulated as partial stacks for three angle-stack intervals, namely, near- (0-15$^o$), mid- (15-30$^o$), and far-offset (30-45$^o$) at the same production times, $t_0$, $t_1$, and $t_2$. Simulation and inversion of full angle gathers was not attempted in this Section. However, extensive numerical exercises showed that the chosen angle-stack intervals provide the best compromise between resolution and uncertainty. The seismic wavelets associated with these three angle-stacks are a simple modification of the post-stack Ricker wavelet and are shown in Figure 3.A.3.4b. Simulation of pre-stack seismic data was performed using the Knott-Zoeppritz equations (Aki and Richards, 2002) specialized for PP waves and corrected for normal-moveout. Subsequently, random noise (*i.e.*, 10% additive zero-mean, uncorrelated Gaussian noise, where the noise percentage is measured in proportion to the global energy of the seismic data set) was added to the simulated post- and pre-stack seismic data in an effort to replicate practical levels of noise in seismic measurements.

## **3.A.3.5 Use of Seismic Data in Reservoir Monitoring**

### *3.A.3.5.1 Production History*

Figure 3.A.3.5 shows plots of cumulative oil and water production simulated for the constructed reservoir model over a period of eight years after the onset of production. These plots indicate that water breakthrough takes place at about 500 days after the onset of production

and, consequently, oil production starts to deviate from a straight line after that time. For the purposes of this Section, the most important information yielded by the waterflood simulation process is the spatial distributions of fluid saturations (*i.e.*, water and oil) and pore pressure. Snapshots of these distributions were "captured" at the times $t_0$, $t_1$, and $t_2$ after the onset of production. As shown in Appendices 3.A.7.5.A and 3.A.7.5.B, the calculation of elastic parameters (*i.e.*, bulk density, compressional-, and shear-wave velocities, or impedances) follows directly from the geostatistically simulated spatial distribution of porosity and from the computed distributions of fluid saturation and pore pressure.

### *3.A.3.5.2 Sensitivity of Elastic Parameters to Variations of Petrophysical Parameters*

Figure 3.A.3.6 shows cross-sections along the center of the oil-saturated sand, and through the water injection well (Seismic Line 100, the vertical axis is two-way seismic travel time), of the absolute values of compressional- and shear-wave velocity and bulk density at time $t_1$ after the onset of production. Comparison between petrophysical and elastic parameters indicate that, for this particular model, compressional-wave velocity remains sensitive to saturation and pressure changes whereas shear-wave velocity is affected mainly by pressure changes. Because the density contrast between oil and water is small, the PAI and SAI have similar behavior to that of compressional- and shear-wave velocity, respectively.

Histograms of petrophysical variables and of elastic parameters were sampled from the reservoir simulations described above in order to explore and quantify a relationship between the two sets of variables. These normalized histograms, shown in Figure 3.A.3.7, were sampled along a hypothetical vertical well intersecting the oil-saturated sand at three different times (*i.e.*, $t_0$, $t_1$, and $t_2$) after the onset of production. Pore pressure changes between $t_0$ and $t_1$ are significant, whereas those between $t_1$ and $t_2$ are negligible. In fact, pore pressure at time $t_2$ along this hypothetical well is greater than pore pressure at time $t_1$ as a consequence of water injection. Also, despite the fact that changes in water saturation are substantial, bulk density does not exhibit significant changes. Such an unfavorable situation occurs because of the small difference between the densities of oil and water. Consequently, the observed changes in compressional- and shear-wave velocity are predominantly due to changes in pore pressure and water saturation.

### *3.A.3.5.3 Sensitivity of Seismic Measurements to Variations of Petrophysical Parameters*

The simulated 4D pre- and post-stack seismic data were examined to evaluate the sensitivity of the seismic response to changes in petrophysical properties caused by dynamic reservoir behavior. Figure 3.A.3.8 shows cross-sections taken near to the center of the oil-saturated sand (Seismic Line 90, the vertical axis is two-way seismic travel time) of the near-, mid-, and far-angle stack seismic data at different production times. Panel (a) of this figure illustrates the near-, mid-, and far-angle stack seismic data at time $t_1$ after the onset of production, panel (b) shows the same angle stacks at time $t_2$ after the onset of production, and panel (c) illustrates the absolute value of the relative time difference of these seismic responses. From the plots shown in Figure 3.A.3.8, it is found that seismic data exhibit a 4-6% difference between times $t_1$ and $t_2$. Amplitude differences between two volumes of time-lapse seismic data are important for the present study because seismic data are the primary input to the inversion algorithm.

### *3.A.3.5.4 Post-Stack Seismic Inversion*

#### 3.A.3.5.4.1 Description of the Algorithm

Post-stack seismic inversion transforms the migrated seismic traces into time-domain variations of PAI. A sparse-spike inversion algorithm (Oldenburg *et al.*, 1983) was used to estimate 1D distributions of PAI from post-stack seismic data contaminated with 10%, zero-mean Gaussian noise. This algorithm imposes upper and lower bounds of PAI consistent with well-log data sampled along the existing five wells. Low frequency information of PAI is missing in the seismic data and hence in the inverted PAIs. Such information is reconstructed by merging low frequency PAI data from well logs with the inverted PAIs.

### 3.A.3.5.4.2 Data Misfit Function

The algorithm used in this Section for the inversion of post-stack seismic data is based on a sparse-spike regularization strategy. This procedure places emphasis on reflectivity models that exhibit a prescribed degree of spatial density of reflection coefficients. Acoustic impedances are further constrained to remain within upper and lower bounds inferred from well logs. Equation (3.A.3.1) describes the objective function ($E$) used in the inversion for the case of post-stack seismic data. The first additive term ($\ell_1$-norm) of this objective function biases the estimation of acoustic impedances toward sparse time sequences of reflectivity coefficients, whereas the second additive term ($\ell_2$-norm) enforces a desired degree of data misfit, namely,

$$E = \sum_i \left( |r_i| + \xi * \left( S^{obs} - S^{est} \right)_i^2 \right), \qquad (3.A.3.1)$$

where $i$ is the sample index, $r$ is the value of the reflection coefficient, $S^{obs}$ and $S^{est}$ are the measured and estimated seismic data, respectively, and $\xi$ is a parameter that controls the relative influence between a low value of data misfit and the sparsity of the estimated reflection coefficients (Oldenburg *et al.*, 1983). The minimization of the objective function given by equation (3.A.3.1) is performed directly in acoustic impedance domain rather than in reflectivity domain.

### 3.A.3.5.4.3 Inversion Resolution

The plots shown in Figure 3.A.3.9 are intended to be a measure of the vertical resolution of the inverted PAI along a time interval of common-mid-point (CMP) post-stack traces in the vicinity of Well No. 2 at time $t_2$ after the onset of production. Panel (a) shows a cross-section of the noisy post-stack seismic data together with a compressional-wave velocity well log. Panel (b) shows a cross-section of the inverted PAI and the actual PAI well log, whereas panel (c) is a cross-plot that provides a direct comparison between the actual and inverted PAI at this well within the sand. In an ideal case, all data in this cross-plot should fall along a straight line of unity slope. As a whole, the two sets of acoustic impedance correlate very well, thereby lending credence to the inversion. A similar comparison cross-plot was constructed for a time interval of seismic traces along the background shale. This cross-plot indicated that the inverted PAIs within the shale section were in closer agreement with the actual PAIs compared to the inverted PAIs within the sand section. Similar results were obtained when evaluating PAIs inverted from post-stack seismic data at times $t_0$ and $t_1$ after the onset of production.

#### 3.A.3.5.4.4 Evaluation of Results

Figure 3.A.3.10 shows cross-sections of forward and inverted PAI near to the center of the oil-saturated sand (Seismic Line 90, the vertical axis is two-way seismic travel time). In order to emphasize the role played by production time, the cross-sections shown in Figure 3.A.3.10 were constructed from the absolute difference of PAI at the production times $t_1$ and $t_2$. For comparison purposes, the left panel (a) of Figure 3.A.3.10 displays a plot of the absolute value of the time difference between distributions of water saturation along the same cross-section. The central panel (b) is a cross-section of the absolute difference of the actual distribution of PAI, whereas the right panel (c) is a cross-section of the corresponding absolute difference of the inverted distribution of PAI. Clearly, the inverted spatial distribution of PAI is a rather smooth version of the actual distribution. This behavior is partly due to both the presence of noise in the inverted post-stack seismic data, and the limited frequency band of the Ricker wavelet. Qualitatively, however, it becomes evident from the plots shown in Figure

3.A.3.10 that PAIs bear no clear and definite resemblance with the actual spatial distribution of water saturation. A similar analysis shows that PAI does not portray a clear and definite resemblance with the spatial distribution of pore pressure either.

### *3.A.3.5.5 Pre-Stack Seismic Inversion*

As a second step of the sensitivity study, angle-stack seismic inversions were performed on the simulated normal-moveout corrected pre-stack seismic data contaminated with zero-mean Gaussian noise. In principle, pre-stack data provide considerably more degrees of freedom than post-stack seismic data to estimate petrophysical parameters from seismic amplitudes. This is due to fact that pre-stack seismic amplitudes are sensitive to bulk density, PAI and SAI, whereas post-stack seismic data are only sensitive to PAI. It is expected, of course, that such an improved sensitivity would translate into better resolving and appraisal properties to infer distributions of petrophysical parameters. The study described in this section is intended to shed quantitative light to the resolving power of pre-stack seismic data. As in the case of the study of post-stack seismic data in the previous section, the assessment of spatial resolution is approached via inversion.

#### 3.A.3.5.5.1 Description of the Algorithm

Pre-stack seismic data were inverted using a sparse-spike algorithm that simultaneously makes use of near, mid, and far offsets to estimate values of bulk density, PAI and SAI. The 1D inversions described here were performed using as input the simulated pre-stack seismic data contaminated with 10%, zero-mean Gaussian noise. Moreover, the inversions were performed with the same offset-dependent wavelets used in the forward simulations (see Figure 3.A.3.4b) and were constrained by trend data sampled along the existing five wells.

3.A.3.5.5.2 Data Misfit Function

For the inversion of pre-stack seismic data, the algorithm works in a similar fashion to that of post-stack inversion. One difference is that the pre-stack inversion algorithm simultaneously considers multiple angle-stacked seismic data and simultaneously enforces constraints on compressional- and shear-wave velocities and bulk density (or compressional- and shear-wave acoustic impedances and bulk density) inferred from well logs. Equation (3.A.3.2) describes the objective function used in the inversion for the case of pre-stack seismic data, namely,

$$E = \sum_{i,j} \left( \left| r_{ij} \right| + \xi * \left( S^{obs} - S^{est} \right)_{ij}^{2} \right), \qquad (3.A.3.2)$$

where $j$ designates the various partial angle-stacks of pre-stack seismic data and the variable $r_{ij}$ identifies angle-dependent reflectivity coefficients. For this particular case, the inversion is performed directly in impedance-density domain.

3.A.3.5.5.3 Inversion Resolution

The plots shown in Figure 3.A.3.11 are intended to be a measure of the spatial resolution of the elastic parameters inverted from pre-stack seismic data along a time interval of CMP gathers in the vicinity of Well No. 2 at time $t_2$ after the onset of production. Panel (a) shows a cross-section of the noisy angle-stack seismic data (near, middle, and far) together with bulk density, PAI and SAI well logs, respectively. Panel (b) shows a cross-section of the inverted distributions of bulk density, PAI and SAI together with the actual well-log data, and panel (c) is a cross-plot that provides a direct comparison between the actual and inverted values of bulk density along Well No. 2 and within the oil-saturated sand. In an ideal case, all data in this cross-plot should fall along a straight line of unity slope. Among the elastic parameters estimated by the 1D inversion of pre-stack seismic data, bulk density exhibits the lowest correlation with its actual distribution. Similar comparison cross-plots were constructed between actual and inverted PAIs and SAIs within both the oil-saturated sand and the background shale. These cross-plots indicated that the spatial resolution and reliability of the inverted distributions of PAI and SAI were higher than those of bulk density. The spatial resolution of the inverted variables was also higher across the background shale segments than across the sand segments. Similar results were obtained when evaluating the spatial distributions of PAI, SAI, and bulk density inverted from pres-stack seismic data at times $t_0$ and $t_1$. Parenthetically, Varela *et al.* (2002) found slightly inferior spatial resolution for the inverted elastic parameters when performing the inversion in elastic velocity domain.

#### 3.A.3.5.5.4 Evaluation of Results

Figure 3.A.3.12 is a graphical summary of the computed (actual) spatial distributions of pore pressure, water saturation, and elastic parameters at reservoir production time $t_0$, $t_1$, and $t_2$. These distributions are shown in the form of cross-section taken near to the center of the oil-saturated sand (Seismic Line 90, the vertical axis is two-way seismic travel time). The corresponding cross-sections of inverted elastic parameters are shown in Figure 3.A.3.13.

In order to emphasize the role played by reservoir production time, Figure 3.A.3.14 shows cross-sections of the absolute differences of forward and inverted bulk density, PAI and SAI taken near to the center of the oil-saturated sand (Seismic Line 90, the vertical axis is two-way seismic travel time). These cross-sections were constructed from the absolute difference of bulk density, PAI, and SAI at the production time $t_1$ and $t_2$. For comparison purposes, the left panel (a) of Figure 3.A.3.14 displays plots of the absolute value of the time difference between spatial distributions of water saturation and pore pressure along the same cross-section. The central panel (b) shows cross-sections of the absolute difference of the actual distributions of bulk density, PAI and SAI, whereas the right-hand panel (c) displays the corresponding absolute difference of the inverted distributions of bulk density, PAI, and SAI. Clearly, the spatial distribution of absolute difference of inverted bulk density exhibits a poor resemblance with the actual distribution. This behavior is due to the limited sensitivity of noisy, narrow band pre-stack seismic data and, more importantly, to relatively small time-lapse variations in bulk density. A similar analysis shows that the spatial distributions of reservoir-time differences of PAI and SAI exhibit a high degree of resemblance with the spatial distributions of reservoir-time differences of water saturation and pore pressure, respectively. However, the distributions of absolute SAI differences constructed with the inverted distributions of SAI are only marginally suggestive of the corresponding absolute differences in pressure and bear no resemble with the distribution of absolute difference of water saturation. On the other hand, the distributions of absolute PAI difference constructed with the inverted distributions of PAI are suggestive of the corresponding absolute differences of water saturation. This exercise also showed that, in general, compared to post-stack seismic data, a more focused and distinguishable image of the saturation and pore pressure distributions could be inferred from the inverted distributions of elastic parameters. The inverted spatial distributions of SAI provided a means to discriminate between pore pressure and fluid saturation effects otherwise undistinguishable with PAI alone. Similar plots to those shown in Figure 3.A.3.14 were constructed for differences in the distributions of elastic parameters between the production times $t_0$ and $t_1$ and between the production times $t_0$ and $t_2$. Conclusions stemming from such plots remain the same as those outlined on the basis of Figure 3.A.3.14.

An analysis similar to that summarized in Figures 3.A.3.13 through 3.A.3.15 was performed using the parametric transformations proposed by Berryman *et al.* (2000) on the basis of Lamé's elastic parameters and bulk density. The idea behind these simple transformations is the possibility of discriminating between fluid, lithology, and porosity effects on the seismic response of rocks using appropriate products and quotients of Lamé's parameters and bulk density. However, because of the small bulk density contrast between oil- and water-saturated sands considered in this Section, it was found that Berryman *et al.*'s (2000) transformations did not shed additional light to lime-lapse reservoir behavior than the standard interpretation based on impedances and bulk density.

The numerical examples considered in this Section did not yield a high point-by-point correlation between saturation and pore pressure and elastic parameters. Because of this, the inversions could not be posed to deterministically estimate spatial distributions of pore pressure and saturation from pre-stack seismic data. Work reported by Johnston *et al.* (2000), Landro (2001), and Lumley (2001) shows that is often difficult to deterministically and uniquely relate time-lapse 3D seismic amplitude variations with time-lapse variations of either pore pressure or saturation. Time-lapse field studies are commonly riddled with uncertainties to the petrophysical cause of time-lapse seismic amplitude variations. Substantial variations in seismic amplitudes can originate from differences in data acquisition and processing of individual time-lapse seismic surveys. Uncertainty in the petrophysical interpretation of time-lapse seismic data is also compounded by inadequate assumptions made in the construction of pre-production reservoir models as well as poor conditioning of thermodynamic fluid behavior.

The work presented in this Section strongly suggests that inversion of single-time pre-stack seismic data could be used to benchmark and quantitatively relate seismic amplitude variations in time with dynamic reservoir changes due to production. Inversion provides a unique framework to assess (a) the quality and reliability of seismic data and (b) the sensitivity of changes in petrophysical parameters due to changes in elastic parameters. The numerical examples described in this Section also suggest that inversion naturally lends itself to a quantitative assessment of the resolution of seismic data to estimate spatial variations of elastic parameters (and of petrophysical parameters) under appreciable tuning conditions. Inverted elastic parameters will naturally exhibit the spatial averaging properties enforced by the underlying wave propagation phenomena.

### 3.A.3.6 Summary and Conclusions

The methodology presented in this Section attempted to quantify the spatial resolution properties of 3D seismic data to time variations in petrophysical properties by way of inversion. A reservoir model was constructed to simulate actual time evolution of reservoir properties due to multiphase flow in the presence of geometrical constraints and thin layering. This reservoir model considered the relatively difficult seismic detection case of water displacing oil. Most time-lapse seismic sensitivity studies reported to date have considered examples of oil-gas and water-gas mixtures wherein seismic responses are highly sensitive to spatial distributions of fluid saturation because of the corresponding large bulk density variations, especially at relatively high values of porosity. In addition, this work assumed that seismic measurements were contaminated with a practical amount of noise, but that otherwise were acquired with large reflection angles in the source-receiver gathers.

It was found that inversion does provide an increase in spatial resolution to detect and quantify time variations of pore pressure and fluid saturation compared to direct differencing of seismic amplitude variations. Moreover, as opposed to seismic amplitude variations, which are sensitivity to layer interface properties, inversion provides a direct quantitative link to layer properties, and hence to petrophysical parameters. The study presented in this Section emphasized that the vertical resolution properties of seismic data provide only a smooth representation of the actual spatial distribution of petrophysical properties. Problems arise in thinly bedded reservoirs where seismic data can only provide a rough spatial average of the actual distribution of petrophysical properties. Excessively smooth spatial distributions of elastic parameters cannot uniquely distinguish between distributions of pore pressure and fluid saturation. Even under these constraints, pre-stack seismic data do embody more quantitative information that post-stack seismic data on the time-varying behavior of producing hydrocarbon reservoirs. Spatial distributions of elastic parameters estimated from pre-stack seismic data provide a more focused and clearer indication of saturation and pore pressure distributions than the spatial distributions of acoustic impedance estimated from post-stack seismic data. It is here suggested that quantitative sensitivity studies of time-lapse seismic data be carried out directly in inverted elastic-property domain rather than in seismic amplitude domain.

Possible further improvements to the sensitivity study developed in this Section could include (a) 1D inversion of full pre-stack gathers instead of joint inversion of three partial angle-stacks, and (b) 2D inversion of pre-stack gathers along specific cross-sections. In the following Section, a sensitivity analysis of the quantitative use of seismic data in reservoir modeling will be presented and analyzed to see their effect on the static and dynamic reservoir responses.

**Table 3.A.3.1: Summary of the geometrical and measurement properties used in the construction of the synthetic subsurface model considered in this Section.**

| Characteristic | Value |
|---|---|
| Seismic grid | 200 inlines<br>200 crosslines |
| Seismic time range | 0 – 1.5 s |
| Seismic time sampling interval | 2 ms |
| Overall average compressional-wave | 2.23 km/s |

| Characteristic | Value |
|---|---|
| velocity at $t_0$ | |
| Overall average shear-wave velocity at $t_0$ | 0.54 km/s |
| Overall average bulk density at $t_0$ | 2.67 g/cm$^3$ |
| Semivariograms used for the population of porosity:<br>Spherical(sill, $\lambda_x, \lambda_y, \lambda_z$) | sand:<br>(1, 610 m, 457 m, 61 m)<br>shale:<br>(1, 914 m, 610 m, 122 m) |
| Post-stack seismic wavelet | 35 Hz Ricker |
| Pre-stack seismic wavelets | angle-dependent Ricker |
| Pre-stack seismic stacks | near : 0 - $15^0$<br>middle : 15 - $30^0$<br>far : 30 - $45^0$ |

**Table 3.A.3.2: Summary of fluid and petrophysical properties associated with the synthetic hydrocarbon reservoir model considered in this Section.**

| Properties | | Values and units |
|---|---|---|
| Fluid | water density | 1.0 g/cm$^3$ |
| | oil density | 0.85 g/cm$^3$ |
| | water viscosity | 1.0 mPa-s |
| | oil viscosity | 1.5 mPa-s |
| | water compressibility | 4.5x10$^{-4}$ MPa$^{-1}$ |
| | oil compressibility | 2.9x10$^{-3}$ MPa$^{-1}$ |
| Reservoir | average $S_{wi}$ | 0.28 |
| | average $S_{or}$ | 0.25 |
| | $\phi(\bar{\phi}, \sigma_\phi)$ | N(0.20, 0.04) |
| | horizontal permeability | $\log(k) = 3\phi + 2.2$ |
| | formation compressibility | 2.47x10$^{-4}$ MPa$^{-1}$ |
| | water end point | 0.3 |
| | oil end point | 0.9 |
| | vertical to horizontal permeability ratio | 0.1 |

| **Properties** | | **Values and units** |
|---|---|---|
| | depth to top of sand | 1219 m |
| Simulation | injection pressure | 17.2 MPa |
| | bottom-hole pressure | 2.1 MPa |
| | number of cells | 81x81x51 |
| | gridblock size | (23m, 23 m, 6m) |
| | production perforations | entire sand interval |

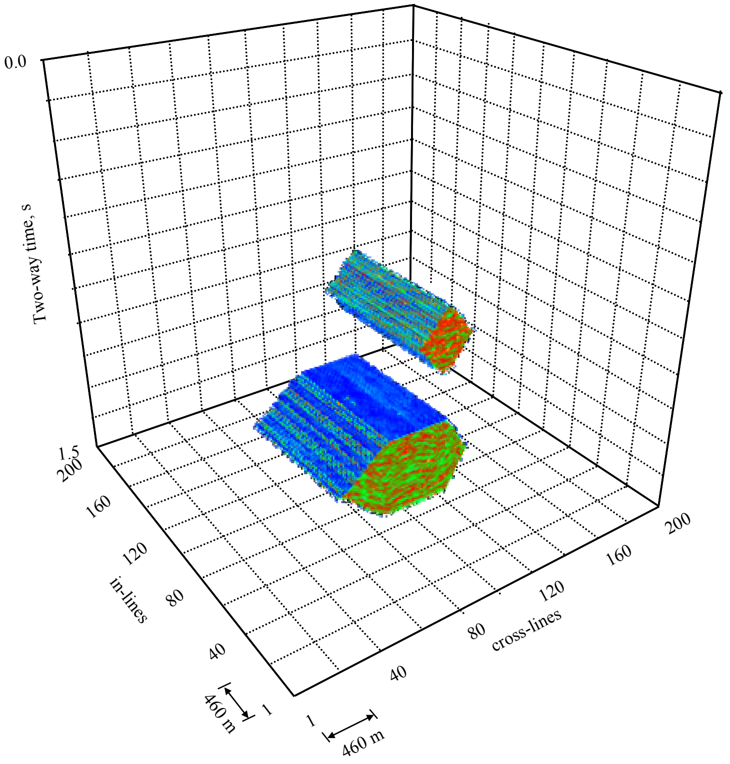

**Figure 3.A.3.1**: Graphical description of the 3D synthetic geologic model used for the numerical simulation of seismic and multi-phase fluid-flow phenomena. The vertical axis is a two-way seismic travel time.

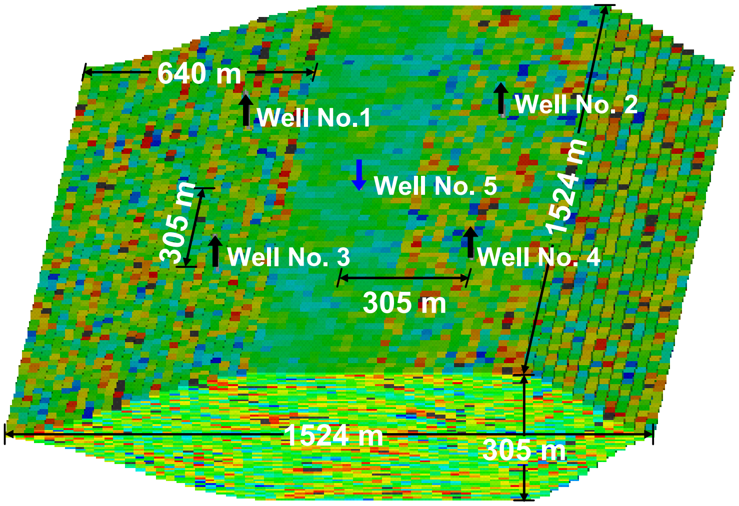

**Figure 3.A.3.2**: Three-dimensional view of the oil-saturated reservoir sand. Sand dimensions, well spacing, and well locations are as indicated on the figure.

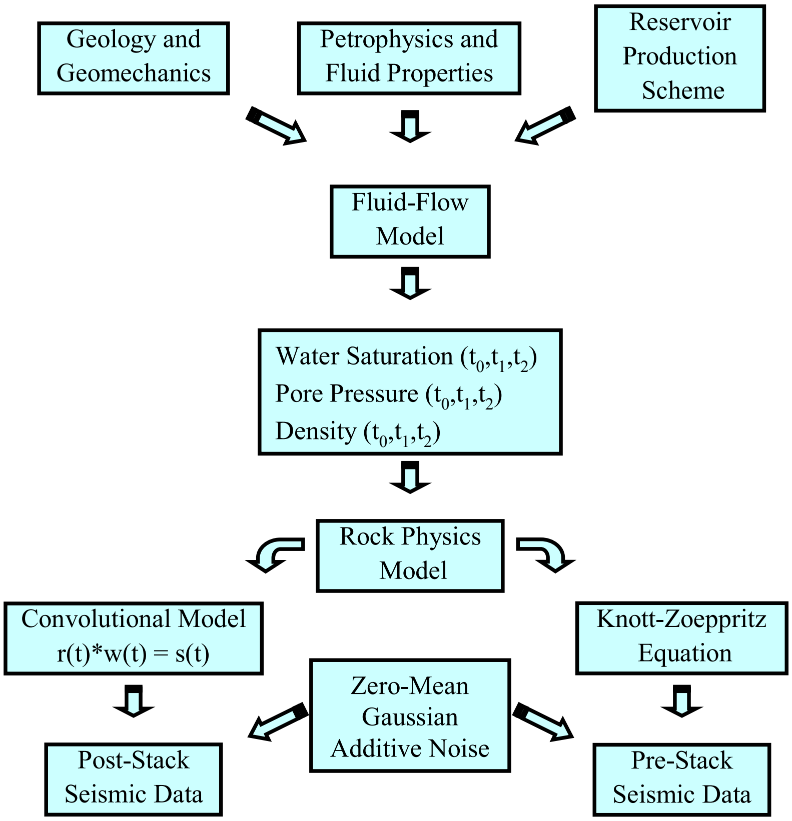

**Figure 3.A.3.3**: Flow diagram adopted in this Section for the forward modeling of post- and pre-stack seismic data. The variables $t_0$, $t_1$, and $t_2$ are used to indicate times of data acquisition measured with respect to the onset of reservoir production.

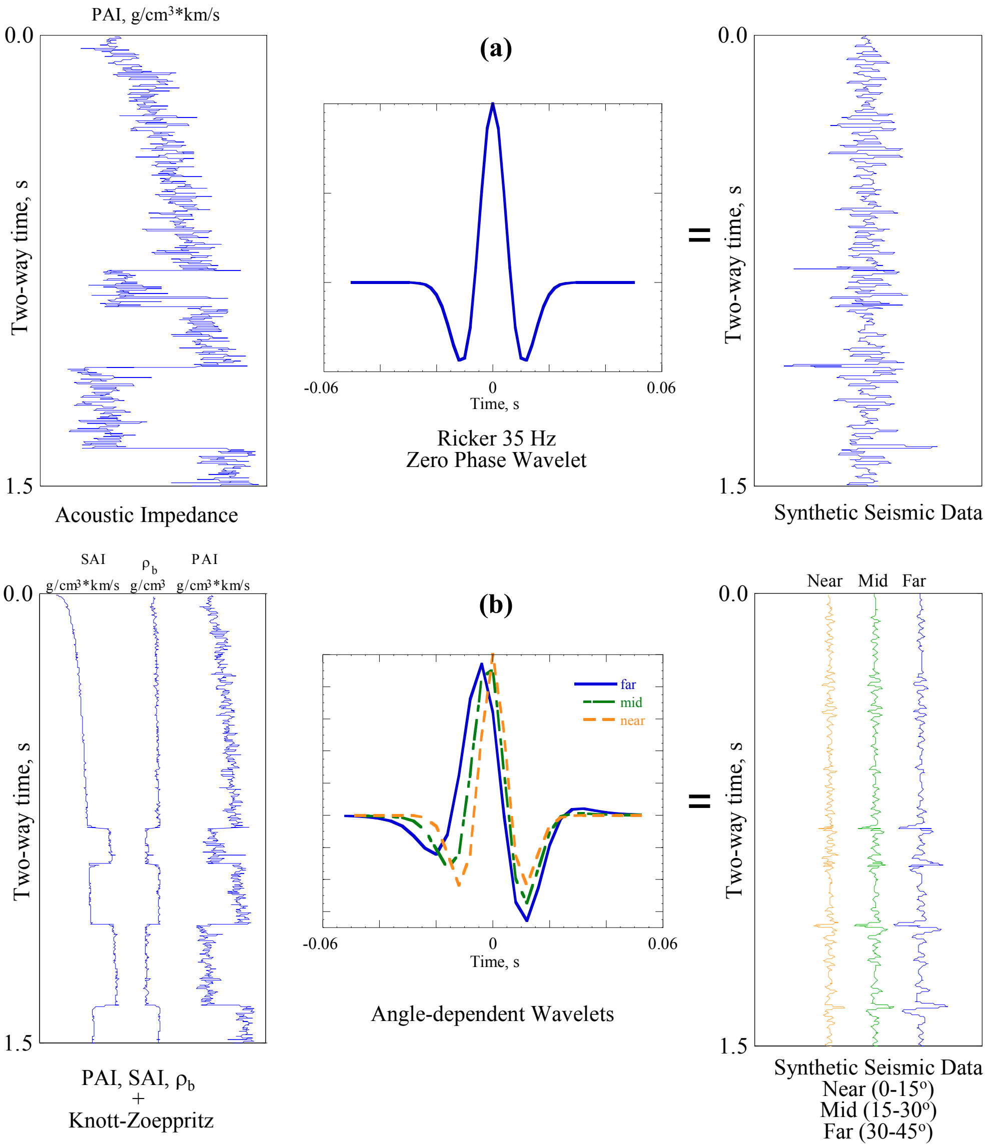

**Figure 3.A.3.4**: Forward seismic modeling. Top panel: (a) shows an acoustic impedance well log, Ricker wavelet, and resulting post-stack seismic data. Bottom panel: (b) shows compressional-, shear-wave acoustic impedance, and bulk density well logs, angle-dependent wavelets, and resulting pre-stack seismic data.

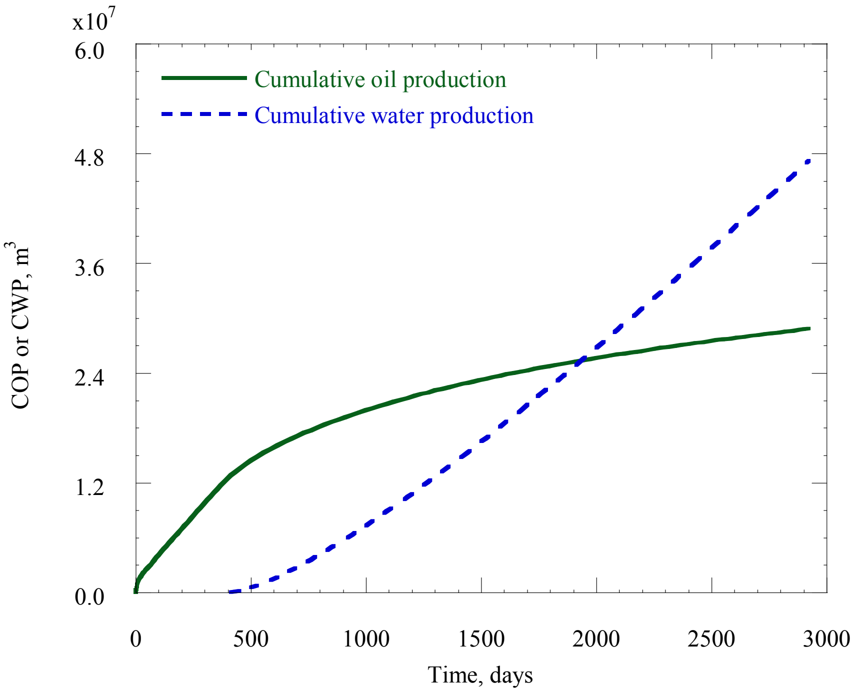

**Figure 3.A.3.5**: Plot of the time evolution of cumulative oil (COP) and water production (CWP) for the waterflood enhanced recovery process.

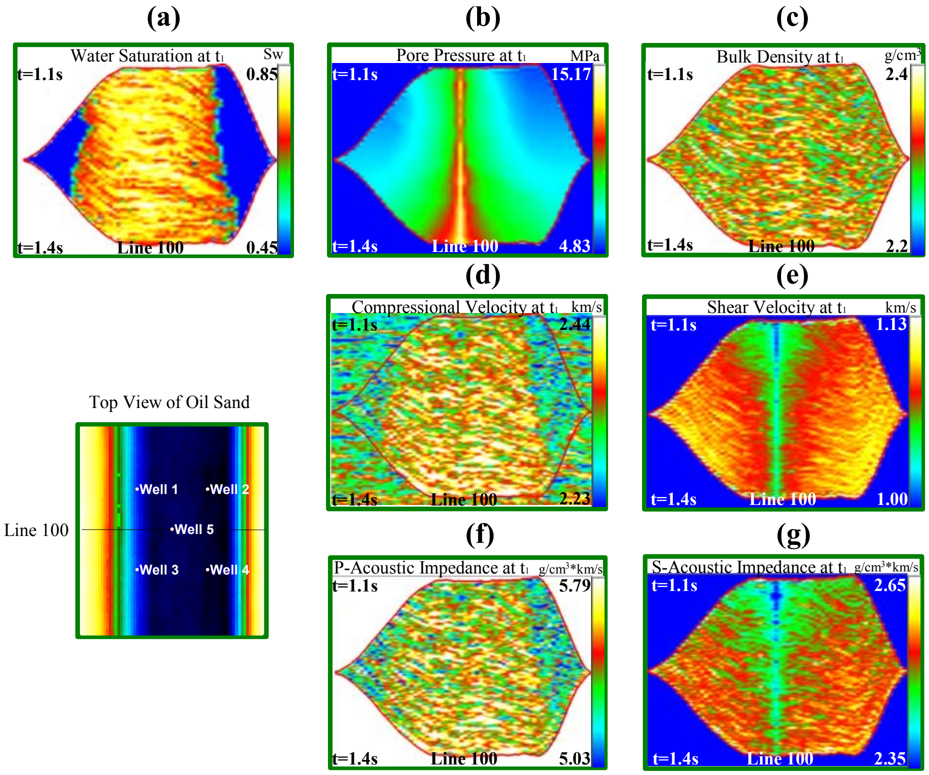

**Figure 3.A.3.6**: Spatial distributions of petrophysical properties and elastic parameters at time $t_1 = 4$ years after the onset of production. The figures show cross-sections of properties along the center of the sand and through the water-injection well (Seismic Line 100, as shown on the top view of the oil-saturated sand, the vertical axis is two-way seismic travel time), including (a) water saturation, (b) pore pressure, (c) bulk density, (d) compressional-wave velocity, (e) shear-wave velocity, (f) compressional-wave acoustic impedance, and (g) shear-wave acoustic impedance.

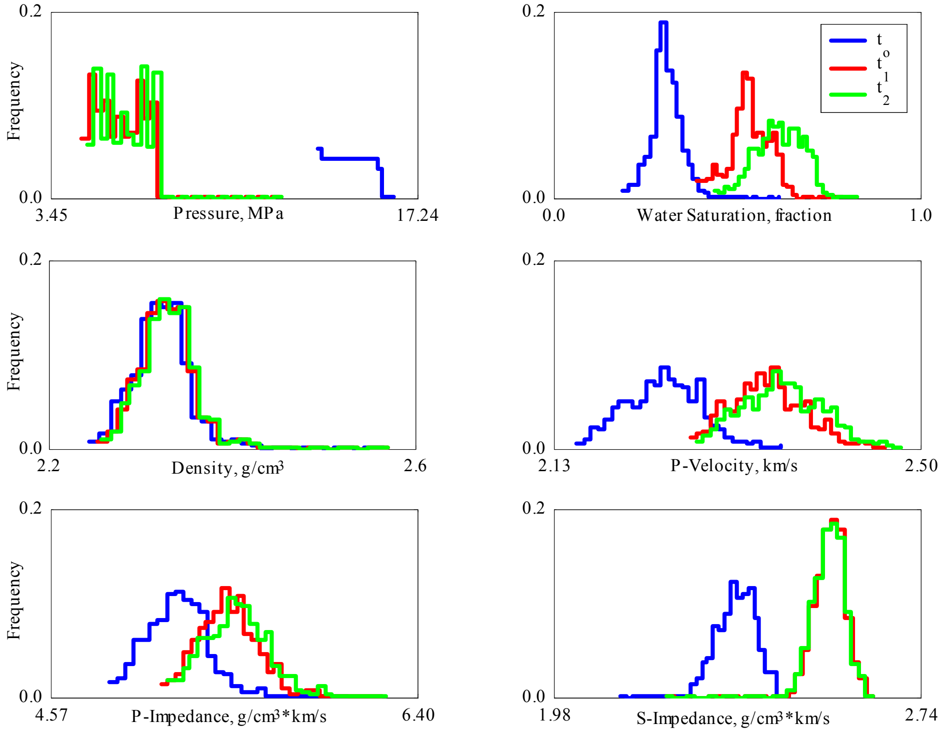

**Figure 3.A.3.7**: Normalized histograms of pore pressure and water saturation, and of their corresponding elastic parameters sampled along a hypothetical vertical well intersecting the oil-saturated sand shown in Figure 3.A.3.2. Sets of histograms are shown for times $t_0 = 0$, $t_1 = 4$, and $t_2 = 8$ years after the onset of production. Histogram normalization was performed against the total number of samples.

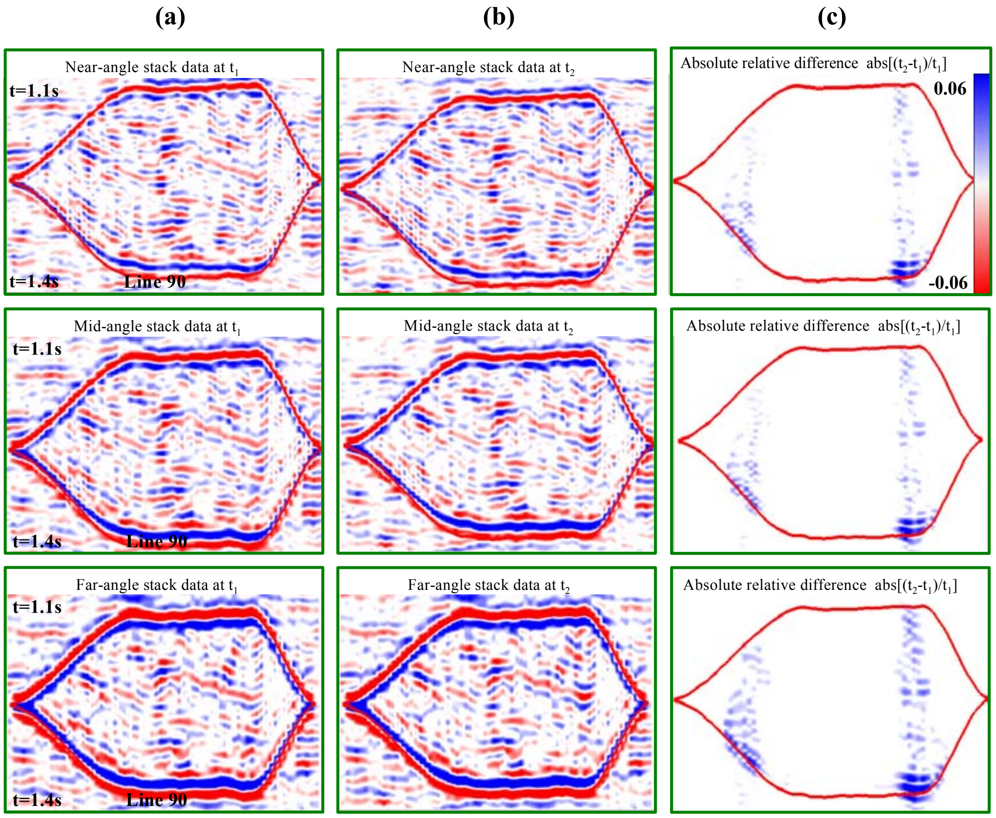

**Figure 3.A.3.8**: Cross-sections of pre-stack seismic data and of their relative production-time differences. The cross-sections are located near to the center of the oil-saturated sand (Seismic Line 90, the vertical axis is two-way seismic travel time). Panel (a) shows the near-angle (0-15$^{o}$), mid-angle (15-30$^{o}$), and far-angle (30-45$^{o}$) seismic stacks at $t_1 = 4$ production years, panel (b) shows the same stacks at time $t_2 = 8$ production years, and panel (c) shows the absolute relative difference of these near-, mid-, and far-angle stacks. The amplitude scale is the same for all the plots.

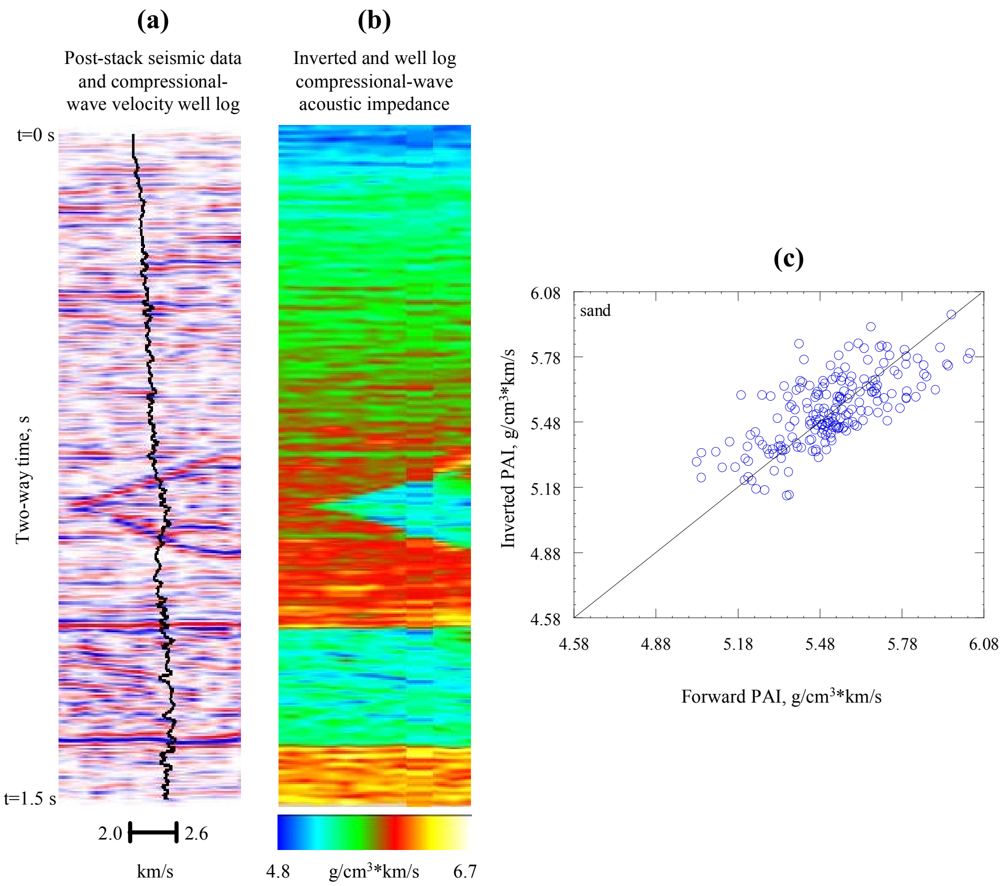

**Figure 3.A.3.9**: Quality control of post-stack seismic inversion along Well No. 2 (see Figure 3.A.3.2) at reservoir production time $t_2$ = 8 years after the onset of production. Panel (a) shows the noisy post-stack seismic data (contaminated with 10% zero-mean, Gaussian noise) and compressional-wave velocity well log. Panel (b) shows the inverted and well log compressional-wave acoustic impedance. Panel (c) shows a cross-plot of the actual and inverted compressional-wave acoustic impedances within the reservoir sand.

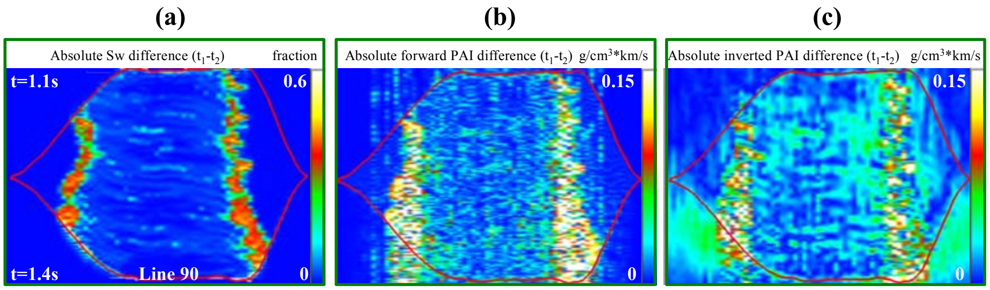

**Figure 3.A.3.10**: Post-stack inversion results. Cross-sections near to the center of the oil-saturated sand (Seismic Line 90, the vertical axis is two-way seismic travel time) of the absolute time differences of (a) water saturation, (b) actual compressional-wave acoustic impedance, and (c) inverted compressional-wave acoustic impedance, calculated from two time snapshots in the production life of the reservoir ($t_2$-$t_1$, where $t_1$ is 4 years and $t_2$ is 8 years after the onset of production.)

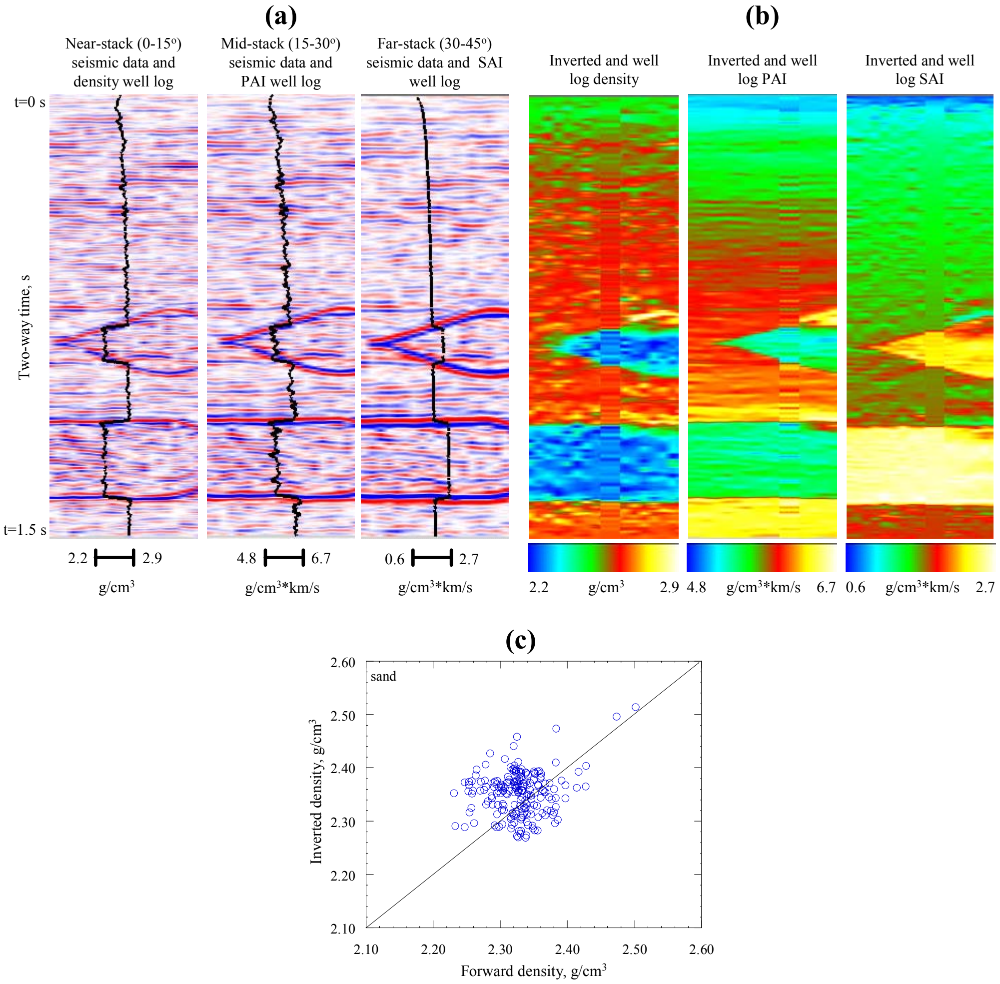

**Figure 3.A.3.11**: Quality control of pre-stack seismic inversion along Well No. 2 (see Figure 3.A.3.2) at reservoir production time $t_2 = 8$ years after the onset of production. Panel (a) shows the three noisy angle-stacks (near, middle and far contaminated with 10% zero-mean, Gaussian noise) and bulk density, PAI, and SAI well logs. Panel (b) shows the inverted and well log bulk density, PAI and SAI. Panel (c) shows a cross-plot of the actual and inverted bulk density within the reservoir sand.

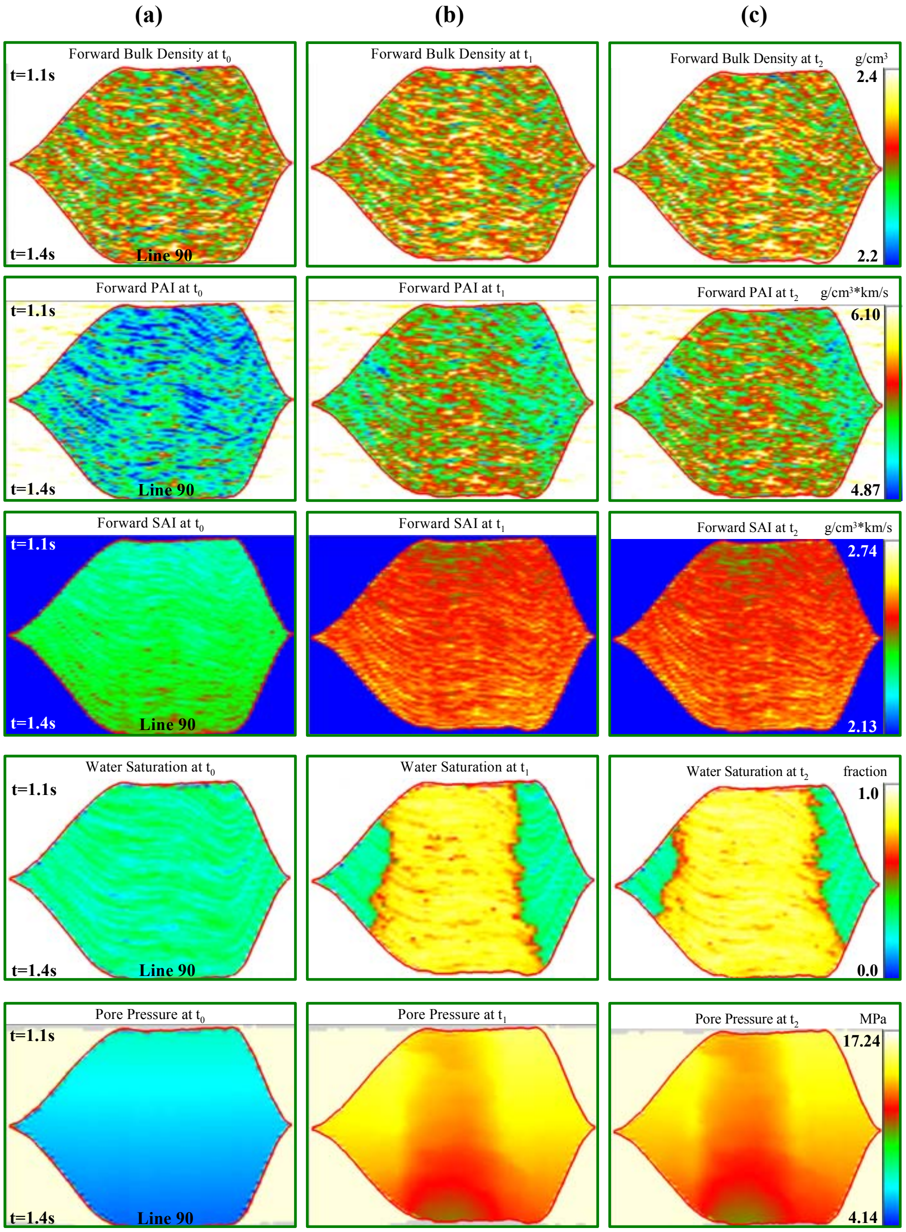

**Figure 3.A.3.12**: Cross-sections near to the center of the oil-saturated sand (Seismic Line 90, the vertical axis is two-way seismic travel time) of the actual elastic and petrophysical parameters at times (a) $t_0 = 0$, (b) $t_1 = 4$, and (c) $t_2 = 8$ years, after the onset of production.

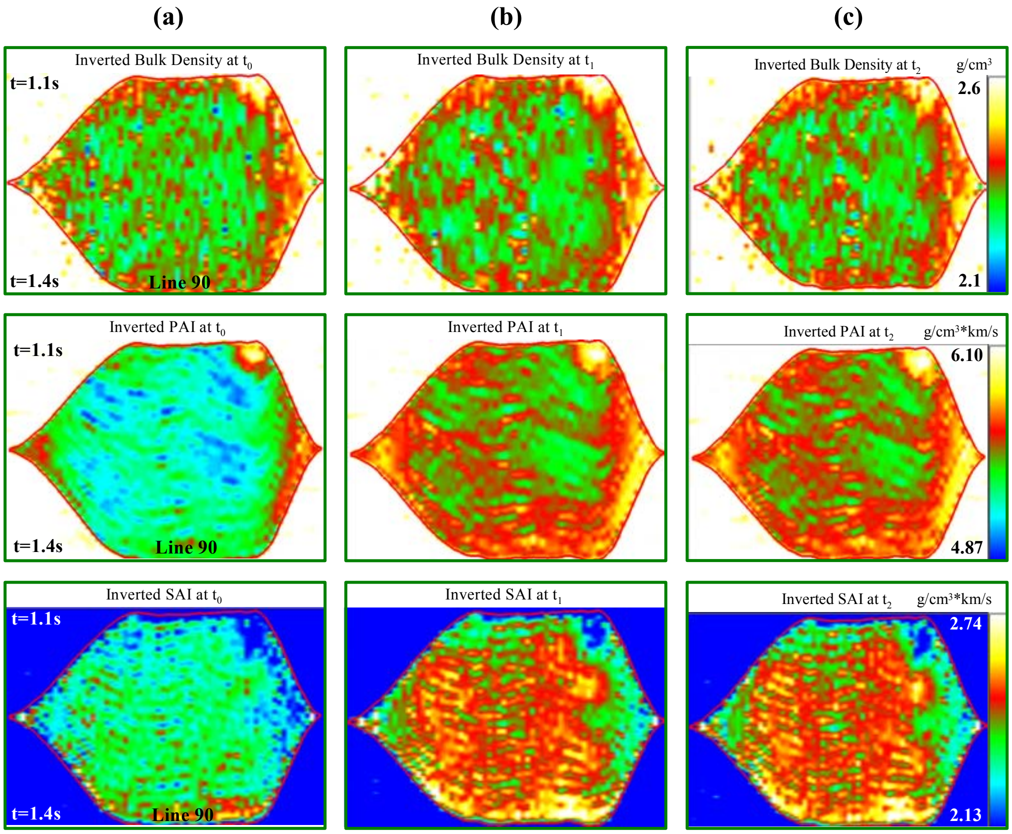

**Figure 3.A.3.13**: Pre-stack inversion results. Cross-sections near to the center of the oil-saturated sand (Seismic Line 90, the vertical axis is two-way seismic travel time) of the inverted elastic parameters at times (a) $t_0 = 0$, (b) $t_1 = 4$, and (c) $t_2 = 8$ years, after the onset of production estimated from pre-stack seismic data.

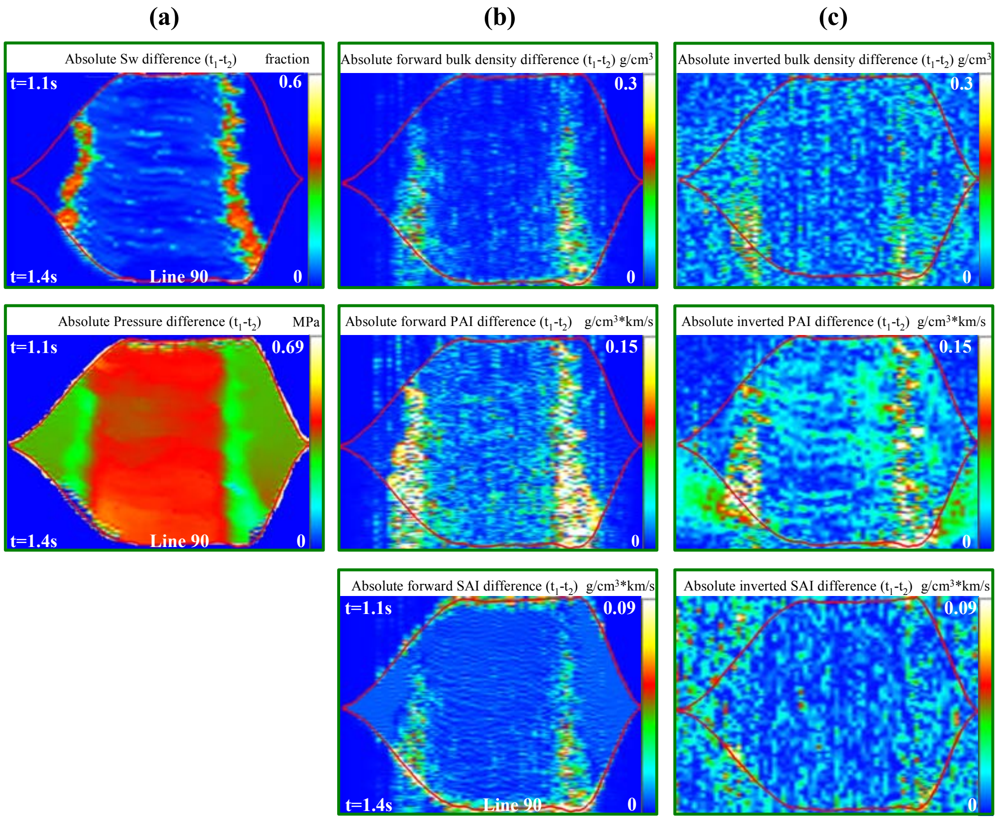

**Figure 3.A.3.14**: Reservoir production time-differences of pre-stack inversion results. The panels show cross-sections near to the center of the oil-saturated sand (Seismic Line 90, the vertical axis is two-way seismic travel time) of the absolute time differences of (a) water saturation and pore pressure, (b) actual bulk density, PAI, and SAI, and (c) inverted bulk density, PAI, and SAI, calculated from two time snapshots in the production life of the reservoir ($t_2$-$t_1$), where $t_1$ is 4 years and $t_2$ is 8 years after the onset of production.)

## 3.A.4: QUANTITATIVE USE OF SEISMIC DATA IN RESERVOIR MODELING

This Section introduces a sensitivity analysis to quantify the value of seismic data in the construction of reservoir simulation models and to assess their impact in the forecast of hydrocarbon production. Initially, the problem is formulated, then the subsurface model is described as well as the forward modeling of the petrophysical, elastic, and seismic parameters. Subsequently, different numerical experiments are performed and analyzed to assess the value of 3D seismic data in static and dynamic reservoir evaluation.

### 3.A.4.1 Introduction

Using 3D seismic data has become a common way to identify the size and shape of putative flow barriers in hydrocarbon reservoirs. However, it is less clear to what extent determining the spatial distribution of engineering properties (*e.g.*, porosity, permeability, pressures, and fluid saturations) can improve predictions (*i.e.*, improve accuracy and reduce uncertainty) of hydrocarbon recovery, given the multiple nonlinear and often noisy transformations required to make a prediction. Determining the worth of seismic data in predicting dynamic fluid production is one of the goals of the study presented in this Section.

The problem of assessing uncertainty in production forecasts is approached by constructing a synthetic reservoir model that exhibits much of the geometrical and petrophysical complexity encountered in clastic hydrocarbon reservoirs. This benchmark model was constructed using space-dependent, statistical relationships between petrophysical variables and seismic parameters. A waterflood condition was simulated numerically in the model to enforce time-varying reservoir conditions. Subsequently, a rock physics/fluid substitution model that accounted for compaction and pressure was used to calculate elastic parameters. Pre-stack and post-stack 3D seismic data (*i.e.*, time-domain amplitude variations of elastic responses) were simulated using local 1D approximations. The seismic data were also contaminated with noise to replicate actual data acquisition and processing errors. Subsequently, an attempt was made to estimate the original distribution of petrophysical properties and to forecast oil production based on limited and inaccurate spatial knowledge of the reservoir acquired from well logs and 3D seismic data.

Multiple realizations of the various predictions were compared against predictions performed with a reference model. Adding seismic data to the static description affected performance variables in different ways. For example, usage of seismic data did not uniformly reduce the variability of the predictions of water breakthrough time; other quantities, such as cumulative oil recovery at a given time, did exhibit an uncertainty reduction as did a global measure of recovery. Different degrees of strength of spatial correlation between seismic and petrophysical parameters were also studied to assess their effect on the uncertainty of production forecast.

Most of the predictions exhibited a bias in that there was a significant deviation between the medians of the realizations and the corresponding value for the reference case. This bias was evidently caused by noise in the various transforms (some of which were introduced deliberately) coupled with nonlinearity. The key nonlinearities seem to be associated with the numerical simulation itself, specifically with the transform from porosity to permeability, with the relative permeability relationships, and with the conservation equations.

### 3.A.4.2 Background and Formulation

Fluid-flow simulations are routinely used as the main input to the economical evaluation of hydrocarbon recovery. Predictions from these simulations have proven to be sensitive to the reservoir description, which is normally known through geology and petrophysics. Because the latter are based primarily on often sparsely-spaced wells, there is usually considerable uncertainty in the description and, hence, uncertainty in the prediction.

Relatively few reservoir characterization studies have made use of quantitative information contained in amplitude variations of 3D seismic data (Debeye at al., 1996; Pendrel and van Riel, 1997). Three dimensional seismic data sample the entire reservoir and thereby offer the possibility of filling the spatial gap between usually sparse well locations. The work reported in this Section is motivated by the same possibility to quantitatively use 3D seismic data to generate geometrical and structural maps, to assess the spatial distribution and size of flow units, and to volumetrically infer some petrophysical properties such as porosity and fluid saturations.

However, there are limits to the use of 3D seismic data for quantitative reservoir description. For instance, (a) the lateral (horizontal) resolution, being largely determined by the distance between adjacent traces, is often no better than 20-50 m, (b) the vertical resolution remains controlled by the frequency content of the underlying seismic wavelet, and is often no better than 5-15 m, hence normally greater than what is needed to model the spatial detail of fluid-flow phenomena, and (c) the transformations between what the seismic data measures and the input to a fluid-flow model are complex, noisy, and non-linear. It is not automatically obvious, therefore, that the use of seismic data will improve simulation predictions, even though they are spatially exhaustive. Determining the relative benefits and trade-offs of the quantitative use of 3D seismic data in reservoir model construction is the goal of this Section.

Several reservoir characterization techniques are considered to quantify the impact of the static reservoir description (*i.e.*, porosity model) on the dynamic forecast of production. Inference and forecast are accomplished using several alternative procedures, namely, (a) a homogeneous reservoir model, (b) a layered reservoir model, (c) 3D geostatistical techniques, and (d) a 3D geostatistical inversion technique that jointly honors 3D seismic data and well logs. The construction procedure implicitly considered (a) the uncertainty associated with statistical relations between petrophysical and elastic parameters, and (b) the effect of relative differences in geometrical support between the well logs and the seismic data. Comparisons of results were performed in model space (*e.g.*, porosity) and data space (*e.g.*, volume of oil production and seismic data). The conceptual geological representation of the model as well as the recovery process are the same for all cases so that differences obtained in dynamic behavior can be traced back to the information assumed available to construct each of the models.

### 3.A.4.3 Construction of a Synthetic Reservoir Model

#### *3.A.4.3.1 Simulation of Reservoir Properties*

The synthetic earth model consists of a reservoir sand embedded in a background shale. Figure 3.A.4.1 shows the geometry and dimensions of the synthetic reservoir sand. The same figure shows the spacing and location of the wells and the distribution of water saturation within the reservoir sand after 4 years of production. Approximately 30 million cells were used to construct a numerical grid to simulate the synthetic seismic data associated with the subsurface model. However, only the reservoir sand was discretized for fluid-flow simulation and this included approximately half a million cells. The size of the blocks used to simulate seismic data and those used to simulate fluid-flow behavior were the same, hence mathematical upscaling was not necessary.

The initial model of porosity was constructed stochastically (Gaussian simulation) using PDFs and semivariograms for each of the two lithologies (sand and shale). The porosity field was assumed to be second-order stationary, normally distributed, and exhibiting a spatial structure described by a prescribed semivariogram. This model is hereafter used as the truth reference case (referred to as case T). Table 3.A.4.1 presents a detailed summary of the conditions and relations used to simulate the process of waterflood. Relationships between porosity, permeability, and water saturation were enforced using well-documented paradigms (Tiab and Donaldson, 1996). These were subsequently used to determine the initial conditions of the reservoir. Relative permeability curves representative of a water-wet medium (Hornarpour *et al.*, 1982) were scaled using power-law functions that depended on residual saturation and endpoints (Lake, 1989). Figure 3.A.4.2 shows the set of capillary pressure and normalized relative permeability curves used in the fluid-flow simulations. These petrophysical relations are spatially invariant. A five-spot waterflood process (one injection well and four production wells) with an unfavorable mobility ratio (endpoint mobility ratio of 1.67) was simulated using a finite-difference algorithm. Seismic data remain insensitive to the small density contrast between oil and water; hence, a waterflood becomes a stringent test for the sensitivity analysis pursued in this work. A second reason for selecting a waterflood recovery process for analysis is so that our results can provide some insights into potential waterfloods in deepwater reservoirs where seismic is a main data source. The production wells were set to a constant bottomhole pressure and the injector well was assumed driven by a constant injection pressure. Fluid and rock properties and fluid-flow simulation conditions associated with case T are described in Table 3.A.4.1.

Permeability cannot be directly inferred from seismic information. A transformation, *i.e.*, $\log k = 10\phi - 0.5$, was used to infer permeability (in md) from porosity (as a fraction). The nonlinear form of this equation is consistent with empirical observations that generally show a linear relationship between permeability plotted on a logarithmic scale and porosity. As the results in this Section will show, the explicit nonlinearity of this relation contributes significantly to the accuracy of the predictions. Permeability-porosity relations, however, are notoriously noisy, a factor that is neglected here. The interplay between the nonlinearity and the noise is known to lead to additional bias in predictions (pp.212 of Jensen *et al.*, 2000). Addressing this complication is left to future work.

### *3.A.4.3.2 Simulation of Seismic Data*

Elastic parameters were calculated using a Duffy and Mindlin's rock physics/fluid substitution model (3.A.7.5.A. Appendix A) that includes the effect of compaction. A local 1D distribution of AI, the product of seismic velocity and bulk density, was assumed to simulate post-stack seismic data across the reservoir model. This was accomplished using a convolution operator (see Section 3.A.2) implemented with a zero-phase Ricker wavelet centered at 35 Hz. Figure 3.A.4.3 shows the Ricker wavelet used in this study and a cross-section of post-stack seismic data along Well No. 1. In addition, pre-stack seismic data were simulated for three angle-stack intervals: near (0-15$^o$), mid (15-30$^o$), and far (30-45$^o$), respectively. The seismic wavelets associated with these three angle stacks are a simple modification of the Ricker wavelet shown in Figure 3.A.4.3. Each angle interval is equivalent to what is normally referred to as an angle pseudo-stack in reflection seismology. The three angle pseudo-stacks were generated using a distinct synthetic wavelet for each angle-stack and by making use of the Knott-Zoeppritz equations (Aki and Richards, 2002). These equations describe the amplitude of transmitted and reflected plane waves as a function of their angle of incidence at a boundary separating regions with unequal elastic properties. Subsequently, random noise (*i.e.*, 10% additive zero-mean, uncorrelated Gaussian noise, where the noise percentage is in proportion to the global energy of the seismic data set) was added to the simulated seismic data in an effort to replicate actual noise in seismic measurements.

### 3.A.4.4 Use of Seismic Data and Other Techniques in Reservoir Characterization

In the model described above all the variables are completely known. However, in the numerical experiments, the reservoir properties are partially and imperfectly known. Figure 3.A.4.4 is a flow diagram that describes the method adopted in this Section for modeling and validating several reservoir characterization procedures.

The amount of data available for quantitative analysis increases as production proceeds. Most of these data are dynamic, in the form of production rates and pressures. Before production begins, the available data are mostly static (*i.e.*, they do not stem from fluid-flow in the reservoir) and it is the value of this type of data that is the subject of this study. The kind of information assumed here is geologic interpretation, noisy seismic data, seismic interpretation (*e.g.*, horizons), well logs, and the degrees of correlation between petrophysical and elastic properties. Well information (*e.g.*, logs and core data) is the most important and direct way to gain insight about reservoir properties. This information can be biased because the well locations are not commonly representative of the entire population and because of their relatively short spatial support. Core data, especially, is subject to biased sampling. Aside from bias considerations, all of the well data substantially undersample the reservoir. It is said that the knowledge of the reservoir is better at the end of its life; but even then knowledge is restricted to inferences made from tests and production history, and to the spatial distribution of the hard data (*i.e.*, wells).

Normally, major uncertainties in the geologic model are not fully considered in the modeling prior and during production because there is a substantial amount of work involved in developing alternative models. The static models evaluated here include different degrees of information in their construction. They comprise simple models (*e.g.*, homogeneous and layered), seismic inversion models, and stochastic models (*e.g.*, geostatistical and geostatistical seismic inversion models). Table 3.A.4.2 summarizes the nomenclature of the estimation models considered in this Section. Since the objective of this study is to evaluate static models and their impact on production forecast, all variables remain the same in the waterflood except for porosity and other petrophysical properties (*e.g.*, permeability), which are assumed to be porosity-dependent. This assumption allows one to perform a direct comparison between model construction, influence of seismic data, and production forecast.

### *3.A.4.4.1 Simple Models*

Two simple models are considered in this Section, namely, homogeneous and uniformly layered. These models are commonly used when relatively few data are available for reservoir characterization and are only useful to make inferences on the average properties of the field. In the homogeneous case (H), the porosity is spatially constant and equal to the mean value. Case H contains the mean statistical information but cannot capture vertical and lateral spatial variability of the petrophysical properties. The uniformly layered model (L) makes use of the well-log data (*i.e.*, porosity) to calculate average properties of each of the 51 simulation layers. Case L exhibits vertical spatial variability but cannot capture lateral spatial variability of the petrophysical properties.

### *3.A.4.4.2 Seismic Inversion Models*

Seismic inversion is a procedure whereby AI is estimated from post-stack seismic data. Related to the mechanical properties of the rocks, AI is often correlated with petrophysical parameters. If there is a relationship between AI and petrophysical parameters then a direct transformation can be used to generate the reservoir parameters (see Figure 3.A.4.5). This is case DAI. Here, the AI estimated from post-stack seismic inversion is transformed into porosity using the relationship shown in Figure 3.A.4.5 (top panel), which in turn was calculated using well-log data. The more correlated the variables are, the more accurate the transformation of AI into the corresponding petrophysical property. Although Figure 3.A.4.5 shows correlation between AI and porosity, and AI and bulk density, there is some scatter around the main trend. In practice, however, there is not always a relationship between AI and petrophysical parameters. This is case AIW. For such a situation, the AI estimated from the post-stack seismic inversion is transformed into porosity using the relationship shown in Figure 3.A.4.6 with a small correlation coefficient ($r^2 = 0.1$). Correlation coefficients ($r^2$) is used as a scale-independent measure of similarity between two variables (see 3.A.7.5.D. Appendix D).

### *3.A.4.4.3 Stochastic Models*

Stochastic modeling allows the generation of equally probable statistical realizations of the spatial distribution of reservoir properties. If these realizations are subject to fluid-flow simulations then the dynamic behavior of the reservoir can also be interpreted in terms of statistical properties. Normally, the range of possible solutions is an important part of the reservoir evaluation since in practical cases an analytical solution to the fluid-flow equations is not available. The stochastic approach is one of the techniques that allow one to integrate different kinds of information into the static description of the reservoir. In this section, the cases studied include: geostatistical models, and geostatistical seismic inversion for porosity and bulk density of the post-stack and far-offset volumes.

Bias and accuracy are important issues when evaluating stochastic realizations since the value of the inferences can be jeopardized by a potential bias in the results. Bias is a statistical sampling or testing error caused by systematically favoring some outcomes over others. Then, it becomes imperative to identify the source of bias in the estimation procedures to properly evaluate the results. In the studies of this Section, the main sources of bias are nonlinear equations, noisy relationships between variables, the nature of the production scheme, and the correctness of the physical model, to name but a few.

#### 3.A.4.4.3.1 Geostatistical Models

Geostatistical modeling (case G) makes use of the information acquired along the five existing wells to build PDFs of reservoir properties (*i.e.*, porosity). Then, through the use of semivariograms, it is possible to build many spatial realizations on the desired variable (*i.e.*, porosity). Each realization has the same probability of occurrence and honors the well data that have been imposed in the process of Gaussian stochastic simulation of porosity.

The calculation of horizontal semivariograms (x- and y-direction) for each lithology is difficult because there are only a few number of points available (*i.e.*, wells), which tends to produce pure nugget semivariograms (Pizarro and Lake, 1997). Figure 3.A.4.7 illustrates the semivariograms considered in this study. Zero-nugget spherical semivariograms were used to construct the porosity distribution in the truth reference case (case T). These semivariograms have two parameters as input: a range, which indicates the extent or size of the spatial autocorrelation, and a variance. The range is different for each of the three coordinate directions in case T. But because of the difficulty of estimating the range, horizontal ranges were used in the statistical models equal to one-half ($\lambda/\lambda_T$ = 0.5) and twice ($\lambda/\lambda_T$ = 2) those used in the reference case ($\lambda_T$). For the vertical semivariograms, wells provide sufficient spatial sampling to calculate the corresponding parameters. The horizontal ranges used in the reference case were approximately equal to the well spacing. Variances for porosity and bulk density were set to the values calculated from the sampled well-log data.

#### 3.A.4.4.3.2 Geostatistical Seismic Inversion Models

Geostatistical inversion provides a framework to quantitatively integrate seismic data, well logs, and geological information in one step (Bortoli *et al.*, 1993; Haas and Dubrule, 1994). In geostatistical inversion, a prior AI model is built and then modified until the global misfit between the measured seismic data and the simulated seismic data is reduced to a prescribed value (usually the global misfit is less than 5% depending on the amount of noise present in the seismic data). Because AI can often be related to petrophysical parameters, geostatistical inversion can be used to directly obtain stochastic models of reservoir parameters that jointly honor the seismic and the well-log data.

In this study, a geostatistical inversion of the noisy post-stack seismic data from case T was performed for porosity (case IP) and bulk density (case ID). The PDFs of those two variables for each lithology are shown in Figure 3.A.4.8. Semivariograms used in the inversions were identical to those described earlier (Figure 3.A.4.7). The relationships used in the geostatistical inversion between AI and porosity, and AI and bulk density for each lithology were calculated from well-log data. These are shown in Figure 3.A.4.5. Given that partial angle offsets of the previously generated pre-stack seismic data are available, a geostatistical inversion was also performed of the far offset seismic data for porosity (case IPEI) and bulk density (case IDEI). Far offsets of seismic data can be important because the AI of the encasing shale is larger than the AI of the reservoir sand (Rutherford and Williams, 1989). The properties obtained from this inversion (porosity and bulk density) were subsequently used in the static description of the reservoir.

### 3.A.4.5 Static and Dynamic Reservoir Evaluation

The two main assumptions underlying the reservoir construction methods described above are the second-order stationarity of the data and the existing relationship between AI and petrophysical parameters. Another important issue is the degree of representativeness of the data (Bu and Damsleth, 1995). It is known that, statistically speaking, well information is rarely representative of the spatially variability and volume under study. Often such a fact is overlooked but the information is nevertheless used because they are a primary and direct source of rock and fluid properties.

### *3.A.4.5.1 Consistency in Data Space for Seismic Data*

To ascertain the consistency of the inferred hydrocarbon reservoir models, an assessment was performed of the error in predicting the 3D seismic data. This was accomplished by simulating the seismic data at the onset of production for each of the construction methods described above. Subsequently, a correlation coefficient was calculated between the seismic data of each case and the seismic data associated with the reference model (case T).

Figure 3.A.4.9 is a map of the correlation coefficient in data space (*i.e.*, seismic data) for an arbitrary statistical realization of case G-1. The average correlation coefficient ($r^2$) is 0.21. Table 3.A.4.3 summarizes the results obtained for the remaining cases considered in this Section. Cases H, L, and G exhibit the smallest correlation coefficients. By construction, cases that make use of seismic data in the definition of the reservoir properties must exhibit large correlation coefficients. For instance, Cases DAI and AIW exhibit the largest correlation since the AI is calculated through seismic inversion. Cases IP, ID, IPEI, and IDEI exhibit a large correlation coefficient. Obtaining a correlation map like the one shown in Figure 3.A.4.9 helps one to validate the predicted results against other sources of data.

### *3.A.4.5.2 Consistency in Model Space for Porosity*

An error assessment was also performed in model space (*i.e.*, porosity). The porosity model of the reference case was compared to the estimated porosity models of all cases. Figure

3.A.4.10 shows a map of correlation coefficients between the actual and estimated porosity for the hydrocarbon reservoir model inferred from an arbitrary realization of case G-1. Table 3.A.4.3 summarizes the results obtained for other cases considered in this Section and shows that cases H, L, and G exhibit the smallest correlation coefficient, whereas cases IP, ID, IPEI, and IDEI exhibit a larger correlation coefficient.

The average correlation coefficients between the measured and simulated seismic data are necessarily larger than those between the actual porosity and seismic-inferred porosity. This is because the latter makes use of additional petrophysical relationships that tend to degrade the correlation. The correlation coefficients between the simulated and measured seismic data are primarily measures of the errors introduced in the forward and inversion steps.

When determining global dynamic behavior (*e.g.*, cumulative oil production) the agreement in model space is secondary. For instance, a good prediction of oil recovery can be achieved with a simple model. However, this agreement becomes important when detailed studies are necessary such as in the determination of an infill drilling location. Here, the cases with high correlation in model space consistently yielded the closest fluid distribution to that of the reference model.

Many of the following results are shown in the form of Box plots. A Box plot enables one to examine a number of variables and to extract the more salient characteristics of their distributions. It also gives one insight to the global behavior of the corresponding variable. In a Box plot, the y-axis displays the variation of the data and the x-axis displays the names of each case. Each vertical box encloses 50% of the data with the median value of the variable displayed as a horizontal line within the box. Bottom and top boundaries of the box define the 25 and 75 percentiles of the variable population. Lines extending from the top and bottom of each box define the minimum and maximum values that fall within a population range. Any value outside of this range, called an outlier, is displayed as an individual point.

In a Box plot, the reproducibility of a prediction is given by the size of the vertical boxes. Bias shows itself as the median value being significantly different from the true value, or when the vertical box does not cover the true case. Therefore, in a sense, increasing the precision of a prediction can contribute to the bias if the median value is not brought closer to the true value. It is important to note also that in nearly every practical case, the true value remains unknown.

#### *3.A.4.5.3 Semivariograms and Property Relationships*

Increasing the range in the property semivariograms amplifies the variability of the dynamic behavior for cases that involve the use of semivariograms (cases G, IP, ID, IPEI, and IDEI). The increased variability is consistently observed in different dynamic parameters. A larger range semivariogram produces slightly smaller correlation coefficients when assessing the quality of the results in data and model space (see Table 3.A.4.3).

If the construction of the static model is based on AI but there is no correlation between AI and petrophysical parameters (see Figure 3.A.4.6) then the initial static description of the reservoir is inconsistent. Case AIW was designed to show that the lack of correlation between acoustic and petrophysical properties causes the seismic data not to contribute positively in the construction of a model of reservoir properties. Nevertheless, seismic data could still be useful for boundary identification. A noisy (scattered) relationship between AI and porosity deteriorates the correlation in model space (see Table 3.A.4.3) and leads to dynamic results that are biased, hence not representative of the reference case T. Figure 3.A.4.11 describes the original oil in place and cumulative oil recovery after 7 years of production for case AIW. Case AIW is evidently incorrect and therefore excluded from further analysis. Since the static model is not accurate, this case underpredicts the oil in place by 82.6% and oil recovery after 7 years of production by 84.6% compared to case T.

### *3.A.4.5.4 Consistency in Data Space for Production Data*

#### 3.A.4.5.4.1 Oil in Place

Estimation of the original oil in place (OOIP) is an important appraisal tool in the early stages of the life of the reservoir. In this study, OOIP is not critical since all the models exhibit the same geometry (*i.e.*, the same geometrical boundaries). The assumption of a known geometry is based on the fact that normally the available seismic data can be used to construct a geometrical model of reservoir compartments. However, it is easily seen that each constructed model produces a different set of static distributions of properties (porosity and porosity-dependent variables) and therefore the OOIP is different in each case. For comparison, the OOIP of each case was normalized against that of case T.

The Box plots of Figures 3.A.4.12 and 3.A.4.13 indicate that the range of variation of normalized OOIP is small (within ± 8% of case T) because it generally satisfies the same global statistics. Variations of OOIP entailed by the realizations for a particular case are also small because even though locally varying, the realizations exhibit identical average properties. OOIP, being itself a global quantity, is more sensitive to averages than to variability. More accurate predictions are obtained for those cases that involve the use of seismic data. Results for a given Case exhibit more variability when the range of the corresponding semivariogram is larger than that used in the reference case. The geostatistical inversion for bulk density overpredicts the OOIP whereas the one for porosity underpredicts the OOIP. This behavior can be related to the strength of the correlation between porosity and AI, and bulk density and AI (see Figure 3.A.4.5).

Figures 3.A.4.12 and 3.A.4.13 embody a conceptual insight that will be a major conclusion of this Section. For none of the geostatistical or seismic inversion cases (G, IP, IPEI, ID and IDEI) do the 25-75 percentile vertical boxes overlap the prediction yielded by the reference case. It is difficult to make firm conclusions about this because of the paucity of realizations (10) on which the results were based. The bias has been exacerbated by the reduction in uncertainty caused by adding more data, which is most evident in Figure 3.A.4.12. In neither case, Figure 3.A.4.12 or 3.A.3.13, is the bias large; however, it will prove to be significant in the global dynamic responses described below. The source of the bias is the noise and the non-linearity of the various transforms required to make the description.

The OOIP for the realizations in all the following cases was set to that of the reference case (case T) so that the dynamic reservoir predictions could be performed assuming a reservoir with the same initial volumetrics.

### 3.A.4.5.4.2 Oil Recovery

Oil recovery represents a global dynamic response at a specific time in the life of the reservoir. It depends mainly on the recovery mechanism, production strategy, and time. An example of this is shown in Figure 3.A.4.14 for an arbitrary realization of cases with $\lambda/\lambda_T$ = 0.5. Figure 3.A.4.15 shows the results of evaluating the normalized oil recovery after 2010 days of production. For none of the geostatistical or seismic inversion cases do the 25-75 percentile vertical boxes overlap the prediction yielded by the reference case. The recovery for cases H, L, and DAI is less than that of case T by 39%, 36%, and 25%, respectively. Median oil recovery for cases with $\lambda/\lambda_T$ = 2 (bottom panel) is within ± 19% of case T. For those cases with $\lambda/\lambda_T$ = 0.5 (top panel) the results are within ± 15% of case T. Even though the outcome of this global variable remains biased, the decrease in relative error in oil recovery comes as a direct consequence of adding new information in the construction of the property models. Table

3.A.4.4 shows the difference between the maximum and minimum values of the normalized oil recovery of the cases shown in Figure 3.A.4.14. Cases involving seismic data (IP, ID, IPEI, and IDEI) entail better forecast precision than the realizations obtained only through the geostatistical case (case G). The latter statement is clear for cases with $\lambda/\lambda_T$ = 0.5. As shown in Table 3.A.4.4, for cases with $\lambda/\lambda_T$ = 2 the differences are small. If oil recovery is evaluated at a given pore volume of water injected, there are small differences and the results are not biased. However, the volume of water injected is determined by the chosen injection strategy (constant injection pressure in our case), as well as by the initial reservoir model description.

#### 3.A.4.5.4.3 Time of Water Breakthrough

Figure 3.A.4.16 shows the normalized time of water breakthrough for all cases considered in this study. A wider variability is observed with respect to the variability of parameters analyzed before (*e.g.*, recovery). The range of variation is between 0.5 and 2 times the water breakthrough time for case T. For some of the cases, the 25-75 percentile boxes overlap the prediction yielded by the reference case. Results shown in Figure 3.A.4.16 are less biased than those of Figure 3.A.4.15 because they do not exhibit an average dynamic response as in the case of oil recovery. Time of water breakthrough represents a dynamic response of the spatial distribution of reservoir properties, especially the permeability distribution.

### *3.A.4.5.5 Value of Information*

Figure 3.A.4.17 shows the oil recovery at the time of water breakthrough normalized with respect to case T for $\lambda/\lambda_T$ = 0.5. Oil recovery represents a global dynamic behavior and, as discussed earlier, time of water breakthrough is closely related to the spatial distribution of properties. For all cases that involve seismic data the 25-75 percentile boxes overlap the value

yielded by the reference case. In Figure 3.A.4.17, one can quantitatively assess the benefits of including more information (*i.e.*, seismic data) into the process of model construction.

Since the measure of accuracy of a prediction depends on the time at which the prediction is taken, a different assessment of accuracy is now considered based on the $\ell_2$-norm of the time record of cumulative oil recovery, given by

$$U(t) = \frac{1}{t_t} \int_{t=0}^{t=t_t} \left[ d_{caseX}(t) - d_{caseT}(t) \right]^2 dt , \tag{3.A.4.1}$$

where $U(t)$ is the global least-squares misfit, $t_t$ is total time of simulation, and $d(t)$ is the cumulative oil recovery. The $\ell_2$-norm is a global measure of recovery that does not depend on a specific time after the onset of the waterflood. Figure 3.A.4.18 illustrates the results of performing such a calculation. Values shown in this figure were normalized against the homogeneous case (T). The horizontal axis identifies the particular case and can also be interpreted as a measure of the information content (scant information content to the left and higher information content to the right). It is clearly seen that the cumulative uncertainty in time decreases as more information is included in the construction of the initial model.

### *3.A.4.5.6 Experiment Assuming Linear Relations*

As emphasized earlier, the present Section hypothesizes that the main sources of bias are nonlinear flow equations, noisy relationships between elastic and petrophysical variables, the production scheme, and the correctness of the physical model. As part of this work, a decision was made to investigate the importance of some of these biases in the predictions of oil recovery. To accomplish such an objective, a special case was designed in which all the relationships used in the fluid-flow simulator were made linear and precise (relative permeability, porosity-permeability), and the fluids exhibited the same viscosity. This case is not realistic but sheds valuable insight to the source of the bias in the prediction of oil recovery.

Simulations were redone for the reference case (T) and case G-2 (designated case G-2L). Results were compared with those presented in Figure 3.A.4.15 and are shown in Figure 3.A.4.19. The prediction of oil recovery for this experiment is less biased and more accurate than in previous results. This suggests that the source of the bias in the prediction of oil recovery is caused by the nonlinearity implicit in the underlying multi-phase fluid-flow equations.

### 3.A.4.6 Summary and Conclusions

The work presented in this Section was an attempt to assess the value of 3D seismic data in the construction of hydrocarbon reservoir models. Several strategies were considered to appraise the influence of the usage of seismic data in the construction of a reservoir model. Numerical experiments focused on the relatively difficult case of a waterflood production system in which water was injected to displace oil as a way to enhance production efficiency. Seismic data are relatively insensitive to detecting spatial variations in oil and water saturations, especially in the presence of low-porosity rock formations (porosities below 15%). Thus, a waterflood experiment constitutes a worst-scenario case study for the usage of seismic data in reservoir characterization studies (as opposed to, for instance, the optimal seismic detection problem of water and gas saturations in thick, high-porosity formations). The main appraisal tool used in this Section to assess the value of seismic data was the comparison of the time record of fluid production measurements with respect to that of a reference (truth) model. As expected, it was impossible to isolate the influence of the usage of seismic data in reservoir construction from technical issues concerning non-uniqueness and the definition of ancillary fluid and petrophysical variables unrelated to seismic measurements. Such ancillary variables included the choice of a porosity-permeability relationship, the choice of global relative permeability and capillary pressure curves, and the choice of degree of spatial smoothness of reservoir variables interpolated from well-log measurements. Despite these difficulties, an attempt was made to compare on equal footing a set of models with different degrees of spatial complexity. This was performed by standardizing the role played by both initial fluid volumetrics and the choice of a production scheme on the forecast of fluid production. Subsequently, quantitative integration was accomplished using various types of seismic data to construct static reservoir models with increasing degrees of spatial complexity. Even with the use of seismic data, the construction of reservoir models remains non-unique (an uncountable set of models exist that honor the complete set of available measurements). Multi-phase fluid-flow simulations associated with each set of models (10 individual models per set) were performed in order to quantify the predictive power of each set of measurements and these time-domain simulations were compared against those of the reference model. Finally, an effort was made to take into account the variability of the time record of production measurements as it directly impacted the measure of appraisal. Global as well as time dependent measures of appraisal were explored to quantify the added value of seismic data. The following conclusions stem from the work described in this Section:

Significant biases in predictions of fluid recovery can be associated with pure fluid-flow phenomena to which seismic measurement remain insensitive. Even with the use of seismic data, sources of prediction bias can be more dominant that an incremental reduction in prediction bias due to the usage of seismic data. Sources of prediction bias associated with fluid phenomena include the nonlinear nature of the underlying multi-phase fluid-flow equations, nonlinear and inaccurate constitutive relationships (*e.g.*, porosity vs. permeability), noisy measurements, variations in the spatial support of input measurements, and the choice of fluid production scheme, among others.

Reservoir models are often constructed with geostatistical methods that make use of spatial semivariograms. It was found that a considerable degree of variability in static and dynamic predictions of reservoir behavior could be caused by the usage of larger than necessary semivariogram ranges. Regardless of the usage of seismic data, accurate estimation of semivariogram functions and parameters thereof is crucial to performing reliable forecasts of fluid production. For instance, the accuracy of predicted oil recovery is adversely affected by an improper choice of semivariogram range.

Lack of correlation between elastic and petrophysical parameters causes the seismic data not to contribute positively to reduce uncertainty in production forecasts. Fluid production forecasts associated with loosely correlated petrophysical-elastic transforms are rendered biased and inaccurate.

Static and dynamic predictions performed from reservoir models constructed with the use of seismic data normally exhibit an incremental decrease in their bias with respect to a nominal prediction bias due to pure fluid-flow phenomena. Global measures of prediction bias show a consistent improvement with respect to predictions derived from models that do not make use of seismic data. This conclusion is valid as long as a high degree of correlation exists between petrophysical and elastic parameters, and follows from comparison of production variables such as recovery efficiency, and time of water breakthrough, for instance.

In this section (Sections 3.A.3 and 3.A.4), an integrated reservoir evaluation with the use of post-stack seismic data and pseudo-angle stack pre-stack seismic data was presented. The next section comprises two Sections that introduce novel approaches for the stochastic inversion of the full gather of pre-stack seismic data and well logs.

**Table 3.A.4.1: Summary of fluid and petrophysical properties assumed in the construction of the numerical reservoir model considered in this Section.**

| Properties | | Values and units |
|---|---|---|
| Fluid | water density | 1.0 g/cm$^3$ |
| | oil density | 0.85 g/cm$^3$ |
| | water viscosity | 1.0 mPa-s |
| | oil viscosity | 5.0 mPa-s |
| | water compressibility | 4.5x10$^{-4}$ MPa$^{-1}$ |
| | oil compressibility | 2.9x10$^{-3}$ MPa$^{-1}$ |
| Reservoir | average $S_{wi}$ | 0.28 |
| | average $S_{or}$ | 0.25 |
| | porosity, $\phi(\bar{\phi},\sigma_{\phi})$ | N(0.21, 0.07) |
| | formation compressibility | 2.5x10$^{-4}$ MPa$^{-1}$ |
| | water endpoint | 0.3 |
| | oil endpoint | 0.9 |
| | z- to x-permeability ratio | 0.1 |
| | y- to x-permeability ratio | 0.7 |
| | depth to top of sand | 1219 m |
| Simulation | injection pressure | 17.2 MPa |
| | bottom-hole pressure | 2.0 MPa |
| | number of cells | 81x81x51 |
| | cell size | 23x23x6 m |
| | production perforations | entire sand interval |

**Table 3.A.4.2: Summary of the nomenclature used for the numerical experiments described in this Section.**

| Case | Key | Semivariogram Perturbations | |
|---|---|---|---|
| | | $\lambda/\lambda_T$ =0.5 | $\lambda/\lambda_T$ =2.0 |
| Reference (True) model | T | - | - |
| Homogeneous model | H | - | - |
| Layered model | L | - | - |
| Direct from AI model | DAI | - | - |
| Direct from AI model (poor correlation transform) | AIW | - | - |
| Geostatistics model* | - | G-1 | G-2 |
| GSI for porosity (post-stack)* | - | IP-1 | IP-2 |
| GSI for porosity (far offset)* | - | IPEI-1 | IPEI-2 |
| GSI for density (post-stack)* | - | ID-1 | ID-2 |
| GSI for density (far offset)* | - | IDEI-1 | IDEI-2 |
| GSI = Geostatistical Seismic Inversion<br>*10 realizations for each semivariogram | | | |

**Table 3.A.4.3: Average correlation coefficients ($r^2$) in model space (porosity) and data space (seismic amplitudes) between an arbitrarily-selected model realization and the reference model.**

| Case | $r^2$ model space (porosity) | $r^2$ data space (seismic data) |
|---|---|---|
| H | - | 0.18 |
| L | 0.18 | 0.21 |
| DAI | 0.44 | 0.98 |
| AIW | 0.09 | 0.98 |
| G-1 | 0.19 | 0.21 |
| IP-1 | 0.54 | 0.87 |
| IPEI-1 | 0.52 | 0.93 |
| ID-1 | 0.53 | 0.87 |
| IDEI-1 | 0.51 | 0.93 |
| G-2 | 0.17 | 0.20 |

| **Case** | $r^2$ **model space (porosity)** | $r^2$ **data space (seismic data)** |
|---|---|---|
| IP-2 | 0.53 | 0.87 |
| IPEI-2 | 0.54 | 0.91 |
| ID-2 | 0.51 | 0.88 |
| IDEI-2 | 0.52 | 0.92 |

**Table 3.A.4.4:** **Range of variation of normalized oil recovery at 2010 days of production.**

| **Case** | **Range* of Variation Normalized Oil Recovery** | |
|---|---|---|
| | **Semivariogram Perturbations** | |
| | $\lambda/\lambda_T$ **= 0.5** | $\lambda/\lambda_T$ **= 2.0** |
| G | 0.072 | 0.1123 |
| IP | 0.042 | 0.084 |
| IPEI | 0.048 | 0.060 |
| ID | 0.024 | 0.096 |
| IDEI | 0.036 | 0.094 |

*Range = (maximum – minimum)

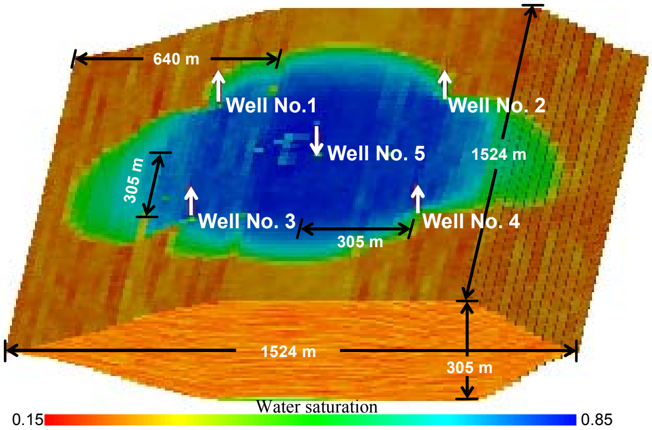

**Figure 3.A.4.1**: Three-dimensional view of the distribution of water saturation in the reservoir sand after 4 years of waterflood. Sand dimensions, well spacing, and well locations are as indicated on the figure.

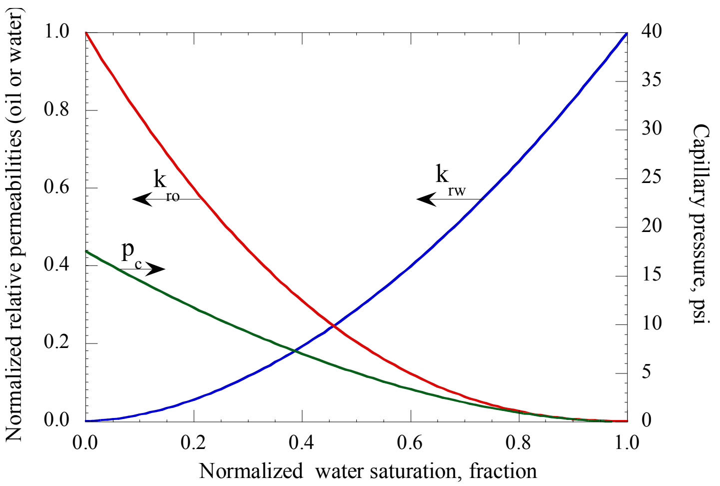

**Figure 3.A.4.2**: Normalized set of relative permeability and capillary pressure curves used to model the waterflood. Normalization of relative permeability was performed against end points.

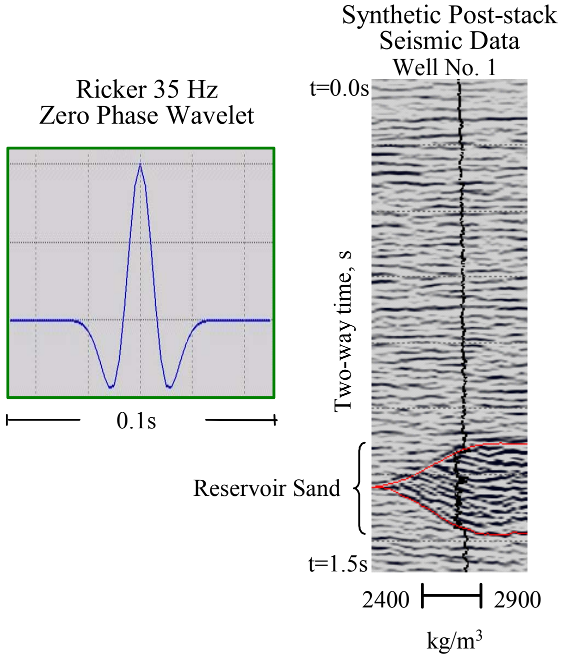

**Figure 3.A.4.3**: Ricker wavelet used in the simulation of post-stack 3D seismic data (left panel) and cross-section of post-stack seismic data along Well No. 1 (right panel).

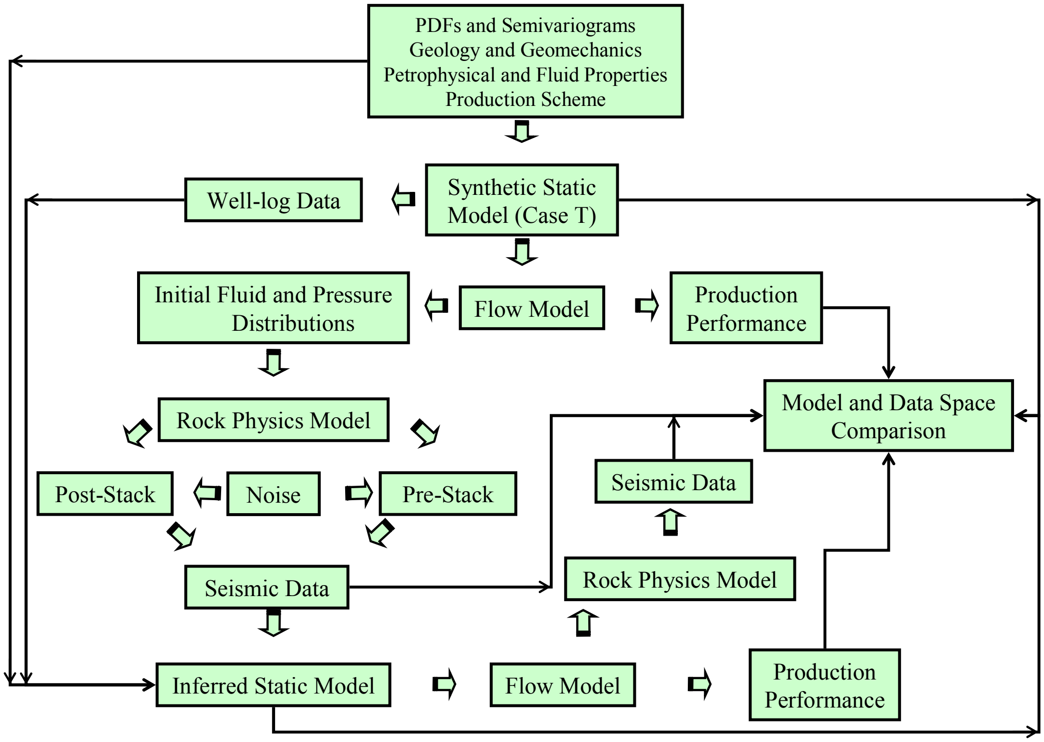

**Figure 3.A.4.4**: Integrated flow diagram describing the method used in this Section for validating static descriptions and dynamic predictions.

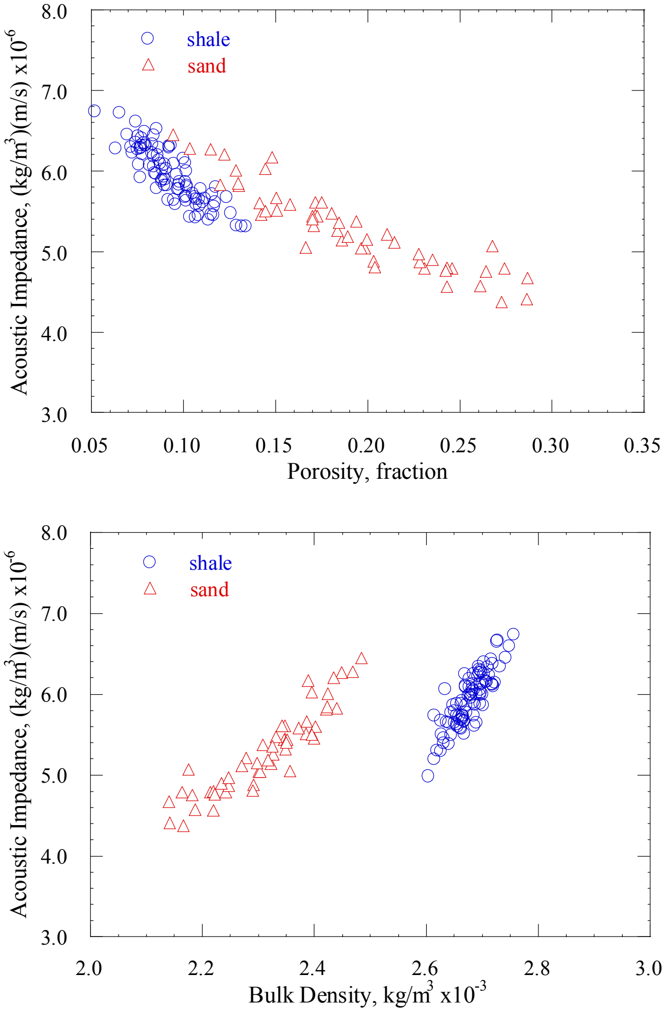

**Figure 3.A.4.5**: Relationship between acoustic impedance and porosity (top panel), and acoustic impedance and bulk density (bottom panel) constructed from well-log data sampled from the reference case T.

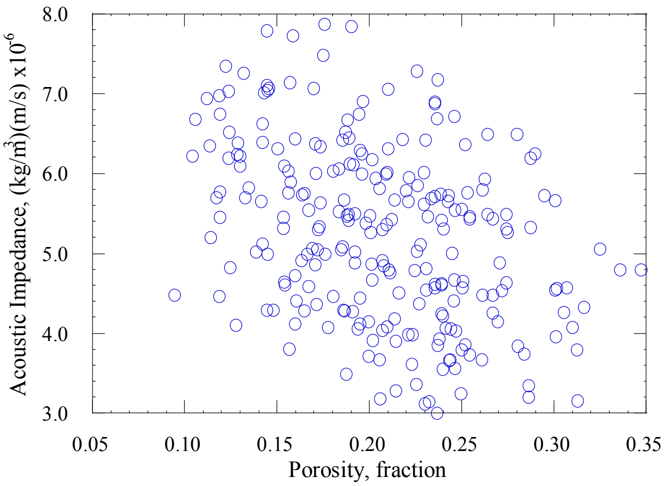

**Figure 3.A.4.6**: Relationship between acoustic impedance and porosity for case AIW. The correlation coefficient ($r^2$) is 0.1.

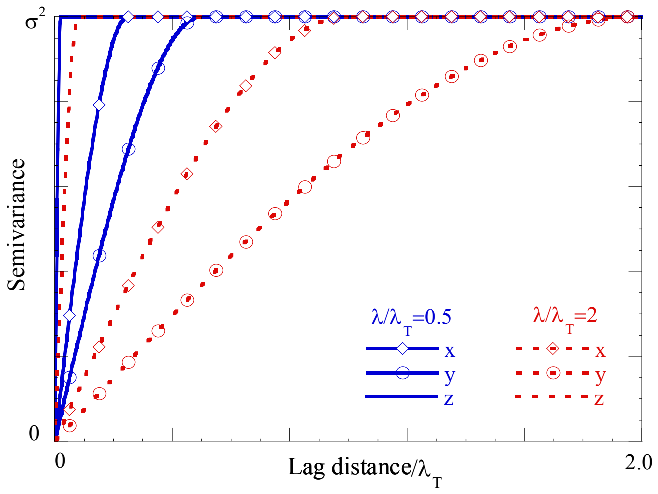

**Figure 3.A.4.7**: Semivariograms within the reservoir sand in the x, y, and z directions used for the stochastic simulations of porosity and bulk density. The variable $\lambda_T$ is the range of the spherical semivariogram used in the construction of the reference model, here identified as case T.

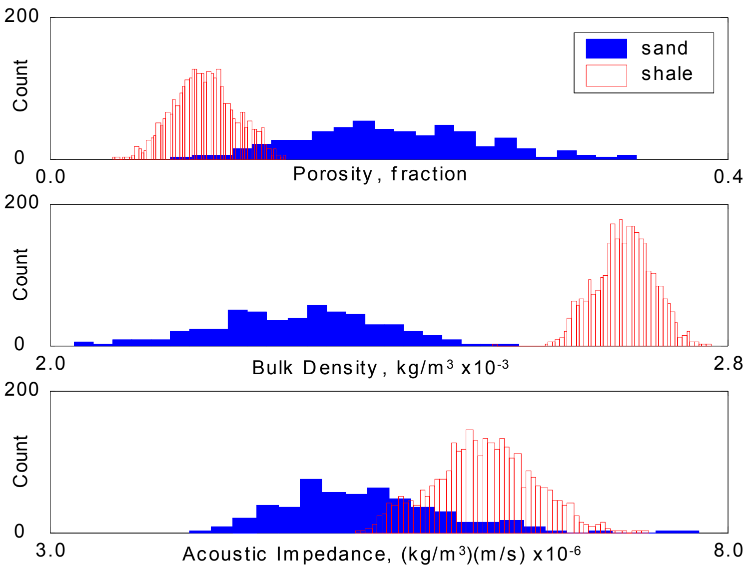

**Figure 3.A.4.8**: Histograms of porosity (top panel), bulk density (mid panel), and acoustic impedance (bottom panel) sampled from well-log data within the reservoir sand and the embedding shale for case T.

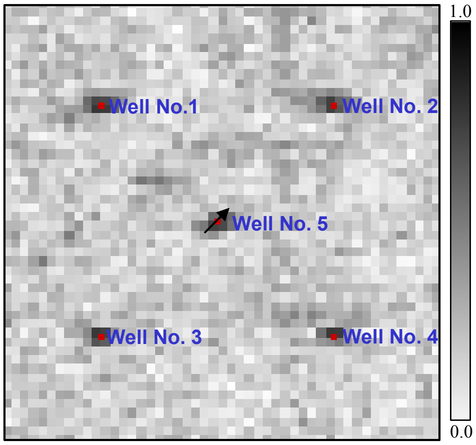

**Figure 3.A.4.9**: Map of correlation coefficient ($r^2$) between vertical columns of seismic amplitudes associated with the geostatistical case G-1 and the reference case T. A coefficient $r^2 = 1$ (dark shading) at a particular pixel indicates perfect correlation. The average $r^2$ for all pixels is 0.21. Table 3.A.4.3 summarizes the average correlation coefficients for additional cases.

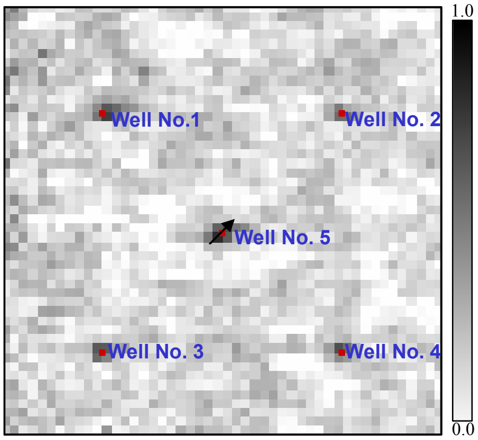

**Figure 3.A.4.10**: Map of correlation coefficient ($r^2$) between vertical columns of porosity associated with the geostatistical case G-1 and the reference case T. A coefficient $r^2 = 1$ (dark shading) at a particular pixel indicates perfect correlation. The average $r^2$ for all pixels is 0.19. Table 3.A.4.3 summarizes the average correlation coefficients for additional cases.

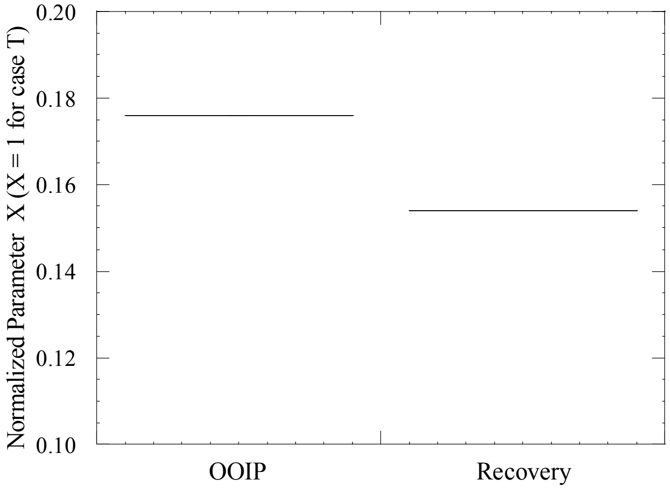

**Figure 3.A.4.11**: Plot of the predicted original oil in place and oil recovery after 7 years of production assuming poor correlation between acoustic impedance and porosity (case AIW). See Table 3.A.4.2 for a definition of the various case studies.

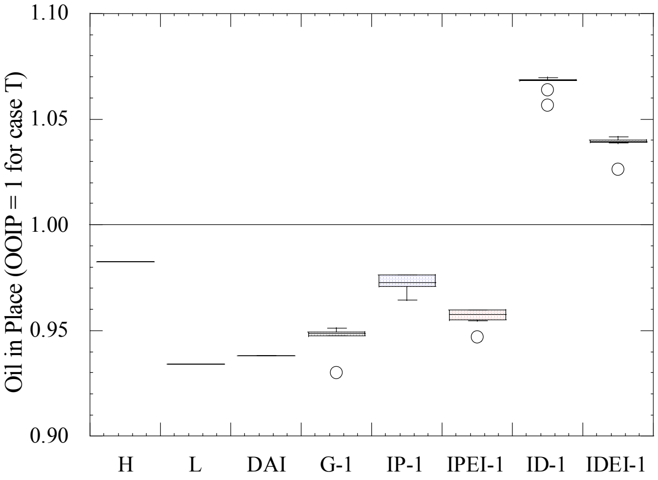

**Figure 3.A.4.12**: Box plot of normalized original oil in place for cases with $\lambda/\lambda_T = 0.5$. See Table 3.A.4.2 for a definition of the various case studies.

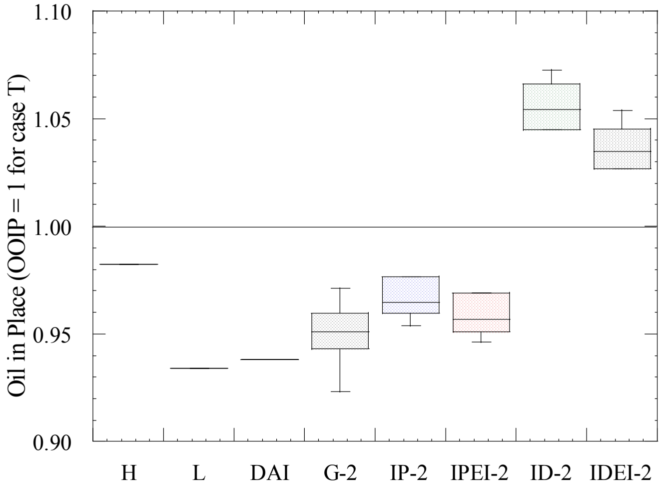

**Figure 3.A.4.13**: Box plot of normalized original oil in place for cases with $\lambda/\lambda_T = 2$. See Table 3.A.4.2 for a definition of the various case studies.

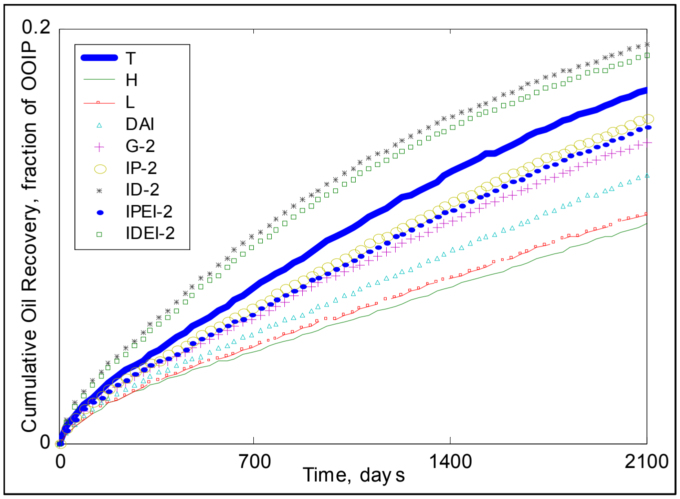

**Figure 3.A.4.14**: Cumulative oil recovery as a function of time for an arbitrarily-selected realization of cases with $\lambda/\lambda_T = 2$. See Table 3.A.4.2 for a definition of the various case studies.

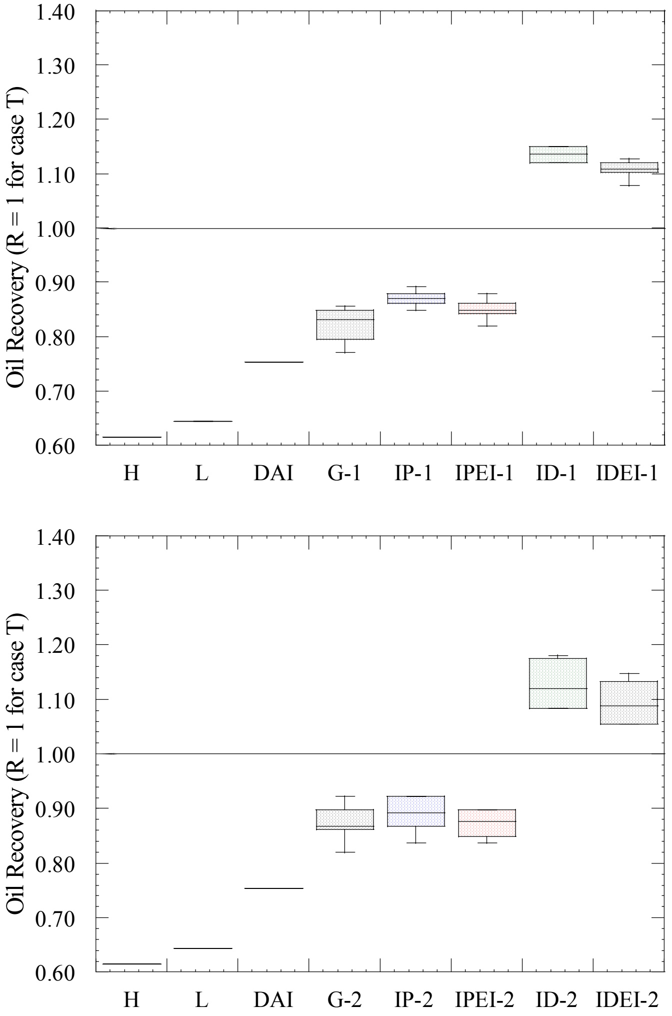

**Figure 3.A.4.15**: Box plot of normalized oil recovery after 2010 days of production. Top panel: $\lambda/\lambda_T = 0.5$. Bottom panel: $\lambda/\lambda_T = 2$. All models were initialized with the same volume of original oil in place. See Table 3.A.4.2 for a definition of the various case studies.

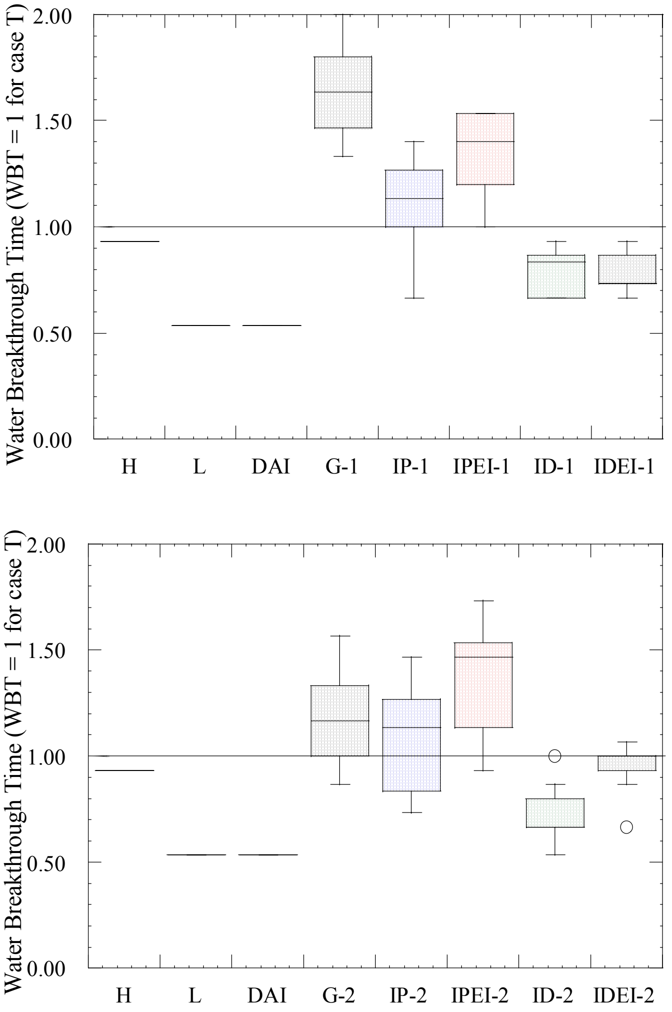

**Figure 3.A.4.16**: Box plot of normalized time of water breakthrough. Top panel: $\lambda/\lambda_T = 0.5$. Bottom panel: $\lambda/\lambda_T = 2$. All models were initialized with the same volume of original oil in place. See Table 3.A.4.2 for a definition of the various case studies.

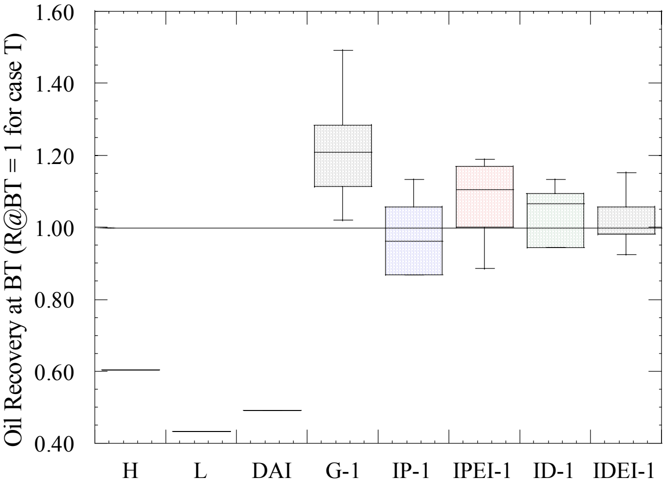

**Figure 3.A.4.17**: Box plot of normalized oil recovery at time of water breakthrough for cases with $\lambda/\lambda_T = 0.5$. See Table 3.A.4.2 for a definition of the various case studies.

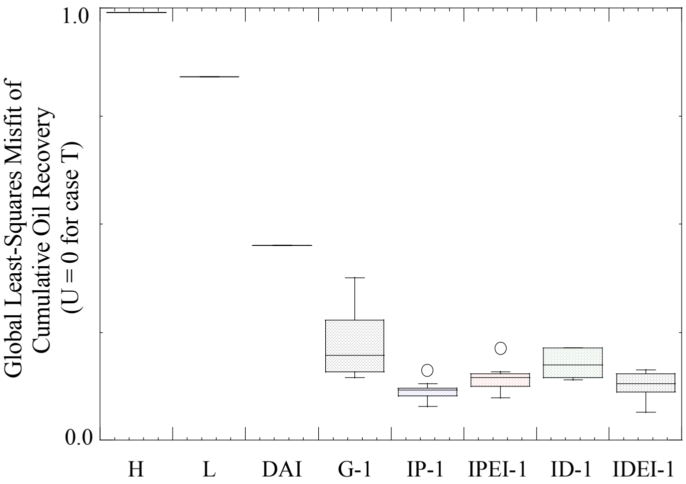

**Figure 3.A.4.18**: Box plot of global least-squares misfit (U) for cases with $\lambda/\lambda_T = 0.5$.

$U(t) = \frac{1}{t_t}\int_{t=0}^{t=t_t}\left[d_{caseX}(t) - d_{caseT}(t)\right]^2 dt$, where d(t) is cumulative oil recovery and $t_t$ is total time of simulation. See Table 3.A.4.2 for a definition of the various case studies.

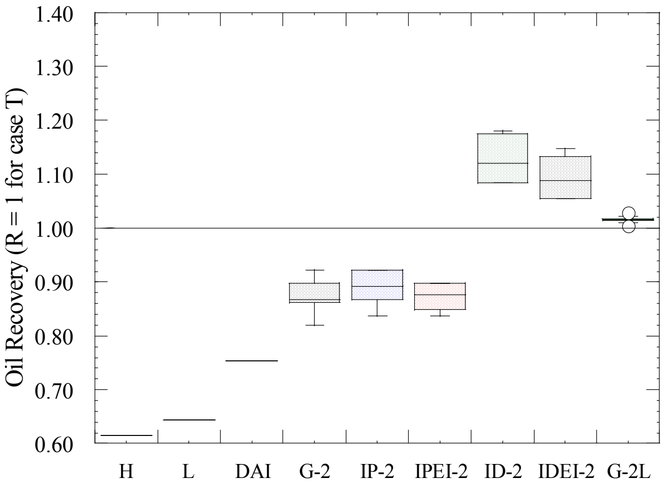

**Figure 3.A.4.19**: Box plot of normalized oil recovery after 2010 days of production for cases with $\lambda/\lambda_T = 2$. All relationships involved in the fluid-flow simulations for case G-2L are linear. See Table 3.A.4.2 for a definition of the various case studies.

## 3.A.5: CONDITIONING RESERVOIR MODELS TO PRE-STACK SEISMIC DATA AND WELL LOGS : NONLINEAR ONE-DIMENSIONAL PRE-STACK SEISMIC INVERSION

This Section describes some factors that control and affect the inversion of 1D pre-stack seismic data. Such factors include optimization technique, sampling strategy, data misfit function, and measures of smoothness. A novel global stochastic inversion technique is introduced to estimate and appraise 1D distributions of elastic parameters from surface pre-stack seismic measurements. Numerical experiments are performed on synthetic data sets to evaluate inversion factors and the novel inversion algorithm.

### 3.A.5.1 Introduction

Estimation of elastic properties of rock formations from surface seismic data is a subject of interest to the exploration and development of hydrocarbon reservoirs. This Section develops a global inversion technique to estimate and appraise 1D distributions of compressional-wave velocity, shear-wave velocity, and bulk density, from normal-moveout corrected PP pre-stack surface seismic measurements. The objective is twofold: to evaluate the effect of the choice of optimization algorithm and data misfit function, of the sampling strategy, and of the degree and type of smoothness criterion enforced by the inversion, and to introduce a new stochastic inversion algorithm that efficiently combines sampling and smoothing strategies borrowed from the field of geostatistical estimation. It is found that the choice of optimization technique can significantly condition the efficiency of the inversion. Extensive numerical experiments show that very fast simulated annealing is the most efficient minimization technique among alternative approaches considered for global inversion. In addition, an appropriate choice of data misfit function is necessary for a robust and efficient match of noisy and sparse surface seismic measurements. Because of the inherent non-uniqueness of the inverse problem, provisions are necessary to control the degree and kind of smoothness criterion enforced in the estimation process.

Several procedures are discussed in this Section to simultaneously enforce smoothness and to assess uncertainty of the estimated elastic parameters. The proposed global inversion algorithm is tested on noisy synthetic data to generate smooth 1D models of compressional- and shear-wave velocity and bulk density. A feasibility analysis is also presented of the resolution and uncertainty of pre-stack seismic data to infer a 1D distribution of elastic parameters measured with wireline logs in the deepwater Gulf-of-Mexico. In general, the proposed inversion algorithm is computationally more efficient than alternative global inversion procedures considered in this Section. It also provides a more flexible way to control the degree of smoothness of the estimated elastic parameters, and naturally lends itself to the assessment of model uncertainty and data sensitivity.

### 3.A.5.2 Background and Formulation

The physical process of reflection, transmission, and mode conversion of plane waves at a horizontal boundary as a function of incident angle has been described by Knott (in 1899) and Zoeppritz (in 1919) and has been explored extensively by several of authors (*e.g.*, Aki and Richards, 2002). Pre-stack seismic data are often used to estimate subsurface petrophysical properties. Independent elastic properties derived from pre-stack surface seismic data include compressional-wave velocity, shear-wave velocity, and bulk density or PAI, SAI, and bulk density as a function of depth or time.

The problem of estimating 1D distributions of elastic parameters from pre-stack seismic data can be approached via nonlinear inversion. This procedure is equivalent to the minimization of an objective function written as the metric of the difference between the measured and numerically simulated pre-stack surface seismic data. In most applications, inversion requires an efficient and accurate forward operator to simulate the measured seismic data. Inversion of pre-stack seismic data yields a 1D distribution of elastic parameters (*i.e.*, compressional- and shear-wave velocities and bulk density) from the information content available in both time and source-receiver space. Approaches to this problem include the use of different approximations of Zoeppritz equations (Wang, 1999) or else angle stacks (Simmons and Backus, 1996). The inversion algorithm considered in this Section makes use of the reflectivity method (Fuchs and Muller, 1971; Kennett, 1983) to compute the full-wave response of a stack of horizontal layers including all converted waves and propagation modes. Specifically, a simplified version of the reflectivity method is used to efficiently compute synthetic seismograms for P waves (primaries only) in offset-time (x, t) domain and devoid of transmission losses.

Estimation methods based on local optimization often fail to produce a global minimum when the starting solution is far from the optimal point and the objective function is multimodal (Tarantola, 1987). Applications of local optimization strategies can be found in the open technical literature (*e.g.*, Tarantola, 1986; Pan *et al.*, 1988; 1994). On the other hand, exhaustive trial-and-error search methods in model space are difficult to implement in an efficient manner because the model space is often extremely large (Sen and Stoffa, 1991; 1995). The efficiency of global optimization methods remains largely controlled by both the expediency of the search algorithm in model space and the computer power available to simulate the measurements. Examples of global optimization techniques can be found in Kirkpatrick *et al.* (1983), Sen and Stoffa (1991), and Stoffa and Sen (1991). Hybrid optimization techniques have also been used to include the most important features of local and global inversion methods (Chunduru *et al.*, 1997; Xia *et al.*, 1998).

The present Section implements a global optimization technique that is based on simulated annealing (SA) as shown in Figure 3.A.5.1. Such a technique makes use of a random-walk search method governed by prescribed transition probabilities to find an optimal global point in model space (Ingber, 1989).

Inversion of pre-stack seismic data into a 1D distribution of elastic parameters remains a highly nonlinear, nonunique process that requires significant forward modeling capabilities. Pre-stack seismic waveforms are modeled assuming a locally 1D distribution of elastic parameters. The problem of estimating the corresponding 1D distribution of elastic parameters is here cast as the global minimization of an appropriately constructed objective function. Global optimization methods described in this Section implement a Monte Carlo guided search method and a minimization schedule based on SA. They are designed to address the multimodality of the objective function without an exhaustive search, and generally pursue the global optimum regardless of the starting point in parameter space. The estimation of model parameters is also performed while enforcing physical constrains (*e.g.*, trends) that eliminate the need to search for inconsistent models that may also honor the measurements.

### 3.A.5.3 Global Optimization Technique

Simulated annealing is a global optimization method that replicates the thermodynamic cooling of a multi-particle physical system (Salamon *et al.*, 2002). The range of possible global energy values adopted by such a system corresponds to the range of values considered by the objective function. Metropolis' procedure emulates the natural process whereby crystal lattices of glass or metal relax to a state of lower energy state of thermal equilibrium. This process is usually referred to as annealing (Metropolis *et al.*, 1953). The idea behind SA is that the objective function relates the global system energy to a given state of the system and various manners to bring the multi-particle system to a lower state of thermodynamic equilibrium.

The optimization algorithm based on SA is given its inception with an initial model, $\mathbf{m}_0$, that has an associated energy, $E(\mathbf{m}_0)$. In this context, the notation $\mathbf{m}$ refers to a vector of size $N$ that contains all of the unknown model parameters ordered in some prescribed fashion and $E$ designates the objective function. A random walk algorithm is then used to select a new location in model space, $\mathbf{m}_i$. The global energy associated with the new location in model space, $E(\mathbf{m}_i)$, is then calculated and compared against the prescribed acceptance test. If the objective function decreases then the new location in model space, $\mathbf{m}_i$, is accepted unconditionally ($\mathbf{m}_0 = \mathbf{m}_i$); otherwise, the change is accepted but only with probability equal to $\exp[-(E(\mathbf{m}_i) - E(\mathbf{m}_0))/T]$, where $T$ is a control parameter called "temperature". Iteratively many locations in model space, $\mathbf{m}_i$, are proposed in sequence. Each new location may be either accepted or rejected according to this criterion. Such a procedure monotonically decreases the system temperature (*i.e.*, cooling schedule) while expectantly reaching the global optimum (see Figure 3.A.5.1). It can be shown that if the rate of temperature decrease is sufficiently slow, a global optimum can be found statistically for the global energy function (Ingber, 1989; 1993).

The numerical study presented in this Section evaluates various random-walk search methods associated with a global optimization based on SA. These search methods include Metropolis (Metropolis *et al.*, 1953), heat bath (Geman and Geman, 1984; Rothman, 1986), and very fast simulated annealing (VFSA; Ingber, 1989). These algorithms make use of the same acceptance/rejection criterion introduced by Metropolis. The difference among them is that

Metropolis SA draws a new sample in model space from a given PDF, heat bath SA produces weighted samples in model space that are always accepted, and VFSA draws a new sample in model space from a 1D Cauchy PDF that is a function of temperature. Metropolis SA and VFSA algorithms are a two-step process whereas heat bath SA is a one-step process.

The search algorithm allows a cooling sc3hedule in which temperature decreases exponentially with iteration number or annealing-time, $n$, given by

$$T = T_0 \exp\left(-qn^{1/N}\right), \tag{3.A.5.1}$$

where $T_0$ is a specified initial temperature, $q$ is a specified temperature decay rate, and $N$ is the dimensionality of the model parameter space (Ingber, 1989). These specified parameters are adjusted in an empirical manner and are often refined to improve the efficiency of the algorithm. Refer to Ingber (1993) for a general summary of practical applications of SA.

### 3.A.5.4 Sampling Technique

The approach to draw an initial model plays a central role in both including apriori model information and optimizing the computational efficiency of the algorithm. Many sampling strategies can be implemented depending upon the information or knowledge that is available apriori about the model. One of the simplest assumptions could be the lack of specific knowledge about the model parameters. In that case, only the minimum and maximum values of the model parameters would be known apriori. The initial model would then be drawn from uniform PDFs spanning the corresponding range of variation. With more apriori information about the model, global PDFs such as Gaussian distributions, for instance, may be used to constrain the search of model parameters including the selection of an initial model. The spatial distribution (*i.e.*, vertical trends), if available, can be used in conjunction with the PDFs of model parameters to draw the initial model and to constrain the subsequent selection of model parameters. In the latter case, each elastic property in the 1D subsurface model will exhibit a vertical property trend and each layer will be associated with a specific PDF. If more information or knowledge were available about the 1D distribution of elastic parameters then this apriori knowledge could be used to further constrain the inversion.

### 3.A.5.5 Data Misfit Function

To assess the similarities or differences between synthetic and measured pre-stack seismic data, several types of fitness or misfit functions were considered in the inversion algorithm. By definition, a solution to the inverse problem, $\mathbf{m}$, entails the smallest misfit or prediction error. There are different metrics, or norms, available to quantify the length or size of the misfit vector. The first type of data misfit function was constructed in the time domain. Equations (3.A.5.2) and (3.A.5.3) define the $\ell_1$- and $\ell_2$-norms of the data misfit vector sampled for all the discrete measurement times and offsets, namely,

$$\ell_1\text{-norm:}\quad \left\|e_t\right\|_1 = \sum_{i=1}^{Noff}\sum_{j=1}^{Nt}\left|e_{ij}\right| = \sum_{i=1}^{Noff}\sum_{j=1}^{Nt}\left|S(x_i,t_j)^{obs} - S(x_i,t_j)^{est}\right|, \tag{3.A.5.2}$$

and

$$\ell_2\text{-norm:}\quad \left\|e_t\right\|_2 = \left[\sum_{i=1}^{Noff}\sum_{j=1}^{Nt}\left|e_{ij}\right|^2\right]^{1/2} = \left[\sum_{i=1}^{Noff}\sum_{j=1}^{Nt}\left(S(x_i,t_j)^{obs} - S(x_i,t_j)^{est}\right)^2\right]^{1/2}, \tag{3.A.5.3}$$

where $S^{est}$ and $S^{obs}$ are the synthetic and measured pre-stack seismic data, respectively, as a function of source-receiver distance, $x_i$, and seismic time $t_j$. In the above equations, $N_t$ is the number of discrete time samples per trace for a given source-receiver offset, and $N_{off}$ is the number of source-receiver offsets available in the pre-stack gather.

The second type of data misfit function was constructed in the frequency domain using the real part of the geometric ($\ell_g$) and harmonic ($\ell_h$) metric of the correlation between synthetic and measured pre-stack seismic data described by Sen and Stoffa (1991), given by

$\ell_g$-norm:

$$\left\| e_f \right\|_g = \sum_{i=1}^{Noff} \left[ \frac{\sum_{j=1}^{Nf} S(x_i, f_j)^{obs} S^*(x_i, f_j)^{est}}{\left( \sum_{j=1}^{Nf} S(x_i, f_j)^{obs} S^*(x_i, f_j)^{obs} \right)^{1/2} \left( \sum_{j=1}^{Nf} S(x_i, f_j)^{est} S^*(x_i, f_j)^{est} \right)^{1/2}} \right], \quad (3.A.5.4)$$

and

$\ell_h$-norm:

$$\left\| e_f \right\|_h = \sum_{i=1}^{Noff} \left[ \frac{\sum_{j=1}^{Nf} S(x_i, f_j)^{obs} S^*(x_i, f_j)^{est}}{\left( \sum_{j=1}^{Nf} S(x_i, f_j)^{obs} S^*(x_i, f_j)^{obs} \right)^{1/2} + \left( \sum_{j=1}^{Nf} S(x_i, f_j)^{est} S^*(x_i, f_j)^{est} \right)^{1/2}} \right], \quad (3.A.5.5)$$

respectively. In the above equations, $f_j$ is frequency, $N_f$ is the number of frequencies, and the superscript (*) designates the complex conjugate operator. Weighted norms may also be considered in which time-frequency data for a given source-receiver offset may be assigned a specific weight. These weights could be designed to put all of the source-receiver data on equal footing and hence to increase the sensitivity of all the source-receiver traces to a perturbation of model parameters. Exploring the option of source-receiver weights, however, goes beyond the scope of this project.

### 3.A.5.6 Measures of Model Smoothness

Additional terms in the objective function are used to constructively bias the solution toward a preconceived notion of model properties. A general objective function that can adopt different metrics, constraints, and apriori information is given by

$$E(\mathbf{m}) = E_{data}\left(\mathbf{S}^{\mathbf{est}}, \mathbf{S}^{\mathbf{obs}}\right) + \alpha E_{model}(\mathbf{m}), \tag{3.A.5.6}$$

where $\alpha$ is a user-defined parameter that controls the relative importance of the two additive components; $E_{data}$ represents the data misfit function (in the present study this term could be any of the misfit functions defined in equations 3.A.5.2 through 3.A.5.5), and $E_{model}$ represents any measure of apriori information and constraints about the model parameters. Normally, the relative weight applied to the data misfit and smoothness terms of the objective function is determined by trial and error as there is no universal method to calculate it in a deterministic fashion.

The continuous version of the term $E_{model}$ in equation (3.A.5.6) is defined as operating on a seismic travel time-domain function $m = m(t)$ that contains the continuous model parameters, that is $v_p(t)$, $v_s(t)$, and $\rho_b(t)$, and is given by

$$E_{model}(m) = \left[\omega\int_{t_0}^{t_1}|m|^2\,dt + \beta\int_{t_0}^{t_1}\left|\frac{dm}{dt}\right|^2 dt + \gamma\int_{t_0}^{t_1}\left|\frac{d^2m}{dt^2}\right|^2 dt\right] + \left[\chi\int_{t_0}^{t_1}\left|\frac{dm}{dt}\right|^1 dt\right], \tag{3.A.5.7}$$

where $\omega$, $\beta$, $\gamma$, and $\chi$ are user-defined positive numbers that control the smoothness of the unknown model $m(t)$, and $t_0$ and $t_1$ are lower and upper time limits of the estimation domain, respectively. The first three terms of equation (3.A.5.7) are measures of the length of the solution based on a $\ell_2$-norm metric. These terms are called size, flatness $(F)$, and roughness

$(R)$, respectively. Menke (1989) emphasizes that such a measure of length is the simplest type of apriori assumption about a particular model. The last term of equation (3.A.5.7) is a measure of flatness ($F_1$) based on a $\ell_1$-norm metric. Usage of a mixed $\ell_2$-$\ell_1$-norm is in some cases appropriate to reduce deleterious Gibb's phenomena in the estimation of the continuous function $m(t)$.

Often, the size and smoothness properties of the model function, $m(t)$, are measured with respect to an apriori reference model (*i.e.*, $m - m_{ref}$). Such a strategy was not used as an explicit measure of simplicity in this Section. Excluding the first additive term, a discrete version of equation (3.A.5.7) can be written as

$$E_{model}(m) = \left[ \mathbf{m}^{\mathbf{T}} \left( \beta \mathbf{W}_{\mathbf{F}}^{\mathbf{T}} \mathbf{W}_{\mathbf{F}} + \gamma \mathbf{W}_{\mathbf{R}}^{\mathbf{T}} \mathbf{W}_{\mathbf{R}} \right) \mathbf{m} \right] + \left[ \chi \left\| \mathbf{W}_{\mathbf{F}_1} \mathbf{m} \right\|_1 \right], \tag{3.A.5.8}$$

where the superscript ($^{\mathbf{T}}$) designates the transpose operator, the vector ($\mathbf{m}$) contains the model parameters, that is $\mathbf{m} = (\rho_{b1}, \ldots, \rho_{bN}, v_{p1}, \ldots, v_{pN}, v_{s1}, \ldots, v_{sN})$, and $\mathbf{W}$ is a weighting block matrix. For the cases considered in this Section, model parameters change with vertical location (*i.e.*, seismic travel time), whereupon model flatness can be calculated using the discrete version of the model parameters and is given by

$$F(\mathbf{m}) = \mathbf{m}^{\mathbf{T}} \left[ \mathbf{W}_{\mathbf{F}}^{\mathbf{T}} \mathbf{W}_{\mathbf{F}} \right] \mathbf{m}, \tag{3.A.5.9}$$

where the block diagonal matrix $\mathbf{W}_{\mathbf{F}}$ can be written as

$$\mathbf{W}_{\mathbf{F}} = \begin{bmatrix} \mathbf{W}_{\boldsymbol{\rho}_{\mathbf{b}}} & & \mathbf{0} \\ & \mathbf{W}_{\mathbf{v}_{\mathbf{p}}} & \\ \mathbf{0} & & \mathbf{W}_{\mathbf{v}_{\mathbf{s}}} \end{bmatrix}. \tag{3.A.5.10}$$

Each of the block matrices included in equation (3.A.5.10) is determined by the type of approximation used to calculate the derivative (*e.g.*, backward, forward, three-point or five-point central difference approximation). For the case of a backward first-difference approximation (Burden and Faires, 1993) used for model parameters that are not regularly spaced, $\mathbf{W_X}$ is given by

$$\mathbf{W_X} = \begin{bmatrix} \frac{-1}{\sqrt{\Delta t_1}} & \frac{1}{\sqrt{\Delta t_1}} & & & \\ & \frac{-1}{\sqrt{\Delta t_2}} & \frac{1}{\sqrt{\Delta t_2}} & & \\ & \cdot & & \cdot & \\ & & & \cdot & \cdot \\ & & & \frac{-1}{\sqrt{\Delta t_{N-1}}} & \frac{1}{\sqrt{\Delta t_{N-1}}} \end{bmatrix}, \qquad (3.A.5.11)$$

where $\mathbf{x}$ is a generic designation for any of the three elastic parameters and $\Delta t$ is the interval between consecutive time samples. The roughness ($R$) of the model parameters can also be calculated in a similar manner as the flatness by discretizing the second derivative operator in place of matrix $\mathbf{W_x}$. The flatness and roughness terms mentioned above are measures under a $\ell_2$-norm metric; however, it is also possible to characterize similar smoothness terms under a $\ell_1$-norm metric as described by the last term of equation (3.A.5.8). In the most general case, the inversion algorithms considered in this Section are formulated as the minimization of the objective function

$$E(\mathbf{m}) = E_{data}\left(\mathbf{S}^{\mathbf{est}}, \mathbf{S}^{\mathbf{obs}}\right) + \beta\left|F(\mathbf{m})\right| + \gamma\left|R(\mathbf{m})\right| + \chi\left|F_1(\mathbf{m})\right|. \qquad (3.A.5.12)$$

### 3.A.5.7 Proposing an Inversion Algorithm

Based on extensive numerical experiments, the proposed inversion algorithm makes use of the most efficient annealing technique (*i.e.*, VFSA), the most efficient data misfit function (*i.e.*, harmonic), and introduces a sampling strategy based on geostatistical concepts. This algorithm makes explicit use of only the data misfit term of the general objective function described in equation (3.A.5.12).

Figure 3.A.5.2 shows a generalized flow diagram of the proposed inversion algorithm. At the outset, an initial model is randomly drawn from PDFs of model parameters (*i.e.*, $v_p$, $v_s$, and $\rho_b$). The type of PDF and the value-range constraints depend on the apriori information available about the model as discussed in previous sections. Subsequently, a specified number of hard-points are randomly chosen. A random walk in time designates the next time sample to be considered for analysis. Selection of the corresponding elastic parameters is performed using a Kriging estimator provided that the time sample remains within the assumed time correlation range of a prescribed semivariogram; otherwise the elastic parameters for this time sample are determined using a VFSA model solution rule. In the most general case, the Kriging of elastic parameters is performed using a fixed semivariogram model (*e.g.*, spherical, Gaussian) and fixed semivariogram parameters (*e.g.*, range, sill). Different semivariogram models can be used for a specific lithology and for a specific elastic parameter provided that apriori information on the corresponding parameters is available. A Metropolis acceptance/rejection criterion is enforced by the algorithm. Once all the discrete-time samples are visited, the current iteration is completed and the target temperature (equation 3.A.5.1) is lowered according to a prescribed cooling schedule. The process described above is performed iteratively until either the data misfit function or the number of iterations meets a previously established criterion. According to

this iterative procedure, the final solution remains conditioned by the starting realization of model parameters. Therefore, various seeds are necessary to evaluate the variability (uncertainty) of the final solution. Such a strategy provides a natural way to assess non-uniqueness and hence to quantitatively appraise the inversion results in the presence of noisy and sparsely sampled pre-stack seismic data.

As emphasized above, the proposed inversion algorithm makes use of a prescribed semivariogram function as a way to enforce a measure of smoothness on the estimated model parameters. Parenthetically, Tarantola (1987) demonstrates that when an exponential covariance operator (*i.e.*, an exponential semivariogram) is used as an integral kernel ($C$) to produce a smooth version of a continuous function in the inversion [*e.g.*, to produce a smooth version, $m_{smooth}$, of the original continuous model, $m$, via the equation $m_{smooth}(y)=\int C(x,y)m(x)dx$] this operation is equivalent to enforcing a model norm written as the weighted sum of the $\ell_2$-norm of the function and the $\ell_2$-norm of its first derivative. In similar fashion, the Kriging operation used in the proposed inversion algorithm to estimate elastic parameters at time samples between hard points implicitly enforces a mixed quadratic model norm in the inversion. The exact representation of such a mixed quadratic norm depends on the specific choice of semivariogram model and semivariogram parameters.

### 3.A.5.8 Validation and Testing of the Inversion Algorithm

Numerical experiments of global inversion were performed using different noisy synthetic data sets that included only PP seismic reflection amplitudes. All the examples assume input data in the form of NMO corrected pre-stack seismic gathers. These numerical experiments are reported in three separate sections. The first section (examples 3.A.5.1 through 3.A.5.4) considers a sensitivity analysis to evaluate the influence of the most important inversion parameters. Results from this analysis are implemented in subsequent exercises and serve as reference for inversion results obtained with the proposed inversion algorithm in the second section (examples 3.A.5.5 through 3.A.5.7). In the final section (example 3.A.5.8), the proposed inversion algorithm is used to assess the sensitivity of pre-stack seismic data to resolve a 1D distribution of elastic parameters constructed from well-log data acquired in the deepwater Gulf of Mexico.

### *3.A.5.8.1 Analysis of Inversion Parameters*

#### 3.A.5.8.1.1 Description of the Synthetic Data Set

Figure 3.A.5.3 shows a 1D synthetic subsurface model consisting of two sand bodies embedded in a background shale layer. The upper sand body is water-filled whereas the lower one is saturated with oil. Panels (a) through (d) in this figure show the corresponding well logs of bulk density, compressional-wave velocity, shear-wave velocity, and lithology. Panel (e) shows the input pre-stack seismic data simulated for a single source-receiver gather corrected for normal moveout. The simulated pre-stack seismic data were also contaminated with 5%, zero-mean Gaussian random noise. A zero-phase Ricker wavelet centered at 35 Hz was assumed in the simulation of the pre-stack seismic data. Simulation of seismic data was performed assuming 10 source-receiver offsets with uniform receiver spacing equal to 300m and a constant time sampling rate of 2ms in the interval from 0 to 1.4 seconds. The number and spacing of receivers were selected to insure sufficient variability in the seismic amplitudes across the pre-stack seismic gather. In this particular case, the maximum offset-to-depth ratio is approximately equal to 2. An appropriate maximum offset-to-depth ratio is critical here to secure measurable sensitivity of the seismic data to elastic parameters, especially in the estimation of shear-wave velocity and bulk density (Castagna and Backus, 1993). The discretization of elastic parameters was performed directly from the well logs shown in Figure 2. This discretization consisted of 50

layers of an average travel time "thickness" of 28ms for each layer and spanning the same time interval as the pre-stack seismic data (*i.e.*, from 0 to 1.4 seconds).

### 3.A.5.8.1.2 Example No. 3.A.5.1: Efficiency of the Annealing Technique

In this example, inversion was performed using various annealing techniques (Metropolis, Heat bath, and VFSA) to yield estimates of compressional- and shear-wave velocity and bulk density. The inversions were implemented under the same operating assumptions and the corresponding computer time was clocked to assess relative computer efficiency. Figure 3.A.5.4 describes the CPU time associated with each technique in relation to the CPU time entailed by VFSA. Exercises considered in this Section consistently indicated that VFSA remained the most efficient SA algorithm for global inversion. Similar results have been reported in the open technical literature (*e.g.*, Ingber, 1993; Sen and Stoffa, 1995; Chunduru *et al.*, 1997). Rothman (1986) suggested that for problems involving a very large number of parameters Heat bath SA could be more efficient than Metropolis SA.

### 3.A.5.8.1.3 Example No. 3.A.5.2: Choice of Objective Function

A similar inversion exercise was performed to appraise the sensitivity of the estimated elastic parameters to the choice of data misfit function. Selecting an appropriate data misfit function is critical to the inversion because some functions are not sensitive to absolute differences in seismic amplitudes. Figure 3.A.5.5 shows the original pre-stack seismic data set (Panel a) and the seismic residuals derived from the inversion with the use of the $\ell_1$ (Panel b), $\ell_2$ (Panel c), geometric ($\ell_g$, Panel d), and harmonic ($\ell_h$, Panel e) data misfit functions described by equations (3.A.5.2), (3.A.5.3), (3.A.5.4), and (3.A.5.5), respectively. In this example, all inversions reached the same number of iterations in the minimization. The harmonic misfit function is sensitive to the absolute seismic amplitude differences and hence produces superior results in terms of data residuals, total misfit, and computational performance.

Such a data misfit function is used as the default option in the remaining examples considered in this Section.

### 3.A.5.8.1.4 Example No. 3.A.5.3: Sampling Techniques in Model Space

Various approaches were considered in this Section to draw an initial model and to constrain subsequent model changes in the search for the minimum of the objective function. These approaches are of significance to enforce apriori model information and to optimize computer efficiency. For simplicity, but without sacrifice of generality, the example described in this section makes use of only the first term of equation (3.A.5.12).

Figure 3.A.5.6 shows inversion results obtained when assuming various types of apriori information about the 1D distribution of elastic parameters and when using various types of sampling strategies. All inversion exercises achieved the same similarity in data space (*i.e.*, small pre-stack seismic data misfit). Panels (a) and (b) in Figure 3.A.5.6 show the uniform and Gaussian PDFs of compressional-wave velocity, shear-wave velocity, and bulk density used to stochastically draw the initial model entered to the inversion. Apriori information about the model assumes that the latter exhibits no specific trend with respect to seismic time (or depth). Therefore, the same PDF is used for all layers. Panels (c) and (d) show cross-plots and correlation coefficients ($r^2$ is used as a scale-independent measure of similarity of two discrete functions, see 3.A.7.5.D. Appendix D) between the actual and inverted elastic parameters estimated using uniform and Gaussian PDFs, respectively. In an ideal case, all data in the cross-plots should fall along a straight line of unit slope. For the case of scant prior information about the unknown model, no reasonable assumption can be made about the 1D variations of the elastic properties and hence a uniform PDF remains the most appropriate choice (Panel a) to sample model parameters. In the latter case, the two sets of actual and inverted elastic parameters do not correlate very well as indicated by the relatively low correlation coefficients shown in Panel (c)

($r^2_{v_p}$ = -0.54, $r^2_{v_s}$ = 0.42, and $r^2_{\rho_b}$ = 0.20) and the 1D distribution of elastic parameters shown in Panel (e). Usage of apriori model information in the form of a Gaussian PDF (Panel b) yields 1D distributions of elastic parameters closer to the actual ones, as indicated by the corresponding correlation coefficients shown in Panel (d) ($r^2_{v_p}$ = -0.11, $r^2_{v_s}$ = 0.51, and $r^2_{\rho_b}$ = 0.67) and the actual and inverted 1D distributions of elastic parameters shown in Panel (f). In this particular case, the enforced Gaussian PDF was adapted from sample histograms of the well logs shown in Figure 3.A.5.3.

Figure 3.A.5.7 shows inversion results obtained when apriori model information includes (a) knowledge that the model exhibits a specific vertical trend, (b) knowledge of lithology (*i.e.*, sand or shale), and (c) ranges of variation about the vertical trend independently for each of the three elastic parameters. In all cases, the inversions entailed the same similarity in data space enforced in previous examples. Panel (a) in Figure 3.A.5.7 shows the vertical trends and lower, mean, and upper bounds for the 1D distribution of unknown elastic parameters. Gaussian PDFs may also be enforced for each layer to constrain the variability of the unknown elastic parameters. Panel (b) shows the corresponding 1D distribution of actual and inverted elastic parameters. Open circles designate the inverted elastic parameters in this panel. The evolution of the negative value of the data misfit function as a function of iteration number is also shown in panel (c). Panel (d) shows a cross-plot between the actual and inverted elastic parameters. The latter results entail better correlation coefficients ($r^2_{v_p}$ = 0.35, $r^2_{v_s}$ = 0.85, and $r^2_{\rho_b}$ = 0.72) than those obtained for the examples described in Figure 3.A.5.6. Subsequent inversion exercises described in this Section employ the same model sampling strategy assumed to obtain the results shown in Figure 3.A.5.7.

### 3.A.5.8.1.5 Example No. 3.A.5.4: Smoothness Criterion

The inverted elastic parameters can sometimes exhibit low correlation coefficients when compared to actual parameters even though these parameters entail a high degree of similarity in data space. Such a situation can also occur in cases where the unknown models are constrained by apriori information such as vertical trends, lithology, and PDFs for each layer (see Figure 3.A.5.7). This common situation arises because of the non-uniqueness implicit in the nonlinear relationship between the data and the model, especially in the presence of noisy and sparse measurements. Common practice shows that a more general objective function such as that shown in equation (3.A.5.12) can be used to address non-uniqueness of the inversion by biasing the search of the unknown model solution toward a specific subset in model space.

Figure 3.A.5.8 shows results obtained for different types and degrees of smoothness enforced by the inversion algorithm. All inversion results described in this figure entailed the same similarity in data space. The second (model flatness) and third terms (model roughness) of equation (3.A.5.12) were the two types of smoothness criteria used to obtain the results shown in Figure 3.A.5.8. The degree of smoothness was controlled by different values of the user-defined parameters $\beta$ and $\gamma$ described in equation (3.A.5.12). Panels (a) through (d) in Figure 3.A.5.8 show cross-plots of actual and inverted elastic properties when 1, 5, 10, and 20% of model flatness was enforced in the inversion. Correlation coefficients between actual and inverted elastic parameters in general increase as the enforced degree of model flatness increases. For instance, for a model flatness of 1%, the correlation coefficients are $r_{v_p}^2$ = 0.39, $r_{v_s}^2$ = 0.85, and $r_{\rho_b}^2$ = 0.76, and for a model flatness of 10% the correlation coefficients are $r_{v_p}^2$ = 0.51, $r_{v_s}^2$ = 0.90, and $r_{\rho_b}^2$ = 0.76. Panels (e) and (f) in Figure 3.A.5.8 also show cross-plots of actual and inverted elastic parameters when both model flatness and model roughness are included in the inversion.

To obtain the results shown in Figure 3.A.5.8, model flatness was kept constant at 20% and model roughness was assumed equal to 10 and 20% in the inversion algorithm. Correlation coefficients between actual and inverted elastic parameters increase as the model roughness increases for a given value of model flatness. For the case of 20% model flatness and 10% model roughness, the correlation coefficients are $r_{v_p}^2$ = 0.69, $r_{v_s}^2$ = 0.91, and $r_{\rho_b}^2$ = 0.84, whereas for the case of 20% model flatness and 20% model roughness the correlation coefficients are $r_{v_p}^2$ = 0.76, $r_{v_s}^2$ = 0.96, and $r_{\rho_b}^2$ = 0.87. Correlations substantially improve when both model flatness and model roughness are included in the objective function described by equation (3.A.5.12).

Next, the $\ell_1$-norm was used to calculate the fourth additive term of the objective function shown in equation (3.A.5.12). This was the type of smoothness criterion used to obtain the results shown in Figure 3.A.5.9. The degree of smoothness was controlled with different values of the user-defined parameter $\chi$. Panels (a) and (b) in Figure 3.A.5.9 show the actual and inverted 1D distributions of elastic parameters when 5% and 10% of $\ell_1$-norm model smoothness is enforced in the inversion algorithm, respectively. For the case of 5% of model smoothness (Panel c), the correlation coefficients are $r_{v_p}^2$ = 0.44, $r_{v_s}^2$ = 0.86, and $r_{\rho_b}^2$ = 0.73, whereas for the case of 10% of model smoothness (Panel b), the correlation coefficients are $r_{v_p}^2$ = 0.42, $r_{v_s}^2$ = 0.89, and $r_{\rho_b}^2$ = 0.82. Results improve when the $\ell_1$-norm smoothness criterion is enforced compared to results shown in Figure 3.A.5.7. However, as shown in Figure 3.A.5.8, more accurate results were obtained when using $\ell_2$-norm measures of smoothness.

The above exercises of the enforcement of smoothness in the inversion are presented here for reference purposes given that such measures of smoothness are commonly used in seismic inversion. As it is shown below, the proposed inversion algorithm described in this Section provides an altogether different way to enforce smoothness in the unknown 1D distributions of elastic parameters.

### *3.A.5.8.2 Evaluation of the Proposed Inversion Algorithm*

#### 3.A.5.8.2.1 Example No. 3.A.5.5: Single Model Realization

Figure 3.A.5.10 shows results in data and model space obtained with the proposed inversion algorithm. Panel (a) in this figure shows the measured and inverted pre-stack seismic data as well as the seismic data residuals. Panels (b) shows the actual and inverted 1D distributions of elastic parameters and panel (c) shows that higher correlation coefficients ($r_{v_p}^2$ = 0.86, $r_{v_s}^2$ = 0.98, and $r_{\rho_b}^2$ = 0.95) are obtained between actual and inverted values of elastic parameters when compared to previous inversion exercises. The number of hard points used by the inversion algorithm corresponds to 10% of the total number of time samples. A zero-nugget, spherical semivariogram of range and normalized sill equal to 0.60 s and 1, respectively, was used to krig (interpolate) elastic parameters between hard points. All inversion results described in this figure entailed the same similarity in data space and made use of the harmonic data misfit function (equation 3.A.5.5). Smoothness was implicitly enforced through the time-sampling strategy used by the proposed inversion algorithm.

#### 3.A.5.8.2.2 Example No. 3.A.5.6: Effect of Semivariogram Range and Number of Hard Points

Table 3.A.5.1 and 3.A.5.2 summarize the results obtained when different vertical correlation ranges and number of hard points were used in the inversion algorithm, respectively. All inversion results described in these tables entailed the same similarity in data space and made use of the harmonic data misfit function. The correlation coefficients shown in Table 3.A.5.1 between the actual and inverted bulk density and shear-wave velocity are approximately the same for all vertical correlation ranges under study. For the case of compressional-wave

velocity, however, the correlation coefficient reaches a peak at a semivariogram range of approximately 0.70s. As emphasized earlier, the Kriging of elastic parameters is by default performed using a spherical semivariogram model with a correlation range equal to 0.60s. Such a range was calculated experimentally from the compressional-wave velocity log. In the most general case, each elastic parameter and lithology could be associated with a specific semivariogram model. Table 3.A.5.1 also shows the normalized computer CPU time required to estimate each inversion result. This CPU time slightly increases as the correlation range increases. Table 3.A.5.2 summarizes similar experimental results obtained when using different numbers of hard points. Neither the correlation coefficients between the actual and inverted elastic parameters nor the computer CPU times exhibit significant differences for the numbers of hard points considered in the experiments.

#### 3.A.5.8.2.3 Example No. 3.A.5.7: Assessment of Uncertainty

Figure 3.A.5.11 describes results from the evaluation of uncertainty of the inverted 1D distributions of elastic parameters. To construct the results shown in this figure, twenty two independent estimations were performed with the proposed inversion algorithm. Each of the inversions was initialized with an independent starting model but the same number of fixed points. The inversion results described in this figure entailed the same similarity in data space. Subsequently, histograms for each set of parameters were sampled at a particular time and used as indicators of variability. These histograms are shown in color-coded format in Figure 3.A.5.11. Clearly, compressional-wave velocity exhibits the largest variability among the three elastic parameters. This behavior is mainly due to the large value-range constraints enforced by the inversion algorithm for this elastic parameter, to the small contrast in velocity between the oil-saturated sand and background shale, and to the effect of a non-optimal seismic signal-to-noise ratio. In general, the inverted distributions of elastic parameters remain consistent with the

actual distributions (identified with the red lines in Figure 3.A.5.11). The overall computer efficiency of the proposed algorithm surpasses the efficiency of alternative inversions techniques described in this study, especially when more smoothness terms are used in the general objective function.

### *3.A.5.8.3 Feasibility Analysis for the Inversion of Field Data*

#### 3.A.5.8.3.1 Description of the Gulf-of-Mexico Data Set

The 1D model under consideration was constructed from well-log data acquired in the deepwater Gulf of Mexico. Figure 3.A.5.12 shows the corresponding well logs along the depth interval from 8000 ft (2438.4 m) to 13200 ft (4023.4 m). A close-up view of the same logs is also shown in the interval of interest from 11600 ft (3535.7 m) to 13200 ft (4023.4 m). The well-log data were converted from depth to normal seismic travel time using the compressional-wave velocity log. Subsequently, the logs were sampled at a constant rate of 2ms to construct the discretized version of elastic parameters. A zero-phase Ricker wavelet centered at 35 Hz was used for the simulation of the 1D pre-stack seismic data in the interval from 2.4 to 3.7 seconds. The assumed source-receiver pre-stack gather consists of 10 traces, corresponding to the same number of receivers spaced at 800m intervals. The maximum offset-to-depth ratio for the simulations is approximately equal to 2. Figure 3.A.5.13 shows the simulated pre-stack seismic traces contaminated with 5%, zero-mean Gaussian random noise. Noisy pre-stack and NMO corrected seismic data input to the proposed inversion algorithm comprised only the zone of interest, from 3.3 to 3.7 seconds. This same time interval comprised the discretized elastic parameters, hence amounting to a total of 200 equal travel-time layers considered for inversion. The experimental spherical semivariogram used in the inversion algorithm was inferred from the well-log data and exhibited a correlation range of 0.04 s and zero-nugget. The sill was assumed to be equal to the variance of the data.

3.A.5.8.3.2 Example No. 3.A.5.8: Assessment of Uncertainty

Figure 3.A.5.14 graphically describes the results obtained from the evaluation of uncertainty for the Gulf-of-Mexico 1D subsurface model using the proposed inversion algorithm. Twenty-two independent inversions were performed to estimate the 1D distribution of elastic parameters. All inversion results described in this figure entailed the same similarity in data space. Inversion results are displayed in the form of color-coded normalized histograms as a function of seismic travel time. Each histogram was constructed at a particular time from samples of elastic parameters yielded by the twenty-two independent estimations. As indicated by Figure 3.A.5.14, shear-wave velocity and bulk density exhibit the most variability with respect to the actual well-log parameters (identified with solid red lines in each panel). In general, the inverted 1D distributions of elastic parameters are in qualitative agreement with the well-log distributions of the same parameters. The variability (uncertainty) of the inverted results considerably increases across thin layers.

### 3.A.5.9 Summary and Conclusions

Various simulated annealing algorithms, objective functions, sampling strategies, and smoothing criteria were explored to perform 1D global inversion of pre-stack seismic data. Both the selection of a specific random-walk search and the construction of the objective function significantly constrained the efficiency of the inversion and the accuracy of the results. Sampling strategies allow one to include apriori information in the inversion, including an additive smoothness term that helps to constrain the range of possible solutions in model space. This Section introduced a new global inversion algorithm based on simulated annealing that enforced sampling and smoothness strategies widely used in the field of geostatistics. The overall computer efficiency of the proposed algorithm for similar inverted results is superior to alternative inversion techniques evaluated in this study, especially when alternative approaches makes use of smoothing terms in the objective functions. Moreover, the new inversion algorithm is capable of rendering estimates of uncertainty in an efficient manner. The flexibility of the proposed algorithm makes it possible to estimate petrophysical properties such as porosity and water saturation that are either deterministically or stochastically related to the elastic parameters.

The next Section shows the development of a new stochastic inversion algorithm to estimate petrophysical properties in one step and elastic properties as by-products from pre-stack seismic data and well logs.

**Table 3.A.5.1: Summary of the relationship between spatial correlation length (range), correlation coefficient ($r^2$), and CPU time when performing the proposed inversion algorithm on the synthetic pre-stack data set described in Figure 3.A.5.3.**

| Range, seconds | $r_{v_p}^2$ | $r_{v_s}^2$ | $r_{\rho_b}^2$ | Relative CPU time |
|---|---|---|---|---|
| 0.10 | 0.057 | 0.974 | 0.976 | 0.878 |
| 0.20 | 0.078 | 0.974 | 0.956 | 0.899 |
| 0.50 | 0.763 | 0.964 | 0.951 | 0.878 |
| 0.70 | 0.814 | 0.9464 | 0.944 | 0.906 |
| 0.90 | 0.594 | 0.971 | 0.962 | 0.846 |
| 1.10 | 0.556 | 0.957 | 0.949 | 1.000 |

**Table 3.A.5.2: Summary of the relationship between number of hard points, correlation coefficient ($r^2$), and CPU time when performing the proposed inversion algorithm on the synthetic pre-stack data set described in Figure 3.A.5.3.**

| Number of Hard Points | $r_{v_p}^2$ | $r_{v_s}^2$ | $r_{\rho_b}^2$ | Relative CPU time |
|---|---|---|---|---|
| 2 | 0.846 | 0.995 | 0.973 | 1.000 |
| 5 | 0.890 | 0.981 | 0.976 | 0.912 |
| 9 | 0.846 | 0.958 | 0.953 | 0.906 |
| 11 | 0.795 | 0.996 | 0.982 | 0.820 |
| 15 | 0.894 | 0.995 | 0.940 | 0.832 |
| 17 | 0.824 | 0.914 | 0.945 | 0.952 |

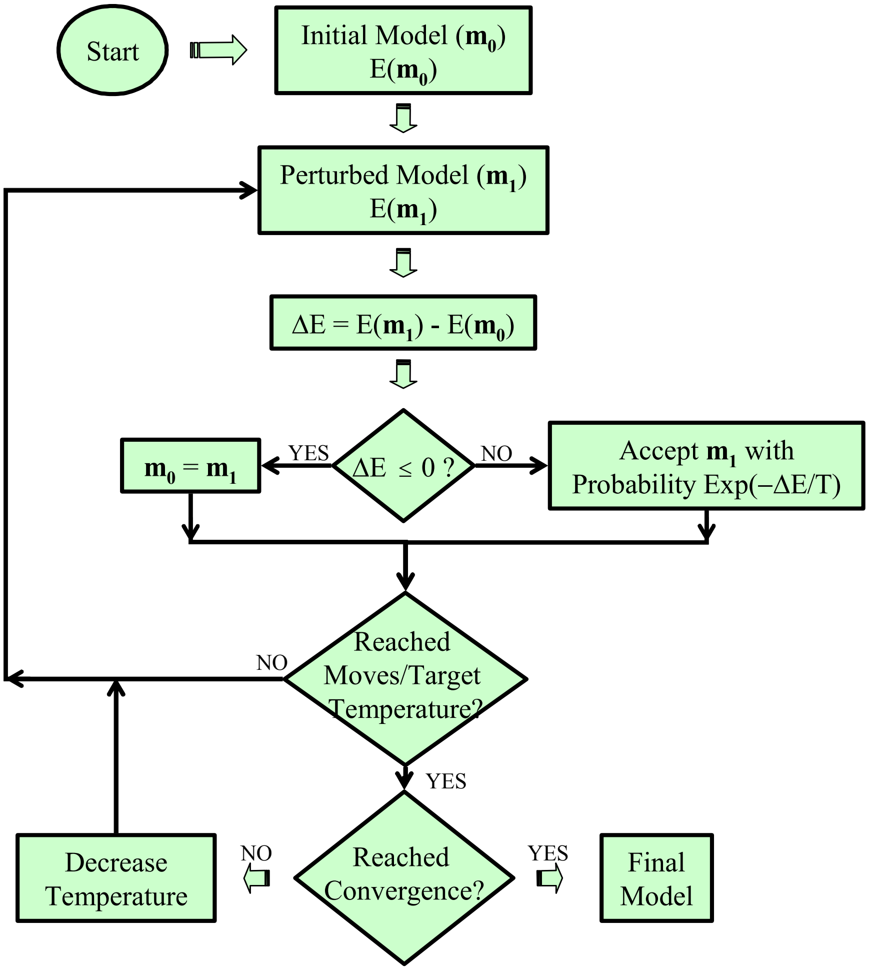

**Figure 3.A.5.1**: Generalized flow diagram for simulated annealing (after Ingber, 1989).

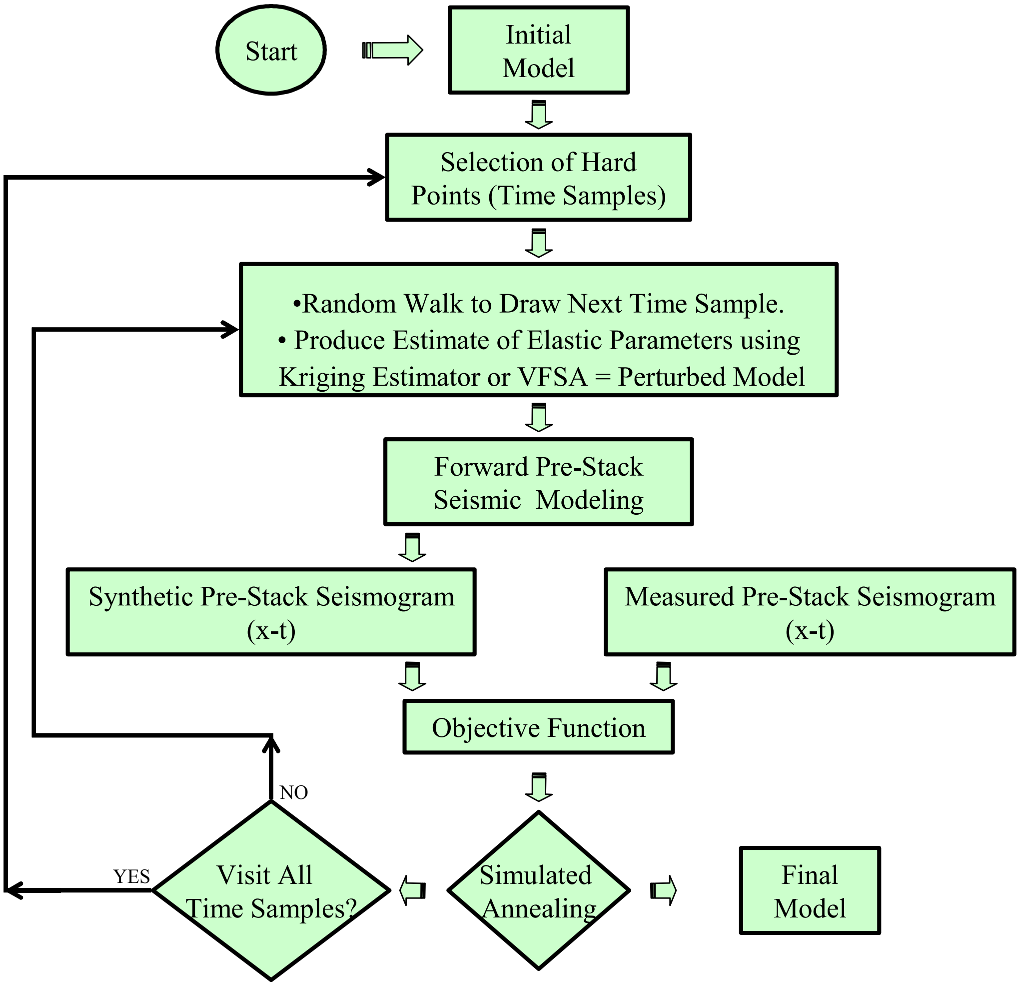

**Figure 3.A.5.2**: Generalized flow diagram of the proposed pre-stack inversion algorithm developed in this Section.

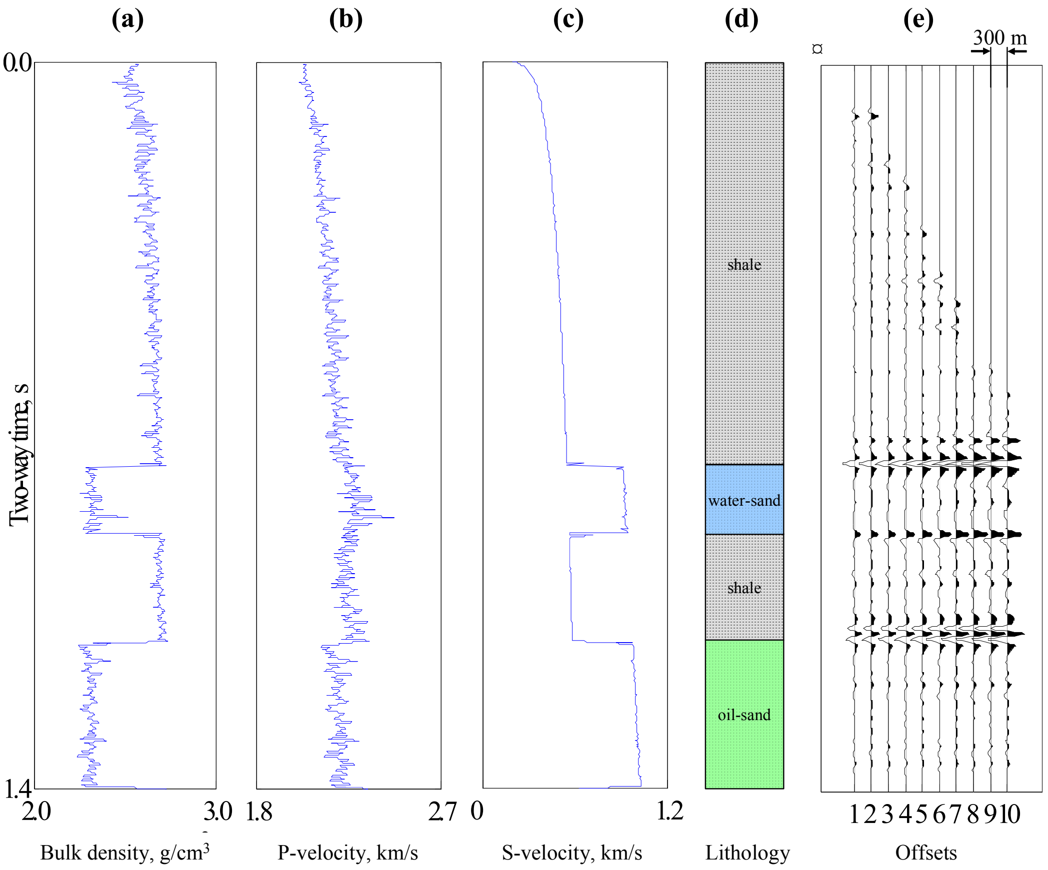

**Figure 3.A.5.3**: Graphical description of the one-dimensional synthetic subsurface model used for the analysis of pre-stack seismic inversion. Panels (a) through (d) show the bulk density, compressional-wave velocity, shear-wave velocity, and lithology-type well logs, respectively, and panel (e) shows the noisy (5%, zero-mean Gaussian random noise) pre-stack seismic data associated with this model (maximum offset-to-depth ratio approximately equal to two). Offset receivers are assumed uniformly spaced at 300m intervals. Simulation of the pre-stack seismic data was performed with a 35 Hz Ricker wavelet. The simulated pre-stack seismic data were further corrected for normal moveout.

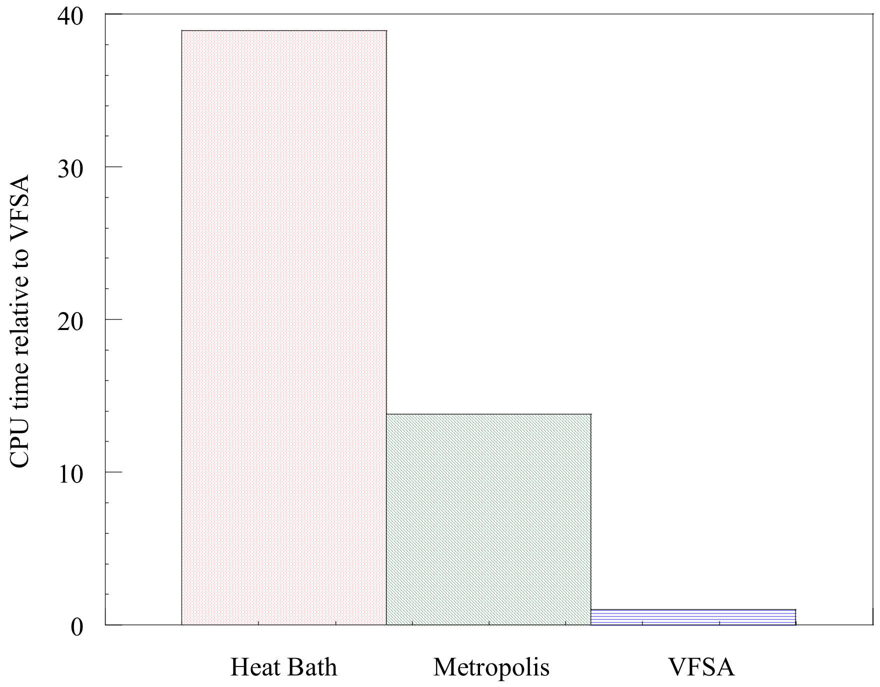

**Figure 3.A.5.4**: Measured CPU times relative to very fast simulated annealing (VFSA) for three types of random-search methods used to approach the same pre-stack seismic inversion problem.

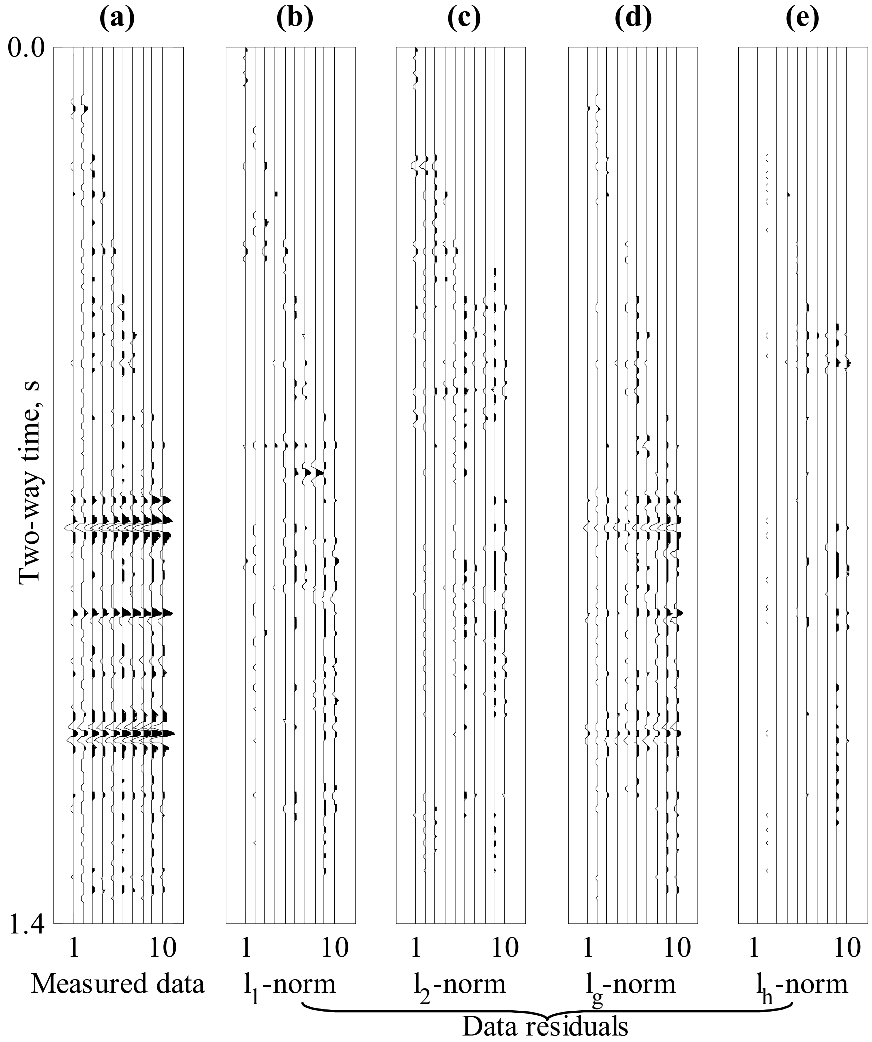

**Figure 3.A.5.5**: Comparison in data space of the performance of the inversion algorithm for different types of data misfit functions after the same number of iterations of the VFSA algorithm. (a) Measured pre-stack seismic data, and data residuals yielded by the inversion using several data misfit functions, namely: (b) $\ell_1$-norm, (c) $\ell_2$-norm, (d) geometric norm, $\ell_g$, and (e) harmonic norm, $\ell_h$. The various misfit functions are described by equations (3.A.5.2) through (3.A.5.5), respectively.

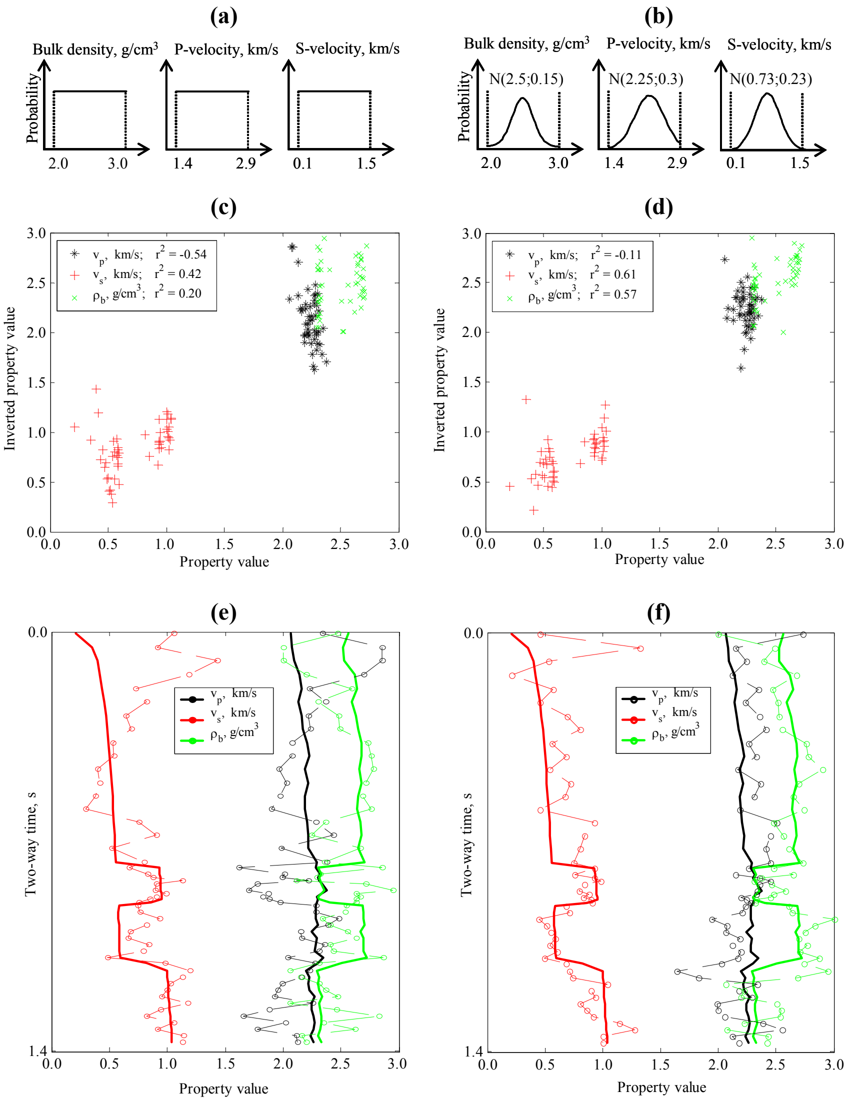

**Figure 3.A.5.6**: Effect of the model sampling technique on the inverted one-dimensional distribution of elastic parameters for the case of no vertical trend imposed apriori on the elastic parameters. Panels (a) and (b) show the uniform and Gaussian probability density functions enforced by the inversion to estimate the elastic parameters shown in panels (c and e) and (d and f), respectively. In panels (c) and (d), $r^2$ is the correlation coefficient and in panels (e) and (f), the inverted distributions of elastic parameters are identified with open circles.

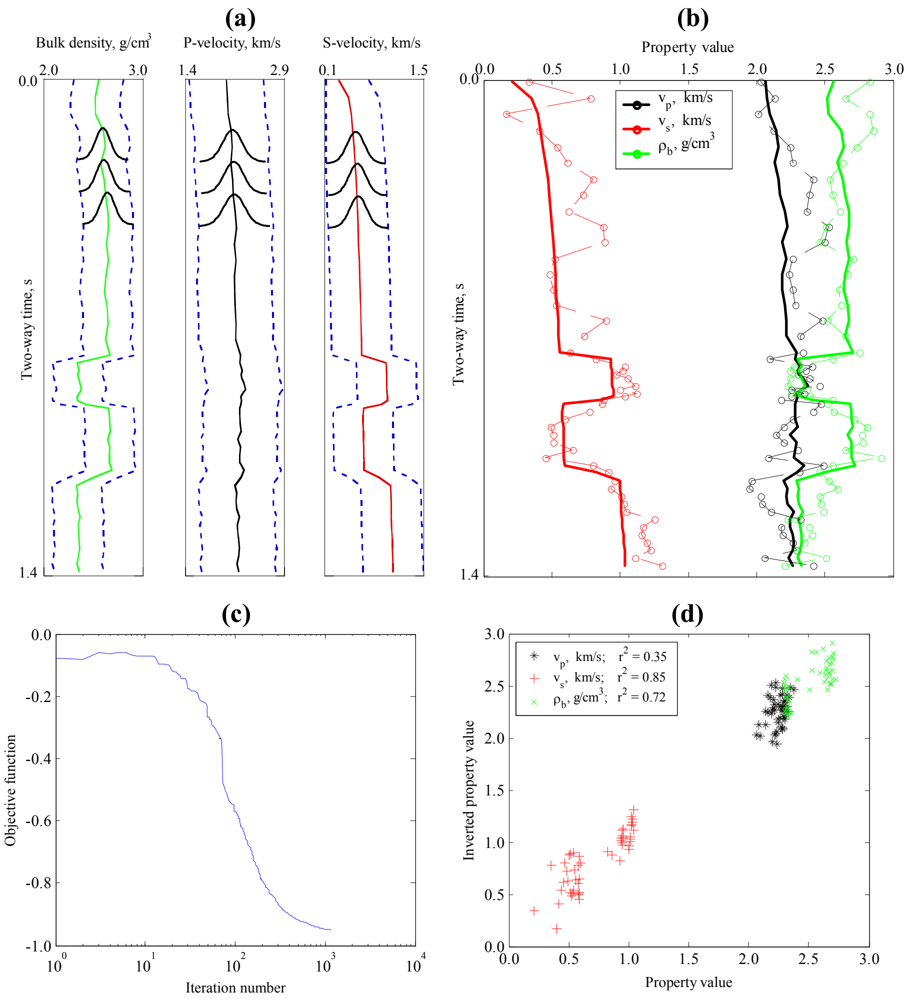

**Figure 3.A.5.7**: Effect of the model sampling technique on the inverted one-dimensional distribution of elastic parameters for the case of a vertical trend imposed apriori on the elastic parameters. Panel (a) shows the vertical trend, minimum, mean, and maximum apriori values of the elastic parameters and the corresponding Gaussian probability density functions enforced by the inversion to estimate the elastic parameters shown in panels (b). The evolution of the negative value of the data misfit function as a function of iteration number is shown in panel (c), whereas panel (d) shows the correlation coefficients ($r^2$) between the actual and inverted elastic parameters. In panel (b), the inverted distributions of elastic parameters are identified with open circles.

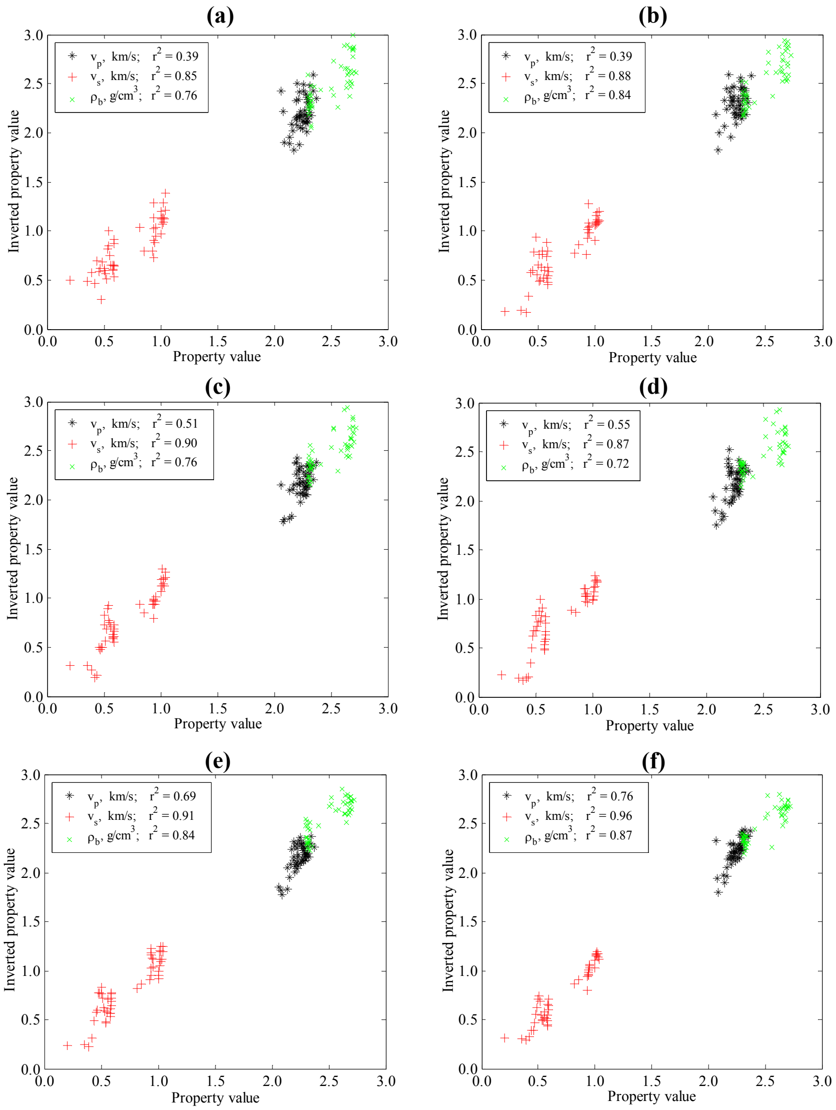

**Figure 3.A.5.8**: Cross-plots of actual and inverted elastic parameters obtained using various types of smoothness criteria and the same measure of similarity in data space. Panels (a) through (d) show results obtained when enforcing a model flatness criterion of 1, 5, 10, and 20%, respectively. Panels (e) and (f) show results obtained when enforcing simultaneously model flatness and model roughness criteria of 20% and 10%, and 20% and 20%, respectively. In all of the panels, $r^2$ is the correlation coefficient.

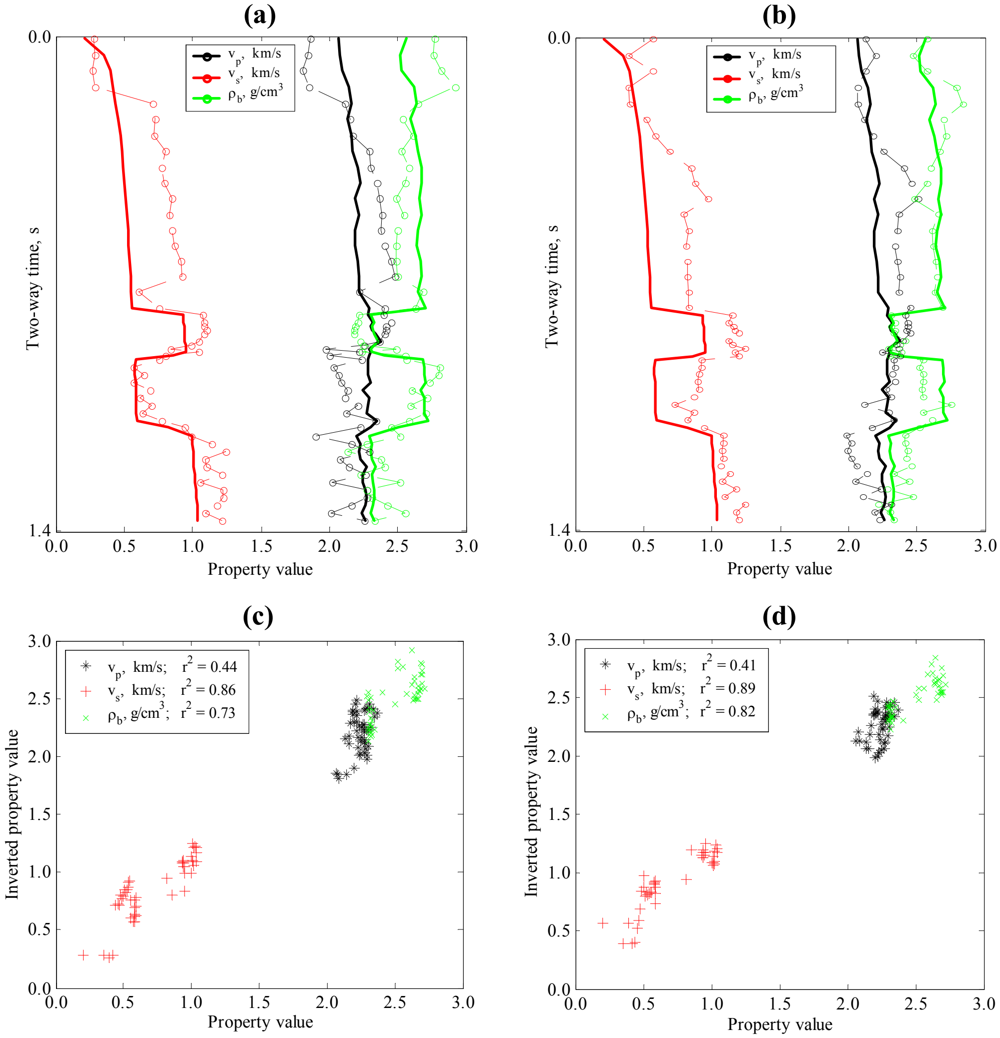

**Figure 3.A.5.9**: Profiles and cross-plots of actual and inverted elastic parameters obtained using an $\ell_1$ -norm metric to enforce model flatness, *i.e.*, by making use of the fourth additive term of the objective function (equation 3.A.5.12). Panels (a and c) and (b and d) show results obtained when enforcing a model flatness criterion of 5 and 10%, respectively. In panels (a) and (b), the inverted distributions of elastic parameters are identified with open circles, and in panels (c) and (d), $r^2$ is the correlation coefficient.

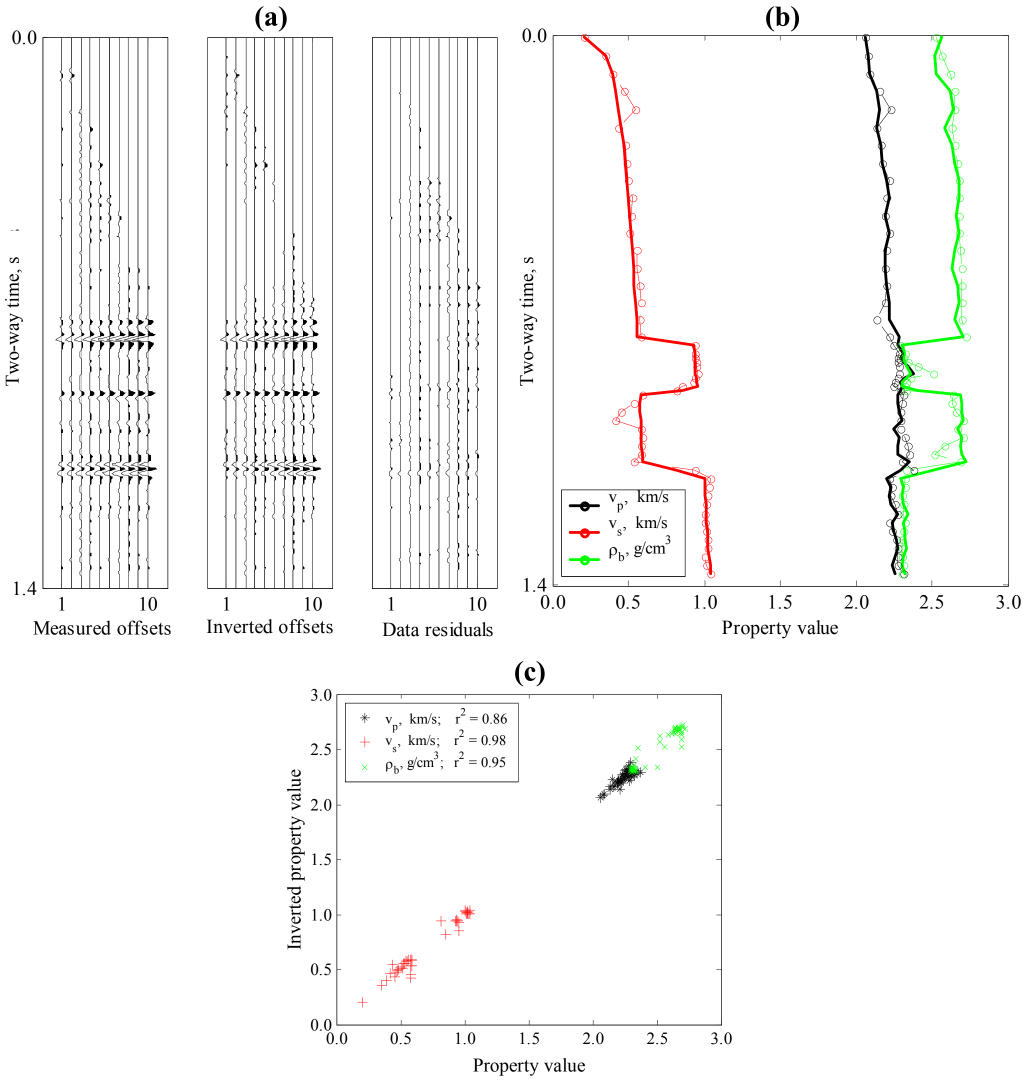

**Figure 3.A.5.10**: Summary of the results obtained with the proposed inversion algorithm: Panels (a) and (b) show inversion results in data space and model space, respectively, and panel (c) shows a cross-plot between actual and inverted elastic parameters together with their associated correlation coefficients ($r^2$). In panel (b), the inverted distributions of elastic parameters are identified with open circles.

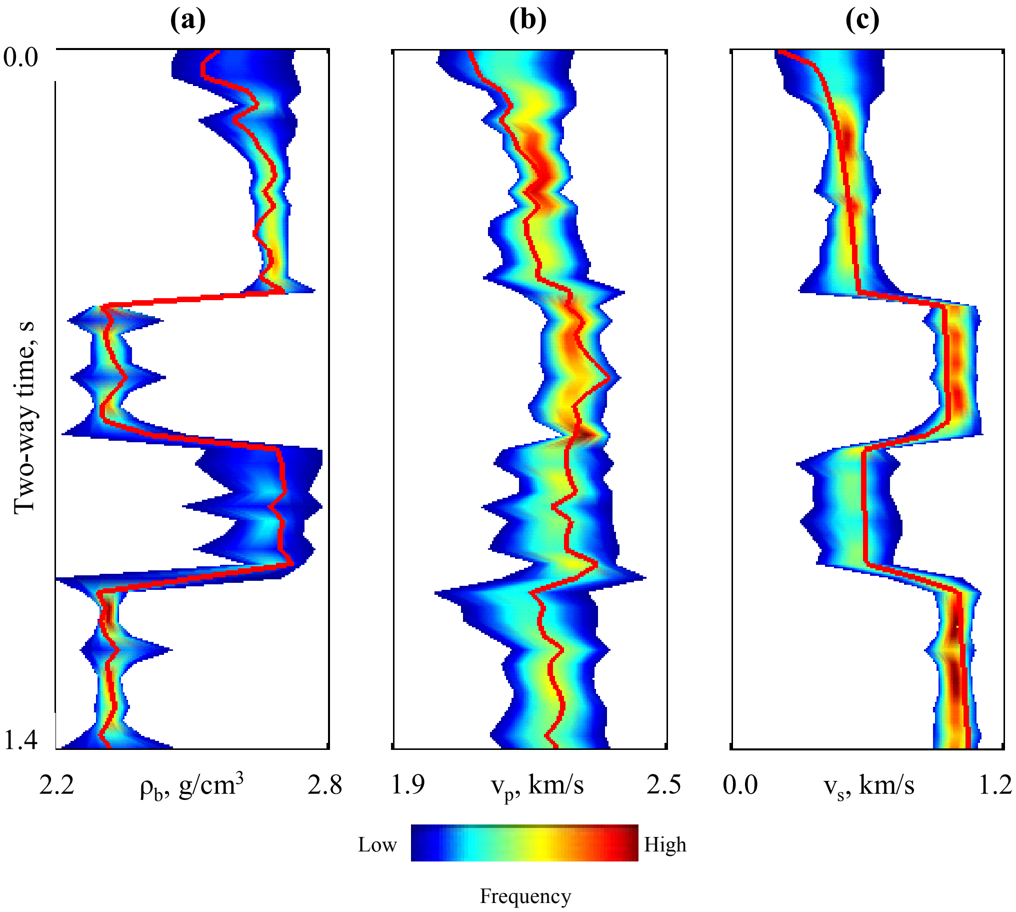

**Figure 3.A.5.11**: Evaluation of the uncertainty of the one-dimensional distributions of elastic parameters yielded by the proposed inversion algorithm: Panels (a), (b), and (c) show color-coded normalized histograms for bulk density, compressional-, and shear-wave velocities, respectively, calculated from 22 independent realizations of inverted elastic parameters. All of the realizations entail the same similarity in data space. The red line identifies the actual distribution of elastic parameters.

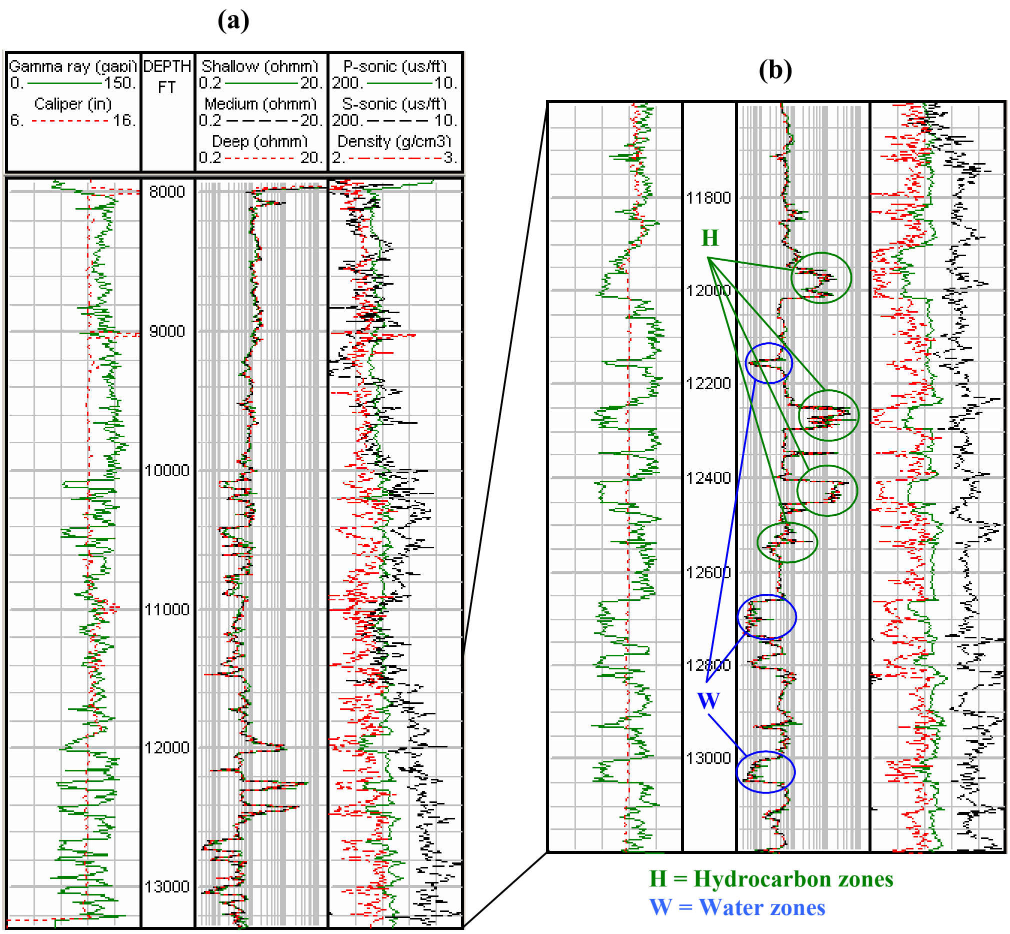

**Figure 3.A.5.12**: Well log description of the one-dimensional subsurface model from the deepwater Gulf of Mexico used for the assessment of the resolution and uncertainty of pre-stack seismic data. Panel (a) shows the complete logged interval, from 8000 ft (2438.4 m) to 13200 ft (4023.4 m), and panel (b) shows the zone of interest, from 11600 ft (3535.7 m) to 13200 ft (4023.4 m). Hydrocarbon and water zones are shown on the logs for reference purposes.

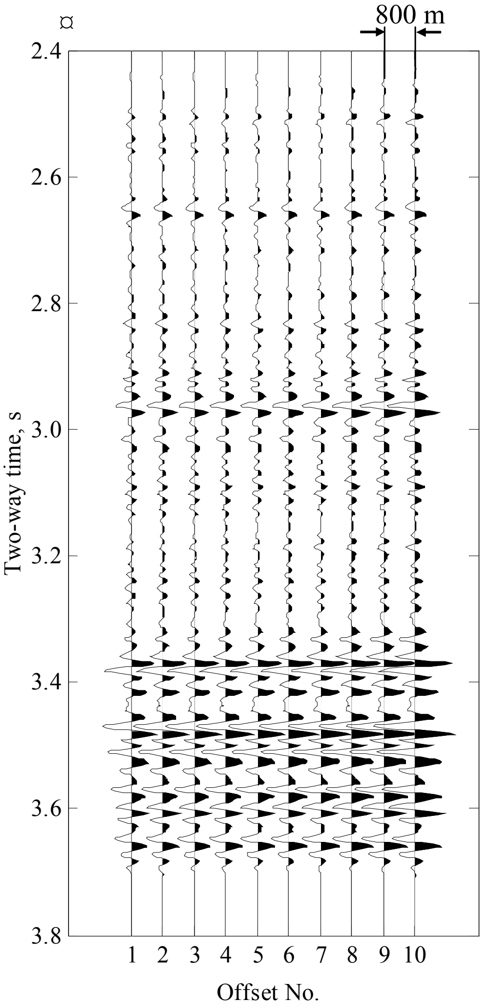

**Figure 3.A.5.13**: Pre-stack seismic traces simulated numerically for the one-dimensional distributions of elastic parameters constructed with the well logs shown in Figure 3.A.5.12. Offset receivers are assumed uniformly spaced at 800m intervals. Simulation of the pre-stack seismic data was performed with a 35 Hz Ricker wavelet. The simulated pre-stack seismic data shown above were further corrected for normal moveout and contaminated with 5%, zero-mean Gaussian noise (maximum offset-to-depth ratio approximately equal to two). Inversion was performed using data within the time interval from 3.3 to 3.7 seconds.

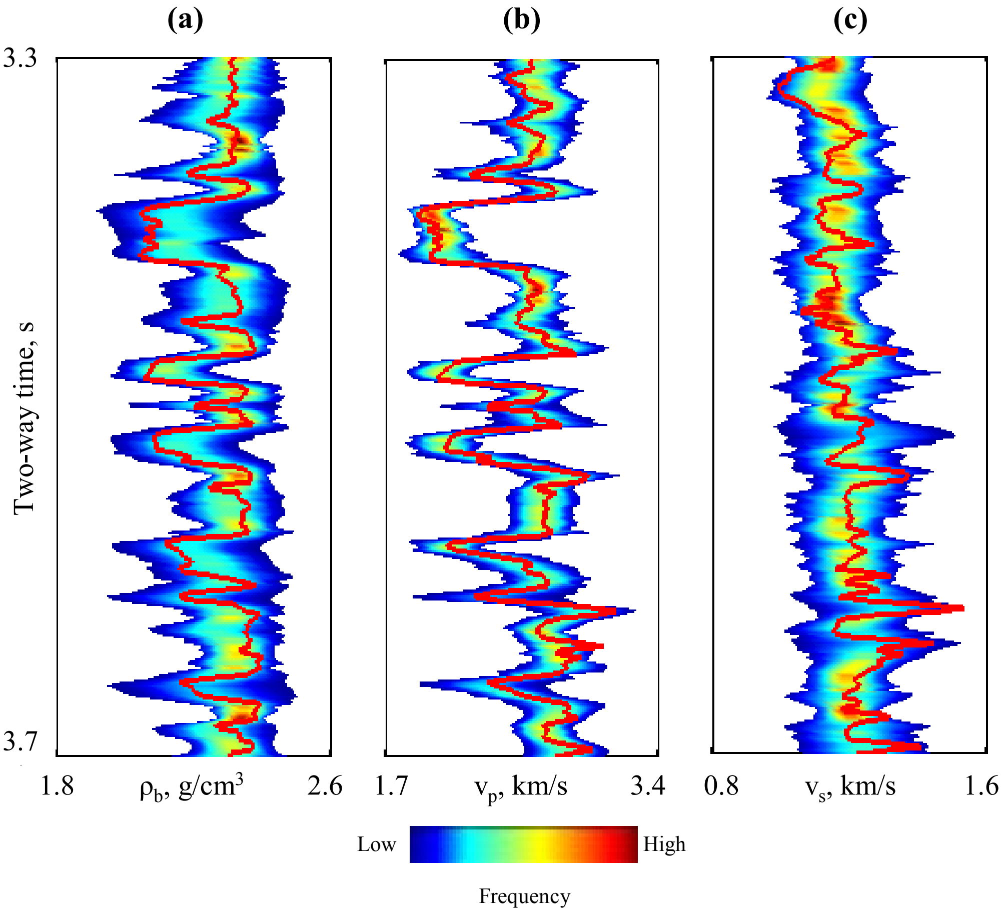

**Figure 3.A.5.14**: Evaluation of resolution and uncertainty of pre-stack seismic data for the subsurface model in the deepwater Gulf of Mexico. Elastic parameters estimated with the proposed inversion algorithm: Panels (a), (b), and (c) show color-coded normalized histograms for bulk density, compressional-, and shear-wave velocities, respectively, calculated from 22 independent realizations of inverted elastic parameters. All of the realizations entailed the same similarity in data space. The red line identifies the actual well-log data.

## 3.A.6: JOINT STOCHASTIC INVERSION OF PRE-STACK SEISMIC DATA AND WELL LOGS

This Section introduces a novel quantitative approach to make use of the full gather of 3D pre-stack seismic data in the construction of reservoir simulation models and to assess their impact on the forecast of hydrocarbon production. The problem is first formulated, then the subsurface model is constructed and a description is provided of the simulation of petrophysical, elastic, and seismic parameters. Subsequently, the novel algorithm is described at length and different numerical experiments are performed and analyzed to validate the proposed joint stochastic inversion algorithm and to assess the value of 3D pre-seismic data in static reservoir evaluation. Finally, a simple example is constructed to illustrate the reduction of uncertainty in the prediction of dynamic behavior as a consequence of using the full gather of 3D pre-stack seismic data in the construction of the static reservoir model.

### 3.A.6.1 Introduction

Integrated reservoir characterization makes use of various types of measurements to construct spatial distributions of petrophysical and fluid parameters. One of the benefits of data integration these measurements is the reduction of uncertainty and hence improved asset recovery, surveillance, and management. This Section describes a novel strategy for the static characterization of hydrocarbon reservoirs based on the extensive use of 3D pre-stack seismic data, well logs, and geological information. Stochastic simulation is used to extrapolate petrophysical variables laterally away from wells subject to honoring the 3D pre-stack seismic measurements. The simulation is performed using a geostatistical procedure that yields high-resolution estimates of inter-well petrophysical and elastic parameters. Numerical studies are carried out in two and three dimensions to evaluate the estimation algorithm as well as to assess different strategies for the inference of petrophysical properties related to elastic parameters.

The estimation algorithm is CPU intensive and is based on global inversion. Examples of application show that the joint inversion algorithm lends itself to accurate estimation of petrophysical properties, such as porosity, that honor the normal-moveout corrected pre-stack seismic data, the well logs, and the prescribed global histograms. Sensitivity analysis and cross-validation exercises are performed to assess the influence of semivariograms parameters and of a particular well in the estimation of inter-well petrophysical properties. Depending on the number of available wells and on the distance between them, the stochastic inversion algorithm can produce estimates of inter-well petrophysical properties with a vertical resolution intermediate between that of seismic data and well logs. In addition, models generated with this inversion scheme yield more accurate predictions of reservoir dynamic behavior when compared to predictions performed with standard geostatistical techniques.

### 3.A.6.2 Background and Formulation

Reservoir management requires geological and petrophysical models amenable to numerical simulation of multiphase fluid flow. These models are used to match production history data, if available, and to evaluate potential production strategies in light of time-dependent economic value of assets. One of the objectives of reservoir characterization is to construct cellular (discrete) spatial distributions of properties, including measurable petrophysical or geological parameters (*e.g.*, lithology, porosity, permeability, permeability anisotropy, shale content, and fluid saturations) from different types of measurements such as seismic data (*e.g.*, travel times, waveform and amplitudes), well logs, and ancillary information (*e.g.*, core samples, and sequence stratigraphy). The central objective of this Section is to describe a novel algorithm to construct spatial distributions of inter-well petrophysical properties that make optimal use of the high vertical resolution of well logs and of the dense lateral sampling of 3D pre-stack seismic measurements.

Statistical modeling techniques, such as Kriging and Gaussian simulation, are widely used for data interpolation and extrapolation (Isaaks and Srivastava, 1989). The same techniques are at the heart of methods used to simulate reservoir properties that honor well-log data and a-priori measures of spatial variability (Chilès and Delfiner, 1999). Seismic measurements are often sensitive to the entire reservoir and hence provide a means to fill the spatial gap between sparse well locations. Amplitude variations of 3D seismic data have been traditionally used to delineate flow-units and, in general, to infer geometrical properties of reservoirs (Brown, 1999; Hilterman, 1999). Some of these approaches make use of seismic attributes to guide, correlate, or constrain the estimation of inter-well geometrical, lithological, and petrophysical properties. Applications and limitations of seismic-guided hydrocarbon reservoir analysis can be found in the technical literature (Maureau and Van Wijhe, 1979; Doyen, 1988; Kalkomey, 1996; Chawathe *et al.*, 1997; Balch *et al.*, 1999). The quantitative use of seismic amplitude variations in space and seismic time (or depth) offers a powerful tool to guide the simulation of inter-well reservoir properties. This approach is referred to in the literature as geostatistical seismic inversion (Bortoli *et al.*, 1993; Haas, 1993; Haas and Dubrule, 1994) and makes use of post-stack seismic data to constrain the geostatistical simulation of inter-well reservoir properties. Improvements and applications of this approach can be found in Debeye *et al.* (1996), Pendrel and van Riel (1997), Torres-Verdín *et al.* (1999), and Grijalba *et al.* (2000).

The inversion algorithm described in this Section is stochastic in nature, makes use of the full gather of 3D normal-moveout corrected pre-stack seismic data, and assumes the existence of quantifiable relationships between petrophysical and elastic parameters. Well-log data are necessary to determine whether the latter relationships can be assumed of a deterministic (*e.g.*, linear) or stochastic nature (*e.g.*, joint probability distribution function). Spatial distributions of reservoir properties between existing wells are obtained with the joint stochastic inversion of 3D pre-stack seismic data and well logs. The inversion is performed using a global optimization technique. In so doing, simulations of inter-well properties are generated and subjected to an acceptance test that guaranties a reduction in the global misfit between the measured pre-stack seismic data and their numerical simulation. To the best of our knowledge, no such algorithm has been reported in the open technical literature. The inversion algorithm is benchmarked using a spatially complex synthetic reservoir model in which all elastic and petrophysical properties are known precisely. Tests of performance are carried out assuming 2D cross-sections and 3D volumes. Measurements input to the algorithm consist of normal-moveout corrected pre-stack seismic traces and well logs. In addition, prescribed semivariograms, histograms, and joint PDFs between elastic and petrophysical parameters are input data that condition the inversion. Inter-well distributions of elastic and petrophysical parameters obtained with the proposed algorithm are compared to those of a reference model as well as to those obtained with standard geostatistical techniques that do not make use of seismic data.

### 3.A.6.3 Construction of the Synthetic Geological Model

Figure 3.A.6.1 is a 3D view of the synthetic subsurface model constructed to perform the numerical experiments described in this Section. This model was constructed to reproduce some of the characteristics of a fluvial depositional environment. Dimensions and geometry were designed to assess seismic resolution in the presence of wavelet tuning. It consists of two sand bodies embedded in a background shale. The upper sand is water filled whereas the lower sand is saturated with oil. Spatial discretization of the model for the calculation of elastic and

petrophysical properties was performed on a regular grid that included approximately 30 millions cells. Pre-stack seismic measurements consist of 200 by 200 common-mid-point (CMP) gathers uniformly separated by a distance of 23 m. Individual traces span the time interval from 0 to 1.5 seconds and are sampled at a rate of 2ms (see Figure 3.A.6.1).

#### *3.A.6.3.1 Description of Petrophysical and Elastic Properties*

Petrophysical properties such as porosity were populated into the reservoir using stochastic algorithms with a prescribed degree of spatial correlation (Chilès and Delfiner, 1999). Initial fluid distributions in the oil saturated sand were calculated by means of correlations (Tiab and Donalson, 1996). Calculation of elastic properties from petrophysical properties was performed using a rock physics model (Duffy and Mindlin, 1957) that included the effect of mechanical compaction. This 3D subsurface model is hereafter termed the reference model, that is, the actual spatial distribution of petrophysical and elastic properties. Table 3.A.6.1 summarizes the geometrical dimensions, average elastic properties, and semivariogram parameters associated with the construction of the hypothetical subsurface model.

#### *3.A.6.3.2 Numerical Simulation of Pre-Stack Seismic Data*

Numerical simulation of pre-stack seismic data was performed using the reflectivity method (Fuchs and Muller, 1971; Kennett, 1983). This method generally computes the full-wave response of a stack of horizontal layers including all converted waves and propagation modes. More specifically, a simplified version of the reflectivity method was used to efficiently compute synthetic seismograms for P waves (primaries only) in offset-time domain devoid of transmission losses. A zero-phase Ricker wavelet (central frequency of 35 Hz) was used for both simulation and inversion of pre-stack seismic data. The time sampling interval was 2ms and offset gathers were corrected for normal moveout. Moreover, 10%, zero-mean, random

Gaussian noise was added to the pre-stack seismic data in an effort to replicate practical levels of acquisition and processing errors. A total of ten pre-stack seismic offsets per CMP gather were considered in this study and the spacing between receivers was assumed uniform and equal to 300 m. The number and spacing of receivers were selected to insure sufficient variability in the seismic amplitudes across the pre-stack seismic gather. In this particular case, the maximum offset-to-depth ratio is approximately equal to 2. Table 3.A.6.2 summarizes the geometrical dimensions and seismic parameters associated with the hypothetical subsurface model. Sub-volumes, cross-sections, and well logs (see Table 3.A.6.1) are extracted from this reference model to perform the numerical experiments described below.

### 3.A.6.4 Geostatistical Modeling

Geostatistical estimation techniques are commonly used in the construction of 3D spatial distributions of reservoir properties. Kriging is a weighted linear interpolation method where the weights are governed by the distance(s) between the interpolation point and the hard point(s) and by the assumed semivariogram. This type of linear interpolation can also include the effect of trends imposed by secondary variables (*i.e.*, cokriging) as well as additional constraints to bias the weights (Chilès and Delfiner, 1999). Kriging is often used to generate models that honor well log data and yield a smooth spatial distribution of properties, thereby dismissing local detail in place of a good average. Figure 3.A.6.2 is a graphical representation of the process of Kriging adapted from Grijalba *et al.* (2000) and Jensen *et al.* (2000). If each hard point in the interpolation process is associated with a local PDF, then the outcome of Kriging is unique and it provides an interpolated local PDF. In turn, the local (collocated) PDF can be transformed into a cumulative distribution function (CDF) from which a random Monte Carlo simulation can be performed of the corresponding variable. Such an estimation technique is referred to as geostatistical simulation and is used in this Section to generate initial distributions of reservoir properties for the proposed inversion algorithm. The same technique is used for comparison purposes. Geostatistical estimation techniques assume that the interpolated variable is the realization of a second-order stationary process (Chilès and Delfiner, 1999). Generation of multiple realizations allows one to assess uncertainty of the interpolated spatial distribution of properties and hence to assess their effect on predictions of dynamic reservoir behavior as a result of multiphase fluid flow.

### 3.A.6.5 Pre-Stack Seismic Inversion

Estimation of elastic parameters such as compressional-wave acoustic impedance (PAI) and shear-wave acoustic impedance (SAI), or compressional-wave velocity ($v_p$), shear-wave velocity ($v_s$), and bulk density ($\rho_b$) of rock formations can be performed via inversion of pre-stack seismic data. These elastic parameters are often related with petrophysical properties through an empirical statistical correlation. A significant amount of work by academia and industry is currently underway to estimate quantitative indicators of fluid and lithology from 3D pre-stack seismic data (Lortzer and Berkhout, 1992; Mukerji *et al.*, 2001; Roy *et al.*, 2002). The inversion algorithm described in this Section yields direct estimates of petrophysical properties and of elastic parameters as by-products. Moreover, these estimates honor multiple-offsets of pre-stack seismic data, well logs, and prescribed global histograms.

### 3.A.6.6 Novel Joint Stochastic Inversion Algorithm

#### *3.A.6.6.1 Description of the Algorithm*

Figure 3.A.6.3 shows a generalized flow diagram of the proposed joint stochastic inversion algorithm. The estimation of inter-well petrophysical parameters (and elastic parameters as by-products) from pre-stack seismic data, well logs, and geological information

(*e.g.*, lithology indicator, horizons), is cast into a global inversion problem. Various factors that control the inversion, including type of optimization technique, selection of objective function, selection of an initial model, sampling strategy, and spatial smoothness, among others, contribute to the spatial resolution and uncertainty of the results as well as to the efficiency of the computer algorithm. Section 3.A.5 carried out a detailed assessment of 1D stochastic inversion of pre-stack seismic data to quantify the influence of all of the above-mentioned inversion factors in the estimation of elastic parameters. Based on those results, the pre-stack stochastic inversion algorithm described in this Section makes use of very fast simulated annealing (VFSA) as a global inversion technique (Ingber 1989; 1993). This implementation of VFSA also makes use of the acceptance/rejection criterion introduced by Metropolis *et al.* (1953). Numerical simulation of pre-stack seismic data is performed using the reflectivity method. In addition, the inversion algorithm enforces a harmonic objective function, initial models constrained by well-log data, a sampling strategy from local PDFs, and honors a prescribed global property histogram.

Initial models of inter-well property distributions obtained with geostatistical simulation are updated with sequential iterations of VFSA. The geostatistical simulation grid is constructed to laterally coincide with the seismic grid but can be adjusted to consider only a subset of the CMP gathers. For convenience but without sacrifice of generality, the vertical axis of the geostatistical simulation grid is measured in seismic vertical travel time. This choice also makes it possible to have seismic horizons provide a geological framework for the simulations. The vertical sampling interval can be adjusted to reflect the desired degree of vertical resolution of the geostatistical simulations (intermediate between the resolution of seismic data and well logs). A default choice for vertical sampling interval is that of seismic data. Well logs input to the geostatistical simulation procedure are previously low-pass filtered (to prevent aliasing effects) and resampled to the desired vertical sampling interval.

In each of the VFSA iterations, all locations of the simulation grid are visited once by a random walk that includes lateral location and time. This random walk designates the point to be considered for analysis (see Figure 3.A.6.3). The convergence criterion enforced by the inversion is adjusted by the user in the form of a target value for the objective function or else by a maximum count for the number of VFSA iterations. Due to the stochastic nature of the algorithm, various initial models are generated with geostatistical simulation to compute multiple inter-well property distributions that honor the well-log data, the specified global property histograms, and the pre-stack seismic data within the prescribed tolerance criterion. The statistical properties of the set of inverted distributions of inter-well properties provide a measure of uncertainty.

### *3.A.6.6.2 Data Misfit Function*

The developments considered in this Section make use of a pre-stack data misfit (or similarity) function in the frequency domain. This seismic data misfit function is adapted from the work of Sen and Stoffa (1995), and is given by

$$\left\| e_f \right\|_h = \frac{1}{N_{CMP}} \sum_{i=1}^{N_{CMP}} \left\{ \frac{1}{N_{off}} \sum_{j=1}^{Noff} \left[ \alpha_j \left( A_{ij} / \left( B_{ij} + C_{ij} \right) \right) \right] \right\}, \quad (3.A.6.1)$$

where

$$A_{ij} = 2 \sum_{k=1}^{Nf} S(x_{ij}, f_k)^{obs} S^{*}(x_{ij}, f_k)^{est}, \quad (3.A.6.2)$$

$$B_{ij} = \left( \sum_{k=1}^{Nf} S(x_{ij}, f_k)^{obs} S^{*}(x_{ij}, f_k)^{obs} \right)^{1/2}, \quad (3.A.6.3)$$

and

$$C_{ij} = \left( \sum_{k=1}^{Nf} S(x_{ij}, f_k)^{est} S^*(x_{ij}, f_k)^{est} \right)^{1/2} . \qquad (3.A.6.4)$$

In the above equations, $x_{ij}$ is source-receiver distance, $f_k$ is frequency, $N_{CMP}$ is number of CMP gathers, $N_{off}$ is number of source-receiver offsets per CMP gather, $\alpha$ is an offset weight factor, $N_f$ is the number of frequencies in each trace for a given offset, $S^{obs}$ and $S^{est}$ identify the measured and numerically simulated pre-stack seismic data, respectively, and the superscript (*) is used to designate the complex conjugate operator.

### *3.A.6.6.3 Estimation of Local PDFs and Sampling Strategy*

When the purpose of the inversion is to estimate elastic parameters only (*e.g.*, PAI, SAI, and bulk density), the initial models of these parameters are drawn from local PDFs, one PDF per elastic parameter, that are calculated at each point using an ordinary Kriging estimator on the well log data (see Figure 3.A.6.2). Similarly, if the objective of the inversion is to estimate a petrophysical property (and elastic parameters as by-products), the initial model of such a property is drawn from local PDFs that are kriged from petrophysical parameters derived from well-log data. Perturbations of properties are performed directly in the petrophysical domain through a random walk in space and time. Because the pre-stack stochastic inversion algorithm operates on elastic parameters, in the most general case a joint PDF is used to enforce a statistical link between the petrophysical and elastic properties. Figure 3.A.6.4 illustrates an example of a joint PDF between petrophysical and elastic properties when the correlation coefficient between them is equal to -0.6. Figure 3.A.6.4 also shows a top view and a cross-section of the same joint PDF.

### *3.A.6.6.4 Honoring Global Histograms and Well-Log Data*

In order to honor user-defined global property histograms, a transformation that preserves the rank of the data is used when performing the inversion. In this transformation, the value associated with the $q$-quantile of the CDF to be transformed is made equal to the corresponding value of the $q$-quantile of the user-specified CDF. Additionally, the inversion algorithm regards well-log data as hard points in model space. The two sets of constraints are enforced on intermediate inversion results yielded by each of the VFSA iterations and after all locations in the model (time and space) have been visited by the random walk (see Figure 3.A.6.3).

### *3.A.6.6.5 Non-Uniqueness and Assessment of Uncertainty*

The non-uniqueness of the inverse problem relates to the space of solutions (*e.g.*, spatial distributions of reservoir properties) that equally honor the well-log and the pre-stack seismic data. Non-uniqueness is reduced by incorporating additional a-priori information to the estimation problem. That is, a variety of constraints (*e.g.*, well logs, histograms) are incorporated to limit the number of plausible solutions to the inverse problem. In addition to the above approach, the inversion algorithm described in this Section allows one to generate multiple equiprobable inversions to quantify the uncertainty of the inverted parameters.

## 3.A.6.7 Validation and Testing of the Proposed Algorithm

Various numerical experiments were performed using the 2D section and the 3D volume described below to validate the proposed joint stochastic inversion algorithm. First, sensitivity analyses were carried out to assess the information content of pre-stack seismic data and spatial resolution of the stochastic inversion when operating in elastic-parameter domain (*i.e.*, inversion results are elastic parameters). Next, a sensitivity analysis of factors affecting the inversion was performed when the proposed inversion algorithm operated in porosity domain (*i.e.*, inversion result is porosity and elastic parameters are obtained as by-products). Finally, examples of the estimation of porosity distributions are described for the synthetic 2D and 3D subsurface models.

### *3.A.6.7.1 Description of a Cross-Section Model*

Figure 3.A.6.5 shows a 2D view of the simulated pre-stack seismic data across the center (Seismic Line 100) of the 3D subsurface reference model described above. Panel (a) in the same Figure 3.A.6. shows both the well locations and the first (nearest) offset seismic trace, and panel (b) shows the last (farthest) offset seismic trace. The cross-section consists of 71 CMP gathers (ten offsets per CMP gather) covering the seismic travel time interval from 0.72s to 1.42s. Two hypothetical wells are located along this cross-section (see Table 3.A.6.1 for a description of well locations). Figure 3.A.6.6 shows the histograms and CDFs of elastic parameters and porosity that were sampled from the assumed well-log data resampled at 2ms intervals. Figure 3.A.6.7 shows cross-plots of the elastic parameters and porosity. Such histograms and cross-plots are used to impose a global constraint on the inversion results and to generate the joint PDFs used by the inversion algorithm, respectively. Unless otherwise specified, all of the 2D numerical experiments reported in this Section were performed using the cross section and histograms described above, and made use of the semivariogram parameters described in Table 3.A.6.1. For convenience, most of the inverted results are reported only in the two-way time window from 1.02 to 1.42s. This time interval completely includes the oil-saturated sand.

### *3.A.6.7.2 Information Content of Pre-Stack Seismic Data*

Figure 3.A.6.8 shows cross-sections along Seismic Line 100 (cross-section model described above) of numerically simulated seismic amplitude variations with source-receiver offset. In principle, pre-stack seismic data embody considerably more sensitivity than post-stack seismic data to estimate petrophysical parameters from seismic amplitudes. This is due to fact

that pre-stack seismic amplitudes are sensitive to PAI, SAI, and bulk density, whereas post-stack seismic data are only sensitive to PAI. It is expected, of course, that such an enhanced sensitivity would translate into better resolving and appraisal properties to infer distributions of petrophysical parameters. The plots shown in Figure 3.A.6.8 clearly indicate a measurable variation of seismic amplitude with an increase in source-receiver offset. Post-stack seismic data, on the other hand, are obtained with the addition (or stacking) of these offsets, thereby improving signal-to-noise ratio but significantly reducing the number of degrees of freedom in the information content of SAI and bulk density. Likewise, stacking implicitly does away with the low-frequency components of PAI and hence one can only work in the seismic travel time domain (the depth reference is irremediably lost).

### *3.A.6.7.3 Spatial Resolution of Post-Stack Seismic Inversion*

Post-stack seismic data are often inverted to obtain acoustic impedances in seismic travel-time domain. Figure 3.A.6.9 shows cross sections along Seismic Line 100 of the post-stack inversion results. Panel (a) shows the average value of inverted AI for ten independent inversions and panel (b) shows the collocated standard deviation of the inverted AI for these ten inversions. Global correlation coefficients ($r^2$ is used as a scale-independent measure of similarity between two variables, see 3.A.7.5.D. Appendix D) were calculated between inverted and actual values of PAI ($r^2_{PAI}$ = 0.970). The standard deviation of these inversions varies anywhere from 0 to 0.40. Inverted PAIs are subsequently compared to pre-stack inversion results.

### *3.A.6.7.4 Spatial Resolution of Pre-Stack Seismic Inversion*

A number of experiments were performed on the cross-section model described above to evaluate the resolution of pre-stack stochastic inversion when estimating of PAI, SAI, and bulk density for 10 independent inversions. All independent realizations yielded by the inversion entailed the same global pre-stack seismic data misfit, honored the well-log data (two wells), and honored the prescribed global property histograms. Figure 3.A.6.10 shows a plot of the average similarity between the measured and inverted pre-stack seismic data as a function of CMP location computed at the first and final iterations of the inversions, respectively. As emphasized earlier, each CMP consists of ten source-receiver offsets. The plot shown in Figure 3.A.6.10 indicates that the measured pre-stack seismic data have been properly honored at the well locations.

Figures 3.A.6.11 and 3.A.6.12 show cross-sections along Seismic Line 100 of the inverted elastic parameters and of their corresponding collocated standard deviation. Figure 3.A.6.11 shows the average value of inverted PAI, SAI, and bulk density for ten independent inversions, and Figure 3.A.6.12 shows the collocated standard deviation of the inverted elastic parameters calculated from those ten inversions. The cross-sections shown in Figure 3.A.6.11 identify the background shale and the oil saturated sand. Global correlation coefficients were calculated between inverted and actual values of elastic parameters ($r_{PAI}^2$ = 0.964, $r_{SAI}^2$ = 0.991, and $r_{\rho_b}^2$ = 0.984, respectively). All of the inverted elastic parameters exhibited high global correlation coefficients. Further analysis of these inversion results showed that the estimated elastic parameters within the sand exhibited more variability than the estimated elastic parameters within the shales (see Figure 3.A.6.12). The estimated PAI within the oil-saturated sand exhibited the most variability as per standard deviation calculations, whereas bulk density exhibited the lowest variability. Also notice that PAIs from post-stack seismic inversion exhibit a global correlation with the actual PAIs than the PAIs from pre-stack seismic inversion. Also the PAIs inverted from post-stack seismic data exhibit a smaller range of variability (standard deviation of ten inversions) than the PAIs obtained from the inversion of pre-stack seismic data.

Varela *et al.* (2003) performed similar inversion experiments in velocity domain and reported a low correlation coefficient for the inverted compressional-wave velocity. This low value was due to (a) the large boundary constraints used in the inversion, (b) small contrast in velocity between the oil saturated sand and background shale, and (c) the effect of a suboptimal seismic signal-to-noise ratio. More than likely, the same factors are the likely responsible for the high variability of the inverted PAI obtained in this study. Results obtained in impedance domain using the 2D section described above show that the global correlation coefficients between inverted and actual values of PAI, SAI, and bulk density are slightly better than those reported by Varela *et al.* (2003) in velocity domain for compressional- and shear-wave velocity and bulk density. Additionally, short offsets are rendered more appropriate to accurately estimate PAI but not compressional-wave velocity. In general, reliable estimates of PAI would be obtained for short seismic offsets whereas long seismic offsets would render reliable estimates of SAI and bulk density. Simultaneous use of short and long seismic offsets also contributes to a more reliable estimation of the low-frequency components of PAI, SAI, and bulk density.

#### *3.A.6.7.5 Cross-Validation*

Experiments were performed on the cross-section model described above to evaluate the effect of the number of wells on the inverted spatial distributions of porosity (and elastic parameters as by-products). The influence of the number of wells in the inversion is important because the initial models entered to the inversion are drawn from local PDFs which are in turn sampled from well logs. Cases considered here include one well, two wells, and three wells. Ten independent inversions were performed for each of the cases described above. All of the inverted realizations entailed the same global pre-stack seismic data misfit, honored the well-log data, and honored the prescribed global property histograms.

Table 3.A.6.3 summarizes results obtained with the inversion algorithm operating in porosity domain. This table describes global correlation coefficients between actual porosity and average values of inverted porosity, and between actual elastic parameters and average values of inverted elastic parameters. Average inverted values were calculated from the ten independent inversions; their corresponding global correlations are high, exhibit small differences among cases, and slightly increase as the number of wells increases. For instance, global correlation coefficients for porosity are $r_{\phi}^2$ = 0.956, $r_{\phi}^2$ = 0.960, and $r_{\phi}^2$ = 0.963 for one, two, and three wells, respectively. For a given case, individual results for each independent inversion exhibit more spatial variability and a lower global correlation coefficient than for the model averaged from the ten inversions. Table 3.A.6.3 also describes the range of variability (standard deviation) of the inversions for each case. The variability of the inverted distributions decreases slightly as the number of wells increases.

Figures 3.A.6.13 and 3.A.6.14 show cross-sections of the inverted porosity and of the collocated standard deviations, respectively, for inversion exercises performed with the cases described in Table 3.A.6.3. The cross-sections shown in Figure 3.A.6.13 correspond to the average value of inverted porosity when honoring hard data from one well, two wells, and three wells, respectively. Figure 3.A.6.14 shows cross-sections of the collocated standard deviation for the same cases. These latter cross-sections emphasize the fact that even though global correlation coefficients for inverted properties are high (as indicated by Table 3.A.6.3), the inverted distributions of porosity (average of ten independent inversions) constrained by the larger number of wells exhibit the most spatial variability.

Figure 3.A.6.15 shows a plot of the similarity between the actual and inverted distributions porosity as a function of CMP location computed at the first and final VFSA iterations of the inversions, respectively, for the case of two wells. This plot indicates that porosity has been properly honored at the well locations and emphasizes the fact that the inversion of pre-stack seismic data has improved the estimation of porosity away from well locations. Another important technical issue to consider is the rate of convergence of the inversion algorithm. Figure 3.A.6.16 shows plots of the evolution of the data misfit function with iteration number for each case under study. The same plot describes the relative contribution of the number of wells to the construction of the initial model input to the inversion. This result clearly indicates that the larger the number of wells used to construct the local field of PDFs, the higher the similarity (the lower the misfit) between the measured and simulated pre-stack seismic data.

### *3.A.6.7.6 Effect of Semivariogram Range*

Estimation and construction of horizontal semivariograms (x- and y-direction) is difficult because there are only a few hard points (*i.e.*, wells) available (Pizarro and Lake, 1997; Isaaks and Srivastava, 1989). Table 3.A.6.4 summarizes results obtained from the stochastic inversion of porosity as a function of the semivariogram range ($\lambda$). As emphasized earlier, the semivariogram range conditions the interpolation of the initial spatial distribution of local PDFs from well-log data. Initial models are sampled point-by-point (space-time) from such PDFs. Numerical experiments were performed on the 2D model described earlier using two wells (see Figure 3.A.6.5). The original semivariogram used to construct the synthetic model exhibits a spatial correlation range equal to $\lambda_T$. This range was assumed to be equal to the range described in Table 3.A.6.1. Cases studied include: $\lambda/\lambda_T$ equal to 0.5, 1.0, and 2.0. For the vertical semivariograms, wells provide sufficient spatial sampling to calculate the corresponding parameters. The global variance for porosity was set equal to that of values calculated from the sampled well-log data. Ten independent inversions were performed for each of the cases described above. Inversion results obtained for all independent realizations entailed the same global pre-stack data misfit, honored the well-log data, and honored the prescribed global property histograms.

In these exercises, porosity is the target petrophysical property while elastic parameters are obtained as by-products of the inversion. Results described in Table 3.A.6.4 indicate that global correlation coefficients between actual porosity and average values of inverted porosity, and between actual elastic parameters and average values of inverted elastic parameters are relatively high and only slightly different among themselves. Average inverted values were calculated from the ten independent inversions. Individual inversions for a given case exhibit more spatial variability and a lower global correlation coefficient than for the corresponding spatial distributions averaged from the ten independent inversions. Table 3.A.6.4 also shows the range of variability (standard deviation) of the ten independent inversions for each case. The latter results entail almost the same variability as the cases described above and clearly indicate the positive contribution of pre-stack seismic data to the extrapolation of petrophysical variables away from wells.

#### *3.A.6.7.7 Description of a 3D Volume Model*

Figure 3.A.6.17 is a 3D visual rendering of the pre-stack seismic data numerically simulated in the neighborhood of the oil-saturated reservoir sand. The same Figure 3.A.6. shows the geometry of the sand and the location of five hypothetical wells (see Table 3.A.6.1 for a description of well locations). Data gathered from these wells is used by the inversion algorithm

to constrain the estimation of inter-well petrophysical and elastic properties. The corresponding seismic volume consists of 81 by 81 CMP gathers covering the seismic travel time interval from 1.10 to 1.42 seconds. Due to computer memory limitations, only five offsets (No. 1, 3 5, 7, and 9) per CMP gather were used in the inversion. All of the 3D numerical experiments reported in this Section were performed using the synthetic 3D model described in Figure 3.A.6.17 and made use of the semivariogram parameters described in Table 3.A.6.1.

### *3.A.6.7.8 Estimation of Porosity*

A number of experiments were performed on the 3D model described in Figure 3.A.6.17 to assess the performance of the pre-stack stochastic inversion algorithm in the estimation of porosity (and PAI, SAI, and bulk density as by-products). As described earlier, initial model parameters are generated with standard geostatistical simulation while final inverted models honor the full gather of pre-stack seismic data, well logs, and prescribed histograms.

### *3.A.6.7.9 Consistency in Data Space for Pre-Stack Seismic Data*

An assessment of the performance of the inversion was carried out in data space. Figure 3.A.6.18 is a map of the average similarity between the measured and inverted pre-stack seismic data for each CMP gather computed at the first (Panel a) and final (Panel b) VFSA iterations of the inversion, respectively, when performing the inversion in porosity domain. The average similarity of seismic data was calculated CMP by CMP and included five offsets per CMP. Maps in Figure 3.A.6.18 indicate that initial models of elastic parameters poorly honor the pre-stack seismic data (overall average correlation of 0.338) whereas final models of elastic parameters properly honor the pre-stack seismic data (overall average correlation of 0.952).

### *3.A.6.7.10 Consistency in Model Space for Elastic Parameters*

An assessment of the inversion was performed in model space for PAI, SAI, and bulk density. The inversion is performed to estimate porosity and elastic parameters are obtained as by-products. Figure 3.A.6.19 is a map of average similarity between the actual and estimated PAI (Panel a), SAI (panel b), and bulk density (Panel c) at the final iteration of the inversion. The average similarity for each elastic parameter was calculated trace by trace. Maps in Figure 3.A.6.19 indicate that estimated values of elastic parameters have been properly honored by the inversion. Average correlations of 0.892, 0.963, and 0.940 were calculated for PAI, SAI, and bulk density, respectively.

### *3.A.6.7.11 Consistency in Model Space for Porosity*

An assessment of the inversion was also performed in model space for porosity. Figure 3.A.6.20 is a map of average similarity between the actual and estimated distributions of porosity computed at the first (Panel a) and final (Panel b) VFSA iterations of the inversion, respectively, when performing the inversion in porosity domain. The average similarity of porosity was calculated trace by trace. Maps in Figure 3.A.6.20 indicate that initial porosity distributions exhibit an overall average correlation of 0.521 whereas the inverted porosity distributions exhibit an overall average correlation of 0.903.

## 3.A.6.8 Dynamic Reservoir Characterization

Dynamic reservoir behavior is a complex process as it is governed not only by the spatial distribution of rock properties (*e.g.*, porosity, permeability, permeability anisotropy) but also by fluid properties, rock-fluid interactions, and production strategies. The analysis presented in this section makes use of a porosity model designated as the reference case (case T), porosity models obtained with standard geostatistics (case G), and porosity models obtained with the proposed inversion algorithm (case I). Knowledge is assumed of fluid and rock-fluid interaction properties, production strategy, and porosity-permeability transformations. The objective is to assess the impact of the underlying porosity model on the forecast of hydrocarbon production when all the remaining reservoir and fluid variables are assumed to be known in a precise manner.

### *3.A.6.8.1 Reservoir Simulation Model*

The cross section model described in Figure 3.A.6.5 was used to numerically simulate a water-oil displacement with one injector and one producer well. The reference case (case T), the models generated with standard geostatistical techniques which do not make use of seismic data (case G), and the models generated by the inversion algorithm which makes use of pre-stack seismic data (case I) were subject to the same enhanced recovery process over a period of 2557 days. In order to focus only on the effect of model construction on dynamic behavior the same fluid and rock properties, and production constraints were assumed for all cases considered in this section. The only properties that changed from model to model were porosity and porosity-derived permeability. Based on standard practice, the permeability field was constructed using a simple porosity-permeability transformation (*i.e.*, $\log(k) = 12\phi - 0.5$). Table 3.A.6.5 summarizes the specific fluid, rock, and production constraints enforced by the numerical simulation of the waterflood process.

### *3.A.6.8.2 Evaluation of Dynamic Reservoir Behavior*

This section considers the evaluation of the effect of the spatial distributions of porosity on the time records of fluid production. The evaluation is used for the appraisal of production reservoir uncertainty. An error assessment over time (or global uncertainty, U) of a dynamic variable was calculated as the $l_2$-norm between the time records of the fluid production associated with the reference case (case T) and those associated with each realization in a given case (case G and case I). This appraisal was performed using equation (3.A.4.1) in Section 3.A.4. Individual errors were normalized against the overall maximum error and then box plots were constructed to appraise the results.

Figures 3.A.6.21, 3.A.6.22, and 3.A.6.23 show box plots of the global uncertainty for oil recovery, average water saturation, and average reservoir pressure, respectively. From these figures it is clear that the magnitude of the prediction error for case G (no use of seismic data) is larger than the magnitude of the prediction error for case I (use of the full gather of pre-stack seismic data) for all the time records considered in this study. The same plots also suggest a bigger variability for case G than for case I. Results shown in Figures 3.A.6.21 through 3.A.6.23 represent global reservoir responses and clearly indicate that more accurate forecasts of dynamic reservoir behavior are calculated from reservoir models generated with the proposed inversion algorithm.

### 3.A.6.9 Summary and Conclusions

The inversion algorithm described in this Section estimates spatial distributions of inter-well elastic parameters with a vertical resolution intermediate between that of seismic data and well logs. Likewise, estimation of inter-well petrophysical parameters (*e.g.* porosity) can be performed whenever a high degree of statistical correlation exists between elastic and petrophysical parameters. The inversion algorithm effectively extrapolates elastic parameters away from existing wells by honoring existing pre-stack 3D seismic data and global property histograms. This extrapolation procedure can be considered an extension of geostatistical inversion of post-stack seismic data in that geostatistical estimation concepts are used to honor well-log data and to enforce a prescribed degree of spatial correlation for the interpolated parameters through the use of semivariograms. However, usage of pre-stack seismic data makes it necessary to adopt specialized data misfit norms in the inversion that can balance and properly synthesize the information content available from CMP gathers. Estimation of spatial distributions of three elastic parameters (PAI, SAI, and bulk density) also makes the inversion much more non-unique and unstable than the estimation of one single elastic parameter (PAI) from post-stack seismic data. Consequently, provisions are necessary to quantify the degree of uncertainty of the inverted property distributions. All of this makes the inversion extremely CPU intensive and hence limits its applicability to field data sets. For instance, joint inversions performed on the 2D subsurface model take approximately twelve hours on a Pentium III processor with 2GHz of physical memory. Parallelization of the inversion algorithm is a natural future step to increase computer efficiency. A significant task remains to advance an additional proof of concept with field data.

Sensitivity analysis showed that an increase in the number of wells used to construct the model entered to the inversion caused the initial data misfit to decrease (the data similarity to increase) and the spatial variability of the inverted property distributions to increase. It was also found that knowledge of semivariogram model and associated parameters is important to generate the initial property distribution entered to the inversion. However, for the synthetic examples considered in this Section, the use of pre-stack seismic measurements substantially diminished the sensitivity of the inversion to the choice of semivariogram parameters and hence reliably guided the estimation of inter-well elastic and petrophysical parameters.

Additional applications of the inversion algorithm described in this Section include the estimation of inter-well lithology groups (or facies) and of their corresponding petrophysical properties (*e.g.* facies-dependent porosity).

As emphasized in this Section, reliable extrapolation and interpolation of property distributions can only be performed with sufficient inter-well spacing and with a sufficient degree of statistical dependence among well-log measurements acquired from different wells. Optimally, well locations should be within the range of semivariograms to allow the estimation of inter-well property distributions with a vertical resolution higher than that of pre-stack seismic data. However, numerical experiments performed with synthetic models indicate that single-well extrapolation is also possible provided that the distance of the extrapolation is within the semivariogram range. In the latter case, the inversion algorithm described in this Section could be used to assess lateral extent and continuity of petrophysical units penetrated by the well.

**Table 3.A.6.1: Summary of the geometrical and measurement properties used in the construction of the subsurface model considered in this Section.**

| Characteristic | Value |
|---|---|
| Overall average compressional-wave velocity | 2.18 km/s |
| Overall average shear-wave velocity | 0.54 km/s |
| Overall average bulk density | 2.65 g/cm$^3$ |
| Porosity sand, $\phi(\bar{\phi}, \sigma)$ | N(0.22, 0.06) |
| Porosity shale, $\phi(\bar{\phi}, \sigma)$ | N(0.09, 0.015) |
| Semivariograms used for the population of porosity: Spherical (sill, $\lambda_x, \lambda_y, \lambda_z$) | sand:<br>S(1, 915 m, 610 m, 30 m)<br>shale:<br>S(1, 1220 m, 825 m, 60 m) |
| Cell location of wells in 2D section | Well No. 1 (94, 1)<br>Well No. 2 (120, 1) |
| Cell location of wells in 3D volume | Well No. 1 (87, 113)<br>Well No. 2 (113, 113)<br>Well No. 3 (87, 87)<br>Well No. 4 (113, 87)<br>Well No. 5 (100, 100) |

**Table 3.A.6.2: Description of the properties used to generate 3D pre-stack surface seismic data for the subsurface model described in Table 3.A.6.1.**

| Property | Value |
|---|---|
| Seismic grid | 200 inlines<br>200 crosslines |
| Separation between lines | 23 m |
| Separation between offsets | 300 m |
| Number of offsets per Common-mid-point (CMP) | 10 |
| Seismic time range | 0 – 1.5 s |
| Time sampling interval | 2 ms |
| Seismic wavelet | 35 Hz zero-phase Ricker |

**Table 3.A.6.3: Global correlation coefficients ($r^2$) between actual and average values of inverted properties (compressional acoustic impedance, PAI, shear acoustic impedance, SAI, bulk density, and porosity), and range of the standard deviation ($\sigma$) calculated from ten independent inversions as a function of the number of wells. Well-log data were used to constrain the inversion and to construct the initial spatial distribution of local PDFs.**

| **Case (No. of Wells)** | **PAI, [km/s*g/cm$^3$]** | | **SAI, [km/s*g/cm$^3$]** | | **Bulk density, [g/cm$^3$]** | | **Porosity, [fraction]** | |
|---|---|---|---|---|---|---|---|---|
| | $r^2$ | **Range of $\sigma$** | $r^2$ | **Range of $\sigma$** | $r^2$ | **Range of $\sigma$** | $r^2$ | **Range of $\sigma$** |
| One well | 0.960 | 0-0.50 | 0.986 | 0-0.27 | 0.983 | 0-0.17 | 0.956 | 0.043 |
| Two wells | 0.967 | 0-0.47 | 0.988 | 0-0.24 | 0.985 | 0-0.14 | 0.960 | 0.041 |
| Three wells | 0.969 | 0-0.40 | 0.989 | 0-0.20 | 0.987 | 0-0.14 | 0.963 | 0.037 |

**Table 3.A.6.4: Global correlation coefficients ($r^2$) between actual and average values of inverted properties (compressional acoustic impedance, PAI, shear acoustic impedance, SAI, bulk density, and porosity), and range of standard deviation ($\sigma$) calculated from ten independent inversions as a function of various semivariogram ranges. The semivariogram ranges are used to construct the initial spatial distribution of local PDFs; $\lambda_T$ designates the original range.**

| Case (range of spatial correlation) | PAI, [km/s*g/cm$^3$] | | SAI, [km/s*g/cm$^3$] | | Bulk density, [g/cm$^3$] | | Porosity, [fraction] | |
|---|---|---|---|---|---|---|---|---|
| | $r^2$ | Range of $\sigma$ | $r^2$ | Range of $\sigma$ | $r^2$ | Range of $\sigma$ | $r^2$ | Range of $\sigma$ |
| $\lambda/\lambda_T = 0.5$ | 0.967 | 0-0.47 | 0.988 | 0-0.22 | 0.985 | 0-0.14 | 0.959 | 0.037 |
| $\lambda/\lambda_T = 1.0$ | 0.967 | 0-0.47 | 0.988 | 0-0.24 | 0.985 | 0-0.14 | 0.960 | 0.041 |
| $\lambda/\lambda_T = 2.0$ | 0.967 | 0-0.41 | 0.988 | 0-0.22 | 0.985 | 0-0.13 | 0.960 | 0.034 |

**Table 3.A.6.5: Summary of fluid and petrophysical properties assumed in the construction of the numerical reservoir model considered in this Section.**

| Properties | | Values and units |
|---|---|---|
| Fluid | water density | 1.0 g/cm$^3$ |
| | oil density | 0.85 g/cm$^3$ |
| | water viscosity | 1.0 mPa-s |
| | oil viscosity | 5.0 mPa-s |
| | water compressibility | 4.6x10$^{-4}$ MPa$^{-1}$ |
| | oil compressibility | 2.9x10$^{-3}$ MPa$^{-1}$ |
| Reservoir | average $S_{wi}$ | 0.24 |
| | average $S_{or}$ | 0.27 |
| | formation compressibility | 2.5x10$^{-4}$ MPa$^{-1}$ |
| | water endpoint | 0.3 |
| | oil endpoint | 0.9 |
| | z- to x-permeability ratio | 0.1 |
| | depth to top of sand | 1219 m |
| Simulation | injection pressure | 13.8 MPa |
| | bottom-hole pressure | 2.8 MPa |
| | production perforations | entire sand interval |

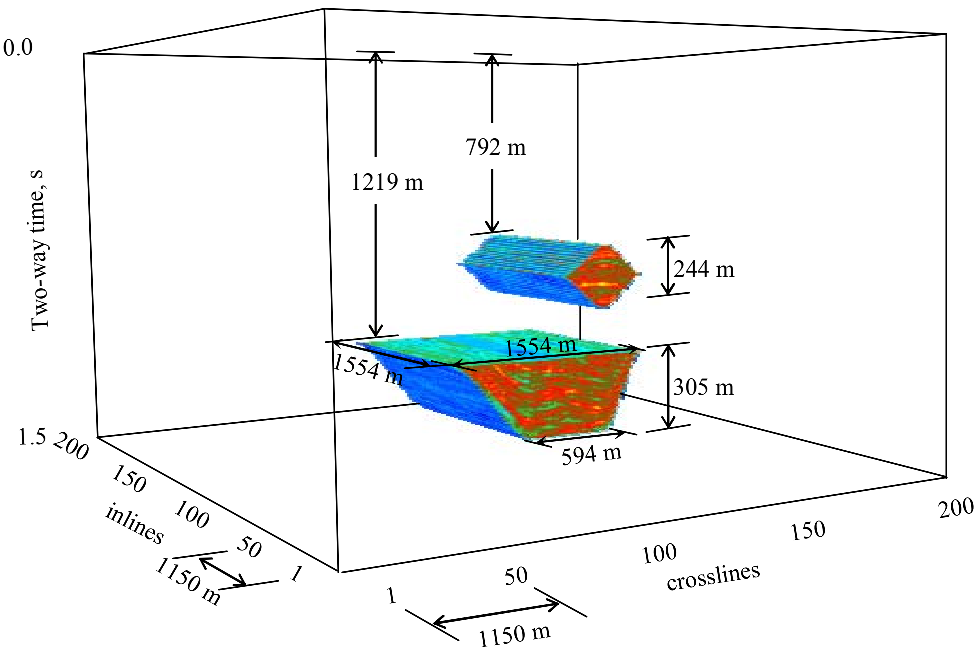

**Figure 3.A.6.1**: Graphical description of the synthetic 3D subsurface model used to validate the joint stochastic inversion algorithm developed in this Section. The top sand is water saturated and the bottom sand is saturated with oil. Refer to Tables 3.A.6.1 and 3.A.6.2 for a description of the associated elastic properties and seismic measurements, respectively.

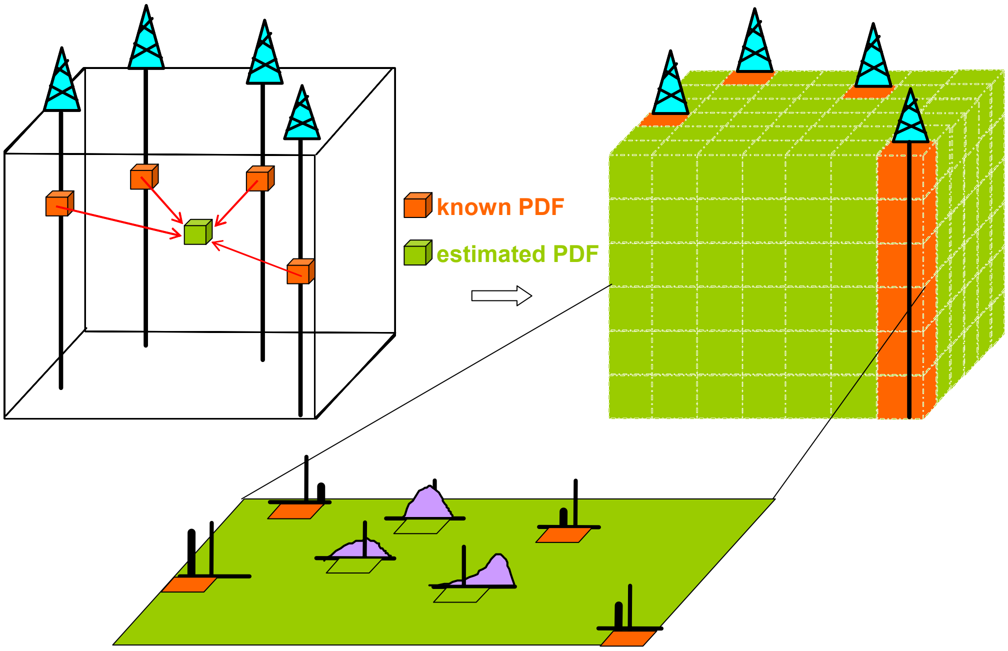

**Figure 3.A.6.2**: Schematic representation of the estimation of interwell local probability density functions (PDF) from welllog data [after Grijalba *et al.* (2000) and Jensen *et al.* (2000)].

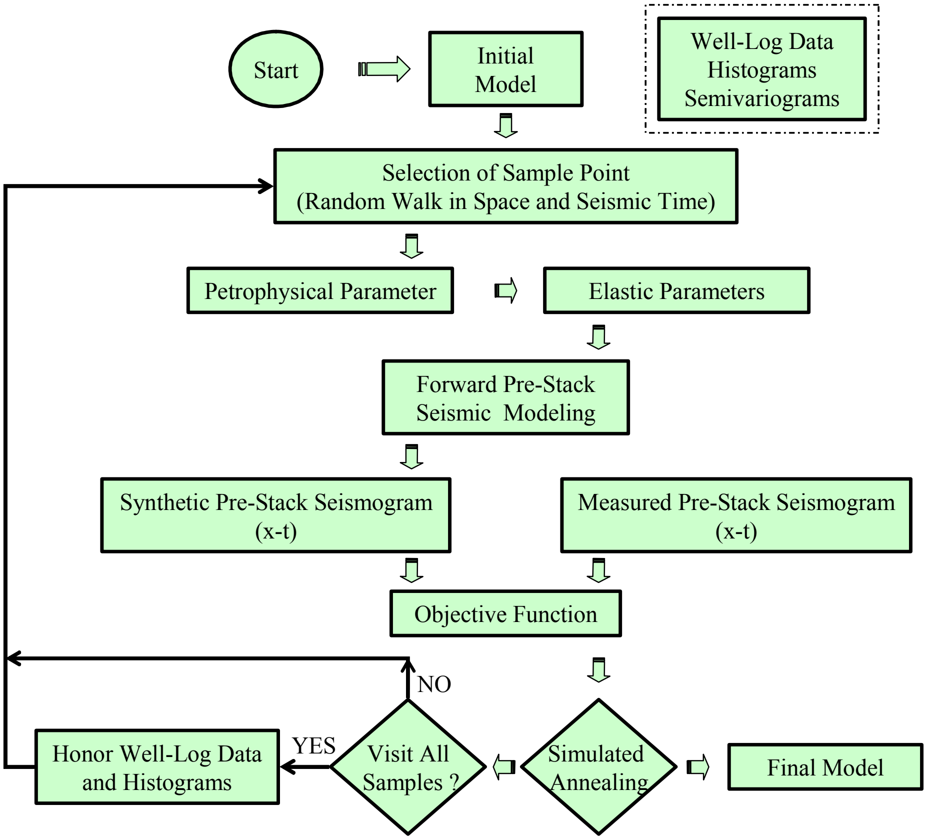

**Figure 3.A.6.3**: Generalized flow diagram of the proposed joint stochastic inversion algorithm developed in this Section.

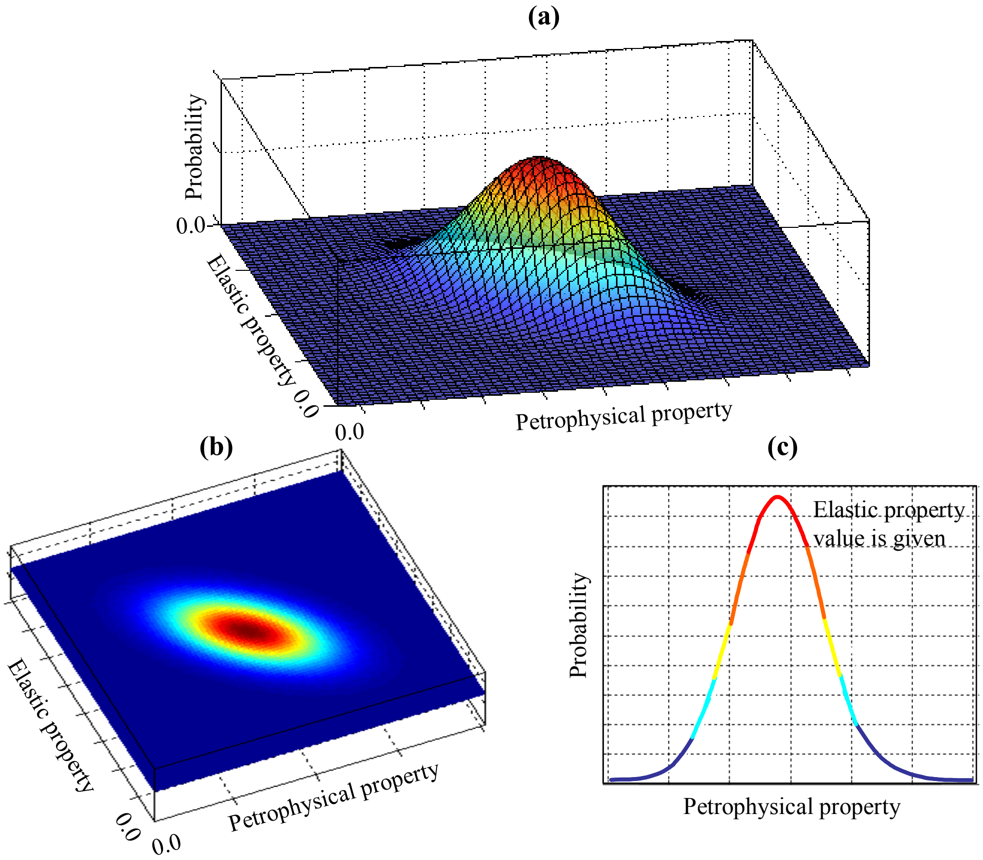

**Figure 3.A.6.4**: Example of a joint probability density function (PDF). Panel (a) shows a theoretical joint probability density function between elastic and petrophysical parameters when the correlation coefficient between them is equal to -0.6. Panel (b) is a top view of the joint PDF and panel (c) shows the PDF of the petrophysical property for a conditional value of elastic property.

(a) First (near) pre-stack seismic offset

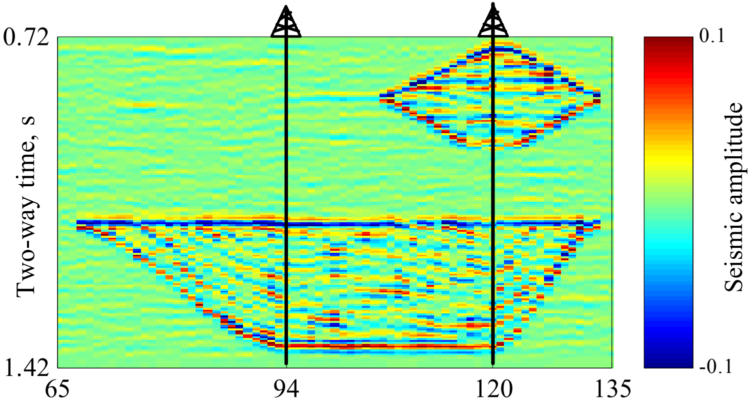

(b) Last (far) pre-stack seismic offset

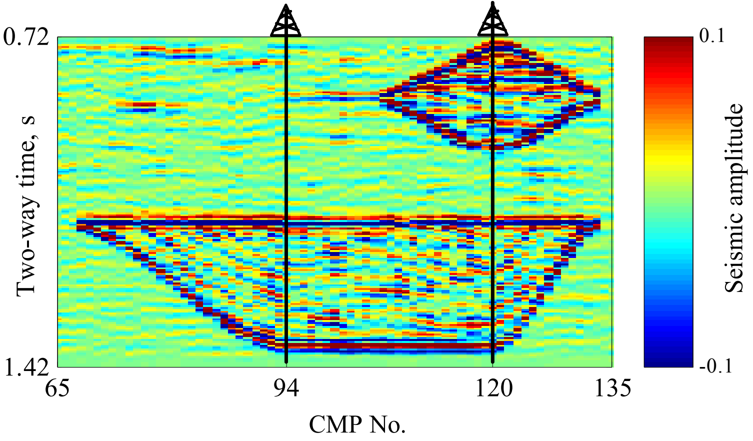

**Figure 3.A.6.5**: Cross-section along the center (Seismic Line 100) of the 3D subsurface model shown in Figure 3.A.6.1 used to perform the validation of the joint stochastic inversion algorithm. Panels (a) and (b) show the first (nearest) and last (farthest) traces of pre-stack seismic gathers, respectively. Common-mid-point (CMP) gathers are separated by a distance of 23m. Data are sampled in vertical travel time domain at a constant rate of 2ms. Locations of two hypothetical wells are also displayed in this figure.

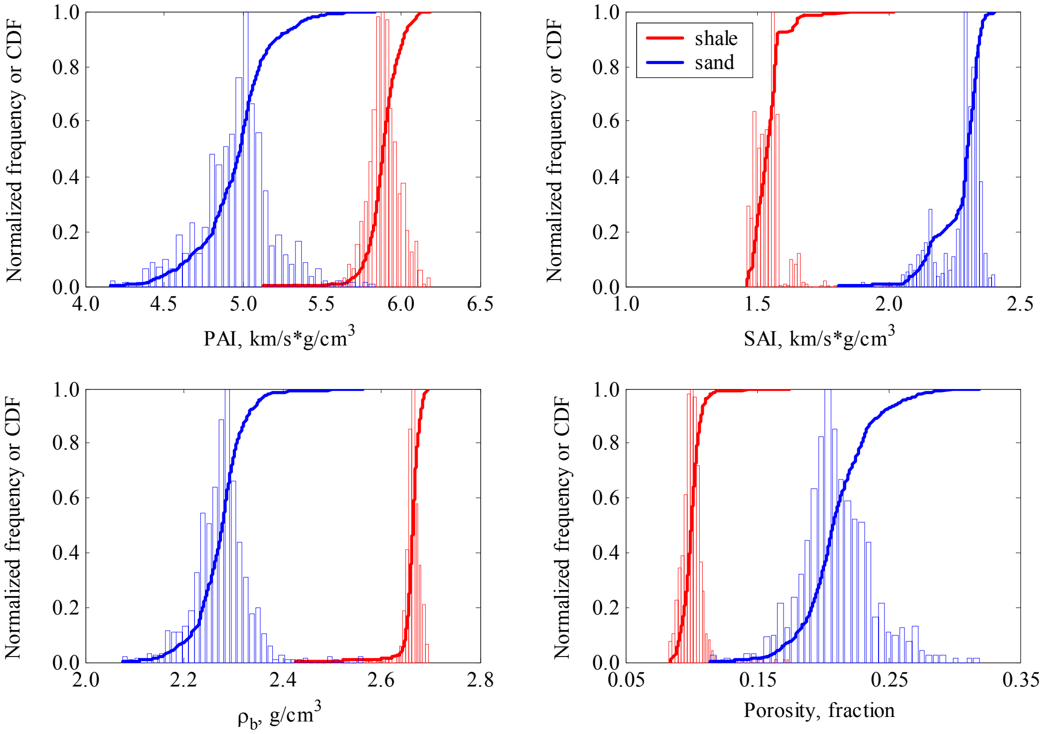

**Figure 3.A.6.6**: Histograms and cumulative distribution functions (CDF) of the elastic parameters (compressional-wave acoustic impedance, PAI, shear-wave acoustic impedance, SAI, and bulk density) and porosity sampled from the two hypothetical wells shown in Figure 3.A.6.5.

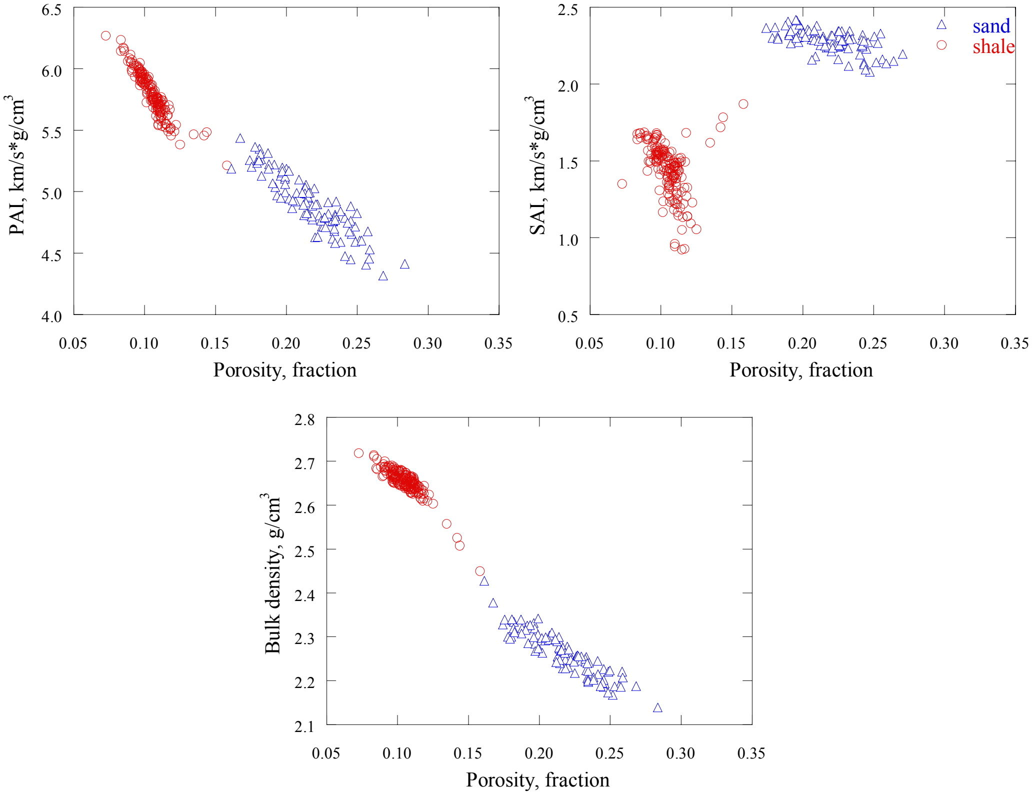

**Figure 3.A.6.7**: Cross-plots describing the lithology-dependent relationship between elastic parameters (compressional-wave acoustic impedance, PAI, shear-wave acoustic impedance, SAI, and bulk density) and porosity.

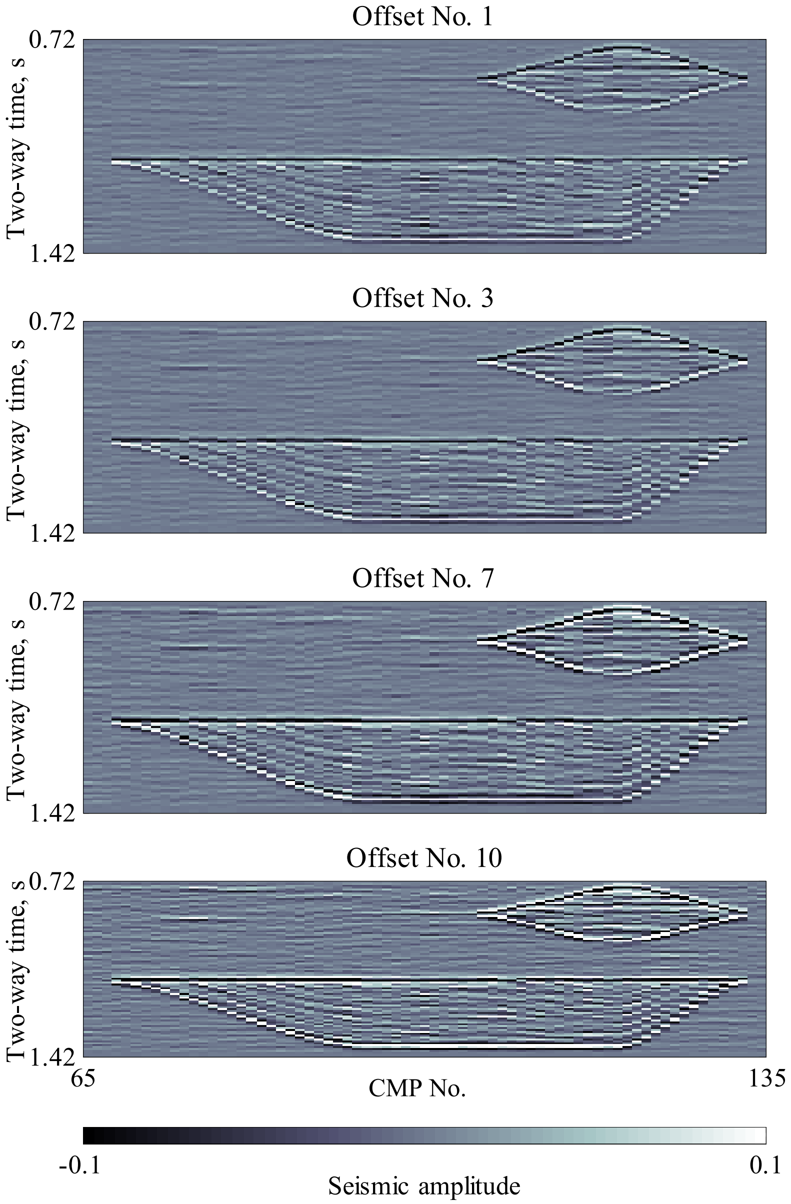

**Figure 3.A.6.8**: Cross-sections along Seismic Line 100 of seismic amplitude variations with source-receiver offset. Offset No. 1 is the nearest and offset No. 10 is the farthest from the source. The separation between offsets is 300 m.

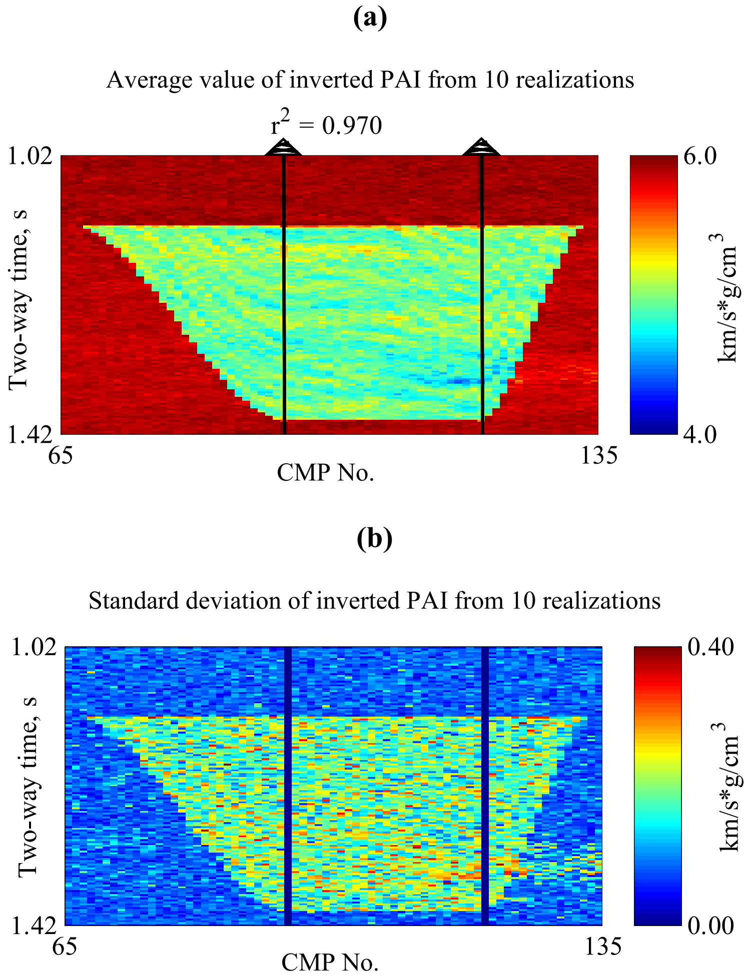

**Figure 3.A.6.9**: Results obtained from the inversion of post-stack seismic data. Panel (a) shows a cross-section of the average value of inverted acoustic impedance (PAI) for ten independent inversions. Panel (b) shows cross-sections of the corresponding collocated standard deviation of the inverted acoustic impedance calculated from ten independent inversions. The global correlation coefficient ($r^2$) is calculated between the average model of inverted acoustic impedance and the actual model of acoustic impedance.

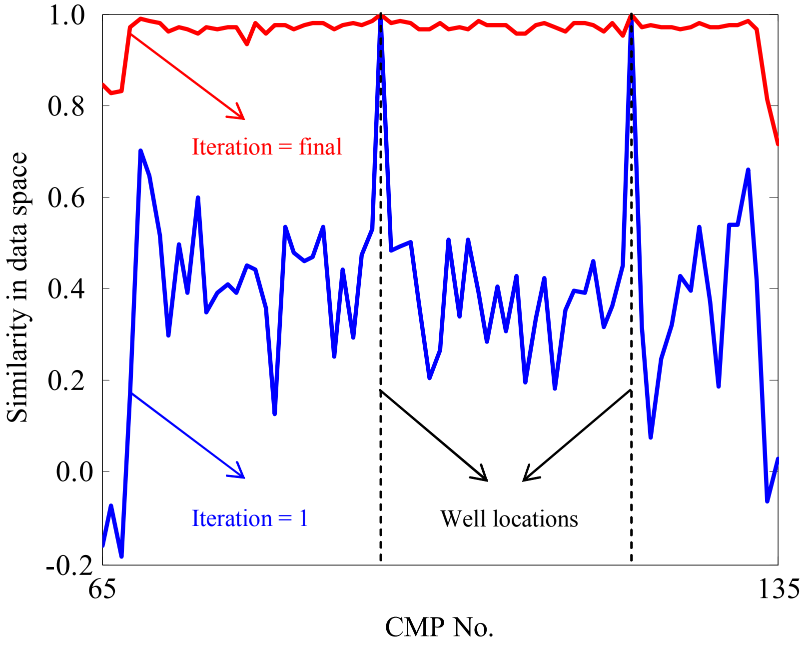

**Figure 3.A.6.10**: Plots of the average similarity between measured and simulated pre-stack seismic data as a function of common-mid-point (CMP) location calculated at the first and final iterations of the inversion. Average similarity is computed for each pre-stack gather in the time interval from 1.02 to 1.42s. Equation 3.A.6.1 quantifies the similarity of pre-stack seismic data used to construct these plots.

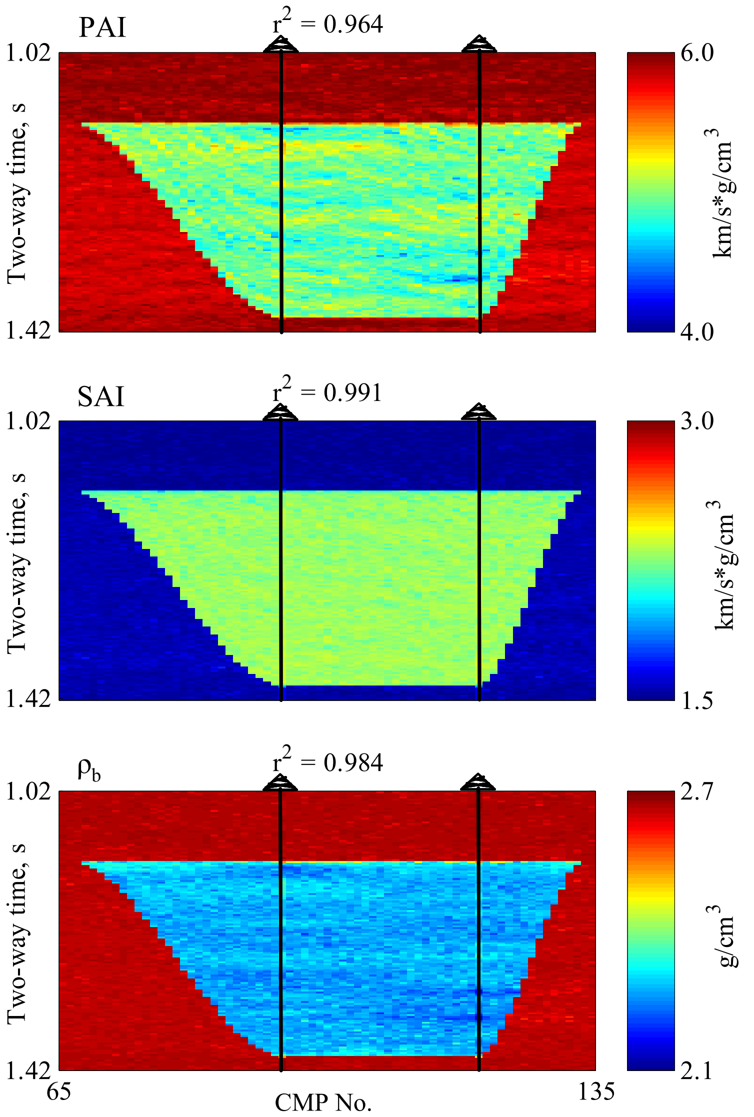

**Figure 3.A.6.11**: Results obtained with the proposed stochastic inversion algorithm operating in elastic-parameter domain. Cross-sections of the average value of inverted compressional-wave impedance (PAI), shear-wave impedance (SAI), and bulk density, respectively, calculated from ten independent inversions. Global correlation coefficients ($r^2$) are calculated between the average models of inverted elastic parameters and the actual models of elastic parameters.

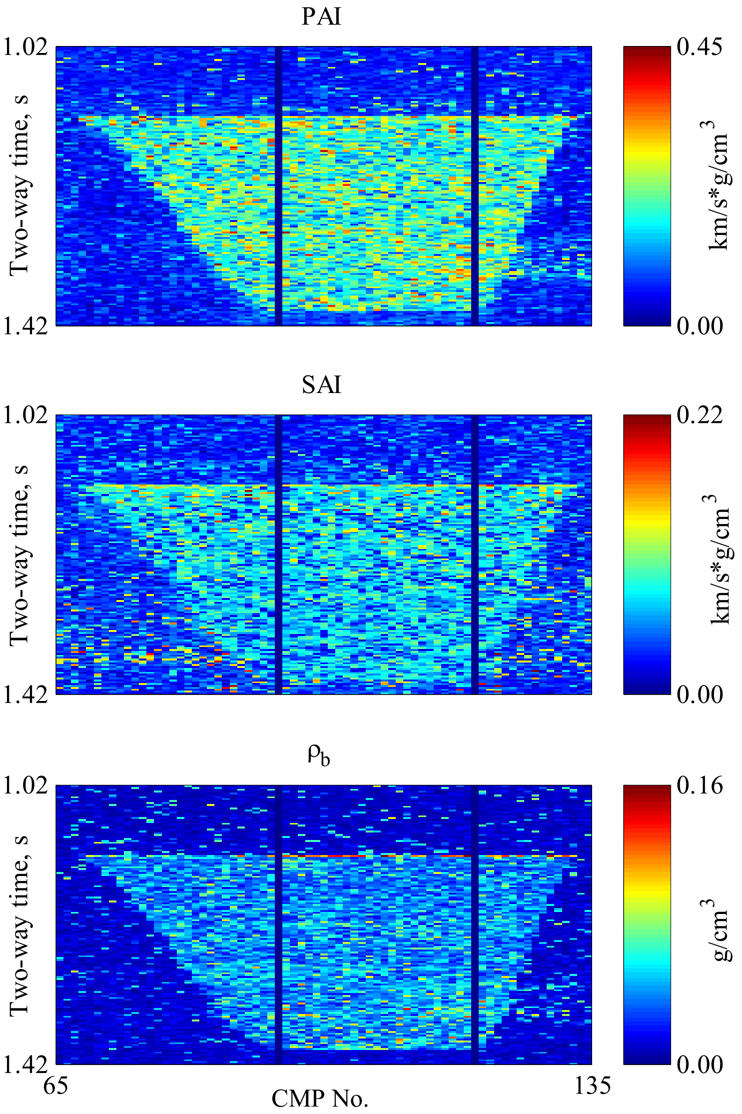

**Figure 3.A.6.12**: Results obtained with the proposed stochastic inversion algorithm operating in elastic-parameter domain. Cross-sections of the collocated standard deviation of inverted compressional-wave impedance (PAI), shear-wave impedance (SAI), and bulk density, respectively, calculated from ten independent inversions.

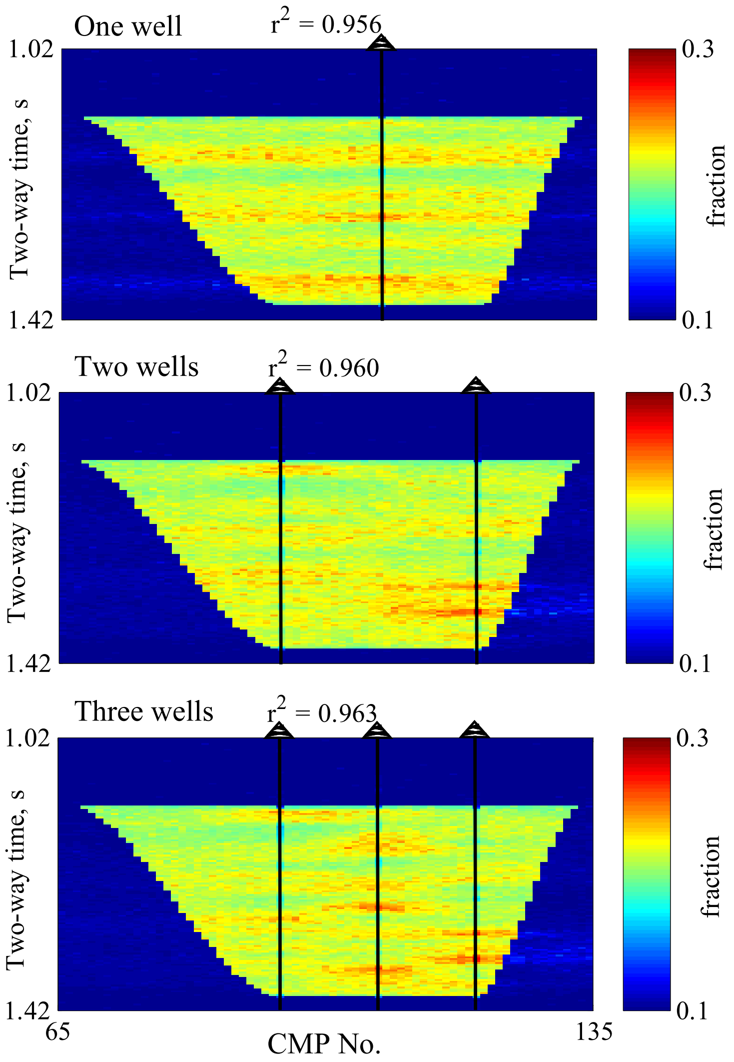

**Figure 3.A.6.13**: Cross-validation results. Cross-sections of the average value of inverted porosity calculated from ten independent inversions for the cases of one, two, and three wells, respectively, used to constrain the inversion algorithm. Global correlation coefficients ($r^2$) are calculated between the average model of inverted porosity and the actual porosity model.

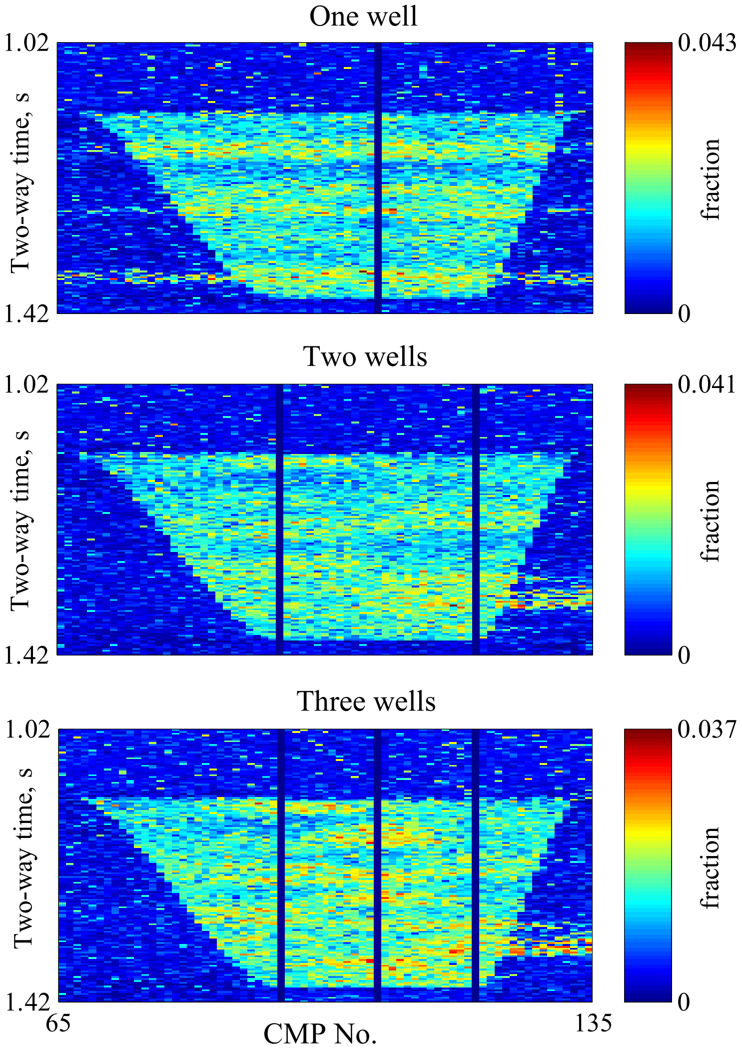

**Figure 3.A.6.14**: Cross-validation results. Cross-sections of the collocated standard deviation of inverted porosity calculated from ten independent inversions for the cases of one, two, and three wells, respectively, used to constrain the inversion algorithm.

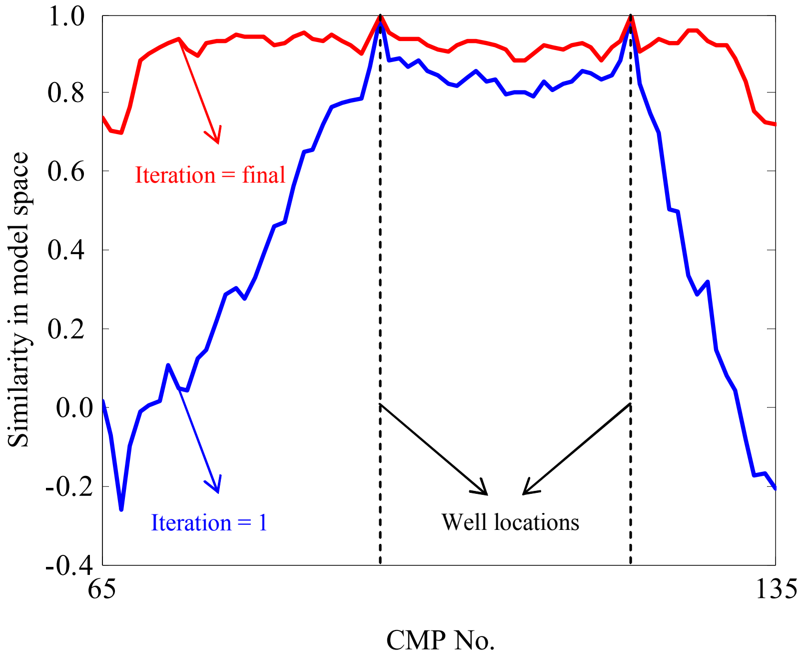

**Figure 3.A.6.15**: Consistency in model space. Plot of the average similarity between actual and inverted porosity as a function of common-mid-point (CMP) location calculated at the first and final iterations of the inversion. Average similarity is computed for each pre-stack gather in the time interval from 1.02 to 1.42s.

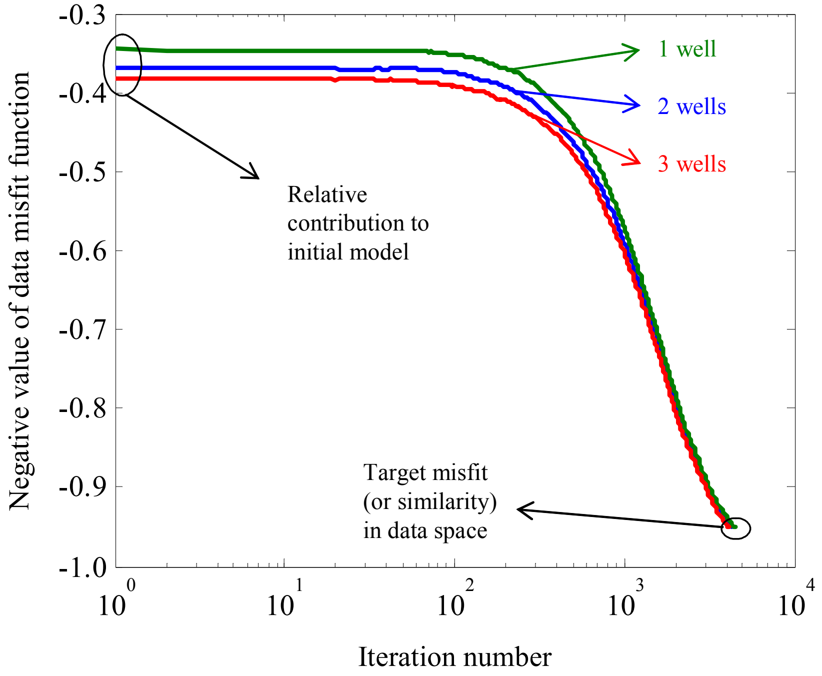

**Figure 3.A.6.16:** Negative value of data misfit or similarity function (see Equation 3.A.6.1) as a function of both iteration number and number of wells used to constrain the stochastic inversion.

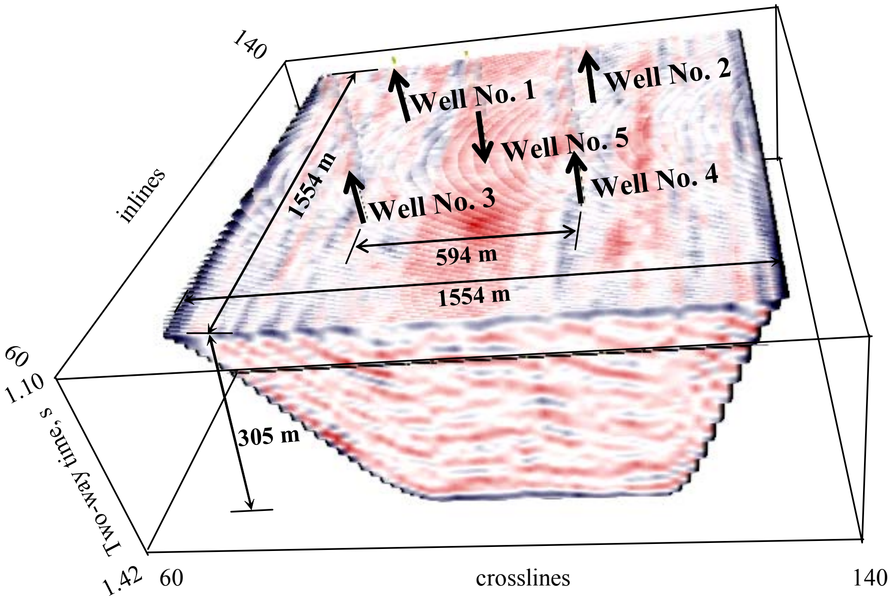

**Figure 3.A.6.17**: Three-dimensional volume in the neighborhood of the oil saturated sand extracted from the 3D subsurface model shown in Figure 3.A.6.1 and used to perform the validation of the stochastic inversion algorithm. Crosslines and inlines are separated by a distance of 23 m. Data are sampled in seismic travel time at a constant rate of 2ms. Locations of five hypothetical wells are also displayed in this figure.

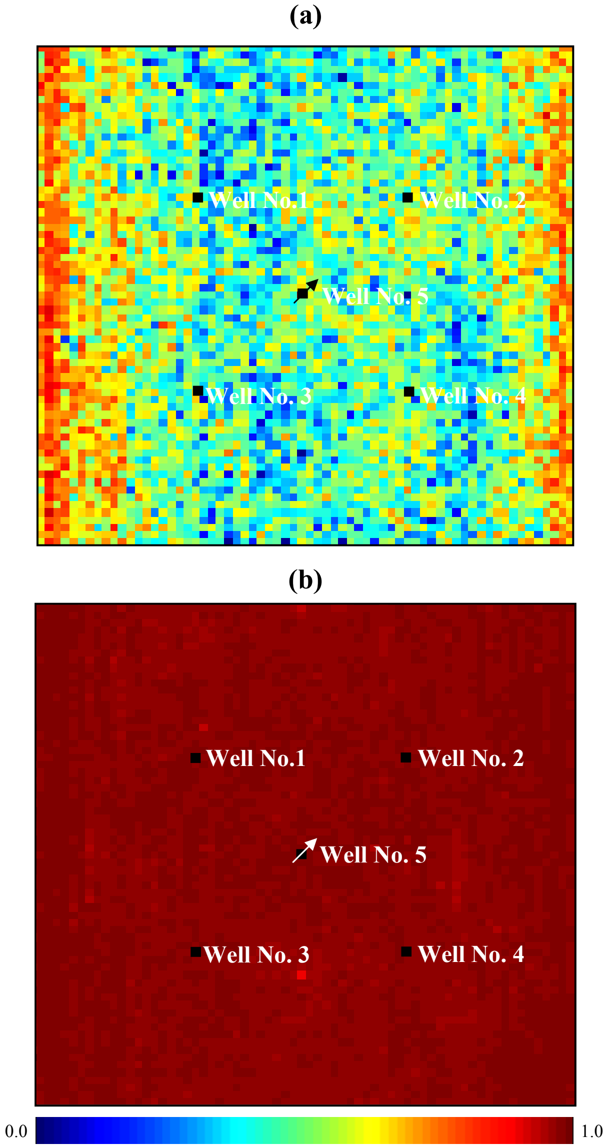

**Figure 3.A.6.18**: Consistency in data space. Average similarity between measured and simulated pre-stack seismic data calculated at the first (Panel a) and final (Panel b) iterations of the inversion, respectively. Average similarity is computed for each pre-stack gather in the time interval from 1.10 to 1.42s. One common-mid-point (CMP) gather consist of five offsets.

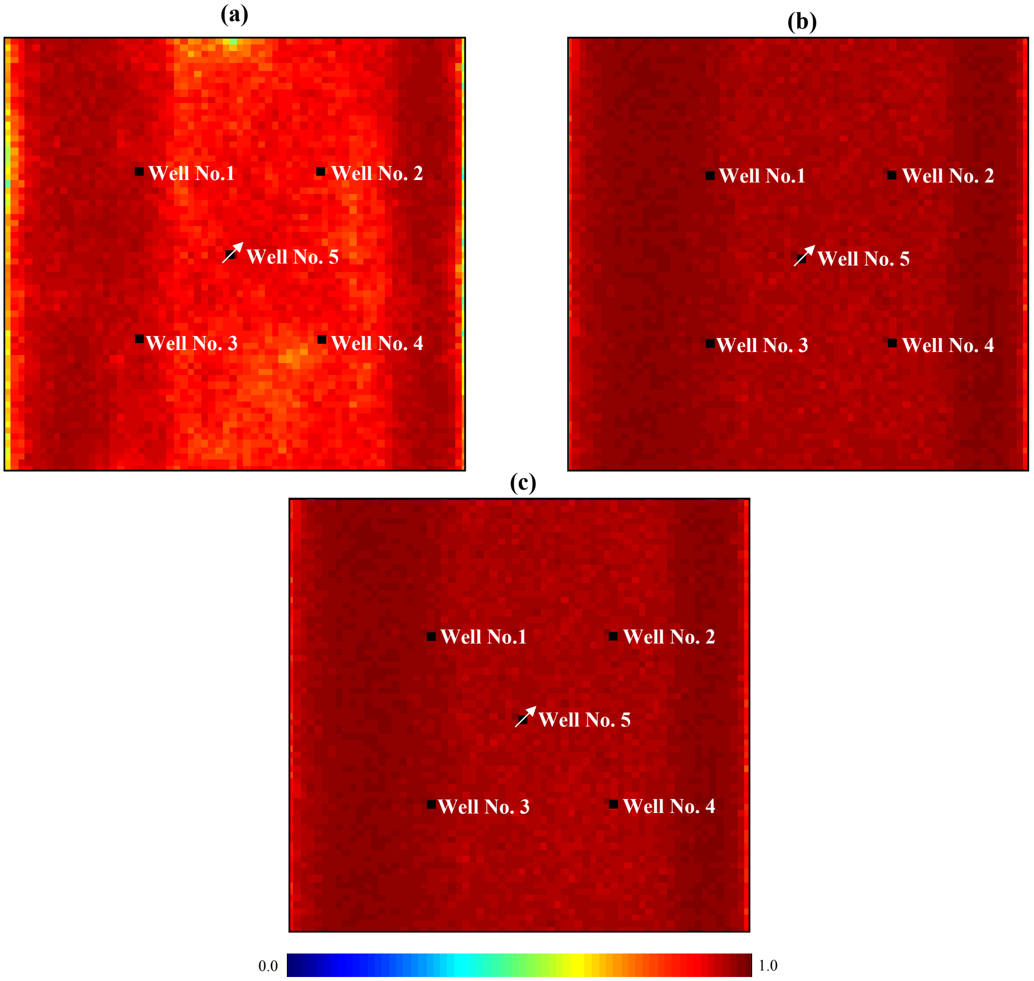

**Figure 3.A.6.19**: Consistency in model space for elastic parameters. Average similarity between actual and inverted PAI (Panel a), SAI (Panel b), and bulk density (Panel c) at the final iteration of the inversion. Average similarity is computed for each elastic parameter trace in the time interval from 1.10 to 1.42s.

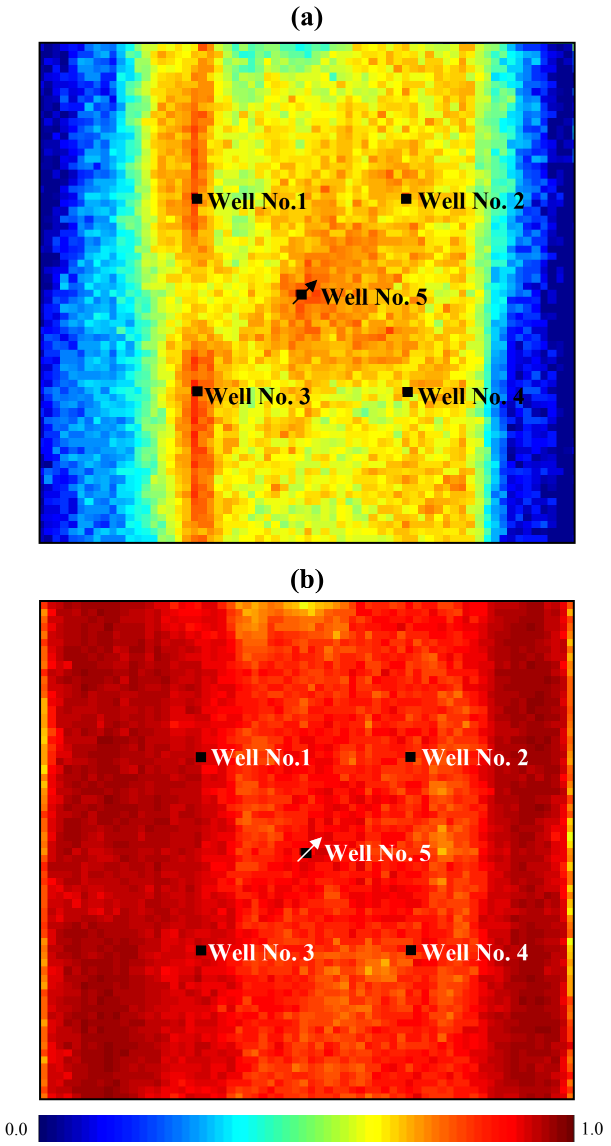

**Figure 3.A.6.20**: Consistency in model space for porosity. Average similarity between actual and inverted porosity at the first (Panel a) and final (Panel b) iterations of the inversion, respectively. Average similarity is computed for each vertical column of porosity in the time interval from 1.10 to 1.42s.

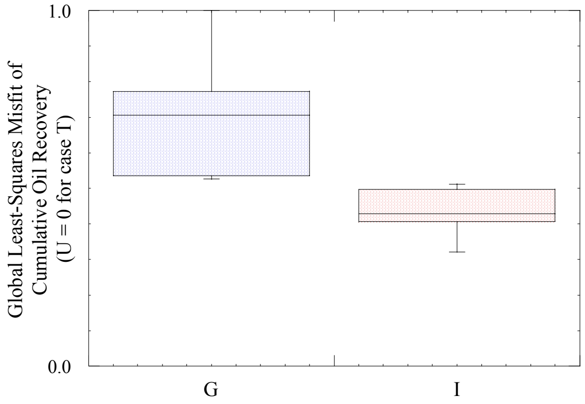

**Figure 3.A.6.21** Box plot representation of the global least-squares misfit (U) calculated for the porosity distributions rendered by standard geostatistics (case G) and the proposed inversion algorithm (case I). The global misfit or uncertainty is computed with the formula

$$U(t) = \frac{1}{t_t} \int_{t=0}^{t=t_t} \left[ d_{caseX}(t) - d_{caseT}(t) \right]^2 dt$$, where d(t) is cumulative oil recovery and $t_t$ is total time of simulation.

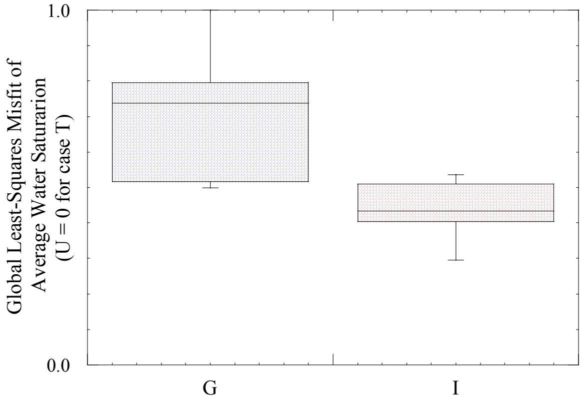

**Figure 3.A.6.22** Box plot representation of the global least-squares misfit (U) calculated for the porosity distributions rendered by standard geostatistics (case G) and the proposed inversion algorithm (case I). The global misfit or uncertainty is computed with the formula

$$U(t) = \frac{1}{t_t} \int_{t=0}^{t=t_t} \left[ d_{caseX}(t) - d_{caseT}(t) \right]^2 dt$$, where d(t) is average water saturation and $t_t$ is total time of simulation.

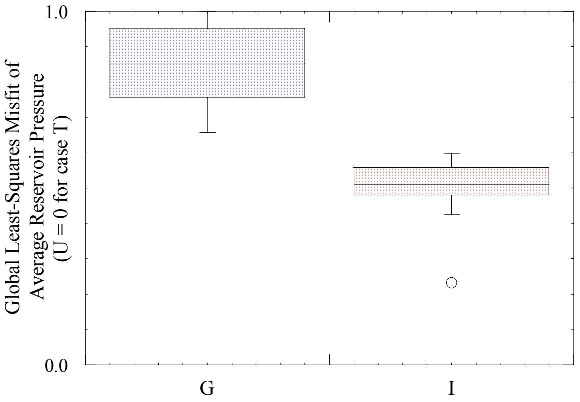

**Figure 3.A.6.23** Box plot representation of the global least-squares misfit (U) calculated for the porosity distributions rendered by standard geostatistics (case G) and the proposed inversion algorithm (case I). The global misfit or uncertainty is computed with the formula $U(t)=\frac{1}{t_t}\int_{t=0}^{t=t_t}\left[d_{caseX}(t)-d_{caseT}(t)\right]^2 dt$, where d(t) is average reservoir pressure and $t_t$ is total time of simulation.

### 3.A.6.10 Nomenclature

*1D* = One-dimension
*2D* = Two-dimensions
*3D* = Three-dimensions
*4D* = Four-dimensions
$a$, $b$ = Vertical slowness [t/L]
*AI* = Acoustic impedance [mL/L$^3$/t]
*AVO* = Amplitude versus offset
$c$ = Fluid compressibility [L$^2$/mL/t$^2$]
$C$ = Kernel function
*CDP* = Common-depth-point
*CMP* = Common-mid-point
$d$ = Depth [L] or data function
$E$ = Young's modulus [mL/t$^2$/L$^2$] or Energy function
$F$ = Flatness
$f$ = Frequency [1/t]
*Hz* = Hertz [1/t]
$k$ = Permeability [L$^2$]
$K$ = Bulk modulus [mL/t$^2$/L$^2$]
$L$ = Length [L]
$m$ = Mass [m] or model function
$\mathbf{m}$ = Model parameter vector
$n$ = Annealing time or iteration number
$N$ = Normal statistical distribution or number of
*NMO* = Normal moveout
$p$ = Pressure or stress [mL/t$^2$/L$^2$]
$P$ = Compressional wave
*PAI* = P-acoustic impedance [mL/L$^3$/t]
*PDF* = Probability density function
*PP* = Incident P-wave and reflected P-wave
$q$ = Temperature decay rate
$r$ = Reflection coefficient function
$R$ = Roughness
$s$ = Seismogram function
$S$ = Saturation, fraction, seismic data, or shear wave
*SAI* = S-acoustic impedance [mL/L$^3$/t]
$t$ = Time [t] or two-way seismic travel time
$T$ = Temperature parameter
$\mathbf{u}$ = Displacement vector
U = Global least-squares misfit
$v$ = Velocity [L/t]
$V$ = Volume [L$^3$]
$w$ = Wavelet function
$\mathbf{W}$ = Weighting matrix

## 3.A.7: SUMMARY, CONCLUSIONS, AND RECOMMENDATIONS

### 3.A.7.1 Summary

The central objective of this project was to develop a novel, efficient, accurate, and robust algorithm to quantitatively integrate 3D pre-stack seismic data, well logs, and geological information in the construction of hydrocarbon reservoir models. This novel algorithm was based on global inversion techniques and stochastic simulation. Emphasis was placed on the use of the full gather of 3D pre-stack seismic amplitude data. The algorithms developed in this project are intended to efficiently combine (a) the dense lateral coverage and amplitude variations of pre-stack seismic measurements and (b) the high vertical resolution of well-log data.

Sensitivity analyses based on global inversion were performed to quantify the benefits, limitations, and operating conditions under which the use of 3D seismic data (*i.e.*, post-stack and pseudo-angle stack seismic data) positively contributed to reducing uncertainty in both the estimation of reservoir properties and the forecast of hydrocarbon production. Examples of such an analysis included reservoir monitoring, that is, the quantitative use of time-lapse 3D seismic data to detect changes in elastic and petrophysical properties caused by dynamic reservoir behavior. Additional examples included reservoir modeling, that is, the quantitative use of pre-production 3D seismic data to construct reservoir simulation models and to appraise their static and dynamic behavior. These studies also emphasized the enhanced sensitivity to the spatial distribution of petrophysical properties available in pre-stack seismic data (*i.e.*, pseudo-angle stacks) over that of post-stack seismic data.

Based on the latter results, an evaluation was performed of different factors that conditioned the estimation of elastic parameters via global inversion of pre-stack seismic data.

Such factors included: the global optimization technique, the objective function, the sampling strategy, and measures of smoothness. Making use of the most efficient and robust methods and parameters, a novel stochastic inversion algorithm was developed based on simulated annealing and geostatistical estimation concepts. This algorithm was designed to estimate elastic parameters and their associated uncertainty in the presence of noisy and sparse seismic measurements.

Finally, using the above results, a stochastic inversion algorithm was developed for the estimation of inter-well petrophysical properties (and elastic parameters as by-products) that honored the full gather of pre-stack seismic data, well logs, property histograms, and geological information. A stochastic simulation procedure was used to extrapolate petrophysical variables laterally away from wells subject to honoring the existing 3D pre-stack seismic data in a direct and accurate manner. Joint PDFs were constructed to establish a non-deterministic (statistical) link between petrophysical and elastic parameters. A global inversion technique was used to update the initial reservoir model of petrophysical variables (generated with stochastic simulations) in response to a discrepancy between measured and synthetic 3D pre-stack seismic data. Such a strategy naturally lent itself to an efficient computer algorithm to assess uncertainty of the constructed reservoir models. Validation and testing of the inversion algorithm was performed on realistic 2D and 3D synthetic subsurface models to estimate elastic parameters and porosity. Limitations of the quantitative use of seismic data arise in cases of low-porosity formations, low fluid density contrast, and lack of correlation between petrophysical and elastic parameters. Static and dynamic comparisons were performed against models generated with standard geostatistical techniques where was found that reservoirs models constructed with the use of seismic data provided closer results to those of the reference case. This exercise also included the assessment of the uncertainty of the estimated inter-well distribution of elastic and petrophysical parameters in the presence of noisy measurements.

### 3.A.7.2 Conclusions

The following is a list of the conclusions that stem from the research work accomplished by this project:

Quantitative use of 3D seismic data improved the detection of spatial variations of petrophysical properties as a result of dynamic reservoir behavior. It also improved the construction of static models and the forecast of dynamic behavior. In reservoir monitoring, inversion of time-lapse seismic data shows that even in a worst-case scenario, such as a waterflood oil-displacement process (small density contrast between water and oil), the fluid front, elastic properties, and petrophysical properties could be inferred from seismic amplitude variations. Estimations performed with pre-stack seismic data (*i.e.*, pseudo-angle stacks) provided more accurate and reliable spatial distributions of elastic and petrophysical parameters than those performed with post-stack seismic data. In the construction of reservoir models, it was found that property distributions that made quantitative use of seismic data in their construction exhibited better similarity in model (*e.g.*, porosity) and data (*e.g.*, seismic data, fluid production data) spaces compared to reservoir models constructed without making use of seismic data (*e.g.*, standard geostatistical models). Similarly, dynamic evaluation of models constructed with the quantitative use of 3D seismic data entailed a reduction in the total uncertainty of production forecast with respect to models constructed using only well-log data.

However, it was also found that practical limitations exist to the quantitative use of seismic data in reservoir characterization. Both acquisition technology and underlying seismic wavelet limit the seismic vertical resolution to approximately 5-25 m. Lateral resolution depends mainly on bin spacing and Fresnel zonation; it often varies between 20 and 100 m. Direct estimation of petrophysical properties from seismic measurements is condition by the statistical degree of correlation between elastic and petrophysical parameter and by their geometrical support (length of resolution and depth of penetration). Low signal-to-noise ratios, processing errors, and lack of correlation between petrophysical and elastic parameters can significantly impair the quantitative use of seismic measurements for any of the algorithmic developments outlined in this project. Moreover, low porosity and highly laminated formations can cause the seismic data to lose sensitivity to fluid boundaries, especially if the density contrast between fluids is small.

Despite the above limitations, sensitivity studies, cross-validation, and testing of the algorithms developed in this project show that, under practical assumptions, the quantitative use of seismic data, especially the full pre-stack gather, allows the construction of more accurate reservoir models than traditional approaches (*e.g.*, standard geostatistical techniques) that do not make explicit use of seismic measurements. The vertical resolution of petrophysical and elastic parameters rendered by the joint stochastic inversion of 3D pre-stack seismic data and well logs are intermediate between that of the seismic and well-log data. Additionally, the stochastic formulation used in the construction of the inversion algorithms provides a natural way to assess uncertainty in the estimated petrophysical and elastic properties and, subsequently, on the corresponding forecast of hydrocarbon production.

### 3.A.7.3 Recommendations for Further Research

The development of the algorithms proposed in this project is based on various operating assumptions, including second-order stationarity and ergodicity of the unknown spatial distributions, and clearly good measurement quality (high signal-to-noise ratios). Moreover, the algorithms assume a high degree of statistical correlation between petrophysical and elastic parameters, and local (trace-by-trace) 1D model of elastic parameters.

Dynamic reservoir behavior is complex because it depends not only on the accurate description of rock properties and of their lateral continuity but also on accurate description of fluid and rock-fluid properties. Some of these properties will not have a direct relationship with elastic parameters and therefore cannot be inferred from seismic measurements. Use of dynamic data, such as time records of fluid production and well-test measurements, in conjunction with the algorithms developed in this project can provide a way to estimate such flow parameters, including permeability, permeability anisotropy, relative permeability, and capillary pressure.

An extended application of the latter recommendation involves the use of time-lapse pre-stack seismic data, not only to condition initial reservoir models (as outlined in this project) but also to estimate dynamic reservoir changes as a result of hydrocarbon production. The sensitivity of time-lapse seismic data to dynamic reservoir changes can also condition estimates of absolute permeability and permeability anisotropy.

The assumption of a locally 1D medium of elastic parameters in the numerical simulation of the pre-stack seismic data should be generalized. This will take into account more realistic wave propagation phenomena in complex 2D and 3D media. Such an approach should also allow for the simulation of laterally varying spatial distributions of elastic parameters within the length of a single common-mid-point gather and, therefore, will more faithfully reproduce actual wave propagation phenomena.

Computer implementation of the proposed algorithms was designed as efficiently as possible. However, the implemented global optimization techniques remain CPU intensive.

Computer parallelization, when appropriate, is an option to improve efficiency of global inversion techniques.

Finally, it is strongly suggested that the novel inversion algorithms proposed and developed in this project be applied to a field data set to further evaluate the feasibility and practical limitations of sparse, noisy, and imperfect seismic and well-log measurements.

## *3.A.7.5.A Appendix A: Rock Physics Models*

### 3.A.7.5.A.1 Empirical Models

Most empirical models are based on experimental data and provide a direct calculation of $v_p$ and/or $v_s$ from knowledge of several rock parameters. The literature provides ample references for a large number of such experimental models. This appendix concentrates on the relationships introduced by Hamilton (1979) and Castagna *et al.* (1985).

#### 3.A.7.5.A.1.1 Hamilton's (1979) Model

The main objective of Hamilton's work was to establish a generalized relationship between $v_p$, $v_s$, $v_p/v_s$, and Poisson's ratio as a function of depth and for different classes of terrigenous sediments and sands. The main results of his work are relationships among the elastic variables as a function of depth for each one of the major rock types. Equations (3.A.7.5.A.1), (3.A.7.5.A.2), and (3.A.7.5.A.3), for instance, describe the compressional- and shear-wave velocities of terrigenous sediments (*e.g.*, silt-clays, turbidites, shales). These equations were calculated using rock samples collected from different parts of the world:

$$v_p = 1.511 + 1.304d - 0.741d^2 + 0.257d^3, \tag{3.A.7.5.A.1}$$

where $v_p$ is given in [km/s] and $d$ is given in [km],

$$v_s = \begin{cases} 116 + 4.65d & 0 < d < 36 \\ 237 + 1.28d & 36 < d < 120 \\ 322 + 0.58d & 120 < d < 150 \end{cases}, \tag{3.A.7.5.A.2}$$

where $v_s$ is given in [m/s] and $d$ is given in [m]. Hamilton (1979) also obtained relationships between compressional- and shear-wave velocities. These relationships are given by

$$v_s = \begin{cases} 3.884v_p - 5.757 & 1.512 < v_p < 1.555 \\ 1.137v_p - 1.485 & 1.555 < v_p < 1.650 \\ 0.991 - 1.136v_p + 0.47v_p^2 & 1.650 < v_p < 2.150 \\ 0.78v_p - 0.962 & v_p > 2.150 \end{cases}, \tag{3.A.7.5.A.3}$$

where $v_p$ and $v_s$ are given in [km/s].

Equations (3.A.7.5.A.4) and (3.A.7.5.A.5) describe the compressional- and shear-wave velocity functions applicable to sands. The associated functional relationships with depth are given by

$$v_p = 1806d^{0.015}, \tag{3.A.7.5.A.4}$$

and

$$v_s = 128d^{0.28}, \tag{3.A.7.5.A.5}$$

where $v_p$ and $v_s$ are given in [m/s] and $d$ is given in [m].

#### 3.A.7.5.A.1.2. Castagna *et al.*'s (1985) Model

Castagna *et al.* (1985) report relationships between compressional- and shear-wave velocities applicable to siliciclastic rocks. Measurements performed on a variety of water-saturated mudrocks suggest that $v_p$ and $v_s$ are controlled mainly by mineralogy. Making use of in-situ sonic and seismic data, the authors find the following relationship between $v_p$ and $v_s$:

$$v_p = 1.16 v_s + 1.36 , \tag{3.A.7.5.A.6}$$

where velocities are given in [km/s].

For sandstones, conventional log analysis was carried out on rocks sampled from the Frio Formation, to determine porosity ($\phi$) and clay content ($V_{cl}$) from gamma ray, neutron, and density logs. The resulting relationships for this formation are as follows:

$$v_p = 5.81 - 9.42\phi - 2.21 V_{cl} , \tag{3.A.7.5.A.7}$$

and

$$v_s = 3.89 - 7.07\phi - 2.04 V_{cl} \tag{3.A.7.5.A.8}$$

where velocities are given in [km/s], and $\phi$ and $V_{cl}$ are given as dimensionless fractions. The correlation coefficient reported was 0.96 for both expressions. These results are similar to those reported by Tosaya and Nur (1982). It is possible to determine the values of $v_p$ and $v_s$ from a zero porosity clay ($V_{cl} = 1$) and clean sand ($V_{cl} = 0$) at a given value of porosity. It is also possible to establish $v_p / v_s$ relations manipulating equations (3.A.7.5.A.7) and (3.A.7.5.A.8). These relationships show that as porosity and clay volume increase, the $v_p / v_s$ also increases. Similar results were also found by Han *et al.* (1986).

### 3.A.7.5.A.2 Theoretical Models

Different theories have been put forth to describe the mechanical behavior of isotropic and homogenous rocks. In general terms, these theories fall in two categories: the first category considers pore geometry while the second one is based on global properties. The models considered in this appendix fall into the second category since they provide more practical results (Castagna and Backus, 1993).

### 3.A.7.5.A.2.1 Biot and Gassmann

Gassmann's theory rests on the assumption that relative motion between the fluid and the rock's skeleton has no influence on seismic wave propagation in fluid saturated rocks (Gassmann, 1951). This assumption is strictly valid at only low frequencies. Relative motion between the fluid and the rocks' skeleton causes energy losses because of the viscosity of the fluid. Biot-Gassmann's theory does not provide a way to evaluate the attenuation effect as a result of the relative motion between the fluid and the rock's skeleton (White, 1983). However, Biot's theory does cover the complete frequency range (Biot, 1956). Geertsma (1961) also developed equations valid for the complete frequency range based on Biot's (1956) work. Geertsma's results are summarized by the equations

$$v_p^2 = \left\{ \left( K_b + \frac{4}{3}\mu_b \right) + \frac{\dfrac{\phi\rho_b}{\kappa\rho_f} + \left(1 - \dfrac{K_b}{K_s}\right)\left(1 - \dfrac{K_b}{K_s} - \dfrac{2\phi}{\kappa}\right)}{\left(1 - \phi - \dfrac{K_b}{K_s}\right)\left(\dfrac{1}{K_s}\right) + \dfrac{\phi}{K_f}} \right\} \left\{ \frac{1}{\left(\rho_b - \dfrac{\phi\rho_f}{\kappa}\right)} \right\} \qquad (3.A.7.5.A.9)$$

and

$$v_s^2 = \left\{ \frac{\mu_b}{\left(\rho_b - \dfrac{\phi\rho_f}{\kappa}\right)} \right\}, \qquad (3.A.7.5.A.10)$$

where $v_p$ is compressional-wave velocity, $v_s$ is shear-wave velocity, $K_b$ is bulk modulus, $\mu_b$ is bulk shear (rigidity) modulus, $K_s$ is rock's dry bulk modulus, $K_f$ is fluid modulus, $\rho_b$ is bulk density, $\phi$ is porosity, and κ is the mass coupling factor which varies from one (no fluid-solid coupling) to infinity (perfect fluid-solid coupling). For the case of perfect coupling, these equations reduce to the zero-frequency case and the velocities become frequency independent.

3.A.7.5.A.2.2 Duffy and Mindlin

Duffy and Mindlin (1957) derived elastic constants assuming a face-centered cubic array of identical spheres. The main results of this model are summarized by the equations

$$v_p^2 = \frac{\left\{ C_{11} + \frac{\left(1 - \frac{C_{11} + 2C_{12}}{3K_s}\right)^2}{\frac{\phi}{K_f} + \frac{1-\phi}{K_s} - \frac{C_{11} + 2C_{12}}{3K_s^2}} \right\}}{\rho_b}, \tag{3.A.7.5.A.11}$$

and

$$v_s^2 = \frac{C_{11} + C_{12}}{2\rho_b}, \tag{3.A.7.5.A.12}$$

where the subscripted $C$ variables are given by

$$C_{11} = \frac{4 - 3\eta}{2 - \eta} \left\{ \frac{3E^2 p_e}{8\left(1-\eta^2\right)^2} \right\}^{\frac{1}{3}}, \tag{3.A.7.5.A.13}$$

and

$$C_{12} = \frac{\eta}{2(2-\eta)} \left\{ \frac{3E^2 p_e}{8\left(1-\eta^2\right)^2} \right\}^{\frac{1}{3}}. \tag{3.A.7.5.A.14}$$

Equations (3.A.7.5.A.15), (3.A.7.5.A.16), and (3.A.7.5.A.17) below summarize the basic definitions of the mechanical parameters used in the Duffy and Mindlin model. Poisson's ratio, $\eta$, can be written as

$$\eta = \frac{3K_b - 2\mu_b}{2(3K_b + \mu_b)}, \tag{3.A.7.5.A.15}$$

where $K_b$ is the bulk modulus, and $\mu_b$ is the shear (rigidity) modulus. The Young's modulus, $E$, is given by

$$E = \frac{9K_b\mu_b}{(3K_b + \mu_b)}, \tag{3.A.7.5.A.16}$$

with

$$p_e = p_{overburden} - p_{pore}, \tag{3.A.7.5.A.17}$$

where $p$ is pressure, and the subscript 'e' stands for effective.

### *3.A.7.5.B. Appendix B: Additional Relationships for Elastic Properties*

The bulk density ($\rho_b$) becomes a simple linear weighted average of the pure component density ($\rho_i$) with weights given by the volume fraction of each component ($\alpha_i$), namely,

$$\rho_b = \sum_{i=1}^{N} \alpha_i \rho_i , \tag{3.A.7.5.B.1}$$

where $i$ designates the component index and $N$ is the total number of components. In the case of a system with two lithologies (*i.e.*, sand and shale) and two fluids (*i.e.*, oil and water), equation (3.A.7.5.B.1) becomes

$$\rho_b = V_{sh}\rho_{sh} + \left(1-\phi-V_{sh}\right)\rho_{ss} + \left(\phi S_w\right)\rho_w + \left[\phi\left(1-S_w\right)\right]\rho_o , \tag{3.A.7.5.B.2}$$

where $\phi$ is porosity, $V_{sh}$ is shale volume, $S_w$ is water saturation, and $\rho$ is density. Subscripts "sh", "ss", "w", and "o" stand for shale, sand, water and oil, respectively.

The bulk modulus ($k_b$) is defined with an empirical relation among the rock's dry bulk modulus ($k_s$), and porosity ($\phi$), given by Geertsma and Smit (1961), namely,

$$\frac{K_b}{K_s} = \frac{1}{(1+50\phi)} . \tag{3.A.7.5.B.3}$$

Hamilton (1971; 1982) also established empirical relationships between matrix bulk modulus, rock's dry bulk modulus, and porosity. A simple formula applicable to clastic sediments is given by

$$\frac{K_b}{K_s} = 10^{-4.25\phi} . \tag{3.A.7.5.B.4}$$

If $\Delta p_{pore}$ is the change in pore pressure, then the change in water volume is given by $-VS_w \Delta p_{pore} / K_w$, where $K_w$ is water bulk modulus (inverse of water compressibility), and the change in oil volume is given by $-VS_o \Delta p_{pore} / K_o$. The total change in volume is the sum of the partial volume changes and is equal to $-V\Delta p_{pore} / K_f$. Consequently, the fluid bulk modulus ($K_f$) is the harmonic average of each of the elemental component values weighted by their respective volume fraction, *i.e.*,

$$\frac{1}{K_f} = \sum_{i=1}^{N} \frac{S_i}{\left(K_f\right)_i} , \tag{3.A.7.5.B.5}$$

or

$$\frac{1}{K_f} = \frac{S_w}{K_w} + \frac{S_o}{K_o} . \tag{3.A.7.5.B.6}$$

where $S_i$ is the saturation of the $i$-th fluid and $N$ is the total number of fluid components.

A central assumption made when estimating elastic parameters of rocks is that the interstitial fluid does not interact with the matrix. This assumption causes the shear modulus ($\mu_b$) of the fluid-saturated rock to be equivalent to that of the dry rock ($\mu_s$), *i.e.*,

$$\mu_b = \mu_s \, . \qquad (3.A.7.5.B.7)$$

## *3.A.7.5.C. Appendix C: Seismic Wave Propagation Fundamentals for Simulating Pre-Stack Seismograms*

### 3.A.7.5.C.1 Preliminaries

Synthetic seismograms in laterally homogeneous (1D) elastic earth models are generally computed by reflectivity method. The method is described in detail in the text book by Kennett (1983). Here the wave equations and plane wave reflection coefficients that are fundamental to the development of a reflectivity type algorithm are summarized. Among the theories and methods available to describe the wave propagation and synthesis of seismograms, the reflectivity method belongs to the category of wavenumber decomposition (Fuchs and Muller, 1971; Kennett, 1983). The name comes from the fact that the function that is integrated is the wavenumber-dependent reflection coefficients, or reflectivity coefficients, of a layered medium.

The wave equation presented in Section 3.A.2 assumes a homogenous, isotropic, and elastic medium. When modeling the subsurface as a stack of horizontally homogenous layers, inside each layer the equation of motion takes a relatively simple form. It is only necessary to match boundary conditions at the vertical interfaces between layers. Neither body forces due to gravity nor seismic sources are included in equation (3.A.2.2) introduced in Section 3.A.2. It is assumed that gravity determines (via self-compression) the constant values of the elastic parameters and that seismic sources are included through known contributions to displacement vector, $\mathbf{u}$.

For the case of reflection and transmission of plane waves at a planar interface, using Cartesian coordinates ($x, y, z$), the interfaces are by convenience located at constant values of $z$ and are assumed independent of the $y$ coordinate. The relationship between the derivative of the displacement ($\mathbf{u}$) and potentials ($\Phi$ and $\Psi$) is given by

$$\mathbf{u_x} = \Phi_x - \Psi_z \ , \ \mathbf{u_z} = \Phi_z + \Psi_x \, . \tag{3.A.7.5.C.1}$$

Wave equations for the scalar potentials $\Phi$ and $\Psi$ are provided by equations (3.A.2.3b) and (3.A.2.4b) in Section 3.A.2, respectively, and $\mathbf{u}_\mathrm{y}$ is given by,

$$\nabla^2 \mathbf{u}_\mathrm{y} = \left( \frac{\rho_b}{\mu_b} \right) \left( \frac{\partial^2 \mathbf{u}_\mathrm{y}}{\partial t^2} \right). \tag{3.A.7.5.C.2}$$

Here, $\nabla^2 = \partial^2/\partial x^2 + \partial^2/\partial y^2$ is the Laplace operator in two dimensions. Equations (3.A.2.3b), (3.A.2.3b), and (3.A.7.5.C.2) imply decoupled propagation of compressional- and shear-waves within the layers (P- and S-waves, respectively).

The boundary conditions require continuity of the stress (traction) and displacement vectors across material interfaces in solid media. At a free surface, the stress components vanish, and the displacements are unspecified. The stress components, normal ($p_{zz}$) and tangential ($p_{zx}, p_{zy}$) stresses, are given by

$$p_{zz} = \lambda(\nabla \cdot \mathbf{u}) + 2\mu(\mathbf{u}_\mathbf{z,z}),\ p_{zx} = \mu(\mathbf{u}_\mathbf{z,x} + \mathbf{u}_\mathbf{x,z}),\ p_{zy} = \mu(\mathbf{u}_\mathbf{y,z}). \tag{3.A.7.5.C.3}$$

By making use of equation (3.A.7.5.C.1), the first three boundary conditions require continuity of the following quantities

$$\frac{\lambda}{v_p^2}\Phi_{tt} + 2\mu(\Phi_{zz} + \Psi_{xz}),\ \mu\left( 2\Phi_{xz} - 2\Psi_{zz} + \frac{1}{v_s^2}\Psi_{tt} \right), \mu\left(\mathbf{u}_\mathbf{y,z}\right), \tag{3.A.7.5.C.4}$$

at all interfaces. On internal material interfaces, it is required that displacement be continuous, that is,

$$\Phi_x - \Psi_z,\ \Phi_z + \Psi_x,\ \mathbf{u}_\mathbf{y} \tag{C.5}$$

The continuity of the quantities in equations (3.A.7.5.C.4) and (3.A.7.5.C.5) at interfaces implies that there is interaction between the P-waves derived from $\Phi$ and the S-waves derived from $\Psi$ (also called SV). S-waves represented by $\mathbf{u}_y$ (also called SH) are polarized horizontally and propagate independently.

### 3.A.7.5.C.2 Reflection and Transmissions at a Planar Interface

First consider the case of one planar interface located at $z = 0$, with homogenous elastic properties above (identified with the subscript 1) and below (identified with the subscript 2). The coefficients of transmission and reflection of plane harmonic waves at this interface are essential for the treatment of a layered medium. Two cases are important to study: downgoing incident waves (propagation takes place in the upper medium) and upgoing incident waves (propagation takes place in the lower medium).

For the first case (downgoing incidence wave), if the incident wave is a P wave, the corresponding secondary waves originating at the interface are P and SV. The following equations describe the corresponding displacement potential in each medium:

$$\begin{aligned}\Phi_1 &= e^{j(\omega t - kx - l_1 z)} && \textit{incident P wave}\\ &\quad + R_{pp}^{d} e^{j(\omega t - kx + l_1 z)} && \textit{reflected P wave,}\end{aligned} \qquad (3.A.7.5.C.6a)$$

$$\Psi_1 = R_{ps}^{d} e^{j\left(\omega t - kx - l_2^{'} z\right)} \qquad \textit{reflected SV wave}, \qquad (3.A.7.5.C.6b)$$

$$\Phi_2 = T_{pp}^{d} e^{j(\omega t - kx - l_2 z)} \qquad \textit{transmitted P wave}, \qquad (3.A.7.5.C.6c)$$

and

$$\Psi_1 = T_{ps}^{d} e^{j\left(\omega t - kx - l_2^{'} z\right)} \qquad \textit{transmitted SV wave}, \qquad (3.A.7.5.C.6d)$$

where $j$ is the $\sqrt{-1}$, $\omega$ is angular frequency, $t$ is time, $k$ is horizontal wavenumber, $l$ and $l^{'}$ are the vertical wave numbers for P and S waves, respectively, the superscript $d$ designates downgoing incident wave, and $R$ and $T$ are reflection and transmission coefficients, respectively. The incident P wave is assumed to exhibit a unity potential amplitude. Therefore, the amplitudes of the secondary displacements are identical to the reflection and transmission coefficients. The expressions in equation (3.A.7.5.C.6) describe plane-waves and satisfy equations (3.A.2.3b), (3.A.2.4b), and (3.A.7.5.C.2).

In equation (3.A.7.5.C.2), all waves travel with the same horizontal wavenumber ($k$) and fulfill Snell's law. The relation between $k$ and the angle of incidence, $\theta$, is given by

$$k = \frac{\omega}{v_{p1}} \sin\theta \,. \tag{3.A.7.5.C.7}$$

On the other hand, the vertical wavenumbers $l_{1,2}$ and $l'_{1,2}$ are given by

$$l_{1,2} = \left( \frac{\omega^2}{v_{p1,2}^2} - k^2 \right)^{1/2} , \tag{3.A.7.5.C.8a}$$

and

$$l'_{1,2} = \left( \frac{\omega^2}{v_{s1,2}^2} - k^2 \right)^{1/2} , \tag{3.A.7.5.C.8b}$$

respectively. Boundary conditions at $z = 0$, for the horizontal displacement $\mathbf{u_x}$, for instance, are given by $\Phi_{1,x} - \Psi_{1,z} = \Phi_{2,x} - \Psi_{2,z}$. Thus, using matrix notation, the reflection and transmission coefficients (Aki and Richards, 2002) are given by

$$Ax = b \,, \tag{3.A.7.5.C.9a}$$

where

$$A=\begin{pmatrix} -k & -l_1^{'} & k & -l_2^{'} \\ l_1 & -k & l_2 & k \\ \rho_1\omega^2-2\mu_1k^2 & -2\mu_1kl_1^{'} & 2\mu_2k^2-\rho_2\omega^2 & -2\mu_2kl_2^{'} \\ 2\mu_1kl_1 & \rho_1\omega^2-2\mu_1k^2 & 2\mu_2kl_2 & 2\mu_2k^2-\rho_2\omega^2 \end{pmatrix}, \qquad (3.A.7.5.C.9b)$$

$$x=\begin{pmatrix} R_{pp}^d \\ R_{ps}^d \\ T_{pp}^d \\ T_{ps}^d \end{pmatrix}, \qquad (3.A.7.5.C.9c)$$

and

$$b=\begin{pmatrix} k \\ l \\ 2\mu_1k^2-\rho_1\omega^2 \\ 2\mu_1kl_1 \end{pmatrix}. \qquad (3.A.7.5.C.9d)$$

If the wavenumber is replaced by slowness, $s$, given by

horizontal slowness: $s=\frac{k}{\omega}=\frac{\sin\theta}{v_{p1}}$, (3.A.7.5.C.10a)

and

vertical slowness:
$$\begin{aligned} a_{1,2}&=\frac{l_{1,2}}{\omega}=\left(v_{p1,2}^{-2}-s^2\right)^{1/2} \\ b_{1,2}&=\frac{l_{1,2}^{'}}{\omega}=\left(v_{s1,2}^{-2}-s^2\right)^{1/2}, \end{aligned} \qquad (3.A.7.5.C.10b)$$

then, matrix $A$ and vector $b$ can be rewritten as

$$A=\begin{pmatrix} -s & -b_1 & s & -b_2 \\ a_1 & -s & a_2 & s \\ \rho_1-2\mu_1s^2 & -2\mu_1sb_1 & 2\mu_2s^2-\rho_2 & -2\mu_2sb_2 \\ 2\mu_1sa_1 & \rho_1-2\mu_1s^2 & 2\mu_2sa_2 & 2\mu_2s^2-\rho_2 \end{pmatrix}, \qquad (3.A.7.5.C.10a)$$

and

$$b = \begin{pmatrix} s \\ a_1 \\ 2\mu_1 s^2 - \rho_1 \\ 2\mu_1 s a_1 \end{pmatrix}, \tag{3.A.7.5.C.10b}$$

respectively. The solution to this linear system of equations is given by

$$R_{pp}^d = \frac{D_2^d - D_1^d}{D_1^d + D_2^d}, \tag{3.A.7.5.C.11a}$$

$$R_{ps}^d = -\frac{2sa_1}{D_1^d + D_2^d}\left[\left(cs^2 - \rho_1 + \rho_2\right)\left(cs^2 + \rho_2\right) + c\left(cs^2 - \rho_1\right)a_2 b_2\right], \tag{3.A.7.5.C.11b}$$

$$T_{pp}^d = \frac{2\rho_1 a_1}{D_1^d + D_2^d}\left[\left(cs^2 + \rho_2\right)b_1 - \left(cs^2 - \rho_1\right)b_2\right], \tag{3.A.7.5.C.11c}$$

and

$$T_{ps}^d = -\frac{2\rho_1 s a_1}{D_1^d + D_2^d}\left[cs^2 - \rho_1 + \rho_2 + ca_2 b_1\right], \tag{3.A.7.5.C.11d}$$

with

$$D_1^d = \left(cs^2 - \rho_1 + \rho_2\right)^2 s^2 + \left(cs^2 - \rho_1\right)^2 a_2 b_2 + \rho_1\rho_2 a_2 b_1 \quad , \tag{3.A.7.5.C.11e}$$

$$D_2^d = c^2 s^2 a_1 a_2 b_1 b_2 + \left(cs^2 + \rho_2\right)^2 a_1 b_1 + \rho_1\rho_2 a_1 b_2, \tag{3.A.7.5.C.11f}$$

and

$$c = 2\left(\mu_1 - \mu_2\right), \quad \mu_{1,2} = \rho_{1,2} v_{s1,2}^2. \tag{3.A.7.5.C.11g}$$

The coefficients in equation (3.A.7.5.C.11) are functions of the velocities and densities of the two media, and of the slowness or angle of incidence.

Following a similar derivation for the second case (upgoing incidence wave), the solution (reflection and transmission coefficients) to corresponding system of equations is given by

$$R_{pp}^{u} = \frac{D_2^u - D_1^u}{D_1^u + D_2^u}, \tag{3.A.7.5.C.12a}$$

$$R_{ps}^{u} = \frac{2sa_2}{D_1^u + D_2^u}\left[\left(cs^2 - \rho_1 + \rho_2\right)\left(cs^2 - \rho_1\right) + c\left(cs^2 + \rho_2\right)a_1 b_1\right], \tag{3.A.7.5.C.12b}$$

$$T_{pp}^{u} = \frac{2\rho_2 a_2}{D_1^u + D_2^u}\left[\left(cs^2 + \rho_2\right)b_1 - \left(cs^2 - \rho_1\right)b_2\right], \tag{3.A.7.5.C.12c}$$

and

$$T_{ps}^{u} = -\frac{2\rho_2 s a_2}{D_1^u + D_2^u}\left[cs^2 - \rho_1 + \rho_2 + ca_1 b_2\right], \tag{3.A.7.5.C.12d}$$

with

$$D_1^u = \left(cs^2 - \rho_1 + \rho_2\right)^2 s^2 + \left(cs^2 + \rho_2\right)^2 a_1 b_1 + \rho_1 \rho_2 a_1 b_2, \tag{3.A.7.5.C.12e}$$

and

$$D_2^u = c^2 s^2 a_1 a_2 b_1 b_2 + \left(cs^2 - \rho_1\right)^2 a_2 b_2 + \rho_1 \rho_2 a_2 b_1. \tag{3.A.7.5.C.12f}$$

## *3.A.7.5.D. Appendix D: Functions of Random Variables*

### 3.A.7.5.D.1 Random Variables and Probability Distribution Function

Possible outcomes of a random process can be quantified numerically through the values of a random variable (*e.g.*, $X, Y$). Then, the specific value (*e.g.*, $x, y$) or range of values taken by a random variable represent different realizations or events. A random variable may be discrete or continuous depending on the sample space (Johnson and Leone, 1977).

The function that measures the probability associated with all possible values taken by a random variable is a probability distribution, or probability density function (PDF). If $f_X$ is the PDF of $X$ then the probability ($P$) of $X$ in the interval $[a,b]$ is given by

$$P(a \le X \le b) = \int_a^b f_X(x)\,dx. \qquad (3.A.7.5.D.1)$$

It follows that the corresponding cumulative distribution function (CDF) is given by

$$F_X(x) = P(X \le x) = \int_{-\infty}^{x} f_X(\psi)\,d\psi. \qquad (3.A.7.5.D.2)$$

### 3.A.7.5.D.2 Descriptors of Random Variables

The mean, average, or expected value, $E(X)$, of a random variable $X$ with PDF $f_X$ is a measure of central behavior, and is defined as

$$E(X) = \mu_X = \int_{-\infty}^{\infty} x f_X(x)\,dx. \qquad (3.A.7.5.D.3)$$

Another important quantity is the measure of dispersion or variability with respect to a central value. Such a quantity is the variance, $Var(X)$, or $\sigma_X^2$, and is given by

$$Var(X) = \sigma_X^2 = \int_{-\infty}^{\infty} (x - \mu_X)^2 f_X(x)\,dx. \qquad (3.A.7.5.D.4)$$

3.A.7.5.D.3 Normal Distribution

The normal or Gaussian distribution is widely used in practical applications. For a random variable $X$, the normal PDF is given by

$$f_X(x) = \frac{1}{\sigma_X \sqrt{2\pi}} \exp\left[ -\frac{1}{2}\left( \frac{x-\mu_X}{\sigma_X} \right)^2 \right] \qquad -\infty < x < \infty, \tag{3.A.7.5.D.5}$$

where $\mu_X$ and $\sigma_X$ are the mean and standard deviation of the distribution, respectively. A short-hand notation for this distribution is $N(\mu_X, \sigma_X)$.

3.A.7.5.D.4 Joint and Conditional Probability Distributions

Given two random variables $X$ and $Y$, the probabilities for all possible couples of ($x$, $y$) can be described with a joint distribution function given by

$$F_{X,Y}(x,y) = P(X \le x, Y \le y) = \int_{-\infty}^{x} \int_{-\infty}^{y} f_{X,Y}(u,v)\, dv\, du. \tag{3.A.7.5.D.6}$$

This joint distribution function must satisfy the following conditions:

i) $\lim_{x\to-\infty} F_{X,Y}(x,y) = 0$, $\lim_{y\to-\infty} F_{X,Y}(x,y) = 0$, $\lim_{x\to\infty} F_{X,Y}(x,y) = F_Y(y)$, and $\lim_{y\to\infty} F_{X,Y}(x,y) = F_X(x)$;

ii) $F_{X,Y}(x,y)$ is nonnegative, and a nondecreasing function of $x$ and $y$;

iii) $\lim_{x,y\to-\infty} F_{X,Y}(x,y) = 0$, and $\lim_{x,y\to\infty} F_{X,Y}(x,y) = 1$.

If $P(X = x)$ depends on the occurrence of $Y$ or vice versa, there is a conditional distribution function of $X$ given $Y$, written as

$$f_{X|Y}(x \mid y) = \frac{f_{X,Y}(x,y)}{f_Y(y)}. \tag{3.A.7.5.D.7}$$

In general,

$$f_{X,Y}(x,y) = f_{X|Y}(x \mid y) f_Y(y), \tag{3.A.7.5.D.8}$$

or

$$f_{X,Y}(x,y) = f_{Y|X}(y \mid x) f_X(x). \tag{3.A.7.5.D.9}$$

However, if $X$ and $Y$ are statistically independent, $f_{X|Y}(x \mid y) = f_X(x)$ and $f_{Y|X}(y \mid x) = f_Y(y)$, whereupon

$$f_{X,Y}(x,y) = f_X(x) f_Y(y). \tag{3.A.7.5.D.10}$$

The associated marginal distribution functions become

$$f_X(x) = \int_{-\infty}^{\infty} f_{X|Y}(x \mid y) f_Y(y)\,dy = \int_{-\infty}^{\infty} f_{X,Y}(x,y)\,dy, \tag{3.A.7.5.D.10}$$

and

$$f_Y(y) = \int_{-\infty}^{\infty} f_{Y|X}(y \mid x) f_X(x)\,dx = \int_{-\infty}^{\infty} f_{X,Y}(x,y)\,dx. \tag{3.A.7.5.D.11}$$

Given two random variables $X$ and $Y$ that are normally distributed, their joint probability density function given by

$$\begin{gathered} f_{X,Y}(x,y) = \frac{1}{2\pi\sigma_X\sigma_Y\sqrt{1-\rho^2}} \times \\ \exp\left[ -\frac{1}{2(1-\rho^2)} \left\{ \left( \frac{x-\mu_X}{\sigma_X} \right)^2 - 2\rho \left( \frac{x-\mu_X}{\sigma_X} \right) \left( \frac{y-\mu_Y}{\sigma_Y} \right) + \left( \frac{y-\mu_Y}{\sigma_Y} \right)^2 \right\} \right], \end{gathered} \tag{3.A.7.5.D.12}$$

or

$$\begin{gathered} f_{X,Y}(x,y) = \frac{1}{\sqrt{2\pi}\sigma_X} \exp\left[ -\frac{1}{2} \left( \frac{x-\mu_X}{\sigma_X} \right)^2 \right] \times \\ \frac{1}{\sqrt{2\pi}\sigma_Y\sqrt{1-\rho^2}} \exp\left[ -\frac{1}{2} \left( \frac{y-\mu_Y-\rho(\sigma_Y/\sigma_X)(x-\mu_X)}{\sigma_Y\sqrt{1-\rho^2}} \right)^2 \right], \end{gathered} \tag{3.A.7.5.D.13}$$

where $-\infty < x < \infty; -\infty < y < \infty$, and $\rho$ is a correlation coefficient yet to be defined (see section 3.A.7.5.D.6).

### 3.A.7.5.D.5 Covariance and Semivariogram

The joint second moment of two random variables, $X$ and $Y$, is defined by the expression

$$E(XY) = \int_{-\infty}^{\infty}\int_{\infty}^{\infty} xy\, f_{X,Y}(x,y)\,dx\,dy\,. \tag{3.A.7.5.D.14}$$

If $X$ and $Y$ are statistically independent, then

$$E(XY) = \int_{-\infty}^{\infty}\int_{\infty}^{\infty} xy\, f_X(x) f_Y(y)\,dx\,dy\,, \tag{3.A.7.5.D.15}$$

or

$$E(XY) = \int_{-\infty}^{\infty} x\, f_X(x)\,dx \int_{\infty}^{\infty} y\, f_Y(y)\,dy = E(X)E(Y)\,. \tag{3.A.7.5.D.16}$$

The joint second moment of $X$ and $Y$ about the their means, $\mu_X$ and $\mu_Y$, is the covariance of $X$ and $Y$, and is given by

$$Cov(X,Y) = E[(X-\mu_X)(Y-\mu_X)] = E(XY) - E(X)E(Y)\,. \tag{3.A.7.5.D.17}$$

The function $Cov(X,Y)$ is a measure of the degree of linear co-dependence between the variables $X$ and $Y$. If $X$ and $Y$ are statistically independent, then it follows that $Cov(X,Y) = 0$.

If a spatial random variable, $X$, is available at different spatial locations ($i, j$), the autocovariance of the data $X_i$ and $X_j$ can be written in terms of the covariance and the distance between the spatial locations ($h$), that is

$$Cov\left(X_i, X_j\right) = E\left[\left(X_i - E\left(X_i\right)\right)\left(X_j - E\left(X_j\right)\right)\right]. \tag{3.A.7.5.D.18}$$

A more general formulation can be written as

$$Cov\left(h\right) = E\left[X_{i+h} X_i\right] - \left[E\left(X_i\right)\right]^2. \tag{3.A.7.5.D.19}$$

In spatial data analysis, the semivariogram or variogram is an alternative to the autocovariance function (Chilès and Delfiner, 1999) described above. Such semivariogram is normally used to model spatial variability and is related to the covariance through the expression,

$$\gamma\left(h\right) = Cov\left(0\right) - Cov\left(h\right), \tag{3.A.7.5.D.20}$$

where $Cov\left(0\right)$ is the variance of the variable $X$.

### 3.A.7.5.D.6 Correlation Coefficient

The statistical correlation between two random variables $X$ and $Y$ is measured by the correlation coefficient, $\rho$, defined as

$$\rho = \frac{Cov\left(X, Y\right)}{\sigma_X \sigma_Y} = \frac{E\left[\left(X - \mu_X\right)\left(Y - \mu_Y\right)\right]}{\sigma_X \sigma_Y}. \tag{3.A.7.5.D.21}$$

Moreover, the range of normalized covariance is $-1 \leq \rho \leq 1$. When $\rho = \pm 1$, $X$ and $Y$ are linearly related, whereas when $\rho = 0$, there is no linear relationship between $X$ and $Y$. For convenience, the correlation coefficient is represented in this project as $r^2$.

### 3.A.7.5.D.7 Kriging Estimator

Kriging is a deterministic interpolation method that provides a unique solution and that does not attempt to represent actual variability of the interpolated variable (Isaaks and Srivastava, 1989). Thus, the smoothing property of kriging dismisses local detail in place of a good average. Below, a brief description is presented of the properties of this interpolation technique.

First let us suppose that the values of property $X$ are known at $N$ different locations (*e.g.*, locations along wells) and that an estimate of this property is desired at a location, $k$. A way to perform an interpolation of $X$ at $k$ is by making use of weighted linear average of the known values of $X$, *i.e.*,

$$\hat{X}_k = \sum_{i=1}^{N} \lambda_i X_i \ , \tag{3.A.7.5.D.22}$$

where the real-valued λ coefficients are the only unknowns weights yet to be determined. By defining the simulation error as the difference between the estimated and true values one obtains

$$\varepsilon = X_k - \hat{X}_k = X_k - \sum_{i=1}^{N} \lambda_i X_i \, . \tag{3.A.7.5.D.23}$$

One way to calculate the λ coefficients is to minimize the variance between the interpolated and true values of $X$. This is equivalent to minimizing the expected value, (E{.}), of the square of the prediction error, *i.e.*,

$$E\left\{\varepsilon^2\right\} = E\left\{\left(X_k - \sum_{i=1}^{N} \lambda_i X_i\right)^2\right\}. \tag{3.A.7.5.D.24}$$

The stationary points of the squared error above are determined by taking the partial derivatives of the mean square error with respect to each of the weights, λ, and by setting them to zero, *i.e.*,

$$0 = E\left\{2\left(X_k - \sum_{i=1}^{N} \lambda_i X_i\right)\left(\sum_{i=1}^{N} X_i \delta_r^i\right)\right\} \ for \ r = 1....N \, , \tag{3.A.7.5.D.25}$$

where $\delta_r^i$=1 if $i = r$ and 0 otherwise. By defining $X_r = \sum_{i=1}^{N} X_i \delta_r^i$ , the following equation is obtained

$$E\{X_k X_r\} = E\left\{\sum_{i=1}^{N} \lambda_i X_i X_r\right\} for\ r = 1....N . \qquad (3.A.7.5.D.26)$$

By making use of the general definition of covariance (equation 3.A.7.5.D.17), between two variables, equation (3.A.7.5.D.26) can be rewritten as

$$\sum_{i=1}^{N} \lambda_i Cov_{XX}(i,r) = Cov_{XX}(k,r)\ \ for\ \ r = 1.....N . \qquad (3.A.7.5.D.27)$$

The λ parameters can be readily obtained by solving the linear system of equations (3.A.7.5.D.24). This in turn yields a value for the property $X$ at a given location within the interpolation space.

When there is a secondary variable that is spatially related to the primary variable, the information of the secondary variable can be used to get better estimates of the primary variable. Cokriging can exploit this characteristic via the expression

$$X_k = \sum_{i=1}^{N} \lambda_i X_i + \sum_{j=1}^{M} \beta_j Y_j , \qquad (3.A.7.5.D.28)$$

where the second variable $Y$ designates the additive component contribution to the primary variable $X$ , and the weights $\beta$ are to be determined by a minimization process similar to that described earlier in connection with the $\lambda$ coefficients.

### *3.A.7.5.E. Appendix E: Fluid Flow in Porous Media*

Modeling fluid-flow in a permeable medium requires mass conservation equations, constitutive equations, and fluid and rock property relations (Bear, 1972; Lake 1989). In a multi-component system, the mass conservation equation for component $i$ is given by

$$\frac{\partial(\rho_i \phi S_i)}{\partial t} + \vec{\nabla} \cdot (\rho_i \vec{v}_i) = -q_{vi}, \tag{3.A.7.5.E.1}$$

where $i$ is the component (water or oil), $\rho_i$ is the fluid density, $S_i$ is fluid saturation, $\vec{v}_i$ is the superficial velocity of phase $i$, $\phi$ is porosity, and $q_v$ is a source or sink term, and $t$ is time. For the fluid-flow considered here, there is mutual immiscibility between both of the fluid components (water and oil) meaning that phases and components are the same.

The constitutive equation is Darcy's law for phase $i$ (oil and water), given by

$$\vec{v}_i - \vec{\vec{k}} \cdot \frac{k_{ri}}{\mu_i} \left( \vec{\nabla} p_i - \zeta_i \vec{\nabla} z \right), \tag{3.A.7.5.E.2}$$

where $p$ is pressure, $z$ is vertical location, $\vec{\vec{k}}$ is the absolute permeability tensor (here assumed diagonal) of the permeable medium, $k_r$ is the relative permeability function, $\mu$ is viscosity, and $\zeta$ is the specific weight of the fluid.

A fluid property relationship is given by the compressibility equation. Accordingly, it is assumed that fluid ($c_i$) and pore ($c_f$) compressibilities,

$$c_i = \frac{1}{\rho_i} \frac{\partial \rho_i}{\partial p} \bigg|_T ,$$

and

$$c_f = \frac{1}{\phi}\frac{\partial \phi}{\partial p}\bigg|_T, \tag{3.A.7.5.E.4}$$

respectively, are constant over the pressure range of interest.

Capillary pressure ( $p_c$ ) and fluid saturations are governed by

$$p_c(S_w) = p_o - p_w, \tag{3.A.7.5.E.5}$$

and

$$S_o + S_w = 1, \tag{3.A.7.5.E.6}$$

respectively. Relative permeabilities are necessary to evaluate the fluid-flow performance of multi-phase systems. A deterministic power law was adopted to describe the dependence of relative permeability on water saturation. This power-law relationship was constructed in the following manner. First define the reduced water saturation as

$$S_w^* = \frac{S_w - S_{wi}}{1 - S_{or} - S_{wi}}. \tag{3.A.7.5.E.7}$$

The relative permeability functions are then given by

$$k_{rw}\left(S_w^*\right) = k_{rw}^o S_w^{*n}, \tag{3.A.7.5.E.8}$$

and

$$k_{ro}\left(S_w^*\right) = k_{ro}^o (1 - S_w^*)^m, \tag{3.A.7.5.E.9}$$

where, $k_{rw}^o$ and $k_{ro}^o$ are the endpoint values of the water-oil relative permeabilities, and $n$ and $m$ are the water and oil saturation exponents, respectively.

## 3.B. INSTITUTE FOR GEOPHYSICS

### 3.B.1. FULL WAVEFORM SEISMIC INVERSION USING A DISTRIBUTED SYSTEM OF COMPUTERS

### 3.B.1.1. Introduction

The aim of seismic waveform inversion is to estimate elastic properties of earth's subsurface layers from recordings of seismic waveform data. This is usually accomplished by using constrained optimization often based on very simplistic assumptions. Full waveform inversion uses a more accurate wave propagation model but is extremely difficult to use for routine analysis and interpretation. This is because computational difficulties arise due to (1) strong nonlinearity of the inverse problem, (2) extreme ill-posedness and (3) large dimensions of data and model spaces. We show that some of these difficulties can be overcome by using (1) an improved forward problem solver and efficient technique to generate sensitivity matrix, (2) an iteration adaptive regularized truncated Gauss-Newton technique, (3) an efficient technique for matrix-matrix and matrix-vector multiplication and (4) a parallel programming implementation with a distributed system of processors. We use message-passing interface (MPI) in the parallel programming environment. The details of the optimization algorithm are outlined in Roy (2002), Sen and Roy (2003) and Roy *et al.* (2003). We will briefly summarize the algorithm below following which we will describe the parallelization aspect in detail.

### 3.B.1.2. Algorithm of regularized Gauss-Newton

The regularized Gauss-Newton as implemented here, differs from the ordinary Gauss-Newton by the way in which the Gauss-Newton update is selected. It is also shown in Roy (2002) that such an update ensures robust descent. We compute regularized Gauss-Newton update corresponding to each *a posteriori* regularization parameter $\alpha$ by minimizing

Tikhonov's functional $T_K$, using nonlinear conjugate gradient (NLCG) method. We prefer NLCG because of its intrinsic property of providing stable and robust computational regime and minimum storage requirements. In the box below we describe our algorithm with a pseudo code.

Let $\mathbf{m}_0$ be the starting model describing the distribution of elastic parameters in a layered model, at the outset of the Gauss-Newton optimization, $\tau$ is the pre-assigned threshold limit for the error functional $E_k$ (it measures the misfit between observed and synthetic data) to attain at its minimum and $\eta$ is the noise estimate in the data.

```
Set maximum iteration counter (ITMAX); $\mathbf{m}_{new} = \mathbf{m}_0$; compute $F(\mathbf{m}_{new})$; $\mathbf{G}$ and $E_k$

    For $k = 0,1,2,\ldots$
        If either $E_k > \tau$ or $k <$ ITMAX
            Set $\mathbf{m}_{old} = \mathbf{m}_{new}$
            Minimize $\tilde{T}_k$ (Eq. 14) through NLCG, which gives $\Delta\mathbf{m}^{\alpha}$
            Update $\mathbf{m}_{new} = \mathbf{m}_{old} + \Delta\mathbf{m}^{\alpha}$
        Else if $E_k > \tau$ and $k \geq$ ITMAX ; Retry with new starting model
            Compute a posteriori $\alpha$ using Eqs. (17) and (18)
        Else "Print new solution upon convergence '
        End If
    End Loop
```

### 3.B.1.3. Computational Issues

While developing an inversion algorithm, the computational efficiency and robustness of the algorithm are of primary concern. Since in a model-based inversion scheme, the forward problem solver gets executed repeatedly, efficiency of forward computation plays a major role in computational efficiency of the algorithm. Our data and model spaces are very large; hence dimension of the sensitivity matrix is also very large. For example, if in an ensemble of seismic traces there are 40 seismic traces, each with 512 samples, the dimension of the data vector is 40×512 (20480). Again if the layered earth model consists of 512 layers then the dimension of the model vector is 3×512 (1536). We therefore immediately realize that major computational time in Gauss-Newton optimization will be consumed by matrix-matrix and matrix-vector multiplications.

### *3.B.1.3.1. Matrix multiplication—fast implementation*

Matrix-matrix multiplication is an essential computational step in realizing Gauss-Newton optimization. In a standard sequential algorithm the time complexity of multiplication of transpose of the sensitivity matrix **G** of order $(N \times M)$ with itself is $O(MN^2)$. If we assume that **G** is a square matrix of order $N$, then a sequential algorithm can achieve the best possible order of time complexity $O(N^{2.3755})$. We, however, desire a more substantial reduction in complexity order, which is only possible if the matrix is considerably sparse. In our application, we identify that the **G** matrix is indeed sparse (Fig. 1). Note that a change in the parameters of one layer affects the response of all the layers below it. In other words, the shallowest layer affects contributions of all the layers and the deepest layer only affects the contribution by itself. Thus for each seismogram ($p$ trace), we compute delay times for the layer in consideration and that of the deepest layer to compute a time window that is used to define a band in the **G** matrix for use in $\mathbf{G}^T\mathbf{G}$ evaluation. We also include the width of the source wavelet in defining the band. Note that the computation of the bandwidth is based on 'P-wave primaries only' model. A tolerance in it (~25 samples) in either end works well in general. This reduces computation cost in sequential algorithm for matrix-matrix multiplication significantly (Fig. 2) resulting in an increase in computation speed by a factor of seven. However, on a distributed memory parallel computer (DMPC) architecture with $P$

processors, a fully scalable parallel algorithm for matrix-matrix multiplication would take $O\left(N^{\alpha}/P\right)$ time, where $N$ is the order of the matrices and $2 < \alpha \leq 3$.

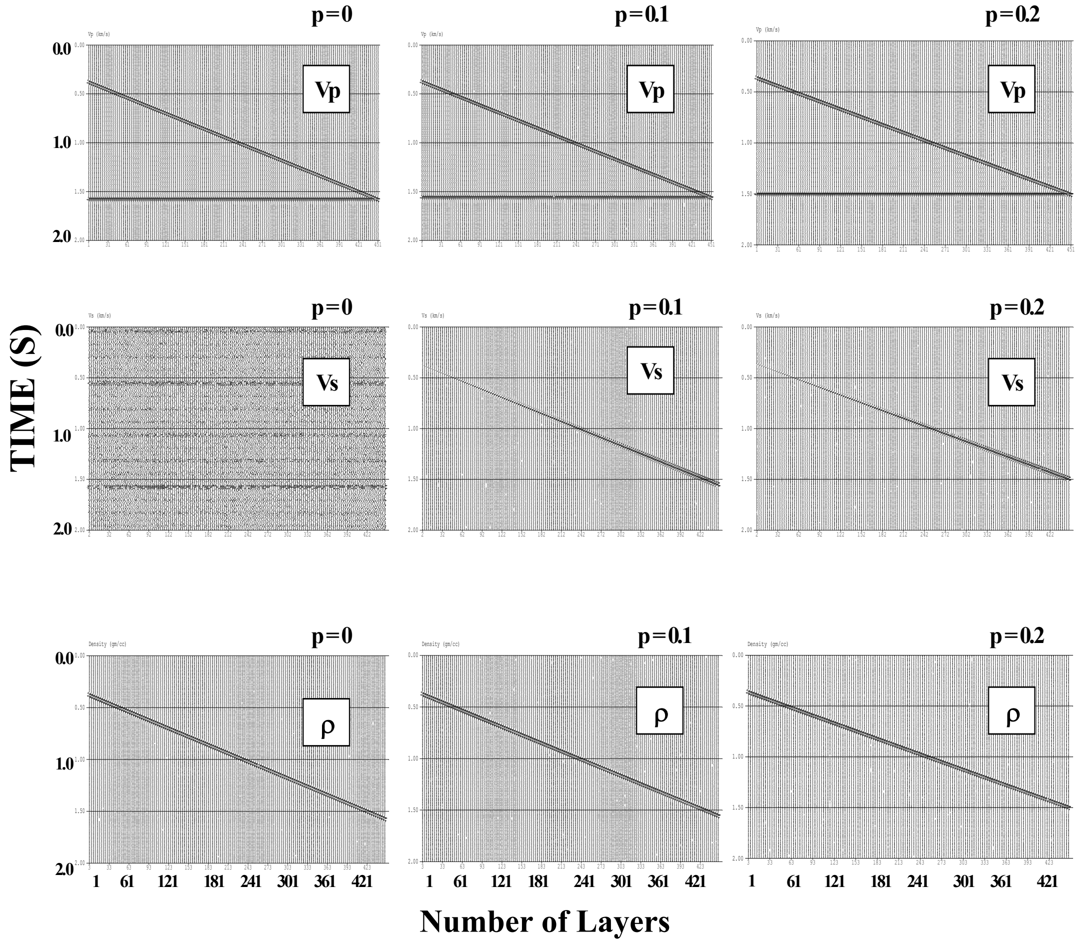

**Figure 3.B.1**. Plots of differential seismograms with respect to P-wave velocity (top row), S-wave velocity (middle row) and density (bottom row) of different layers of an earth model for three different values of ray-parameters (0.0, 0.1 and 0.2 sec/km at the left, middle and right column respectively): Each differential seismogram is a vector of Frechet derivatives with respect to model parameters. It is obvious that for p=0, the seismograms are not sensitive to changes in the shear wave velocity.

### *3.B.1.3.2. Truncated Regularized Gauss-Newton*

We used a truncated regularized Gauss-Newton (TRGN), a variant of RGN, to improve the computation efficiency of the inversion algorithm. At the onset of RGN while the starting model is far from the optimal one, a precise estimate of RGN update does not make much difference in the updated model (*Nash*, 2000). On the other hand, a precise estimate of the RGN update will be necessary as the updated model approaches the optimal one. Thus, the wasteful computation for a precise estimate of the model update can be avoided if any early termination in the inner loop of RGN is invoked adaptively. Dembo and Steihaug (1983) originally proposed such strategy of early termination in a large-scale unconstrained optimization problem through a truncated Newton (TN) algorithm. However, invoking early termination not only lowers the computational burden but also offers an additional regularization in the computation.

#### *3.B.1.3.3. Parallel computation*

Easy availability of low cost high performance computational facilities, demand of intrinsically high computational cost due to the presence of strong nonlinearity in a full waveform pre-stack inversion and large dimension of the computational regime (large data and model spaces) are some of the motivating factors for parallelization of the inversion algorithm. As our interest lies with resource utilization and portability of the software in different platforms, we design our algorithm using message-passing interface (MPI) on distributed memory parallel computer (DMPC) with a homogeneous cluster of PCs that are connected with a high speed network. A DMPC consists of finite number of processors each with its own local memory. These processors (if identical) form a homogeneous cluster and communicate with each other via MPI using high-speed network. The computations and communications in DMPC are globally synchronized into either computation or communication step. In any of the steps, a processor either remains in operation or stays idle. Hence, a busy processor in a computation step generally performs arithmetic or logical operation and elapses a constant amount of time. On the other hand, in a communication step, the processors send and receive messages via network and build a one-to-one communication. Note that each processor can receive at most one message in a communication step and elapse time of communication for each processor is assumed to be constant. Hence, the time complexity of a parallel computation on a DMPC is the sum of number of computation steps and communication steps. To reduce the wait time in communication mode, the implementation of fast electronic network is important. In our present numerical experiment, we use 32 PCs aided with AMD Athlon processors, 1GB RAM connected in a Linux cluster interconnected with high speed Myrinet™.

### 3.B.1.4. Algorithmic structure

For a nonlinear optimization problem, Schnabel (1995) identified three stages of parallelization; they include (1) parallelization of function and/or the derivative evaluation in the algorithm; (2) parallelization of linear algebra kernels; and (3) modifications of the basic algorithms, which increase the degree of intrinsic parallelism. While a coarse-grained parallelism can be invoked to the stages (1) and (3) of parallelization, fine-grained parallelism often becomes necessary in stage (2) of parallelization.

In many occasions, with a single level parallelism, a coarse-grained parallelism is favored over fine-grained parallelism. The reasons for such preference are (1) availability of concurrency at high-level language representation, and (2) superiority of concurrency achieved over fine-grained parallelism in a distributed system. Note that in a fine-grained parallelism, concurrency is available at low-level language representation. In our parallel implementation of the inversion algorithm, we have primarily adopted a single level coarse-grained parallelism. Within the DMPC architecture while evaluating a numerical method, a coarse-grained parallelization requires very little inter-processor communication and therefore loss of parallel efficiency due to communication delay as the number of processor increases (assuming that there are enough separable computations to utilize the additional processors) is insignificant. Fine-grained parallelism, on the other hand, involves much more communication among processors and care must be taken to avoid the case of inefficient machine utilization in which the communication demand among processors outperform the amount of actual computational work to be performed. We will discard fine-grained parallelization in the present context as we primarily focus on single level coarse-grained parallelization of the algorithm. We adopt here a master-slave paradigm using the MPI standard (Snir *et al.* 1996). Such paradigm increases granularity as desired. Figure 2 is the schematic plot of the algorithmic architecture that we have implemented in our application.

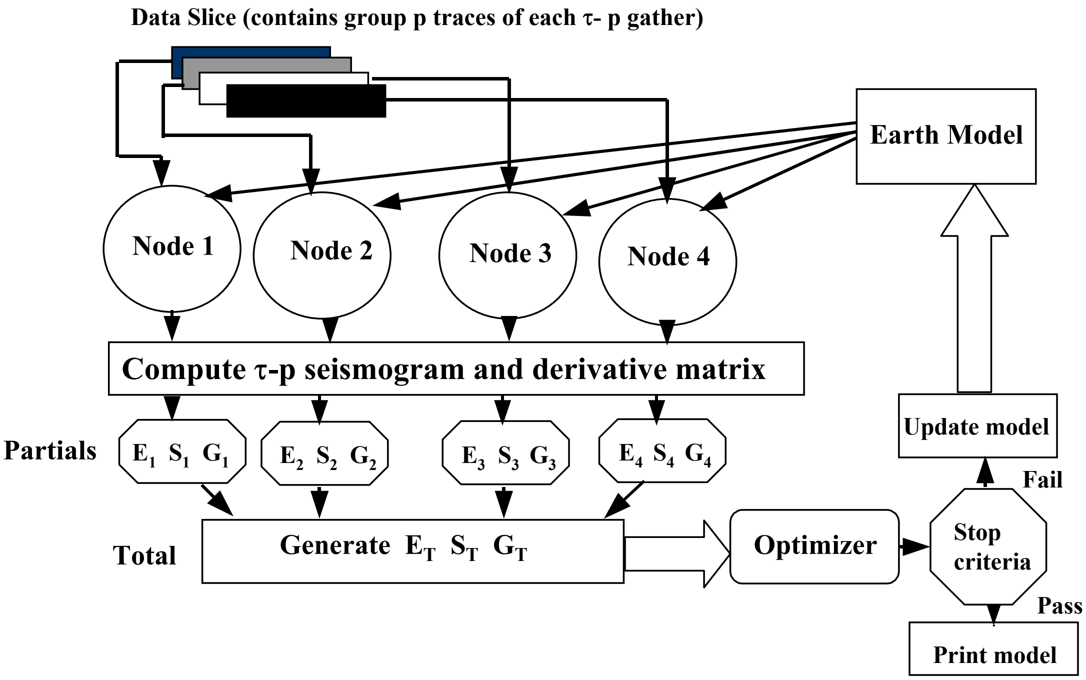

**Figure 3.B.2**. Schematic plot of algorithmic structure. The data are distributed from master node to several nodes (slave). Note that algorithm uses single program multiple data (XPMD) type parallel

computation. $E_i$, $S_i$, $G_i$ correspond to the partial values of error function, sensitivity matrix and $G^TG$ computed at processor *i*. The totals $E_i$, $S_i$, $G_i$ are computed using a global 2 sum.

Depending on the numerical method being designed, the first step of parallel algorithm is the module specification in which a method is decomposed into appropriate sub-methods with necessary specification of data dependency of entire data structure. All such sub-methods are recognized as modules. Once, the module is specified, the next step is to design schedule for the execution of each independent module. As in DMPC architecture, the communication between each processor is one-to-one and is of constant time, the design of the schedule becomes rather simple. The remaining last step is load balancing at each node, which is primarily a data distribution strategy.

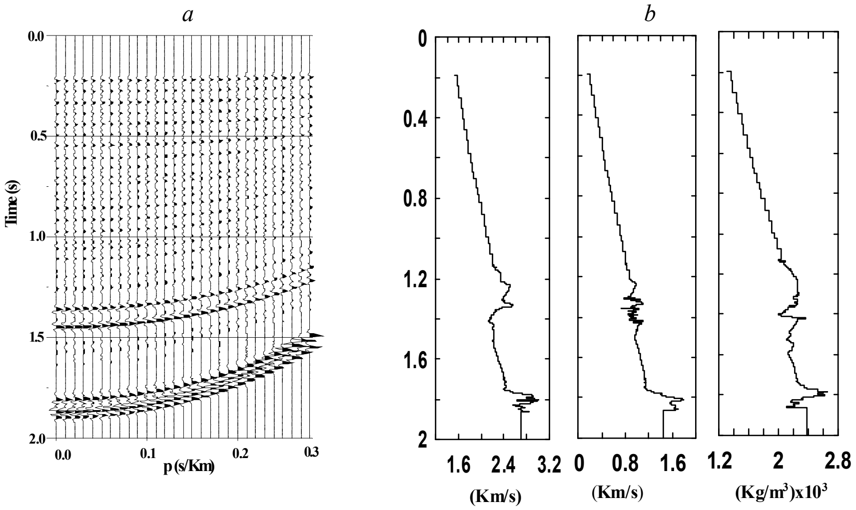

**Figure 3.B.3 (a)** Plot of synthetically generated τ-p seismograms with 5% random noise derived from a true earth Model presented in the adjacent panel. The source wavelet used is Ricker wavelet with 35 Hz peak frequency. **(b)** Plot of P-, S-velocities and density with two-way time. Note that the layer thickness is expressed in terms of two-way travel time by P-wave in a medium.

### *3.B.1.4.1. Load balancing strategy*

Load balancing is the method of dividing the amount of work to two or more processors so that an optimal amount of work gets done in the same amount of time with a minimal wait-time for each processor. Load balancing can be implemented with hardware, software, or a combination of both. A successful load balancing improves the scalability of the parallel program. A pure exploitation of parallelism does not lead to scalable parallel programs if the number of concurrent modules is not equal to the number of processors. Note that in our application (Figure 3.B.3) of inversion of plane wave seismograms, computations of plane wave seismograms are independent of each other.

Thus we distribute the tasks of generation of plane wave seismograms and their sensitivity matrices to different processors. If there are $N$ seismograms to be modeled and the number of available processors is $P$, each processor is assigned $N/P$ seismograms. If $N$ is an integral multiple of $P$, we have perfectly balanced distribution of tasks. Otherwise, the tasks are so distributed that difference in load distribution between the different processors is minimal. Note that with a single program multiple data (SPMD) programming paradigm, such a strategy has the advantage of providing high scalability. Once the synthetic seismograms and the sensitivity matrices are computed, they are transferred to the master node where model updates are computed using the Newton update formula.

### 3.B.1.5. Performance analysis of algorithm

We have implemented the parallelized version of the full waveform inversion algorithm for 2-D seismic data in pre-stack domain. The 2-D seismic data are represented by groups of seismic traces, where each group corresponds to a surface nodal point (also called common mid-point or CMP gather) of the 2-D grid. In order to realize inversion of entire 2-D seismic data (also known as 2-D seismic line), we invert seismic data corresponding to each surface nodal point. Thus, our parallelized version of inversion algorithm in any computation cycle handles groups of seismic traces belonging to a CMP. Note that we have used ($\tau$-$p$) transformed seismic data in our algorithm. We invoked master-slave paradigm where in master node we first divide the group (domain) into subgroups (sub domain) such that size of the sub groups remains the same, *i.e.*, in each sub group we assign certain number of seismic traces. Efforts are made to distribute the traces equally, if possible. Otherwise the differences are kept to a minimum. Each sub group is then allocated with the processing elements (PE) as slaves. Each PE reads the earth model and computes synthetic response and the sensitivity matrix corresponding to the designated observed seismic traces. Once computation is completed, all results are summed in the designated node (usually master node), where optimization code runs. Efficient summation is achieved using a power of 2 global sum method (Sen *et al.,* 1999). We use our algorithm on both the test case and real data set. The run of the algorithm on the test case is important, as it allows the study of the applicability of the method to real world situation and performance analysis of the algorithm. In our performance analysis test for parallel algorithm, the dimension of both data and model spaces play a major role in computational demand. Hence, we will focus mainly how parallel algorithm affects on data and model space dimensions and the number of PE used in the computation. In our test case, we use two sets of ($\tau$-$p$) seismic gather with 30 and 60 traced within a ray-parameter range of 0-0.3sec/km. Each trace contains 512 data samples with a sampling interval of 4ms. The earth model is made up of three profiles corresponding to P- and S-velocity and density of the medium. The number of data points and the sampling interval of those profiles are 453 and 4 ms respectively. This means that the earth model is assumed to be a pack of 453 layers whose thickness in terms of two-way time is 4 ms. Note that the two-way normal reflection time is computed by dividing the thickness with half the P-wave velocity of the layer. The synthetic data used in the performance analysis are shown in Fig. 3.B.5(a); the earth model parameters used in the computation of test seismograms are shown in Fig 3.B.5(b). We use the compute time for single iteration on the synthetic data set for a detailed performance analysis described below.

### *3.B.1.5.1. Elapsed time vs. number of processors*

In Figures 3.A.4(a) and 3.A.4(b) we plot elapsed time vs. number of processors and inverse of the number of processors respectively using 30 and 60 traces. Figure 3B.4(a) clearly demonstrates that with the increase of processors in the system elapsed time continues to fall. However, the rate of decrease slows down for the increase of processors from 10 to 20 in both the synthetic data examples. Figure 3.B.4(b) also depicts almost linear trend, which immediately indicates that the sequential components of the algorithm remains nearly constant with the processors.

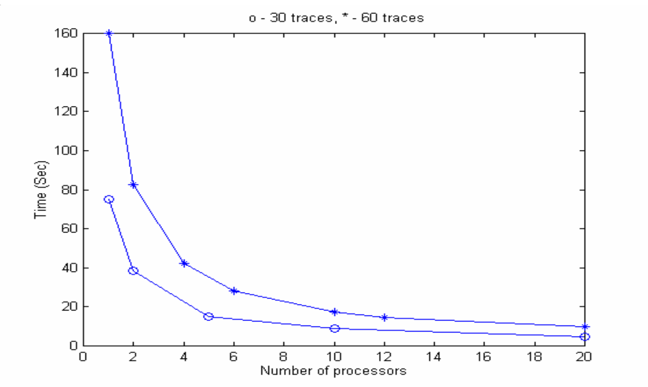

**Figure 3.B.4. (a)** The plot of the elapsed time versus the number of processors. Elapsed time decreases with the addition of the processor.

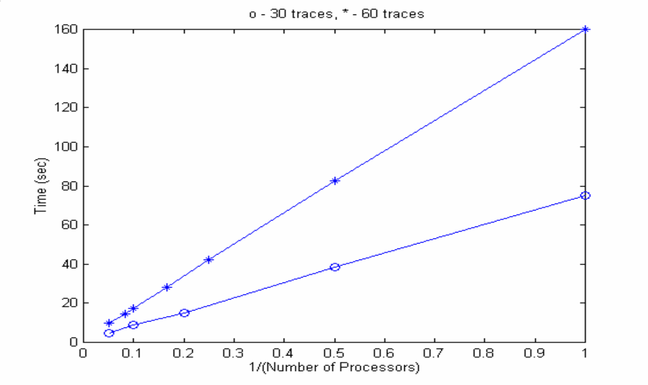

**Figure 3.B.4 (b)** Plot of the elapsed time versus the inverse of the number of processors: the plot is almost linear, indicating that the sequential components of the algorithm are nearly constant. Similar trends are observed for the two datasets containing 30 and 60 traces.

### *3.B.1.5.2. Speedup, overhead, efficiency, performance measure and efficacy on homogeneous clusters*

The speedup is the measure of acceleration for a parallel algorithm running on distributed processors with respect to the best sequential algorithm running on a sequential computer. Hence, with a parallel architecture if $T(P)$ is the time taken by $P$ processors in executing a parallel algorithm and $T(1)$ is the time taken by best sequential algorithm on a single processor then the speedup due to $P$ processors can be written as

$$S(P) = \frac{T(1)}{T(P)}\,. \tag{3.B.1}$$

In an alternative definition due to Amdahl (1987), if a parallel algorithm $\mathcal{A}$ is such that part of it, say $\alpha$ fraction (known as Amdahl fraction), is not parallelizable, then the speedup $S(P)$ is given by

$$S(P) = \frac{P}{1+(P-1)\alpha}\,. \tag{3.B.2}$$

The above equation suggests that the speedup can attain the maximum value $1/\alpha$ no matter how many processors are used for parallel computation. Hence, if 5% of the algorithm is not parallelizable, then the maximum possible speedup is 20. In a most ideal situation, when $\alpha \approx 0$, the curve of speedup versus number of processors follows a linear trend else it deviates to a sub-linear trend and may saturate normally. The above definition of speedup thus provides the basis for selecting an optimal number of processors for parallel algorithm. Interestingly, with a given problem size, the efficiency (which is a measure of average fraction of time that each processor effectively use while running a parallel algorithm) decreases with the number of processors. Note that as the number of processors increases inter-processor communication cost, idle time due to synchronization etc increase; this is expressed in terms of a metric called overhead which is defined as

$$Ov = PT(P) - T(1) . \tag{3.B.3}$$

Therefore, there exists a functional relationship between efficiency and overhead and is expressed as

$$E(P) = \frac{T(1)}{PT(P)} = \frac{1}{1 + \frac{Ov}{T(1)}} . \tag{3.B.4}$$

Thus, while overhead increases the efficiency of the parallel architecture decreases. However, substantial reduction of overhead can be achieved by increasing the granularity, which is measure of amount of computational work done before processors have to communicate. Figures. 3.B.5(a), 3.B5(b), and 3.B.5(c) are the plots of speedup, overhead and efficiency versus number of processors for the two sets of synthetic data. The speedup curve demonstrates a near linear trend, which indicates a good scalability of the algorithm and suggests that only a small fraction of code used is not parallelizable. We have found that only about 2% of our code is not parallelizable. A full-scale parallelization of an algorithm for a highly nonlinear inverse problem is difficult to achieve unless the algorithm is intrinsically decomposable. Nevertheless, in most practical situations full scale decomposition and parallelization of an algorithm is not advisable as overhead grows considerably with the addition of the processor. We observe (Fig. 3.B.5(b)) that the overhead is minimal using five processors and it increases with the increase of number of processor. However, if the problem size increases on a fixed number of processors, efficiency increases. We may keep the efficiency fixed and increase the problem size and number of processors, as overhead increases slower than the problem size. This indicates good scalability of our algorithm.

We have applied the inversion algorithm to both synthetic and field seismic data. Inversion results for the synthetic example shown in Figure 3.B.3 are presented in Figures 3.B.6(a) and 3.B.6(b). Note that data-fit is excellent; so is the model recovery. Convergence

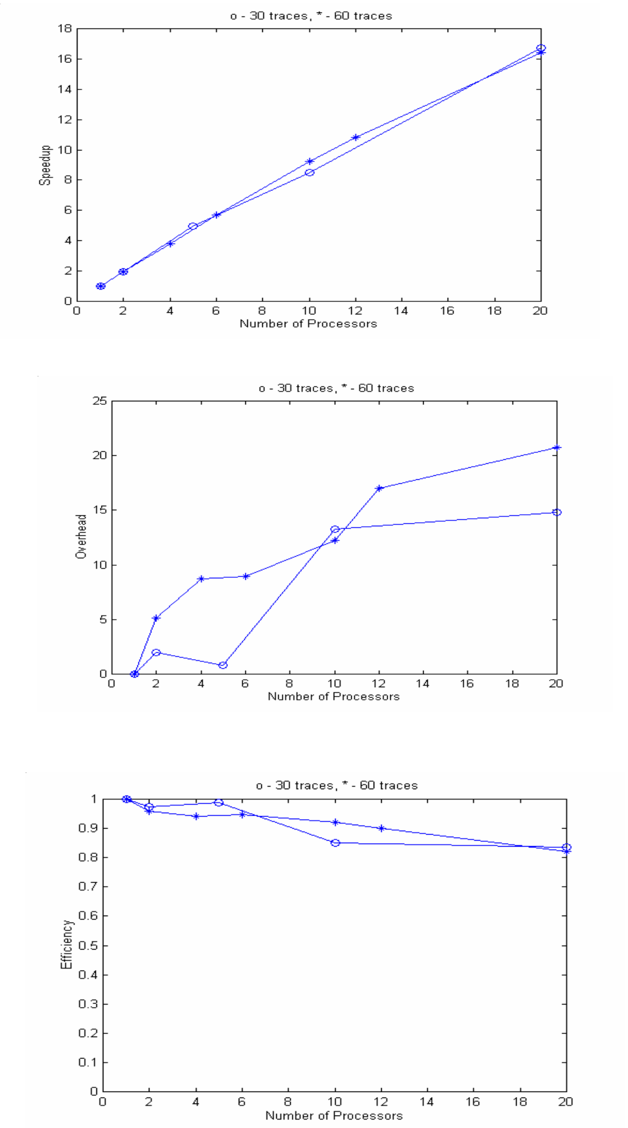

**Figure 3.B.5 (a)** Plot of speedup versus the number of processors: speedup curve nearly follows a linear trend indicating good scalability. **(b)** Plot of overhead versus the number of processors, and (c) plot of efficiency versus the number of processors. Similar trends are observed for the two datasets.

was reached in 50 iterations. The results obtained are in good agreement with the true model.

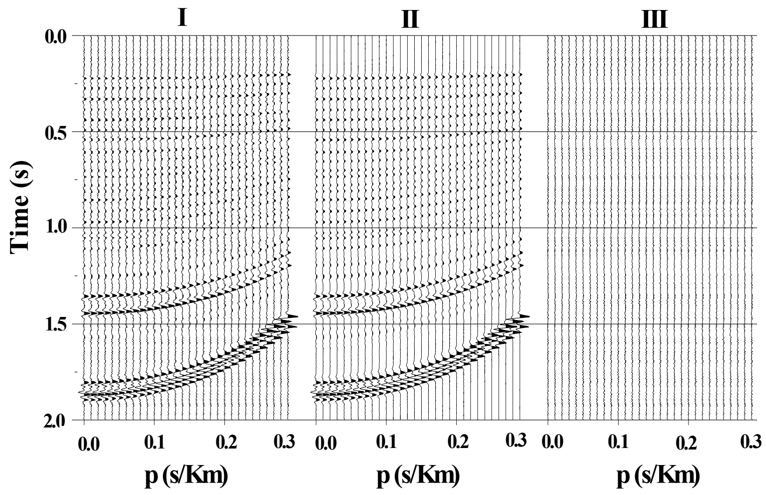

(a)

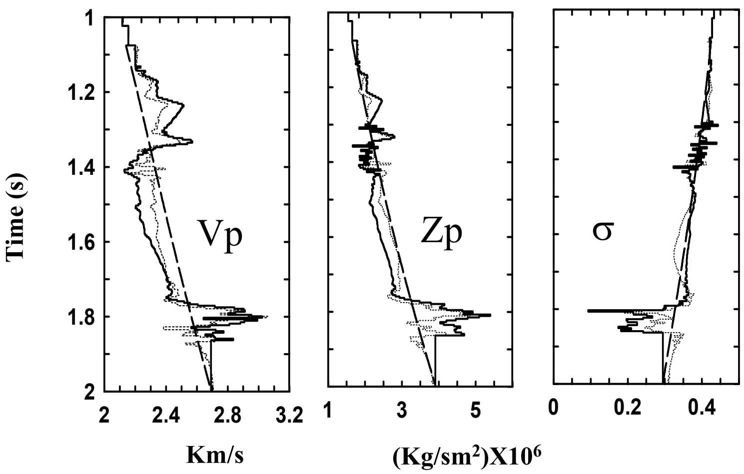

(b)

**Figure 3.B.6 (a)** Plot of data fir presented in three panels; the left panel is observed data, the middle panel id the best fit data and the right panel is the data residual. **(b)** Plots of true (solid line), initial guess (dashed line), and the inverted model (dotted line)

## 3.B.2. DIRECT ESTIMATION OF PETROPHYSICAL PARAMETERS VIA FULL WAVEFORM INVERSION OF PRE-STACK SEISMIC DATA

### 3.B.2.1. Introduction

A detailed study of static and dynamic behavior of a producing hydrocarbon reservoir is essential for the production planning of a reservoir. Interestingly, the characterization of a reservoir can primarily be realized through an estimate of spatio-temporal variability of petrophysical properties, such as porosity, fluid saturation, permeability, pore pressure etc., in the precinct of a given geological model for the reservoir. With the aid of modern wireline measurements augmented by core analysis, it is possible to estimate the one- dimensional variability of the petrophysical parameter in the close vicinity of a well fairly precisely. However, the approach is insufficient to account for lateral heterogeneity of the petrophysical properties of the reservoir. It is widely acknowledged that it is impossible to delineate a subsurface map of both vertical and lateral variation of petrophysical parameters using a limited number of wells and well logs unless supplemented by some other methods, such as geostatistical estimates, inversion of seismic data, etc. Geostatistical methods used to estimate lateral heterogeneity of petrophysical parameters of a reservoir could be useful if the number of wells with necessary well logs is considerably large. On the other hand, a surface seismic method provides more detail lateral coverage, although vertical resolution is limited to the seismic scale. Thus, reflection seismic data can be even more useful if estimates of the petrophysical parameters can be made directly from seismic data.

The effect of variation of the petrophysical properties such as porosity, fluid saturation, and lithology on the elastic moduli of the rocks and hence on the seismic velocity field has been a much studied subject. However, little has been reported so far on the estimation of petrophysical properties of the medium directly from measured seismic wave field. The objective of this paper is to study the feasibility of determining petrophysical parameters directly from full waveform inversion of pre-stack seismic data. At the outset, we give a brief background of theoretical studies in the determination of relationship between petrophysical and the elastic parameters of the rocks.

### 3.B.2.2. Relation between rock physics and petrophysical properties

The seminal works in establishing a relationship between elastic moduli and petrophysical parameters are due to Biot (1941, 1956) and Gassmann (1951) while studying the propagation of seismic waves through a pack of elastic spheres saturated with fluid. Biot-Gassmann theory allows the estimation of the bulk and shear moduli of a fluid-saturated rock formation via the equation

$$K^* = K_d + \frac{K_f\left(1-\frac{K_d}{K_m}\right)^2}{\phi+\frac{K_f}{K_m}\left(1-\phi-\frac{K_d}{K_m}\right)}, \tag{3.B.1}$$

where, $\phi$ is total porosity and $K^*$, $K_f$, $K_m$, $K_d$ are the bulk modulii of the rock saturated with fluid, the fluid, the mineral grains and the rock skeleton or the frame, respectively, and

$$G^* = G_d\,, \tag{3.B.2}$$

where, $G_d$ is the shear modulus of the frame.

It is assumed that fluid saturation plays an insignificant role in the variation of the shear modulus. Note that the frame moduli $K_d$ and $G_d$ are not the moduli due to dry rock; instead those are moduli of irreducible water-saturated rock. The above equation is based on the assumptions that the frequency of the seismic wave is low enough (theoretically zero) so that the studied rock can be considered macroscopically homogeneous, porosity and permeability are high enough, rock-fluid system is closed, and that fluids present in the rock should not interact with the rock matrix and must have negligible viscosity. The conditions described above are too stringent and hence are rarely met in most practical situations. The above equations work satisfactorily for unconsolidated water saturated sands (Wang, 2000). Thus, if all five input parameters are known then elastic moduli of a rock saturated with a fluid or a mixture of fluids can be obtained. However, precise estimates of all these input variables are difficult to obtain, as strong variability exists due to lithology, clay content, pore structure, pore aspect ratio, type of fluid content, etc. These input parameters are either measured in the laboratory or *in situ* using well logs. One of the most common log-derived parameters is porosity using either nuclear or acoustic logs. The bulk modulus of the fluid mixture can be calculated using Wood's equation (Wood, 1941) as

$$\frac{1}{K_f} = \frac{S_w}{K_w} + \frac{S_o}{K_o} + \frac{S_g}{K_g} \quad , \tag{3.B.3}$$

where, $K_w, K_o$ and $K_g$ are bulk moduli of water, oil and gas, respectively, $S_w$, $S_o$ and $S_g$ are the water, oil and gas saturations respectively. For any two phase fluid

$$\frac{1}{K_f} = \frac{S_w}{K_w} + \frac{1 - S_w}{K_{hc}} \quad . \tag{3.B.4}$$

Equation (4) can be simplified to

$$K_f = \frac{K_w K_{hc}}{K_{hc} S_w + K_w (1 - S_w)} \quad . \tag{3.B.5}$$

If the laboratory measured data for bulk moduli of the individual fluid are available and if the water saturation of the rock is obtained from well logs and the well-established empirical formula, then bulk modulus of the rock saturated with a mixture of fluids such as water-gas or water-oil can be obtained. Note that there is a strong dependency of $K_f$ on the estimation of the water saturation. Mineral constituents of a rock also have a strong effect on the rock's elastic moduli. Elastic moduli of mineral grains $K_m$ and $G_m$ can be obtained using the Voigt-Reuss-Hill (VRH) average method (Hamilton, 1971) if the rock type and its mineral contents are known. If $M$ is the effective grain modulus which can be either $K_m$ or $G_m$ then $M$ can be written in terms of Hill average (Hill, 1952) as

$$M = 0.5 * (M_v + M_r), \tag{3.B.6}$$

where $M_v$, $M_r$ are the Voigt (1928) and Reuss (1929) averages, respectively, given by

$$M_v = \sum_{i=1}^{n} c_i M_i \ , \tag{3.B.7}$$

and

$$M_r = \sum_{i=1}^{n} \frac{c_i}{M_i} \ , \tag{3.B.8}$$

where, $c_i$ and $M_i$ are the volume fraction and modulus of the $i$-th component, respectively. Note that although precise measurements of large number of mineral species are available, an accurate estimate of the volume fraction of the mineral grains present in the rock is not always possible especially from log measurements. For example, in a clastic sediment deposit, if the rocks are made up of only two species of mineral grains such as pure sand and clay (only with one variety of clay such as illite or kaolinite) then effective elastic grain moduli of the rock formation can be obtained using the above equations provided the volume fraction for each mineral present in the rock is known. It is possible to make an estimate of shale volume from natural gamma ray logs. However, Xu and White (1995) showed that

VRH estimate is insufficient for sand clay mixture as it does not account for the aspect ratio of the pore space associated with clay and sand respectively. Moreover, log analysis of natural gamma ray logs gives shale volume not the clay content. Xu and White (1995) suggested the following time average equations to determine P- and S- wave velocities $V_m^P$ and $V_m^S$ of the mineral for a rock composed of a shale-sand mixture

$$\frac{1}{V_m^P} = \frac{1-v_{sh}^*}{V_s^P} + \frac{v_{sh}^*}{V_{sh}^P} \quad , \tag{3.B.9}$$

and

$$\frac{1}{V_m^S} = \frac{1-v_{sh}^*}{V_s^S} + \frac{v_{sh}^*}{V_{sh}^S} \quad , \tag{3.B.10}$$

where,

$$v_{sh}^* = \frac{v_{sh}}{1-\phi} \quad , \tag{3.B.11}$$

$\phi$ is the effective porosity estimated from logs and $v_{sh}$ is the percent volume of the shale in the rock. The bulk density of the rock can also be written as

$$\rho_m = (1-V_{sh}^*)\rho_s + V_{sh}^*\rho_{sh} \quad . \tag{3.B.12}$$

According to Gassmann (1951), the bulk modulus of the frame is related to the porosity of the rock through Biot's coefficient, $\beta$ (Biot, 1941), which is defined as the ratio of change in fluid volume to the change in formation volume. The relation is given by

$$K_d = K_m(1-\beta) \quad . \tag{3.B.13}$$

Lee (2002) proposed the following empirical relation to compute Biot's coefficient and showed that $\beta$ asymptotically approaches the value of one with an increase in the rock's porosity:

$$\beta = \frac{\left(A_1 - A_2\right)}{1 + \exp\left[\left(\phi + \tau_1\right)/\tau_2\right]} + A_2 \quad , \tag{3.B.14}$$

where, $A_1 = -183.05186$, $A_2 = 0.99494$, $\tau_1 = 0.56468$ and $\tau_2 = 0.10817$.

Using equations 3.B.1 and 3.B.12 we obtain

$$K^* = K_m(1-\beta) + \frac{K_f \beta}{\phi + \frac{K_f}{K_m}(\beta - \phi)} \quad . \tag{3.B.15}$$

Equation 3.B.14 can be rewritten as

$$K^* = K_m(1-\beta) + \beta^2 \xi \quad , \tag{3.B.16}$$

where, $\xi$ is a modulus that measures the variation in hydraulic pressure needed to force an amount water into the formation without any change in the formation volume and is related to the Biot's coefficient $\beta$ through the equation

$$\frac{1}{\xi} = \frac{\left(\beta - \phi\right)}{K_m} + \frac{\phi}{K_f} \quad . \tag{3.B.17}$$

Therefore, the porosity $\phi$ and the water saturation $S_w$ play the most important role in determining the bulk modulus of a fluid-saturated rock. Contrary to Gassmann's (1951) assumption, Lee (2002) showed that the shear modulus also exhibits a dependence on the rock's water saturation, $S_w$, and proposed the following formula for the shear modulus of a fluid-saturated rock:

$$G^* = \frac{G_m K_m (1-\beta)(1-\phi)^2 + G_m \beta^2 \xi (1-\phi)^2}{K_m + 4G_m\left[1-(1-\phi)^2\right]/3} \quad . \tag{3.B.18}$$

The Effective formation bulk density for the fluid saturated rock can thus be written as

$$\rho^* = (1-\phi)\rho_m + \phi\rho_f \quad , \tag{3.B.19}$$

where,

$$\rho_f = S_w \rho_w + (1-S_w)\rho_{hc} \, , \tag{3.B.20}$$

where, $\rho_w$ and $\rho_{hc}$ are the densities of water and hydrocarbon, respectively. Once $K^*$, $G^*$ and $\rho^*$ are known the velocities of P- and S- waves can be determined from the well-known formulas

$$V_P = \sqrt{\frac{K^* + \frac{4}{3}G^*}{\rho^*}} \quad , \tag{3.B.21}$$

and

$$V_S = \sqrt{\frac{G^*}{\rho^*}} \quad . \tag{3.B.22}$$

### 3.B.2.3. Sensitivity of P- and S-wave velocities to porosity and saturation

In the preceding section, we established the relationships between seismic velocities and bulk density with the rock's porosity and fluid saturation. In the following, we study the variation of seismic velocity field with fractional changes in porosity and saturation. In other words, we determine the sensitivities of both P- and S-wave velocities to a variation of porosity and saturation. For sensitivity calculations, we make use of the following equations

$$\frac{\partial V_P}{\partial \phi} = \frac{1}{2\rho^* V_P}\left[\frac{\partial K^*}{\partial \phi} + \frac{4}{3}\frac{\partial G^*}{\partial \phi}\right] - \frac{V_P}{2\rho^*}\frac{\partial \rho^*}{\partial \phi} \quad , \tag{3.B.23}$$

$$\frac{\partial V_s}{\partial \phi} = \frac{1}{2\rho^* V_s}\frac{\partial G^*}{\partial \phi} - \frac{V_s}{2\rho^*}\frac{\partial \rho^*}{\partial \phi} \quad , \tag{3.B.24}$$

$$\frac{\partial V_P}{\partial S_w} = \frac{1}{2\rho^* V_P}\left[\frac{\partial K^*}{\partial S_w} + \frac{4}{3}\frac{\partial G^*}{\partial S_w}\right] - \frac{V_P}{2\rho^*}\frac{\partial \rho^*}{\partial S_w}. \quad , \tag{3.B.25}$$

and

$$\frac{\partial V_s}{\partial S_w} = \frac{1}{2\rho^* V_s}\frac{\partial G^*}{\partial S_w} - \frac{V_s}{2\rho^*}\frac{\partial \rho^*}{\partial S_w} \quad . \tag{3.B.26}$$

The necessary formulas calculating Fréchet derivative of $K^*$, $G^*$ and $\rho^*$ with respect to $\phi$ and $S_w$ are presented in Appendix-I. In the following we present a numerical experiment to study the effect of sensitivities on various lithological factors. We consider a model of sand with and without any clay content and saturated with either water or water and gas. In Figures 3.B.7 and 3.B.8 we present sensitivity curves with respect to porosity for fixed values of water saturation and clay content**.**

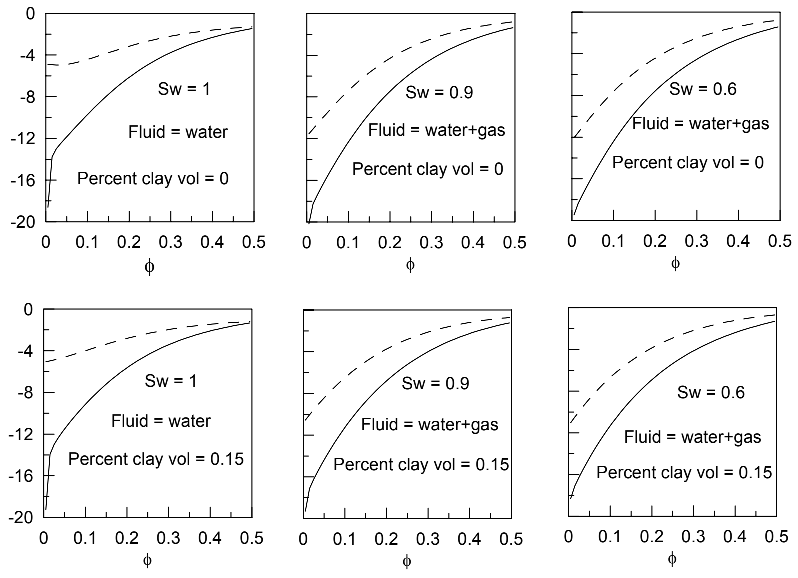

**Figure 3.B.7.** Plot of sensitivities for both P- (solid line) and S-wave (broken line) velocities with respect to porosity versus porosity for different values of saturation and clay content. Curves presented in the upper panel are for clean sand saturated with water or water and gas while curves in the lower panel are fordirty sand contaminated with 15% clay content Sensitivities for both P- and S-wave vary strongly with porosity for any value of saturation.

Note that in Figure 3.B.7 the sensitivities for both P- and S-wave velocities with respect to porosity vary strongly with porosity irrespective of the saturation or the lithological factor, such as clay content. Interestingly, a sharp variation of sensitivity of S-velocity with an increase in porosity is noticeable in both the upper and lower panels of the sensitivity plot. Such behavior is contrary to the general view that presence of gas affects little the S-velocity. On the other hand, in Figure 3.B.8 it is clear that for wide range of values of water saturation the variation of sensitivities both for P- and S-wave velocities remain constant with an increase in saturation except near the vicinity of high saturation values where there is an extremely sharp change in sensitivity values for both P- and S-wave velocities with the presence of gas.

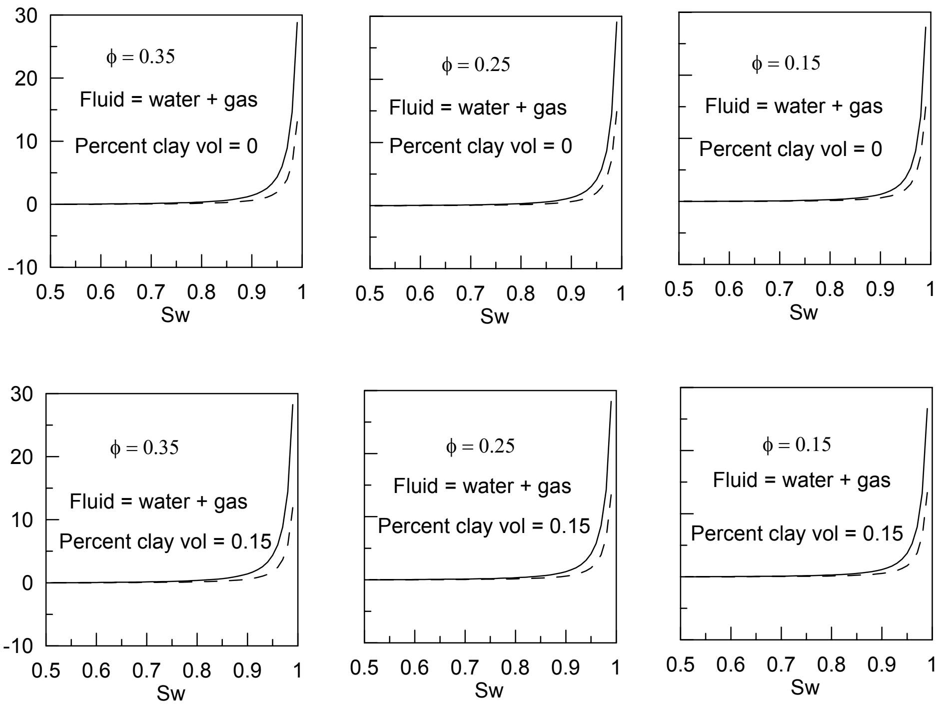

**Figure 3.B.8.** Plot of sensitivities for both P- (solid line) and S-wave (broken line) velocities with respect to saturation versus saturation for different value of porosity and clay content. Curves presented in the upper panel are for clean sand saturated with water or water and gas while curves in lower panel are for dirty sand contaminated with 15% clay. Both P- and S- velocity remain flat for most of the saturation value except near to the higher end of saturation, where it shows a vary strong variation.

Figures 3.B.9(a) and 3.B.9(b) show plots of P- and S-wave velocities as functions of porosity for different values of saturation over a clean sand model. With a given saturation value, both P- and S-velocity curves decrease with an increase in porosity. Interestingly, presence of gas causes a higher rate of change for both P- and S-velocities. Note that further increase in gas volume has little effect on the change of velocity with porosity. In Figure 3.B.9(c) we

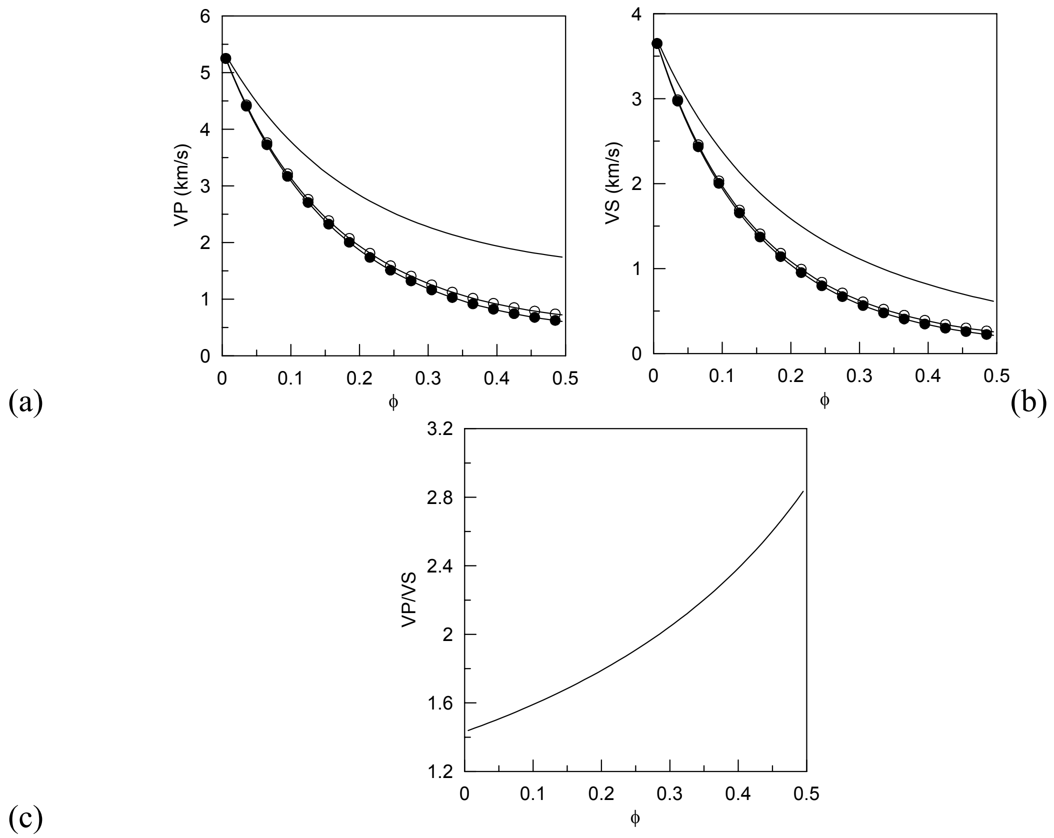

**Figure 3.B.9 (a)** Plot of P- velocities and **(b)** plot of S- velocities with respect to porosity for different values of saturation. The continuous line corresponds to 100% water saturation, the line with open circle corresponds to 90% saturation, and the line with filled circles corresponds to 60% saturation. Model considered is clean sand saturated either with water or water and gas. Panel **(c)** is the VP/VS ratio versus porosity, which continues to increase nonlinearly with porosity and the nature of curves remains the same irrespective of saturation.

plot Vp/Vs ratio with respect to porosity. Note that Vp/Vs ratio continues to increase non-linearly with porosity irrespective of saturation. To develop a comprehensive idea about the characteristics of both P- and S-wave velocities with porosity and saturation we present color filled contour maps in Figures 3.B.10(a) and 3.B.10(b).

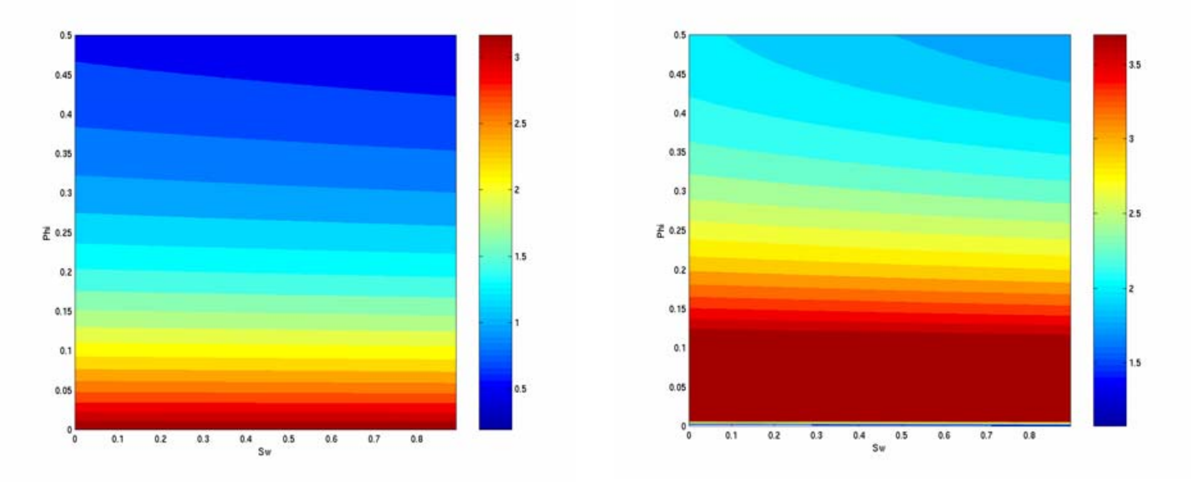

**Figure 3.B.10 (a)**Contour maps of P- velocity and (b) contour maps of S- velocity as functions of porosity and saturation.

The above contours maps show either low slope or else remain constant for a wide range of saturation values. This immediately suggests that the resolving limit of saturation from waveform inversion will also be very small.

### 3.B.2.4. Determination of petrophysical parameters and seismic velocities from well logs

In our study, we consider a set of well-log measurements acquired in the deepwater Gulf of Mexico. We make use of nuclear logs (both neutron and bulk density) and acoustic logs to determine the effective porosity of the rock formations while we use deep resistivity and porosity logs to determine water saturation using the Simandoux model. We also use the natural gamma log to estimate the percent volume of shale. In Figure 3.B.11, we present wireline-log derived porosity, saturation and percent clay content of the geological section. The log indicates presence of shale, sand sequence, and possibility of having shaly-sand or sandy shale formations. In our analysis, we consider the following log as the reference for true effective porosity and saturation of the area. In Figure 3.B.12, we present P-, S-velocities and density obtained from sonic and density logs and the corresponding values calculated using petrophysical formulas as discussed in the preceding section. Note that the predicted values of P-, S-velocities, and bulk density are in good agreement with the log-measured values.

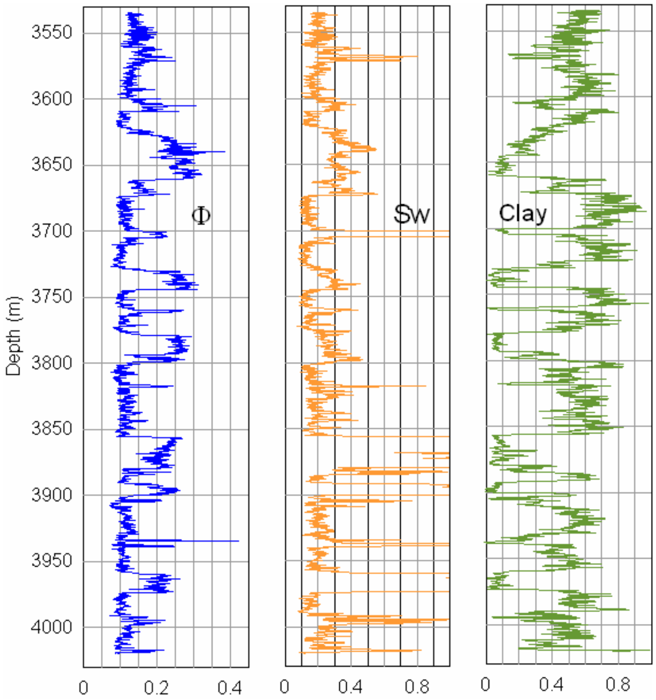

**Figure 3.B.11** Plots of wireline-log-derived porosity (blue line), water saturation (orange line) and percent clay volume (green line) with depth

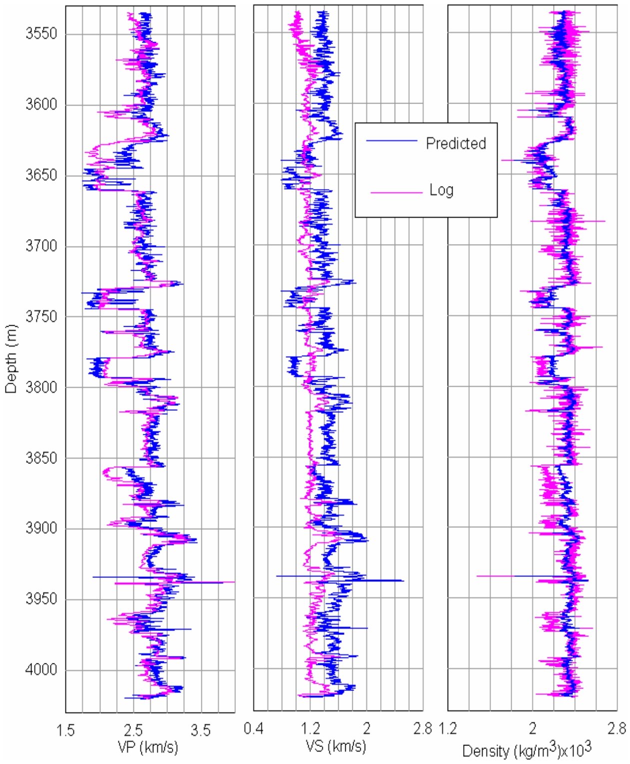

**Figure 3.B.12.** Plots of log-measured (magenta line) and predicted (blue line) values of P-, S-velocities and bulk density with depth.

In our numerical experiment, we consider those predicted values of velocities and density to be the true representations of the subsurface. We then convert these logs (Figure 3.B.12) from depth to seismic time the computation of the synthetic seismic wave field. Time converted profiles of P-, S-velocities and density are shown in Figure 3.B.13.

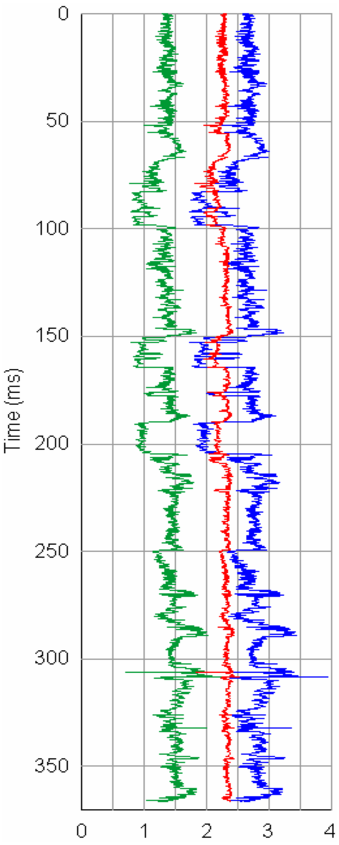

**Figure 3.B.13**. Plot of predicted values of P-, S-velocities and bulk density with two-way vertical travel time in (ms).

### 3.B.2.5. Waveform inversion in the determination of petrophysical parameters

At the outset of our numerical experiment with waveform inversion, we generate seismic gathers in the *τ-p* domain using the velocity and density profiles shown in Figure 3.B.13. To obtain a realistic *τ-p* seismic section we embed the above profiles by adding water and thick shale layers at the top, mimicking a marine geometry. We then generate a synthetic *τ-p* seismic section with a 4 ms sampling interval using a 40Hz Ricker wavelet. The synthetically generated *τ-p* seismic section is shown in Figure 3.B.14.

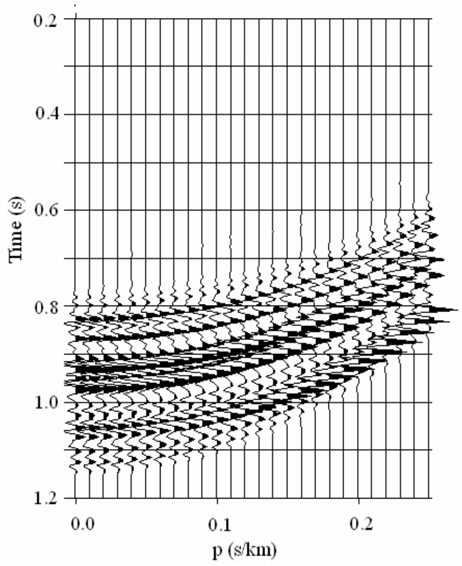

**Figure 3.B.14**. Synthetically generated $\tau$-$p$ seismic section using the time converted velocities and the density profile shown in Figure 3.B.7.

It is well recognized that, because the seismic signal is band limited, the vertical resolution of the seismic derived model is limited within the seismic scale. However, we consider a full-scale over-parameterized model in which each layer has a thickness equal to 4 ms two-way time. We then invert the $\tau$-$p$ seismic section using an adaptively regularized, truncated Gauss-Newton inversion algorithm (Sen and Roy, 2003; Roy *et al.*, 2003) assuming a constant half-space value of porosity and saturation as the *a priori* petrophysical model. For comparison with the true value of porosity and saturation, we first make a depth to time conversion of porosity and saturation logs and then resample them to 4 ms as a coarse representation. We present our inverted results as logs with 4 ms sampling interval in Figure 3.B.15. Note that the estimated porosity is in good agreement with the true value. However, the algorithm fails to retrieve the true saturation values. This is expected based on our study of sensitivities reported in the previous section. Figure 3.B.16 indicates a very good data-fit.

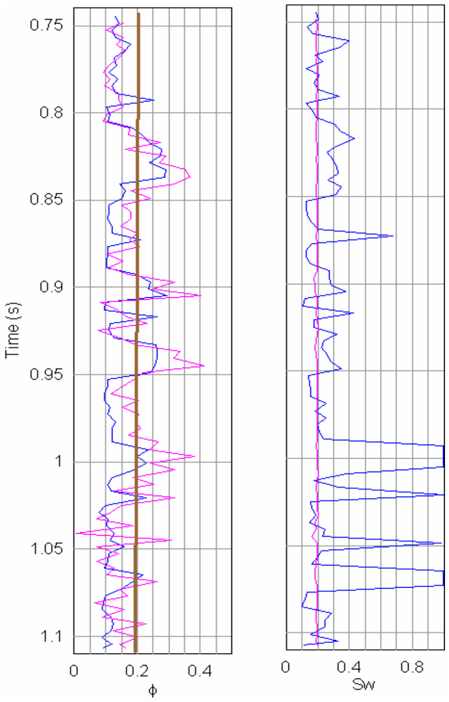

**Figure 3.B.15**. Plot of inverted porosity profile (magenta line) overlaid on true profile (blue line).

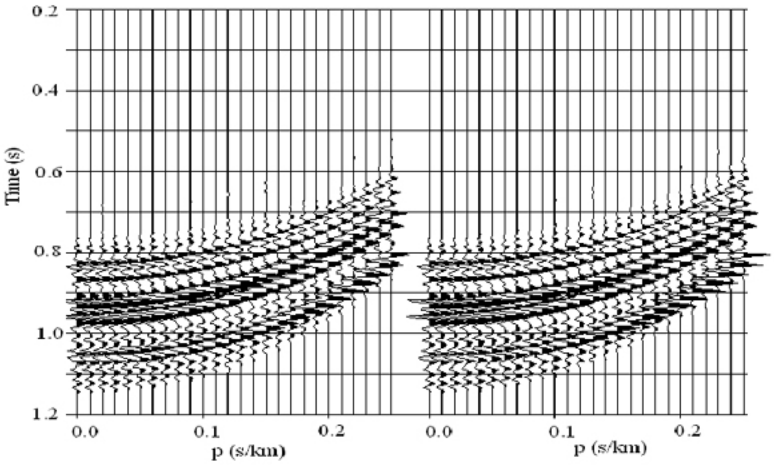

**Figure 3.B.16.** Plot of $\tau$-$p$ seismic section after inversion (left panel) and the original one (right panel)

### 3.B.2.6. Conclusions

We studied the feasibility of using full waveform inversion of pre-stack seismic data in the direct estimation of petrophysical parameters such as porosity and saturation. In determining the relationship between elastic moduli with porosity and saturation we use Lee's (2002) extension of the Biot-Gassmann model. With the sensitivity study we observe that the sensitivity of porosity to the seismic velocities (both P- and S) is considerable while that of the saturation is insignificant. This reflects in our inversion results. While it is possible to make a robust estimate of the porosity even with a flat prior, the algorithm fails to make any appropriate estimate of the saturation despite an excellent data fit.

### 3.B.3.7. Appendix I

Using equations (3.B.15) and (3.B.16), we can write

$$K^* = K_m(1-\beta) + K_m \frac{F(S_w)\beta}{K_m\phi + F(S_w)(\beta-\phi)} \quad , \tag{3.B.27}$$

where

$$F(S_w) = \frac{K_w K_{hc}}{\left(K_w - K_{hc}\right)S_w + K_w} = \frac{N}{D} \quad . \tag{3.B.28}$$

Taking partial derivatives with respect to $\phi$ and $S_w$ in (3.B.27) and using (3.B.28) we obtain

$$\frac{\partial K^*}{\partial \phi} = -K_m \frac{\partial \beta}{\partial \phi} + K_m \frac{F(S_w)\dfrac{\partial \beta}{\partial \phi} D - \left[ K_m + F(S_w)\left( \dfrac{\partial \beta}{\partial \phi} - 1 \right) \right] N}{D^2} \quad , \tag{3.B.29}$$

and

$$\frac{\partial K^*}{\partial S_w} = K_m \frac{F'(S_w)[\beta(D-N) + \phi N]}{D^2} \quad , \tag{3.B.30}$$

where, by taking the partial derivative with respect to $\phi$ in equation (3.B.13),

$$\frac{\partial \beta}{\partial \varphi} = -\frac{(A_1 - A_2)\exp\left[\left(\phi + \tau_1\right)/\tau_2\right]}{\tau_2\left\{1 + \exp\left[\left(\phi + \tau_1\right)/\tau_2\right]\right\}^2} \quad , \tag{3.B.31}$$

and by taking the derivative with respect to $S_w$ in equation (3.B.28),

$$F'(S_w) = -\frac{(K_{hc} - K_w)K_w K_{hc}}{\left[\left(K_{hc} - K_w\right)S_w + K_w\right]^2} \quad . \tag{3.B.32}$$

Again in equation (3.B.17) for the sake of simplicity we express $G^*$ as

$$G^* = \frac{G_n^*}{G_d^*} \quad , \tag{3.B.33}$$

where,

$$G_n^* = G_m K_m (1-\beta)(1-\phi)^2 + G_m \beta^2 \xi (1-\phi)^2 , \tag{3.B.34}$$

and

$$G_d^* = K_m + \frac{4}{3} G_m \left[1 - (1-\phi)^2\right] \quad . \tag{3.B.35}$$

Now, from (3.B.7)

$$\partial_x\left[G^*\right] = \frac{G_d^* \partial_x\left[G_n^*\right] - G_n^* \partial_x\left[G_d^*\right]}{\left[G_d^*\right]^2} \quad , \tag{3.B.36}$$

where the derivative index, *x,* can be either $\phi$ or $S_w$. We may then write

$$\begin{aligned}\partial_{\phi}\left[G_n^*\right] = &-2G_m K_m(1-\beta)(1-\phi) - G_m K_m (1-\phi)^2 \frac{\partial \beta}{\partial \phi} \\ &-2G_m \beta^2 \xi (1-\phi) + 2G_m \beta \xi (1-\phi)^2 \frac{\partial \beta}{\partial \phi} \\ &+ G_m \beta^2 (1-\phi)^2 \frac{\partial \xi}{\partial \phi}\end{aligned} \quad , \tag{3.B.37}$$

where

$$\frac{\partial \xi}{\partial \phi} = -\frac{K_f K_m \left[ K_f \left( \frac{\partial \beta}{\partial \phi} - 1 \right) + K_m \right]}{\left[ K_f (\beta - \phi) + K_m \phi \right]^2} \quad , \tag{3.B.38}$$

and

$$\partial_{\phi}\left[G_d^*\right] = -\frac{8}{3} G_m (1-\phi) \quad . \tag{3.B.39}$$

Similarly,

$$\partial_{Sw}\left[G_n^*\right] = G_m \beta^2 (1-\phi)^2 \frac{\partial \xi}{\partial S_w} \ , \tag{3.B.40}$$

where

$$\frac{\partial \xi}{\partial S_w} = -\frac{F'(S_w)\left[K_m - (\beta - \phi) K_f\right]}{\left[K_f (\beta - \phi) + K_m \phi\right]^2} \ , \tag{3.B.41}$$

and

$$F'(S_w) = -\frac{K_w K_{hc} (K_{hc} - K_w)}{\left[(K_{hc} - K_w) S_w + K_w\right]^2} \quad . \tag{3.B.42}$$

Again, from 3.B.18 and 3.B.19 we get

$$\frac{\partial \rho^*}{\partial \phi} = \rho_f - \rho_m \ , \tag{3.B.43}$$

and

$$\frac{\partial \rho^*}{\partial S_w} = \phi(\rho_w - \rho_{hc}) \ . \tag{3.B.44}$$

# 4. CONCLUSIONS

During the three-year period of this project, we investigated some of the fundamental issues related to estimating reservoir parameters from seismic, well log and fluid flow data. In all of our investigations, the primary goal was to obtain reasonably accurate estimates of these parameters with minimal computation effort. In addition we also investigated the effects of different data to the resolution of reservoir models estimates. We developed a full waveform inversion algorithm that is applied in the plane wave domain. The algorithm is based on a conjugate gradient algorithm in which the regularization weight is estimated automatically in each iteration. We implemented our full waveform inversion algorithm (that includes all internal multiples and converted waves) on a cluster of personal computers. We found that our algorithm is highly scalable and shows almost a linear speedup up to 16 nodes on a cluster. Thus we were able to develop a very efficient and accurate algorithm for full waveform inversion that can be used routinely for seismic data analysis. Application to an OBC dataset from the Gulf of Thailand revealed several gas zones.

Most seismic inversion algorithms provide with maps of elastic properties which are then mapped to petrophysical parameters using simple empirical formulas. To address this we developed a rigorous waveform inversion algorithm that directly provides flow parameters. We employed a modified Biot-Gassmann equation that was validated with a suite of well logs from the Gulf of Mexico. Analytic formulae were developed for computing sensitivity of seismograms to porosity and saturation. We found that the porosity is very well determined but the seismic data are insensitive to the changes in saturation.

We developed novel approaches to joint inversion of seismic and well log data and demonstrated that incorporating prior information from well logs can enhance the resolution of seismic waveform inversion significantly. We built upon the development carried out in the first two years to develop methodologies for the integration of 3D seismic data, pre-stack and post-stack, with time records of fluid production measurements. Efficient implementation of joint inversion of seismic and fluid flow data depend on the efficient forward modeling of seismic and fluid flow, realistic mapping of petrophysical parameters to elastic parameters, and efficient algorithms for inversion. All these aspects were tested rigorously during this year. Finally we developed a novel, efficient algorithm to estimate spatial distributions of porosity and permeability by jointly inverting 3D pre-stack seismic data and time records of fluid production measurements. This algorithm was successfully tested on synthetic data contaminated with random noise. It was also found that fluid production measurements acquired in production wells often don't have the degrees of freedom necessary to accurately estimate permeability distributions in the inter-well region. However, the use of pre-stack seismic data helps improve the resolution of porosity maps in the inter-well regions.

# 5. REFERENCES

Aki, K., and Richards, P.G. (2002). Quantitative Seismology: University Science Books.

Al-Najjar, N.F., Brevik, I., Psaila, D.E., and Doyen, P.M. (1999). 4D seismic modelling of the Statfjord field: Initial results: SPE 56730 presented at the Annual Technical Conference and Exhibition held in Houston, Texas, October 3-6.

Balch, R.S., Stubbs, B.S., Weiss, W.W., and Wo, S. (1999). Using artificial intelligence to correlate multiple seismic attributes to reservoir properties: SPE 56733 presented at the Annual Technical Conference and Exhibition, Houston, Texas, October 3-6.

Bassiouni, Z. (1994). Theory, measurement, and interpretation of well logs: SPE Textbook Series Vol. 4.

Bear, J. (1972). Dynamics of fluids in porous media: Dover Publications.

Ben-Menahem, A., and Singh, S.J. (1999). Seismic waves and sources: Dover Publications.

Berryman, J.G., Berge, P., and Bonner, B.P. (2000). Transformation of seismic velocity data to extract porosity and saturation values for rocks: J. Acoust. Soc. Am., Vol. 107, No. 6, 3018-3027.

Biot, M.A. (1956). The theory of propagation of elastic waves in fluid-saturated solids, I lower frequency range, II higher frequency range: J. Acoust. Soc. Am., Vol 28, No. 2, pp. 168-191.

Bortoli, L.J.F., Alabert, F., Haas, A., and Journel, A.G. (1993). Constraining stochastic images to seismic data: In Geostatistics Tróia 1992, A. Soares, ed. Kluwer, Dorrecht, Netherlands, Vol. 1, pp. 325-337.

Bourgoyne, A.T., Millheim, K.K., Chenevert, M.E., and Young, F.S. (1991). Applied drilling engineering: SPE Textbook Series Vol 2.

Brown, A.R. (1999). Interpretation of three-dimensional seismic data: AAPG Memoir Series Vol. 42.

Bu, T., and Damsleth, E. (1995). Errors and uncertainties in reservoir performance predictions: SPE 30604 presented at the Annual Technical Conference and Exhibition, Dallas, Texas, October 22-25.

Burden, R.L., and Faires, J.D. (1993). Numerical Analysis: PWS Publishing Co.

Castagna, J.P., Batzle, M.L., and Eastwood, R.L. (1985). Relationship between compressional wave and shear wave velocities in clastic silicate rocks: Geophysics, Vol. 50, No. 4, pp. 571-581.

Castagna, J.P., and Backus, M.M. (1993). Offset-dependent reflectivity: Theory and practice of AVO analysis: Society of Exploration Geophysics.

Castagna, J.P., Swan, H.W., and Foster, D.J. (1998). Framework for AVO gradient and intercept interpretation: Geophysics, Vol. 63, No. 3, pp. 948-956.

Castagna, J.P. (2001). Recent advances in seismic lithology analysis: Geophysics, Vol. 66, No. 1, pp. 42-46.

Chawathe, A., Ouenes, A., and Weiss, W.W. (1997). Interwell property mapping using crosswell seismic attributes: SPE 38747 presented at the Annual Technical Conference and Exhibition, San Antonio, Texas, October 5-8.

Chilès, J.P., and Delfiner, P. (1999). Geostatistics: John Wiley and Sons.

Christie, M.A. (1996). Upscaling for reservoir simulation: SPE 37324, Distinguished Author Series Article.

Christie, M.A., and Blunt, M.J. (2001). Tenth SPE comparative solution project: A comparison of upscaling techniques: SPE 66599 presented at the SPE Reservoir Simulation Symposium held in Houston, Texas, February 11-14.

Chunduru, R.K., Sen, M.K., and Stoffa, P.L. (1997). Hybrid optimization methods for geophysical inversion: Geophysics, Vol. 62, No. 4, pp. 1196-1207.

Cominelli, A., Seymour, R., Stradiotti, A., and Waggoner, J. (2002). Integrating time-lapse data in the history match of a gas-condensate reservoir: EAGE 64 Annual Conference and Exhibition, Florence, Italy, May 27–30.

Debeye, H., Sabbah, E., and van der Made, P.M. (1996). Stochastic inversion: SEG 66 Annual International Meeting held in Denver, Colorado, November 10-15.

Descalzi, C., Rognoni, A., and Cigni, M. (1988). Synergetic log and core data treatment through cluster analysis: A methodology to improve reservoir description: SPE 17637 presented at the International Meeting on Petroleum Engineering held in Tianjin China, November 1-4.

Dorn, G.A. (1998). Modern 3D seismic interpretation: The Leading Edge, Vol. 17, No. 9, pp. 1262-1269.

Doyen, P.M. (1988). Porosity from seismic data: A geostatistical approach: Geophysics, Vol. 53, No. 10, pp. 1263-1275.

Duffy, J., and Mindlin, R.D. (1957). Stress-strain relations and vibrations of a granular medium: J. Appl. Mech. Vol. 24, pp. 585-593.

Elmore, W.C., and Heald, M.A. (1969). Physics of waves: Dover Publications.

Fuchs, K., and Muller, G. (1971). Computation of synthetic seismograms with the reflectivity method and comparison with observations: Geophys. J. R. Astr. Soc., Vol. 23, No. 23, pp. 417-433.

Gassmann, F. (1951). Elastic waves through a packing of spheres: Geophysics, Vol. 16, No. 4, pp. 673-685.

Geertsma, J. (1961). Velocity-log interpretation: The effect of rock bulk compressibility: Soc. Pet. Eng., Vol. 1, pp. 235-248.

Geertsma, J., and Smit, D.C. (1961). Some aspects of elastic wave propagation in fluid-saturated porous solids: Geophysics, Vol. 26, No. 2, pp. 169-181.

Geman, S., and Geman, D. (1984). Stochastic relaxation, Gibbs distributions, and the Bayesian restoration of images: IEEE Trans., Vol. PAMI-6, No. 6, pp. 721-741.

Grijalba-Cuenca, A., Torres-Verdín, C., and Debeye, H.W. (2000). Geostatistical inversion of 3D seismic data to extrapolate wireline petrophysical variables laterally away from the well: SPE 63283 presented at the Annual Technical Conference and Exhibition, Dallas, Texas, October 1-4.

Haas, A. (1993). Simulation de reservoirs pétroliers par inversion géostatistique: Cahiers de Géostatistique, Fasc. 3, Ecole des Mines de Paris, 87-99.

Haas, A., and Dubrule, O. (1994). Geostatistical inversion: a sequential method for stochastic reservoir modeling constrained by seismic data: First Break, Vol.12, No.11, pp. 561-569.

Hamilton, E.L. (1971). Elastic properties of marine sediments: J. Geophys. Res., Vol. 76, No. 2, pp. 579-604.

Hamilton, E.L. (1979). Vp/Vs and Poisson's ratios in marine sediments and rocks: J. Acoust. Soc. Am., Vol. 66, No. 4, pp. 1093-1101.

Hamilton, E.L., Bachman, R.T., Berger, W.H., Johnson, T.C., and Mayer, L.A. (1982). Acoustic and related properties of calcareous deep-sea sediments: J. Sed. Pet., Vol. 52, No. 3, pp. 733-753.

Han, D., Nur, A., and Morgan, D. (1986). Effect of porosity and clay content on wave velocities in sandstones: Geophysics, Vol. 51, No. 11, pp. 2093-2107.

Hilterman, J.F. (1999). Seismic amplitude interpretation: Society of Exploration Geophysicists.

Hornarpour, M., Koederitz, L.F., and Harvey, A.H. (1982). Empirical equations for estimating two-phase relative permeability in consolidated rocks: Journal of Petroleum Technology, Vol. 34, pp. 2905-2908.

Ingber, L. (1989). Very fast simulated re-annealing: Math. Comput. Modelling, Vol. 12, No. 8, pp. 967-973.

Ingber, L. (1993). Simulated annealing: practice versus theory: Math. Comput. Modelling, Vol. 18, No.11, pp. 29-57.

Isaaks, E.H., and Srivastava, R.M. (1989). Applied geostatistics: Oxford University Press.

Jensen, J.L., Lake, L.W., Corbett, P.W.M., and Goggin, D.J. (2000). Statistics for petroleum engineers and geoscientists: Elsevier Science Publishing Co.

Johnson, N.L., and Leone, F.C. (1977). Statistics and experimental design in engineering and the physical sciences: John Wiley and Sons.

Johnson, W.W. (1994). Permeability determination from well logs and core data: SPE 27647 presented at the Permian Basin Oil and Gas Recovery Conference held in Midland, Texas, March 16-18.

Johnston, D.H., Eastwood, J.E., Shyeh, J.J., Vauthrin, R., Khan, M., and Stanley, L.R. (2000). Using legacy seismic data in an integrated time-lapse study: Lena field, Gulf of Mexico: The Leading Edge, Vol. 20, No. 3, pp. 294-302.

Journel, A.G., and Huijbregts, C.J. (1978). Geostatistical reservoir characterization constrained by 3D seismic data: Annual International Meeting of the European Association of Exploration Geophysicists.

Journel, A.G., and Huijbregts, C.J. (1978). Mining Geostatistics: Academic Press.

Kalkomey, C.T. (1996). Use of seismic attributes as predictors of reservoir properties: Potential risks: SEG 66 Annual International Meeting held in Denver, Colorado, November 10-15.

Kennett, B.L.N. (1983). Seismic wave propagation in stratified media: Cambridge University Press.

Kirkpatrick, S., Elatt, C.D., and Vecchi, M.P. (1983). Optimization by simulated annealing: Science, Vol. 220, No.4598, pp. 671-680.

Kumar, A., Farmer, C.L., Jerauld, G.R., and Li, D. (1997). Efficient upscaling from cores to simulation models: SPE 38744 presented at the SPE Annual Technical Conference and Exhibition held in San Antonio, Texas, October 5-8.

Lake, L.W. (1989). Enhanced Oil Recovery: Prentice Hall.

Landro, M. (2001). Discrimination between pressure and fluid saturation changes from time-lapse seismic data: Geophysics, Vol. 66, No. 3, pp. 836-844.

Liner, C.L. (1999). Elements of 3D seismology: PennWell Publishing.

Lortzer, G.J.M., and Berkhout, A.J. (1992). An integrated approach to lithologic inversion, Part I: Theory: Geophysics, Vol. 57, No. 2, pp. 233-244.

Lumley, D.E. (2001). Time-lapse seismic reservoir monitoring: Geophysics, Vol. 66, No. 1, pp. 50-53.

Maureau, G.T.F.R., and van Wijhe, D.H. (1979). The prediction of porosity in the Permian (Zechstein 2) carbonate of eastern Netherlands using seismic data: Geophysics, Vol. 44, No. 9, pp. 1502-1517.

Mavko, G., Dvorkin, J., and Mukerji, T. (1998). The rock physics handbook: Tools for seismic analysis in porous media: Cambridge University Press.

Menke, W. (1989). Geophysical data analysis: Discrete inverse theory: International Geophysics Series, Vol. 45, Academic Press.

Merkel, R.H., Barree, R.D., and Towle, G. (2001). Seismic response of Gulf of Mexico reservoir rocks with variations in pressure and water saturation: The Leading Edge, Vol. 20, No. 3, pp. 290-299.

Metropolis, N., Rosenbluth, A.W., Rosenbluth, M.N., Teller, A.H., and Teller, E. (1953). Equation of state calculations by fast computing machines: J. Chem. Phys., Vol. 21, No. 6, pp. 1087-1092.

Mukerji, T., Jørstad, A., Avseth, P., Mavko, G., and Granli, J.R. (2001). Mapping lithofacies and pore-fluid probabilities in a North Sea reservoir: Seismic inversions and statistical rock physics: Geophysics, Vol. 66, No. 4, pp. 988-1001.

Oldenburg, D.W., Scheuer, T., and Levy, S. (1983). Recovery of the acoustic impedance from reflection seismograms: Geophysics, Vol. 48, No. 10, pp. 1318-1337.

Pan, G.S., Phinney, R.A., and Odom, R.I. (1988). Full-waveform inversion of plane-wave seismograms in stratified acoustic media: Theory and feasibility: Geophysics, Vol. 53, No. 1, pp. 21-31.

Pan, G.S., Young, C.Y., and Castagna, J.P. (1994). An integrated target-oriented pre-stack elastic waveform inversion: Sensitivity, calibration, and application: Geophysics, Vol. 59, No. 9, 1392-1404.

Pendrel, J.V., and van Riel, P. (1997). Estimating porosity from 3D seismic inversion and 3D geostatistics: SEG 67 Annual International Meeting held in Dallas, Texas, November 2-7.

Pizarro, J.O., and Lake, L.W. (1997). A simple method to estimate inter-well autocorrelation: paper presented at the 1997 Fourth International Reservoir Characterization Technical Conference, Houston, Texas.

Rothman, D.H. (1986). Automatic estimation of large residual statics corrections: Geophysics, Vol. 51, No. 2, pp. 332-346.

Roy, I.G., Sen, M.K., Torres-Verdín, C., and Varela, O.J. (2002). Pre-stack inversion of a Gulf of Thailand OBC data set: SEG 72 Annual International Meeting held in Salt Lake City, Utah, October 6-11.

Rutherford, S.R., and Williams, R.H. (1989). Amplitude versus offset in gas sands: Geophysics, Vol. 54, No. 6, pp. 680-688.

Salamon, P., Sibani, P., and Frost, R. (2002). Facts, conjectures, and improvements for simulated annealing: Society for Industrial and Applied Mathematics.

Sams, M.S., Atkins, D., Said, N., Parwito, E., and van Riel, P. (1999). Stochastic inversion for high resolution reservoir characterisation in the Central Sumatra Basin: SPE 57260 presented at the Asia Pacific Improved Oil Recovery Conference held in Kuala Lumpur, Malaysia, October 25-26.

Sen, M.K., and Stoffa, P.L. (1991). Nonlinear one-dimensional seismic waveform inversion using simulated annealing: Geophysics, Vol. 56, No. 10, pp. 1624-1638.

Sen, M.K., and Stoffa, P.L. (1995). Global optimization methods in geophysical inversion: Elsevier Science Publishing Co.

Sheriff, R.E. (1984). Encyclopedic dictionary of exploration geophysics: Society of Exploration Geophysicists.

Simmons, J.L., and Backus, M.M. (1996). Waveform-based AVO inversion and AVO prediction-error: Geophysics, Vol. 61, No. 6; pp. 1575–1588.

Stoffa, P.L., and Sen, M.K. (1991). Nonlinear multiparameter optimization using genetic algorithms: Inversion of plane-wave seismograms: Geophysics, Vol. 56, No. 11, pp. 1794-1810.

Tarantola, A. (1986). A strategy for nonlinear elastic inversion of seismic reflection data: Geophysics, Vol. 51, No. 10; pp. 1893-1903.

Tarantola, A. (1987). Inverse problem theory: Methods for data fitting and model parameter estimation: Elsevier Science Publishing Co.

Tiab, D., and Donaldson, E.C. (1996). Petrophysics: Theory and practice of measuring reservoir rock and fluid transport properties: Gulf Publishing Co.

Torres-Verdín, C., Victoria, M., Merletti, G., and Pendrel, J.V. (1999). Trace-based and geostatistical inversion of 3-D seismic data for thin-sand delineation: An application to San Jorge Basin, Argentina: The Leading Edge, Vol. 18, No. 9, pp. 1070-1076.

Torres-Verdín, C., Grijalba-Cuenca, A., and Debeye, H. (2000) A comparison between geostatistical inversion and conventional geostatistical simulation practices for reservoir delineation: AAPG Hedberg Research Conference on Applied Reservoir Characterization Using Geostatistics, The Woodlands, Texas, December 3-6.

Tosaya, M.N., and Nur, A. (1982). Effects of diagenesis and clays on compressional velocities in rocks: Geophysics, Res. Lett., 9, pp. 5-8.

Varela, O.J., Torres-Verdín, C., Sen, M.K., and Roy, I.G. (2002). Assessing dynamic reservoir behavior with time-lapse pre-stack seismic data: a sensitivity study based on inversion: EAGE 64 Annual Conference and Exhibition, Florence, Italy, May 27–30.

Varela, O.J., Torres-Verdín, C., Sen, M.K. (2003). Joint stochastic inversion of pre-stack seismic data and well logs for high-resolution reservoir delineation and improved production forecast: SEG 73 Annual International Meeting held in Dallas, Texas, October 26-31.

Victoria, M., Merletti, G., Grijalba-Cuenca, A., and Torres-Verdín, C. (2001). Lateral and vertical discrimination of thin-bed fluvial reservoirs: Geostatistical inversion of a 3D data set: SPE 69485 presented at the Latin American and Caribbean Petroleum Engineering Conference, Buenos Aires, Argentina, March 25-28.

Wang, Y. (1999). Approximations to the Zoeppritz equations and their use in AVO analysis: Geophysics, Vol. 64, No. 6, pp. 1920-1927.

White, J.E. (1983). Underground sound: Application of seismic waves: Elsevier Science Publishing Co.

Wyllie, M.R.J., Gregory, A.R., and Gardner, G.H.F. (1958). An experimental investigation of factors affecting elastic wave velocities in porous media: Geophysics, Vol. 23, No. 3, pp. 459-493.

Xia, G., Sen, M.K., and Stoffa, P.L. (1998). 1D elastic waveform inversion: A divide-and-conquer approach: Geophysics, Vol. 63, No. 5, pp. 1670-1684.

Yilmaz, O. (2000). Seismic data analysis: Processing, inversion, and interpretation of seismic data: Society of Exploration Geophysicists.

# 6. APPENDICES

## 6.A. MANUSCRIPTS SUBMITTED FOR PUBLICATION IN REFEREED TECHNICAL JOURNAL

Varela, O. J., Torres-Verdín, C., Sen, M. K., and Roy, I. G., 2003, Using time-lapse 3D seismic data to detect dynamic reservoir behavior due to water-oil displacement: a numerical study based on inversion, submitted for publication, **Geophysics**.

Varela, O. J., Torres-Verdín, C., and Sen, M. K., 2003, Enforcing smoothness and assessing uncertainty in nonlinear one-dimensional pre-stack seismic inversion: submitted for publication, **Geophysical Prospecting**.

Varela, O. J., Torres-Verdín, C., and Sen, M. K., 2003, Joint stochastic inversion of pre-stack seismic data and well logs for high-resolution reservoir delineation: submitted for publication, **Geophysics**.

Wu, J., Torres-Verdín, C., Varela, O. J., and Sen, M. K., 2004, Joint inversion of pre-stack 3D seismic data and time records of fluid production measurements, a numerical feasibility study: submitted for publication, **Geophysics**.

Roy, I. G., Sen, M.K., and Torres-Verdin, C**.**, 2004, Seismic waveform inversion on a cluster of personal computer, Concurrency and Computation, in press.

Roy, I. G., Sen, M. K., Torres-Verdín, C., and Varela, O. J., 2002, Pre-stack inversion of a Gulf-of-Thailand OBC data set: in press, **Geophysics**.

Sen, M.K., and Roy, I.G., 2003. Two Problems in pre-stack inversion: computation of differential seismograms and iteration adaptive regularization, **Geophysics**, 68(6), 2026-2039.

## 6.B. EXPANDED REFERENCED CONFERENCE ABSTRACTS

Varela, O. J., Torres-Verdín, C., and Sen, M. K., 2003, Joint stochastic inversion of pre-stack seismic data and well logs for high-resolution reservoir delineation and improved production forecast (Expanded Abstract): **Society of Exploration Geophysicists (SEG) 73th Ann. Internat. Mtg.**, Dallas, TX, October 26-31.

Varela, O. J., Torres-Verdín, C., and Sen, M. K., 2003, *Enforcing smoothness and assessing uncertainty in one-dimensional pre-stack seismic inversion* (Expanded Abstract): **European Association of Geoscientists and Engineers (EAGE) 65th Ann. Conference and Exhibition**, Stavanger, Norway, June 2-6.

Varela, O. J., Torres-Verdín, Sen, M. K., and Roy, I. G., 2002, *Assessing dynamic reservoir behavior with time-lapse pre-stack seismic data: a sensitivity study based on inversion* (Expanded Abstract): **European Association of Geoscientists and Engineers (EAGE) 64th Ann. Conference and Exhibition**, Florence, Italy, May 27-30.

Varela, O. J., Torres-Verdín, and Lake, L. 2002, *A numerical simulation and sensitivity study to assess the value of 3D seismic data in reducing uncertainty in reservioir production forcasts* (Expanded Abstract): **Society of Petroleum Engineers (SPE) 2002 Annual International Meeting,** San Antonio, TX, September 29-October 2.

Gambus, M., Torres-Verdín, C., and Schile, C. A., 2002, *High-resolution geostatistical inversion of a seismic data set acquired in a Gulf of Mexico gas reservoir* (Expanded Abstract): **Society of Exploration Geophysicists (SEG) 72th Ann. Internat. Mtg.**, Salt Lake City, Utah, October 6-11.

Roy, I. G., Sen, M. K., Torres-Verdín, C., and Varela, O. J., 2002, *Pre-stack inversion of a Gulf of Thailand OBC data set* (Expanded Abstract): **Society of Exploration Geophysicists (SEG) 72th Ann. Internat. Mtg.**, Salt Lake City, Utah, October 6-11.

Torres-Verdín, C., Wu, Z., Varela, O. J., Sen, M. K., and Roy, I. G., 2002, *Joint inversion of reservoir production measurements and 3D pre-stack seismic data: proof of concept* (Expanded Abstract): **Society of Exploration Geophysicists (SEG) 72th Ann. Internat. Mtg.**, Salt Lake City, Utah, October 6-11.

Varela, O. J., and Torres-Verdín, C., 2004, *Pre-stack seismic data reduces uncertainty in the appraisal of dynamic reservoir behavior* (Expanded Abstract): **Society of Exploration Geophysicists (SEG) 74th Ann. Internat. Mtg.**, Denver, CO, October 10-15.